LARGE EDDY SIMULATIONS OF COMPRESSOR TURBULENCE



Ahmad Waleed Nawab

St Catherine's College
University of Oxford

A thesis submitted for the degree of
Doctor of Philosophy

February 2020

To my parents, Amber and Saeed, and to my wife, Sana.

Large Eddy Simulations of Compressor Turbulence

Ahmad Waleed Nawab, St. Catherine's College, University of Oxford

A thesis submitted for the degree of *Doctor of Philosopy*, Trinity term 2019, under the supervision of Professor Luca di Mare.

ABSTRACT

The DPhil thesis enclosed herein reports an investigation into turbulence in compressor passages, carried out using large eddy simulations (LES) of a repeating compressor stage. The thesis starts with a description of all the numerical tools used to conduct the research. First, the underlying assumptions of LES, as well as the governing equations and the discretization methods used in the in-house CFD solver, AU3X, are explained. This is followed by a brief account of the mesh generator developed in the current DPhil. Its ability to generate high-quality multi-block structured grids of turbomachinery blade passages, whilst also ensuring perfectly-balanced domain partitioning, is demonstrated. Finally, a novel sliding plane algorithm, developed with the aim of minimizing the communication cost in massively-parallel computations, is presented.

In the early stages of the DPhil, research was also carried out into the Re_τ scaling of the Proper Orthogonal Decomposition (POD) modes of the two-point correlation tensor in turbulent channel flow. The POD modes represent an optimal basis for the two-point correlation tensor. The research conducted showed that POD modes corresponding to the large, i. e. half the channel height, streamwise and spanwise lengthscales exhibited good Re_τ scaling once the large wall-normal modes were removed. Modes corresponding to smaller streamwise and spanwise lengthscales exhibited near universality even with the inclusion of the large wall-normal modes.

The focus of the investigation into turbulence in compressor passage turbulence was the Reynolds and deterministic stress fields. The repeating compressor stage computations were performed at three points on a compressor speed line; at the design condition and at two higher flow coefficients. In most of the domain, the Reynolds stresses were larger than the deterministic stresses, and also played a larger role in the time-mean momentum balance. At the blade leading edge and passage inlet however, the deterministic stresses and deterministic stress divergence were comparable to, or larger than, the Reynolds stresses. The deterministic stresses were also significant in large phase-dependent unsteady flow features, i. e. the pressure side separation bubbles in the higher flow coefficient runs.

In the Reynolds stress budget, the deterministic stress field creates two additional budget terms: the deterministic production rate and the deterministic diffusion rate. The deterministic production and diffusion rate contributed significantly to the turbulent kinetic energy budget at the passage inlet and in the pressure side separation bubble. The deterministic production rate also appears in the deterministic stress budget, but with an opposite sign to that in the Reynolds stress budget. It is accompanied by another term that governs the rate at which Reynolds stresses transport periodic fluctuations. These were found to be the dominant terms in the deterministic kinetic energy budget throughout the blade surface boundary layers.

CONTENTS

1 Introduction 1
2 Numerical methods 3
2.1 Governing equations . . . 3
2.1.1 Scale separation and filtering . . . 3
2.1.2 Filtered transport laws . . . 6
2.2 Discretization schemes . . . 7
2.2.1 Spatial discretization . . . 7
2.2.2 Temporal discretization . . . 9
2.3 Implicit pressure correction . . . 11
2.3.1 Solution of pressure-correction . . . 13
2.4 Subgrid-scale modelling . . . 15
2.5 Grid generation . . . 18
2.6 Sliding plane . . . 27
3 Re_τ scaling of POD modes 35
3.1 Introduction . . . 35
3.2 Numerical Methods . . . 37
3.2.1 DNS database . . . 37
3.2.2 Two-point velocity correlation and the Proper Orthogonal Decomposition . . . 38
3.2.3 Symmetry groups . . . 39
3.2.4 Finite domain effects . . . 40
3.3 Two-point correlation POD modes . . . 41
3.3.1 Re_τ scaling of eigenvalues . . . 41
3.3.2 Two-point correlations and Re_τ scaling of eigenvectors . . . 42
3.4 Reynolds-stress budget . . . 54
3.5 Two-point correlations from Large Eddy Simulations . . . 56
3.6 Conclusions . . . 60
4 Deterministic and Reynolds stresses in compressor passages 61
4.1 Introduction . . . 61
4.2 Deterministic and Reynolds stress transport laws . . . 64
4.3 Repeating compressor stage . . . 66
4.4 Post-processing . . . 70
4.5 Grid refinement . . . 71
4.6 Subgrid-scale kinetic energy . . . 74
4.7 Integral lengthscales . . . 74
4.8 Mean flow . . . 77
4.9 Unsteady flow . . . 93
4.10 Reynolds and deterministic stress - inlet and outlet profiles . . . 99
4.11 Reynolds and deterministic stresses - mid-span contours and boundary layer profiles . . . 103
4.12 Reynolds stress and Deterministic stress divergence . . . 117

4.13 Reynolds and deterministic stress budgets 122
4.13.1 Kinetic energy budget 122
4.13.2 Shear stress budgets 141
4.13.3 Pressure-gradient velocity correlation 153
4.14 Statistical convergence 155
4.15 Summary and conclusions 159
5 Conclusion 161

Bibliography 163

LIST OF SYMBOLS

CHAPTER 1 INTRODUCTION

Acronyms

CFD	Computational Fluid Dynamics
RANS	Reynolds-averaged Navier-Stokes
LES	Large eddy simulation
POD	Proper orthogonal decomposition

CHAPTER 2 NUMERICAL METHODS

Acronyms

AU3X	In-house LES solver
LES	Large eddy simulation
DNS	Direct numerical simulation
SGS	Subgrid-scale stress
STS	Subtest-scale stress
CFL	Courant Friedrichs Lewy number
MPI	Message passing interface
LHS	Left-hand side
RHS	Right-hand side

Greek symbols

η	Kolmogorov scale
$\Delta(\mathbf{x})$	Filter-width
τ_{ij}^{s}	Subgrid-scale stress tensor
ν	Kinematic viscosity
ρ	Density
ω_i	Velocity vector
ν_{SGS}	Subgrid-scale viscosity
$\widetilde{\Delta}$	Test-filter width
ϵ_T	Truncation error due to non-uniform grid-spacing

Latin symbols

L	Most energetic lengthscale
Re	Reynolds number
$G(\mathbf{x}-\mathbf{x}', \Delta(\mathbf{x}))$	Filter function
$\mathbf{k_c}$	Cut-off wavenumber
u_i	Velocity vector
P	Pressure
r_i	Radius vector
C_s	SGS model scaling constant
$\overline{S}_{ij}$	Resolved strain-rate tensor
$\overline{L}_{ij}$	Resolved turbulent stress

$w(\mathbf{k}_i)$	Pulsation function
$\mathbf{e}^n$	Error vector at current iteration
$\mathbf{P}'$	Pressure-correction
$\mathbf{x}$	Grid-point distribution
$\mathbf{s}$	Parametric coordinate vector
B	Number of blocks on one side of sliding plane
N	Number of participating intervals in sliding plane
M	Number of overlaps for a sliding plane interval

Operator

$\bar{\cdot}$	Resolved quantity i. e. larger than cut-off lengthscale
$\tilde{\cdot}$	Test-filtered quantity

CHAPTER 3 Re_τ SCALING OF POD MODES

Acronyms

POD	Proper orthogonal decomposition
AU3X	In-house LES solver
LES	Large eddy simulation
DNS	Direct numerical simulation
PIV	Particle image velocimetry
RANS	Reynolds-averaged Navier-Stokes

Greek symbols

ν	Kinematic viscosity
δ	Half the height of the channel
Φ_{ij}	Two-point spectral density tensor
$\lambda^{(n)}$	n^{th} order eigenvalue
$\xi^{(n)}$	n^{th} order eigenfunction scaled by square-root of n^{th} order eigenvalue
ϵ_{ij}	Viscous dissipation rate

Latin symbols

Re_τ	Reynolds number based on friction velocity and channel height
u_τ	Friction velocity
y	Distance from wall in physical coordinates
y^+	Distance from wall in inner coordinates
L_x, L_y, L_z	Domain size in x, y, z directions
N_x, N_y, N_z	Number of cells in domain in x, y, z directions
$\Delta x^+, \Delta y^+, \Delta z^+$	Grid-spacing in inner coordinates
N_f	Number of statistically independent samples of the flowfield
T	Averaging time period of turbulent statistics
k_x, k_z	Wavenumbers in x, z directions
l_x, l_z	POD mode lengthscales in x, z directions
u_i'	Fluctuating component of velocity vector
$f^{(n)}$	n^{th} order eigenfunction
D	Weight factors for non-uniform grid-distribution in y direction
A_{ij}	General Hermitian matrix

T_i	i^{th} order Chebychev polynomial
C_{ij}	Matrix of Chebychev coefficients corresponding to i^{th} velocity component and j^{th} order polynomial
P_{ij}	Mean-flow production rate
T_{ij}	Turbulent transport rate
D_{ij}	Viscous diffusion rate

Operator

$\bar{\cdot}$	Time-mean
$\hat{\cdot}$	Fourier coefficient
$\cdot^*$	Complex conjugate
$\mathrm{Re}(\cdot)$	Real component of complex number
$\mathrm{Im}(\cdot)$	Imaginary component of complex number
$\tilde{\cdot}$	No-slip correction for truncated eigenvector
$\|\|\cdot\|\|^2$	Euclidean norm

CHAPTER 4 DETERMINISTIC AND REYNOLDS STRESSES IN COMPRESSOR PASSAGES

Acronyms

DS	Deterministic stress
DKE	Deterministic kinetic energy
TKE	Turbulent kinetic energy
RS	Reynolds stress
LES	Large eddy simulation
DNS	Direct numerical simulation
SS	Suction side
PS	Pressure side

Greek symbols

ν	Kinematic viscosity
μ	Dynamic viscosity
ρ	Density
ϵ_{ij}	Viscous dissipation rate
Π_{ij}	Pressure-gradient velocity correlation
Φ_{ij}	Turbulent/deterministic diffusion rate
Ω	Rotor row rotational speed
ϕ	Flow coefficient
ψ	Work coefficient
$\bar{\tau}_{ij}$	Time-mean Newtonian viscous stress tensor
$\bar{\tau}_w$	Time-mean wall shear-stress
Δ	Filter width
$\widehat{\Delta}$	Test-filter width
$\rho(\tau)$	Autocorrelation function
δ^*	Boundary layer displacement thickness

θ^*	Boundary layer momentum thickness
η	Distance along boundary layer probe in outer coordinates
η^+	Distance along boundary layer probe in inner coordinates
χ_{ij}	Transport term in pressure-gradient velocity correlation split
ζ_{ij}	Redistributive term in pressure-gradient velocity correlation split

Latin symbols

u_i	Velocity vector
P	Pressure
P_{ij}	Mean-flow production rate
T_{ij}	Deterministic/turbulent transport rate
V_{ij}	Viscous diffusion rate
D_{ij}	Deterministic production/turbulent dissipation rate
Re_c	Reynolds number based on true rotor chord and speed at mid-span
c	True blade chord
u_τ	Friction velocity
V_{ref}	Axial velocity used to compute flow coefficient
n_i	Blade surface normal vector
$\Delta s^+, \Delta n^+, \Delta r^+$	Grid-spacing in inner coordinates in streamwise, wall-normal and radial directions
q^2_{SGS}	Subgrid-scale turbulent kinetic energy
C_I	Proportionality constant in subgrid-scale turbulent kinetic energy model
$\|S\|$	Strain rate magnitude
T_τ	Integral timescale
L_τ	Integral lengthscale
C_p	Pressure coefficient
C_{ax}	Axial chord
$\overline{P}_{in}$	Azimuthally averaged pressure at passage inlet
C_f	Skin-friction coefficient
H	Boundary layer shape-factor
U_{ref}	Reference freestream velocity for integral boundary layer quantities

Operator

$\langle\cdot\rangle$	Phase-locked average
$\bar{\cdot}$	Time-mean component
$\tilde{\cdot}$	Organized unsteady component
$\cdot'$	Fluctuating/stochastic unsteady component
$\frac{D\cdot}{Dt}$	Total derivative
$\oint \cdot$	Circular line-integral
$\hat{\cdot}$	Test-filtered quantity
$\|\|\cdot\|\|^2$	Euclidean norm

Subscripts

x	Axial direction
s	Streamwise direction
n	Wall-normal direction
w	Tangential direction
r	Radial direction

1 INTRODUCTION

As part of the global drive to reduce mankind's carbon footprint, the aviation industry also faces an ambitious set of goals. The targets laid out in Flightpath 2050 include a 50% reduction in CO_2, 90% reduction in NO_x and 65% reduction in perceived noise as compared to levels in the year 2000[15]. Industry leaders have identified boosting the pressure ratio of the gas turbine compressor, as well as its efficiency, as key components of achieving these targets[38].

One of the main challenges faced by compressor designers is simulating the turbulence in compressor passages. Due to their low computational cost, the industrial tool of choice for Computational Fluid Dynamics (CFD) simulations of turbulent flow are the Reynolds-averaged Navier-Stokes (RANS) equations coupled with turbulence closures. In such a computation, only the mean component of the flow is solved, and the turbulence is modelled based on a combination of *a priori* assumptions, empirical correlations and properties of the mean flow. The shortcomings of RANS-based turbulence models in predicting compressor passage flows, as well as those in turbines[123][104], are well-documented[103]; for compressors at off-design conditions, solutions obtained from a RANS-based computation can even fail to converge[78]. As a lack of confidence in the CFD predictions can severely limit the design space available to engineers[78], there is a clear need for more accurate numerical tools for simulating turbulent flows in compressor passages.

A necessary first step towards developing higher-fidelity turbulence models is an improved understanding of turbulence in compressor passages. If one wishes to conduct such research numerically, scale-resolving simulations must be used. Turbulence acts to transport kinetic energy from the large, macroscopic lengthscales of the flow, all the way down to the small lengthscales where the kinetic energy can be dissipated by viscosity. Energy is not however simply deposited from the large to the small scales, but rather gradually cascaded down via interactions of scales of similar size. Any computation hoping to investigate turbulence in compressor passages must be able to resolve these non-linear and unsteady interactions. Exponential advances in computing power over the latter half of the twentieth century have made it possible to use scale-resolving techniques such as large eddy simulations (LES) to investigate flow in compressor passages at representative conditions.

The current DPhil project used LES computations to study the turbulence in compressor passages. In order to recreate more realistic operating conditions, simulations of an entire compressor stage were carried out, in a repeating stage configuration, rather than an isolated blade. The unsteady flow in a compressor passage was decomposed into a time-mean, periodic and stochastic (turbulent) component, and the stress fields induced by periodic (deterministic stress) and stochastic (Reynolds stress) perturbations about the time-mean flow were investigated in detail. The interaction of the two stress fields was also examined.

Chapter 2 explains the numerical methods and tools that were used to carry out the LES runs of a repeating compressor stage. This includes a description of the underlying theory of LES, of the assumptions and discretization techniques used in the in-house Navier-Stokes solver, of the numerical grid generation tool developed for obtaining high-quality and perfectly load-balanced multi-block structured grids, and of the novel sliding plane algorithm developed for block-structured grids in massively parallel computations.

In the early stages of the DPhil, research was carried out into the universality of the proper orthogonal decomposition (POD) modes of the two-point velocity correlation tensor in plane-channel flow. The two-point correlation tensor quantifies the time-averaged effects of turbulent structures, and the POD modes represent an optimal basis for it[33]. Therefore, understanding their scaling behaviour can potentially unlock a lot of physical insight into the nature of wall-bounded turbulent flows. Moreover, the discovery of universality in the POD modes allows them to potentially be used in models applicable to computations of flow in compressors. One pertinent example would be the specification of turbulence at the inlet of scale-resolving simulations. This research also allowed an opportunity to validate the in-house LES solver by comparing its results against a database of direct numerical simulations of plane channel flow[19],[18],[20]. The research on the POD modes of two-point correlations is presented in Chapter 3. It has also been published in a journal article[88].

Chapter 4 discusses the repeating stage compressor computations and comprises the bulk of the research work of the current DPhil. Computations were carried out at three different points of a compressor speed line. For each computation, the deterministic and Reynolds stresses, as well as the stress budget terms, were studied in detail throughout the domain, with a special emphasis on the blade surface boundary layer profiles. Part of the research reported in this chapter has been submitted to a conference and is currently under review[89].

Chapter 5 is a summary of the key findings of the current DPhil, as well as recommendations for future work that would serve to enhance and extend the research presented herein.

2 NUMERICAL METHODS

The current chapter gives an overview of all the numerical methods relevant to the research reported in this thesis. It is structured so that the background theory underpinning large eddy simulations, as well as the pre-existing elements of the in-house solver AU3X, are described first. Subsequently, the numerical tools developed during the current DPhil are presented. This includes the addition of the subgrid-scale model to AU3X, a multi-block structured grid generator for turbomachinery blade passages and the sliding plane algorithm used to perform the repeating compressor stage simulations.

2.1 Governing equations

2.1.1 *Scale separation and filtering*

As alluded to in the introduction, turbulent flow acts to distribute energy from large lengthscales to smaller ones. Typically, the largest lengthscales will be of a similar size to the defining features of the mean flow. In channel flow for example, the largest, and most energetic, lengthscale, L, would be comparable to the height of the channel. The smallest dynamically lengthscale, commonly referred to as the Kolmogorov scale, η, is small enough for viscous effects to become significant and smooth out the small-scale fluctuations induced by turbulence, at the expense of the kinetic energy of the smallest scales[117]. Viscous effects thus act to dissipate turbulent kinetic energy, and prevent the creation of scales smaller than η[117]. An ideal solution of the Navier-Stokes equations would have a sufficiently fine resolution to capture all the relevant lengthscales. For a statistically homogeneous and isotropic turbulent flow, the ratio between the most energetic lengthscale and the smallest dynamically active scale can be approximated with the following relation[100]:

$$\frac{L}{\eta} = \mathcal{O}\left(Re^{3/4}\right) \tag{1a}$$

$$Re = \frac{\rho L U}{\mu} \tag{1b}$$

As a result, for many flows of engineering interest, i. e. $Re \approx 10^5$ and upwards, the computational cost required to resolve all the lengthscales is often prohibitively expensive. Practical turbulent flows thus demand the use of suitable approximations, that comprise of a coarser description of the flow and allow a reduction in the range of scales needing to be resolved.

Large Eddy Simulation (LES) is one such approach. It is constructed around the central premise of categorizing turbulent flow into large and small scale features. The large scale turbulent structures are characteristic of each flow and thus highly anisotropic[101]. Due to it being so problem dependent, the turbulence at these large scales would argu-

ably be impossible to model and must be solved[90]. The small scale turbulence structures on the other hand have been found to be almost isotropic and highly universal, making them much more amenable to modelling[90].

The large-scale quantities are discerned from the flow by performing a convolution with a filter function:

$$\bar{f}(\mathbf{x}) = \int_{\Omega} G(\mathbf{x}-\mathbf{x}', \Delta(\mathbf{x}))f(\mathbf{x}')d\mathbf{x}' \tag{2}$$

In Equation 2, $G(\mathbf{x}-\mathbf{x}', \Delta(\mathbf{x}))$ is the filter function, $f(\mathbf{x})$ is any flow quantity and $\Delta(\mathbf{x})$ is the support of the filter, which is inhomogeneous in the general case, i. e. can vary throughout the solution domain. Three commonly used filter-functions, the box, the Gaussian and the spectral cut-off filter, are shown in Table 1:

FILTER	$G(\mathbf{x}-\mathbf{x}', \Delta(\mathbf{x}))$	$\hat{G}(\mathbf{k}, \Delta(\mathbf{x}))$
box	$\begin{cases} \frac{1}{\Delta(\mathbf{x})} & \text{if } \lvert\mathbf{x}-\mathbf{x}'\rvert \leqslant \frac{\Delta(\mathbf{x})}{2}, \\ 0 & \text{otherwise} \end{cases}$	$\frac{\sin\left(\mathbf{k}\frac{\Delta(\mathbf{x})}{2}\right)}{\mathbf{k}\frac{\Delta(\mathbf{x})}{2}}$
gaussian	$\sqrt{\frac{6}{\pi\Delta(\mathbf{x})^2}}\, exp\Big(-\frac{6(\mathbf{x}-\mathbf{x}')^2}{\Delta(\mathbf{x})^2}\Big)$	$exp\Big(-\frac{(\Delta(\mathbf{x})\mathbf{k})^2}{24}\Big)$
spectral cut-off	$\frac{\sin(\mathbf{k_c}(\mathbf{x}-\mathbf{x}'))}{\mathbf{k_c}(\mathbf{x}-\mathbf{x}')}$, with $\mathbf{k_c} = \frac{\pi}{\Delta(\mathbf{x})}$	$\begin{cases} 1 & \text{if } \lvert\mathbf{k}\rvert \leqslant \mathbf{k_c}, \\ 0 & \text{otherwise} \end{cases}$

Table 1: Common filter functions in physical and spectral space[102]

Conceptually, the filter width, $\Delta(\mathbf{x})$, is often thought of as the lengthscale below which contributions to the turbulent kinetic energy are modelled rather than resolved. Table 1 however shows that this is only true in the case of the spectral cut-off, as the box and gaussian filters don't remove any frequencies from the solution field, but rather simply attenuate them. Furthermore, the support of these filters is non-local in spectral space, meaning that these filtering operators affect even the largest lengthscales present in the flow. Thus a strictly correct implementation of the box or Gaussian filters would require a grid resolution fine enough to resolve the entire turbulent kinetic energy spectrum, thereby reducing the computational cost savings afforded by LES as compared to Direct Numerical Simulations (DNS). As one would one expect, practical LES computations are rarely this well-resolved.

Moreover, most of the LES computations of complex geometries reported in literature (and many even of simple geometries) do not make use of any explicit filtering at all[75]. The conventional practice is to instead rely on the filtering introduced by the discrete representations of continuous transport laws. If a one-dimensional box filter is used, the Leibniz rule in conjunction with Equation 2 can be used to readily show that the convolution integral simplifies to a typical central difference approximation[5]:

$$\frac{\partial \bar{f}}{\partial x} = \frac{\partial}{\partial x}\int_{\Omega} G(x-x',\Delta x)f(x')dx' \tag{3}$$

$$= \frac{1}{\Delta x}\frac{\partial}{\partial x}\int_{x-\frac{1}{2}\Delta x}^{x+\frac{1}{2}\Delta x} f(x')dx' \tag{4}$$

$$\approx \frac{f(x+\frac{1}{2}\Delta x) - f(x-\frac{1}{2}\Delta x)}{\Delta x} \tag{5}$$

A risk of not using any explicit filtering is the potential introduction of aliasing errors into the solution. Non-linear interactions of the resolved scales can generate frequencies higher than the mesh can resolve, causing aliasing of the resolvable frequencies[75]. Fortunately, the effects of aliasing errors on flow statistics can be mostly negated by simply refining the grid[75].

An unavoidable consequence however of relying solely on the filtering effects of discrete operators is that one can no longer formulate a closed mathematical expression relating the filtered and unfiltered flow fields; the details of the interactions of resolved and unresolved fields remain unknown[82]. LES, at least in the way it is most commonly used, is thus most realistically interpreted as a method that approximates the large-scale flow features and their energy transfer with the unresolved flow, as opposed to it representing a formal relationship between the resolved and subgrid components of the flow[135]. Its chief utility is thus in obtaining instantaneous information of the large-scale flow features and turbulent structures.

As a final note on filtering, it is well known that unless the filter width is spatially homogeneous, it does not commute with spatial differentiation:

$$\overline{\frac{\partial f}{\partial x}} \neq \frac{\partial \bar{f}}{\partial x} \tag{6}$$

According to Jones et al[56], the error associated with commuting filtering and differentiation can be estimated by the expression shown in Equation 7:

$$\overline{\frac{\partial f}{\partial x}} = \frac{\partial \bar{f}}{\partial x} - \overline{\frac{\partial \bar{f}}{\partial \Delta}}\overline{\frac{d\Delta}{dx}} \tag{7}$$

In all the computational grids used in the current DPhil, mesh expansion ratios were no greater than 1.1. The commutation error is therefore one order of magnitude smaller than its corresponding spatial derivative, allowing it to safely be neglected.

2.1.2 *Filtered transport laws*

Equation 8b shows the filtered incompressible Navier-Stokes equations for a Newtonian, constant viscosity fluid:

$$\frac{\partial \overline{u}_j}{\partial x_j} = 0 \tag{8a}$$

$$\frac{\partial \overline{u}_i}{\partial t} + \frac{\partial \left(\overline{u}_i \overline{u}_j + \tau^s_{ij}\right)}{\partial x_j} = \frac{1}{\rho}\frac{\partial \overline{P}}{\partial x_i} + \nu \frac{\partial^2 \overline{u}_i}{\partial x_j \partial x_j} + 2\epsilon_{ijk}\omega_j \overline{u}_k + \epsilon_{ilh}\epsilon_{hjk}\omega_l \omega_j r_k \tag{8b}$$

$$\tau^s_{ij} = \overline{u_i u_j} - \overline{u}_i \overline{u}_j \tag{8c}$$

$$\omega_i = \left[\Omega_x, \Omega_y, \Omega_z\right] \tag{8d}$$

$$r_i = \left[0, R\sin(\theta), R\cos(\theta)\right] \tag{8e}$$

The second-last term on the right-hand side of Equation 8b is the Coriolis force, and the last term the centrifugal force. These only apply when the Navier-Stokes is solved in a rotational frame of reference.

In Equation 8b, filtering of the non-linear convection term gives rise to the subgrid-scale (SGS) stress tensor, τ^s_{ij}. The SGS stress tensor contains all the information about how the flow interacts with lengthscales pertaining to the unresolved portion of the turbulent kinetic energy spectrum. A model is needed to compute τ^s_{ij} in order to close Equation 8b. SGS modelling is discussed in detail in Section 2.4.

2.2 Discretization schemes

AU3X is the incompressible LES solver used in the current DPhil, and its numerics are based on the work of Jones et al[56]. Jones et al's solver has successfully been used in LES computations of jets in cross flows[135], and LES of wall-bounded turbulent flow[24]. The current section succinctly explains the reasoning behind the choice of spatial and temporal discretization schemes in AU3X. A more detailed account can be found in [135].

2.2.1 *Spatial discretization*

The spatial discretization of the convection terms of the Navier-Stokes, $\frac{\partial(\overline{u}_i\overline{u}_j)}{\partial x}$ in Equation 8b, is a significant potential source of error in an LES computation[56]. In AU3X, a 2^{nd} order central-difference scheme is used. The reasoning for choosing this scheme can be understood by examining the different types of truncation error associated with approximated numerical representations of differential operators.

Assuming periodic boundary conditions, the exact, $u(\mathbf{x}, t)$, and the approximate, $\widetilde{u}(\mathbf{x}, t)$, solutions of the governing partial differential equations (PDEs) can be represented by a spatial Fourier decomposition, as shown in Equation 9. Interpreting each Fourier harmonic as a plane wave, a pulsation function, $w(\mathbf{k}_i)$, can be attached to each wave. The pulsation function can be thought of as the speed at which a particular wave propagates through the solution domain. The explicit dependence of w on $\mathbf{k}$ is determined by the nature of the PDEs being solved[44].

$$u(\mathbf{x}, t) = \sum_{\mathbf{k}_{min}}^{\mathbf{k}_{max}} \widehat{U}(\mathbf{k}) e^{I\mathbf{k}_i \cdot \mathbf{x}} e^{-Iw(\mathbf{k}_i)t} \tag{9a}$$

$$\widetilde{u}(\mathbf{x}, t) = \sum_{\mathbf{k}_{min}}^{\mathbf{k}_{max}} \widehat{\widetilde{U}}(\mathbf{k}) e^{I\mathbf{k}_i \cdot \mathbf{x}} e^{-I\widetilde{w}(\mathbf{k}_i)t} \tag{9b}$$

In Equation 9, $I = \sqrt{-1}$. Based on the representation in Equation 9, the approximate and exact solutions can differ either in terms of the wave amplitude or the wave speed. When comparing the exact and approximate solutions, errors in the wave amplitudes are called diffusive, or diffusion, errors, whereas errors in wave speeds are called dispersive errors[44]. As suggested by Equation 9, both diffusive and dispersive errors are a function of wavenumber, $\mathbf{k}$. In the context of LES, diffusive errors can be interpreted as an attenuation or amplification of turbulent kinetic energy. Dispersion errors on the other hand represent an incorrect distribution of turbulent kinetic energy across the spectrum[135]. Examining diffusion and dispersion errors thus offers a deeper insight into the capabilities and merits of various discretization schemes; simply examining the global order of accuracy of a scheme only illuminates how the truncation error scales with mesh refinements.

Linear finite difference schemes for evaluating derivatives of PDEs fall into two categories: symmetric and asymmetric.The two-point central difference scheme is an example of a symmetric scheme:

$$\left.\frac{\partial f}{\partial x}\right|_i = \frac{f_{i+1} - f_{i-1}}{2\Delta x} + \mathcal{O}(\Delta x^2) \tag{10}$$

An example of an asymmetric scheme is the three-point upwind difference scheme, which for a positive convective velocity is given as:

$$\left.\frac{\partial f}{\partial x}\right|_i = \frac{3f_i - 4f_{i-1} + f_{i-2}}{2\Delta x} + \mathcal{O}(\Delta x^2) \tag{11}$$

It should be noted that both Equation 10 and Equation 11 represent the case of a uniform mesh. Both are also 2^{nd} order accurate in space; the total truncation error (dispersive plus diffusive) in the local approximation of the first derivative scales with the square of changes in grid size.

A mechanism for quantifying the diffusive and dispersive errors of different discretization schemes based on Warming and Hyett's[132] modified equation analysis of one-dimensional transport of a passive scalar, i. e. the Cauchy problem, is shown in [135]. The key findings from that analysis are reiterated here.

Symmetric and asymmetric schemes suffer from dispersive errors to a comparable degree. As the degree of accuracy of the scheme is increased, both symmetric and asymmetric discretization schemes show a reduction in not only the magnitude of the dispersive error, but also a reduction in the wavenumber range over which it is significant[135].

As for the diffusion error, the numerically dissipative nature of asymmetric discretization schemes is well-established. Shyy found that an asymmetric discretization of the convection terms introduced a dissipative error that scaled with the cell Peclet number, $Pe_c = u\Delta x/\nu$[106]. In the case of $Pe_c \approx \mathcal{O}(10)$, which is common for LES computations, this can introduce a numerical diffusion at the smallest resolved scales which is as large as the SGS stresses[135]. An asymmetric discretization of the convection terms can thus even lead to an unphysical laminarisation of the flow[56].

Symmetric discretization schemes on the other hand produce no diffusion errors for uniform grids. Although symmetric discretization schemes on expanding or contracting grids do lead to diffusion errors, they are minimal for moderate expansion ratios. Moreover, the diffusion errors of both symmetric and asymmetric schemes suffer to a similar extent from varying grid sizes[135].

Symmetric and asymmetric schemes thus offer similar performance in terms of dispersion error, but symmetric schemes are superior with regards to how little diffusion error they introduce into the solution. One aspect in which asymmetric schemes show superior performance is in terms of the boundedness of the solution. The concept of boundedness can be interpreted in many different ways, and a thorough summary of all the various definitions can be found in Laney[64]. It can essentially be understood as requiring the numerical solution to be subject to the same bounds as the physical system it approximates; violations of boundedness manifest themselves as unphysical spurious oscillations, i. e. local under-shoots and overshoots in the numerical solution[32]. These oscillations are often referred to as 'wiggles', and not only is the presence of wiggles in the solution unaesthetic, it can lead to unphysical values that can potentially harm the reliability and stability of the numerical solution[46].

A proclivity to producing wiggles is a known weakness of symmetric discretization schemes. This is a direct consequence of their lack of diffusion error. In under-resolved regions of the flow, where the grid is not fine enough to adequately resolve gradients,

the numerical error may be significant and the lack of numerical dissipation allows unphysical wiggles to develop[32]. The dissipative properties of asymmetric schemes inhibit the development of unphysical oscillations.

Godunov's theorem states that all linear discretizatons of the convection terms higher than first-order are not guaranteed to be bounded[107]. Hence, asymmetric discretization schemes can also produce wiggles; they just do so to a lesser extent than symmetric ones. Furthermore, the root cause of the unphysical oscillations is inadequate grid refinement. Locally refining the grid is thus an effective way of removing, or at least reducing to a manageable level, the wiggles produced by symmetric schemes. It can also be argued that whilst boundedness is critical for physically non-negative quantities such as density, and turbulent kinetic energy, as well as species concentrations which must lie between 0 and 1, for quantities such as velocity and pressure a small degree of wiggles can be tolerated[135].

Based on the above arguments, AU3X uses a central differencing scheme to discretize the convection terms. Many other researchers have also arrived at the same conclusion, and used a symmetric discretization of the convection terms in their incompressible LES computations, with examples ranging from the early channel flow of Deardorff[17], to more complex geometries including flows over riblets[14] and backward facings steps[61].

Having chosen a central differencing scheme, all that remains is to decide between a 2^{nd} order scheme, or a higher-order scheme. One clear benefit of using a high-order central differencing scheme is the reduction in dispersion error, especially at lengthscales close to the cut-off wavenumber. Ghosal showed that in order to ensure the dispersive error was of a smaller magnitude than the SGS stresses, a 2^{nd} order scheme requires twice the number of grid points as compared to a 4^{th} order scheme and more than four times as many points as an 8^{th} order scheme[35].

Whilst high-order central differencing schemes do offer potential reductions in dispersive error, this comes at the expense of increased computational cost. They also require a larger computational stencil, and the cost of inverting the resulting sparse matrix for implicit methods grows faster than linearly with the size of the stencil[135]. Furthermore, higher-order central differencing schemes can also have a greater propensity for generating oscillatory wiggles[135][63].

Therefore while high-order central difference schemes offer a reduced dispersion error, especially at high wavenumbers, they increase the complexity of the computational stencil. Moreover, they also carry a greater risk of unphysical oscillations. Faced with this choice, many incompressible LES computations have preferred lower-order central differencing combined with a finer grid[105]. Based on the same reasoning, AU3X uses 2^{nd} order central differencing to discretize the convection terms of the Navier-Stokes.

2.2.2 *Temporal discretization*

For an explicit treatment of the diffusion term in the Navier-Stokes, $\nu \frac{\partial^2 u_i}{\partial x_j \partial x_j}$, the stability constraint shown in Equation 12 is imposed on the time-step, Δt:

$$\frac{\nu \Delta t}{\Delta x^2} \leqslant \frac{1}{2} \tag{12}$$

Therefore the fine grids necessary near viscous walls in order to allow the dynamic SGS models to switch-off, see Section 2.4, would impose excessive restrictions on the time-step. This is a well-known problem for LES of wall-bounded flows[82]. An implicit treatment of the diffusion term in the Navier-Stokes was thus adopted for the current work. The pressure correction, see section Section 2.3, was also performed implicitly in order to guarantee a time-accurate evolution of the pressure. The implicit pressure correction is by far the most computationally expensive component of the LES calculations. The additional cost of also treating the convection term, $\frac{\partial(u_i u_j)}{\partial x_j}$, implicitly is deemed negligible, leading to a fully implicit treatment in time.

Taylor states that if the mean flow kinetic energy is significantly greater than the turbulent kinetic energy, turbulent structures can be approximated as "frozen" and are simply transported by the mean flow[116]. Although originally postulated for flows with zero mean-shear, Taylor's hypothesis has been found to be valid in incompressible turbulent boundary layers for components of the turbulent kinetic energy spectrum corresponding to a wavelength much smaller than the boundary layer thickness[68]. Taylor's hypothesis therefore binds together the spatial and temporal resolution of an LES computation. The benefits of using a temporal discretization scheme with a greater order of accuracy than the spatial scheme are therefore unclear, especially in the case of $\mathrm{CFL} = \frac{u\Delta t}{\Delta x} \approx \mathcal{O}(1)$.

It was thus decided to use a fully-implicit 2^{nd} order temporal discretization scheme. Two potential candidates are a three-level backward difference scheme, Equation 13a, and the two-level Crank-Nicholson scheme, Equation 13b[135]. Both schemes are shown for the case of one-dimensional transport of a passive scalar, ϕ, in semi-discrete form, i. e. the convection and diffusion terms are expressed analytically rather than discretely.

$$\frac{3\phi_i^{n+1} - 4\phi_i^n + \phi_i^{n-1}}{2\Delta t} = -u\frac{\partial \phi^{n+1}}{\partial x}\Big|_i + \nu\frac{\partial^2 \phi^{n+1}}{\partial x \partial x}\Big|_i \tag{13a}$$

$$\frac{\phi_i^{n+1} - \phi_i^n}{\Delta t} = -u\frac{1}{2}\left(\frac{\partial \phi^{n+1}}{\partial x}\Big|_i + \frac{\partial \phi^n}{\partial x}\Big|_i\right) + \nu\frac{1}{2}\left(\frac{\partial^2 \phi^{n+1}}{\partial x \partial x}\Big|_i + \frac{\partial^2 \phi^n}{\partial x \partial x}\Big|_i\right) \tag{13b}$$

The behaviour of the dispersive error of both schemes is similar, but the Crank-Nicholson has lower levels of diffusion error[135]. However the Crank-Nicholson scheme suffers from non-linear stability issues in flows involving convection[135, 30]. The tendency for instability is even greater if it is coupled with a non energy conserving discretization for the pressure correction[135]; see Section 2.3. The backward difference scheme on the other hand is unconditionally stable, even though it can lead to oscillatory behaviour if the time-step is too large[30]. Due to its superior stability properties, the temporal discretization in AU3X is thus performed using the three-level backward difference scheme shown in Equation 13a.

2.3 Implicit pressure correction

For an incompressible flow, whenever the equation for conservation of momentum is solved, the velocity field obtained does not necessarily satisfy mass conservation, and is therefore not divergence free. The law of momentum conservation expressed in terms of this intermediate velocity, $\overline{u}_i^*$, is shown in Equation 14.

$$\frac{\partial \overline{u}_i^*}{\partial t} + \frac{\partial \overline{u}_i^* \overline{u}_j^*}{\partial x_j} = -\frac{1}{\rho}\frac{\partial \overline{P}^n}{\partial x_i} + \frac{\partial \overline{\tau}_{ij}^*}{\partial x_j} \tag{14}$$

It is worth noting that $\overline{\tau}_{ij}^*$ in Equation 14 is the viscous plus the SGS stress tensor, and the overbar indicates the resolved component of the flow. The intermediate velocity field can be made divergence free by modifying the pressure field using a correction. The correct value of the pressure at the current time step is thus the value at the previous time-step plus the pressure-correction: $\overline{P}^{n+1} = \overline{P}^n + \overline{P}'$. The pressure-correction can be calculated by computing the divergence of Equation 14:

$$\frac{\partial}{\partial x_i}\left(\frac{\partial \overline{u}_i^*}{\partial t}\right) + \frac{\partial}{\partial x_i}\left(\frac{\partial \overline{u}_i^* \overline{u}_j^*}{\partial x_j}\right) = -\frac{1}{\rho}\frac{\partial}{\partial x_i}\left(\frac{\partial \overline{P}^{n+1}}{\partial x_i} - \frac{\partial \overline{P}'}{\partial x_i}\right) + \frac{\partial}{\partial x_i}\left(\frac{\partial \overline{\tau}_{ij}^*}{\partial x_j}\right) \tag{15}$$

The ultimate aim of solving Equation 15 is to obtain a divergence free velocity field, whilst deviating as little as possible from $\overline{u}_i^*$, which already satisfies momentum conservation. Obtaining a divergence free velocity field can thus be viewed as a constrained optimization problem, where the pressure correction acts as a Lagrange multiplier[31].

When the true solution at a particular time-step is obtained, the first term on the left-hand side of Equation 15 is zero, and so is the pressure-correction. Hence in the converged state, the divergence of the convective and viscous terms balances $\frac{1}{\rho}\frac{\partial}{\partial x_i}\left(\frac{\partial \overline{P}^{n+1}}{\partial x_i}\right)$. This realization forms the basis of the projection method, a widely used approach for computing the pressure-correction in unsteady flows[31]. The projection method assumes that the correction to $\overline{u}_i^*$ is minimized if the divergence of the pressure-correction gradient only acts on the first term on the left-hand side of Equation 15:

$$\frac{\partial}{\partial t}\left(\frac{\partial \overline{u}_i^*}{\partial x_i}\right) \approx \frac{\partial}{\partial x_i}\left(\frac{1}{\rho}\frac{\partial \overline{P}'}{\partial x_i}\right) \tag{16}$$

Given that Equation 16 is solved implicitly, and that the time-derivative only represents iterations within a time-step, Equation 16 can safely be approximated using a backwards-euler formulation:

$$\begin{aligned} \frac{1}{\Delta t}\left(\frac{\partial \overline{u}_i^*}{\partial x_i} - \frac{\partial \overline{u}_i^n}{\partial x_i}\right) &\approx \frac{\partial}{\partial x_i}\left(\frac{1}{\rho}\frac{\partial \overline{P}'}{\partial x_i}\right) \\ \frac{1}{\Delta t}\left(\frac{\partial \overline{u}_i^*}{\partial x_i}\right) &\approx \frac{\partial}{\partial x_i}\left(\frac{1}{\rho}\frac{\partial \overline{P}'}{\partial x_i}\right) \end{aligned} \tag{17}$$

A finite volume formulation of Equation 17 can be expressed as:

$$\int_\Omega \left(\frac{\partial \overline{u}_i^*}{\partial x_i}\right) d\Omega = \frac{\Delta t}{\rho}\int_\Omega \frac{\partial}{\partial x_i}\left(\frac{\partial \overline{P}'}{\partial x_i}\right) d\Omega \tag{18}$$

Assuming a one-dimensional problem with a uniform grid, and evaluating the divergence in Equation 18 using the Gauss theorem, the following equation is obtained:

$$\Delta S\left(\overline{u}_i^*\Big|_{i+\frac{1}{2}} - \overline{u}_i^*\Big|_{i-\frac{1}{2}}\right) = -\frac{\Delta t \Delta S}{\rho}\left(\frac{\partial \overline{P}'}{\partial x}\Big|_{i+\frac{1}{2}} - \frac{\partial \overline{P}'}{\partial x}\Big|_{i-\frac{1}{2}}\right) \tag{19}$$

In Equation 19, ΔS is the cell-face area and $\cdot\Big|_{i+\frac{1}{2}}$ indicates a value evaluated at the face shared by cell i and $i+1$. The right-hand side of Equation 19 can be evaluated by computing $\frac{\partial \overline{P}'}{\partial x}$ at the cell face as an average of $\frac{\partial \overline{P}'}{\partial x}$ in the centres of the neighbouring cells:

$$\overline{u}_i^*\Big|_{i+\frac{1}{2}} - \overline{u}_i^*\Big|_{i-\frac{1}{2}} = \frac{\Delta t}{\rho}\left(\frac{1}{2}\left(\frac{\partial \overline{P}'}{\partial x}\Big|_{i+1} + \frac{\partial \overline{P}'}{\partial x}\Big|_{i}\right) - \frac{1}{2}\left(\frac{\partial \overline{P}'}{\partial x}\Big|_{i} + \frac{\partial \overline{P}'}{\partial x}\Big|_{i-1}\right)\right) \tag{20}$$

In the solution of the momentum equation, the pressure-gradient at the cell center was evaluated using the Gauss theorem, and the cell-face values of the pressure were interpolated using a linear interpolation of the values at the centres of neighbouring cells. If the same approach is applied to the right-hand side of Equation 20, the following expression is obtained:

$$\overline{u}_i^*\Big|_{i+\frac{1}{2}} - \overline{u}_i^*\Big|_{i-\frac{1}{2}} = \frac{\Delta t \Delta S}{4\rho}\left(\overline{P}'_{i+2} - 2\overline{P}'_i + \overline{P}'_{i-2}\right) \tag{21}$$

The right-hand side of Equation 21 represents a discrete Poisson equation for the pressure-correction on a grid twice as coarse as the current one. Equation 21 will thus not be able to detect pressure-correction variations in adjacent cells and can potentially permit a checkerboard pressure field[31]. A more compact computational stencil can be obtained by evaluating the pressure-correction gradients in Equation 19 directly at the cell face[98], denoted by the subscript 1Δ:

$$\frac{\partial P'}{\partial x}\Big|_{i+\frac{1}{2},1\Delta} \approx \frac{P'_{i+1} - P'_i}{\Delta x} \tag{22}$$

The expression in Equation 22 is formed by central differences and is therefore 2^{nd} order accurate. Evaluating the right-hand side of Equation 19 using the compact gradient stencil in Equation 22 leads to the following equation:

$$\overline{u}_i^*\Big|_{i+\frac{1}{2}} - \overline{u}_i^*\Big|_{i-\frac{1}{2}} \approx \frac{\Delta t}{\rho}\left(\frac{\overline{P}'_{i+1} - \overline{P}'_i}{\Delta x} - \frac{\overline{P}'_i - \overline{P}'_{i-1}}{\Delta x}\right) \tag{23a}$$

$$\overline{u}_i^*\Big|_{i+\frac{1}{2}} - \overline{u}_i^*\Big|_{i-\frac{1}{2}} \approx \frac{\Delta t}{\rho \Delta x}\left(\overline{P}'_{i+1} - 2\overline{P}'_i + \overline{P}'_{i-1}\right) \tag{23b}$$

The use of the compact gradient stencil however introduces an inconsistency in the numerical solution. The momentum equations were solved by evaluating the pressure gradient using the Gauss theorem, and the resulting velocity field is used to construct the left-hand side of Equation 23b. To correct this inconsistency between the left and

right-hand sides, the difference between the Gauss theorem and compact stencil approximations of the known pressure field, $\overline{P}^n$, must be added to mass-flux approximations at the cell-faces:

$$\begin{aligned}\overline{u}_i^*\Big|_{i+\frac{1}{2}} - \overline{u}_i^*\Big|_{i-\frac{1}{2}} + \left(\frac{\partial \overline{P}^n}{\partial x}\Big|_{i+\frac{1}{2}} - \frac{\partial \overline{P}^n}{\partial x}\Big|_{i+\frac{1}{2},1\Delta} - \frac{\partial \overline{P}^n}{\partial x}\Big|_{i-\frac{1}{2}} + \frac{\partial \overline{P}^n}{\partial x}\Big|_{i-\frac{1}{2},1\Delta}\right) \\ = \frac{\Delta t}{\rho}\left(\frac{\partial \overline{P}'}{\partial x}\Big|_{i+\frac{1}{2},1\Delta} - \frac{\partial \overline{P}'}{\partial x}\Big|_{i-\frac{1}{2},1\Delta}\right)\end{aligned} \tag{24}$$

Equation 24 can be interpreted as adding a central difference approximation of the 4^{th} derivative of the pressure field to the right-hand side of the pressure-correction problem. If the oscillations in the pressure field are large, the 4^{th} derivative will be large and the pressure correction will act to smooth out the oscillations[31].

Due to the fact that the pressure gradient has been evaluated differently in the momentum and pressure-correction equations, the numerical scheme no longer conserves kinetic energy[31]. The conservation error is proportional to the 4^{th} derivative of the pressure field. This is one of the reason why the dissipative but stable backward difference scheme was preferred for the temporal discretization over the Crank-Nicholson scheme, which is known to be unstable when applied to non-energy conserving discretizations [135].

Once the pressure-correction equation is solved, the mass-flow rate at the cell faces is corrected using Equation 25a and the velocity field using Equation 25b. Although the corrected velocity field is now divergence free, there is no guarantee that it satisfies momentum conservation. The momentum and pressure-correction equations are thus solved iteratively multiple times within every time step until a satisfactory level of convergence is achieved.

$$\overline{u}_i^*\Big|_{i+\frac{1}{2}} = -\frac{\Delta t}{\rho}\left(\frac{\partial \overline{P}'}{\partial x}\Big|_{i+\frac{1}{2},1\Delta}\right) \tag{25a}$$

$$\overline{u}_i^{n+1} = \overline{u}_i^* - \frac{\Delta t}{\rho}\left(\frac{\partial \overline{P}'}{\partial x_i}\right) \tag{25b}$$

2.3.1 *Solution of pressure-correction*

The multigrid method is used to invert the Poisson equation for the pressure-correction, Equation 17. It is widely regarded as one of the most efficient iterative matrix inversion techniques, as it can deliver the same convergence rate as the best Fast Poisson Solvers, but without their limited conditions of applicability[47].

The error in an iterative solution method can be defined as the difference between the value of the unknown at the current iteration n and the exact solution, i. e. [47]:

$$\boldsymbol{e}^n = \mathbf{q}^n - \overline{\mathbf{q}} \tag{26}$$

In Equation 26, $\mathbf{q}^n$ is the unknown variable at the current iteration and $\overline{\mathbf{q}}$ is the exact solution. A bold-faced character indicates a matrix. A conventional iterative technique,

such as Jacobi or Gauss-Seidel iterations, will remove the high-frequency component of $\boldsymbol{e}^n$, i. e. smooth the error, within a few iterations, but will be very slow to dampen out the low frequency component of the error spectrum[47]. If the smoother error is then interpolated onto a coarser grid, the low frequency component of the error spectrum will be comparable to the grid-spacing and thus can be smoothed out by a few iterations on the coarser grid. Having used the coarser grid to remove the low frequency errors, the solution can now be interpolated back on the original grid. This is the operating principle of the multigrid method[47].

The linear system for the pressure-correction, $\mathbf{P'}$, is defined in Equation 27a and its residual in Equation 27b. The superscripts in Equation 27 denote the current grid-level.

$$\mathbf{A}\mathbf{P'}^{h}_{n+1} = \mathbf{Q}^{h}_{n} \tag{27a}$$

$$\mathbf{R}^{h}_{n} = \mathbf{A}\mathbf{P'}^{h}_{n} - \mathbf{Q}^{h}_{n} \tag{27b}$$

$$\Delta\mathbf{P'}^{h}_{n} = \mathbf{P'}^{h}_{n+1} - \mathbf{P'}^{h}_{n} \tag{27c}$$

$$\mathbf{A}\Delta\mathbf{P'}^{h}_{n} = -\mathbf{R}^{h}_{n} \tag{27d}$$

The inversion of Equation 27a always starts at the finest grid-level. After a few Red-Black Gauss-Seidel smoothing iterations, the high-frequency component of the error has been removed. The residual at the current grid-level is then interpolated to a coarser grid level, as per Equation 28. This step is called restriction.

$$\mathbf{R}^{h+1}_{n} = \mathbf{I}^{h+1}_{h}\mathbf{R}^{h}_{n} \tag{28}$$

Coarser grid levels are constructed by only choosing alternate grid-lines in the preceding level. Hence in a three-dimensional computation, one cell at grid-level $h+1$ corresponds to eight cells at grid-level h. In the multigrid implementation in AU3X, the restriction operator, $\mathbf{I}^{h+1}_{h}$, simply adds the residuals of the eight cells at grid-level h that comprise one cell in grid-level $h+1$. After interpolating the residuals onto grid-level $h+1$, Equation 27d is solved to remove the low-frequency errors. The corrections to the unknown variable on the coarser grid, $\Delta\mathbf{P'}^{h+1}_{n}$, are then interpolated back onto the finer grid. This step is called prolongation and is shown in Equation 29.

$$\Delta\mathbf{P'}^{h}_{n} = \mathbf{I}^{h}_{h+1}\Delta\mathbf{P'}^{h+1}_{n} \tag{29}$$

In the current implementation, the prolongation operator simply copies the correction computed at level $h+1$ to all its constituent cells in level h. For all of the LES computations reported in the current work, a total of four grid-levels were used to invert Equation 17.

2.4 Subgrid-scale modelling

The simplest and most commonly used type of models are the eddy-viscosity models. They are based on a physical analogy with molecular viscosity: the flow properties associated with the large-scale flow are randomly transported by small eddies, without any preferred direction[24]. The necessary requirement for this assumption to hold is for there to be a wide spectral gap between the resolved and unresolved scales, as is the case for molecular diffusion and even the smallest dynamically active lengthscales present in turbulent flows[117]. Even if this seperation in size does exist between the very large and the unresolved scales, it is clearly an invalid assumption in the immediate vicinity of the cut-off point[62]. Fortunately, the error associated with using an eddy viscosity to model turbulent kinetic energy transfer from the resolved to the unresolved flow is confined to a narrow band of wavenumbers immediately below the cut-off wavenumber[62]. This can help to explain how despite eddy viscosity models consistently performing poorly in accurately reproducing SGS stresses in *a priori* testing [94], they can nevertheless generate physically realistic turbulent kinetic energy spectra for the resolved parts of the flow[79]. Meneveau[79] attributed the success of eddy viscosity based models to their ability to correctly reproduce SGS energy dissipation rates, as well as the two-point correlation between the resolved velocity and SGS stresses.

Based on the analogy with molecular viscosity, a Boussinesq expression is used to model the anisotropic part of the SGS stress tensor as a product of the local mean strain-rate and an eddy-viscosity:

$$\tau^s_{ij} - \frac{1}{3}\delta_{ij}\tau^s_{kk} = -2\nu_{SGS}\overline{S}_{ij} \tag{30a}$$

$$\overline{S}_{ij} = \frac{1}{2}\left(\frac{\partial \overline{u}_i}{\partial x_j} + \frac{\partial \overline{u}_j}{\partial x_i}\right) \tag{30b}$$

$$\nu_{SGS} = C_s l v \tag{30c}$$

As the trace of τ^s_{ij} corresponds to the turbulent kinetic energy contained within the unresolved component of the flow, it cannot be correlated to $\overline{S}_{ij}$ whose trace tends to zero due to the the incompressibility constraint (Equation 8a). As such, the convention in incompressible flow is to absorb the turbulent kinetic energy contained within the unresolved component of the flow into the pressure. In compressible flows, it needs to be explicitly modelled[83].

Using arguments based on dimensional analysis, the eddy-viscosity is typically expressed as a product of a characteristic length-scale, a velocity-scale and a proportionality constant. Given that eddies of similar sizes interact in a turbulent energy cascade[117], the lengthscale associated with the eddy viscosity in Equation 30c can be taken as the characteristic length of the smallest resolved scale, the filter-width. A further assumption that can be made is that the wavenumber that marks the boundary between the resolved and unresolved components of the flow lies in the inertial subrange of the turbulent kinetic energy spectrum. Consequently, the SGS stresses are assumed to be in statistical equilibrium with the resolved flow; the SGS stresses dissipate all the energy transferred to them from the resolved portions of the turbulent kinetic energy spectrum[34].

The above assumptions form the basis of the seminal Smagorinsky SGS stress model[51]:

$$\tau^s_{ij} - \frac{1}{3}\delta_{ij}\tau^s_{kk} = -2(C_s\Delta(\mathbf{x}))^2|\overline{S}|\overline{S}_{ij} \tag{31a}$$

$$|\overline{S}| = \sqrt{2\overline{S}_{kh}\overline{S}_{kh}} \tag{31b}$$

The Smagorinsky model was originally intended as a non-linear artificial dissipation term to provide an energy sink in under-resolved computations of turbulent flow[24]. Although it has enjoyed widespread use, researchers have found that the scaling constant, C_s, requires some tuning based on the computation. Lilly determined that in the case of homogeneous isotropic turbulence, the optimal value was $C_s \approx 0.23$[67], whereas Deardorff determined a different value in the case of plane channel flow, $C_s \approx 0.1$[17]. Moreover, the Smagorinsky model's assumption of the subgrid scales being in statistical equilibrium with the resolved scales breaks down in the near-wall viscous region and in the laminar-to-turbulent transitional region[34]. In the viscous sub-layer of a turbulent boundary layer, even the idea of a wide spectral gap between the resolved and unresolved scales eddy-viscosity modelling is predicated upon no longer holds[117]. LES has however successfully been used to model non-equilibrium flows by incorporating a mechanism to locally dampen the SGS stresses, accompanied with localized grid refinement sufficient for resolving the viscous scales[93][90].

To address these shortcomings, Germano et al[34] proposed a dynamic SGS model that locally computed the appropriate value of C_s. By allowing C_s to drop down to zero, the dynamic model also incorporates a mechanism for effectively switching-off the SGS stresses in non-equilibrium regions.

Germano's dynamic model is based on the premise of defining a second filtering operator called the test filter, $\widetilde{G}$, with a corresponding test filter-width $\widetilde{\Delta}$ that is larger than the original SGS filter-width, Δ. A successive application of both filtering operators to the Navier-Stokes leads to the subtest-scale (STS) stress tensor, as shown in Equation 32[66].

$$\frac{\partial\widetilde{\overline{u}}_i}{\partial t} + \frac{\partial\left(\widetilde{\overline{u}}_i\widetilde{\overline{u}}_j + T^s_{ij}\right)}{\partial x_j} = \frac{1}{\rho}\frac{\partial\widetilde{\overline{P}}}{\partial x_i} + \nu\frac{\partial^2\widetilde{\overline{u}}_i}{\partial x_j\partial x_j} \tag{32a}$$

$$T_{ij} = \widetilde{\overline{u_i u_j}} - \widetilde{\overline{u}}_i\widetilde{\overline{u}}_j \tag{32b}$$

Upon relating the STS and SGS stress tensors in terms of a quantity that can be explicitly computed, a new term called the resolved turbulent stress, L_{ij}, arises[34].

$$L_{ij} = \widetilde{\overline{u}_i\overline{u}_j} - \widetilde{\overline{u}}_i\widetilde{\overline{u}}_j \tag{33a}$$

$$L_{ij} = T^s_{ij} - \widetilde{\tau^s}_{ij} \tag{33b}$$

$$L_{ij} - \frac{1}{3}\delta_{ij}L_{kk} = -2C_sM_{ij} \tag{33c}$$

$$M_{ij} = \widetilde{\Delta}^2|\widetilde{\overline{S}}|\widetilde{\overline{S}}_{ij} - \Delta^2\widetilde{|\overline{S}|\overline{S}_{ij}} \tag{33d}$$

The SGS model constant C_s can then be computed by applying a least squares error minimisation approach to Equation 33c[66]:

$$C_s = \frac{1}{2}\left(L_{ij}M_{ij}/M_{ij}^2\right) \tag{34}$$

The authors found however that the denominator in Equation 34 could become small, and some spatial averaging of C_s was required for computational stability[66]. They proposed averaging over planes in the statistically homogeneous directions. Piomelli et al proposed a more local formulation of Germano's dynamic model that only required averaging over a compact test filter cell[92]. The authors also proposed a more stable formulation of C_s, one that did not involve a difference of two similar terms in its denominator[92]:

$$C_s = \frac{1}{2}\frac{\left(L_{ij} - \frac{1}{3}\delta_{ij}L_{kk} - 2C^*\widetilde{\beta_{lk}}\right)\alpha_{lk}}{\alpha_{mn}\alpha_{mn}} \tag{35a}$$

$$\beta_{ij} = \Delta^2|\overline{S}|\overline{S}_{ij} \tag{35b}$$

$$\alpha_{ij} = \widetilde{\Delta}^2|\widetilde{\overline{S}}|\widetilde{\overline{S}}_{ij} \tag{35c}$$

In the research conducted for the current DPhil, the SGS model used was Piomelli's localised formulation of the Germano dynamic model, as shown in Equation 35. C^* is the value of C_s from the previous outer-iteration. The test-filtered field was computed by averaging over a computational molecule including the adjacent cells, in each direction. Therefore, $\widetilde{\Delta} \approx 3\Delta$[56]. The SGS model constant was clipped between zero and Deardorff's recommendation for channel flow of 0.1[17], also confirmed by Piomelli's simulations of channel flows [93][92].

C_s is clipped to enhance numerical stability, and is based off of previous experience of LES computations of complex flows involving viscous walls[24]. The upper limit based on Deardorff's recommendation is chosen so as to avoid excessively high levels of SGS stresses. In Piomelli's simulation of rotating channel flow, C_s was not found to exceed 0.09[92]. Given the very fine grid resolutions being used for the current work, $C_s = 0.1$ was hence chosen as a safe upper limit.

It should be noted that in non-equilibrium regions of the flow where one would like to switch-off the SGS stresses, the grid has to be sufficiently refined so as to resolve even the smallest dynamically active turbulent lengthscale. If this condition is met, the difference between the STS and SGS stresses becomes zero, and thus C_s also becomes zero.

2.5 Grid generation

It is difficult to overstate the importance of high-quality grids in CFD computations; the properties of the grid play an essential role in determining the overall accuracy[45]. Thompson et al showed that for a one-dimensional grid, non-uniform grids introduce an additional truncation error, ϵ_T, in the spatial discretization scheme proportional to the product of the second-derivatives of the grid-spacing and the flow-field[118]:

$$\epsilon_T \propto \frac{\partial^2 \mathbf{x}}{\partial \xi \partial \xi} \frac{\partial^2 \mathbf{q}}{\partial \mathbf{x} \partial \mathbf{x}} \tag{36}$$

In Equation 36, the distribution of grid-points throughout the domain is expressed as a function of a generalized curvilinear-coordinate, i. e. $\mathbf{x} = f(\xi)$, and $\mathbf{q}$ is any flow variable. According to Equation 36, rapid variations in grid-size would thus cause an additional numerical diffusion; if $\frac{\partial^2 \mathbf{x}}{\partial \xi \partial \xi}$ is expressed as a viscosity, the right-hand side of Equation 36 resembles a typical diffusion term. This numerical diffusion could also be negative, and hence have a de-stabilising effect on the flow[118]. Turkel[122] demonstrated that unless the grid-stretching is algebraic, i. e. the ratio between the sizes of adjacent cells is constant, then formally second-order accurate discretization schemes are reduced to first-order.

In the case of two or three-dimensional grids, the orthogonality of grid-lines has also been identified as having an important effect on accuracy. Hirsch[45] showed that significant deviations from orthogonality of the angles between grid-lines will lead to a reduction in the order of accuracy of the spatial discretization scheme. As simulations of turbulent flow are characterised by rapid variations, and hence high-gradients, grid-quality is particularly critical in LES[45].

Due to the integral role the grid plays in determining the overall accuracy of a CFD simulation, obtaining high-quality grids became a leading priority for the research conducted in the current DPhil. The first decision that had to be made was whether to use unstructured and structured grids. The general guidance is that structured or block-structured grids offer superior accuracy, as well as reduced CPU time and memory requirements, as compared to unstructured grids[45]. The experience of the DPhil's candidate research group in grid generation for turbomachinery CFD corroborates this assertion[131],[129],[128].

The DPhil candidate's research group already has an in-house block-structured grid generator for turbomachinery blade passages[129]. The in-house grid generator uses Dirichlet orthogonality: it assumes the grid-point distribution on the domain boundaries is fixed, and only the internal points are manipulated to try to achieve grid-line orthogonality throughout the domain[57]. Although this approach offers some advantages in robustness[128], it suffers from the requirement to set the surface and volume grid-point distributions independently. Consequently, a high degree of trial-and-error would be needed to achieve the optimal grid-point distribution; it would be very difficult to determine *a priori* whether a given surface grid-point distribution would yield a high-quality grid in the volume as well. This trial-and-error was deemed impractical for the very large grid sizes envisaged for the research in the current DPhil.

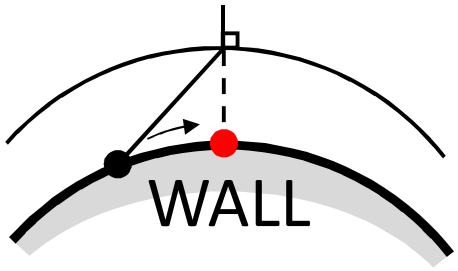


Figure 1: Sliding points along surface to achieve orthogonality at domain boundaries

The mechanism by which the degree of trial-and-error necessary to generate high-quality grids can be reduced is to manipulate both the surface and volume grid-point distributions simultaneously by allowing the grid-points to slide along the surfaces representing domain boundaries. This is the Neumann orthogonality method[57], as illustrated in Figure 1. It was thus decided to develop a new grid-generation tool that would allow grid-points to slide along the surfaces representing domain boundaries.

The development of a new grid-generation tool was seen as a natural opportunity to solve another challenging aspect of large-scale CFD computations; a well-balanced domain-decomposition. In massively-parallel CFD computations involving $\mathcal{O}(10^4)$ processors, achieving a well-balanced domain decomposition is key to realizing the potential benefits of parallelization[40]. Put simply, unless the computational domain is partitioned into groups of cells of roughly equal amounts, the processors handling larger groups of cells will act as bottlenecks and slow down the entire computation. Rather than attempting to perform the domain-decomposition *a posteriori*, a simpler method would be to define the block boundaries *a priori* and then populate the region bounded by the block boundaries with the same number of points. Such an approach would guarantee domain partitions of equal size, all without the need to resort to complex decomposition algorithms.

Following this line of reasoning, a block-partitioning tool for turbomachinery blade passages was developed. Starting from a base layout, shown in Figure 2, this tool allows additional blocks to be inserted if further grid refinement is desired. The block boundaries generated are matching, ensuring that each block face is only in contact with one other block face. This is also true across the periodic interface and across the blade metal. The latter characteristic is only strictly necessary if the tip-gap region of a rotor blade is also to be meshed. While the grid-generator currently cannot mesh the tip-gap region, enforcing matching block boundaries across the blade metal means that this feature can be added in the future.

Once a block layout has been defined, transfinite interpolation[27] is used to mesh each block using the same number of points to create an initial mesh, as shown in Figure 3.

The mesh shown in Figure 3 comprises of matching blocks containing the same number of cells. The final step is to manipulate the positions of the grid points so as to achieve smooth variations in cell size and orthogonal grid-lines in as much of the do-

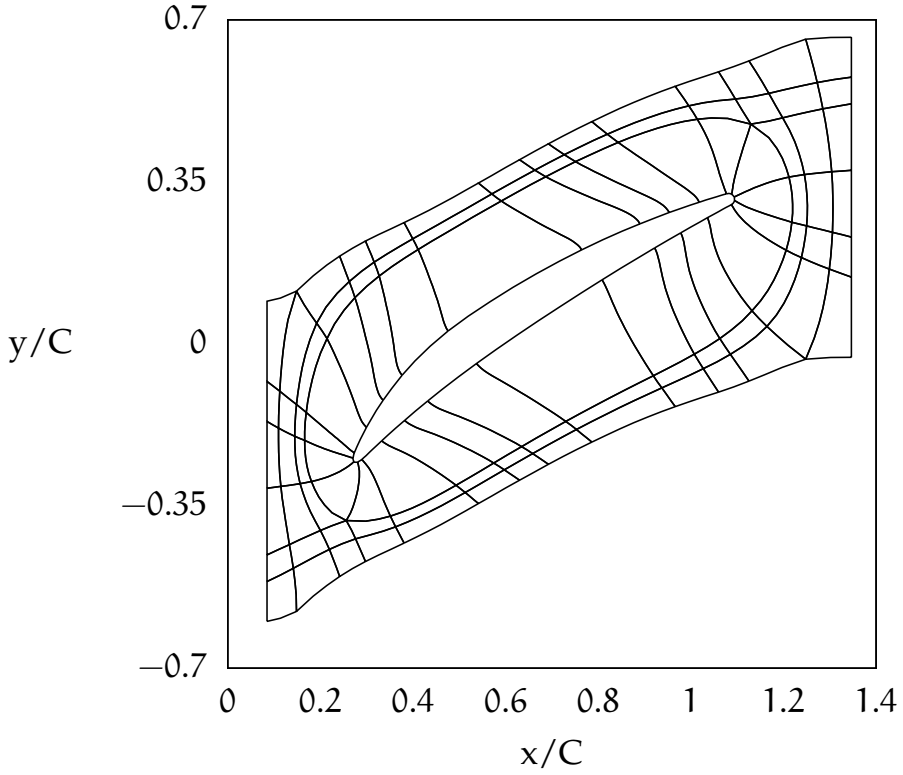


Figure 2: Base block layout for meshing turbomachinery blade passages

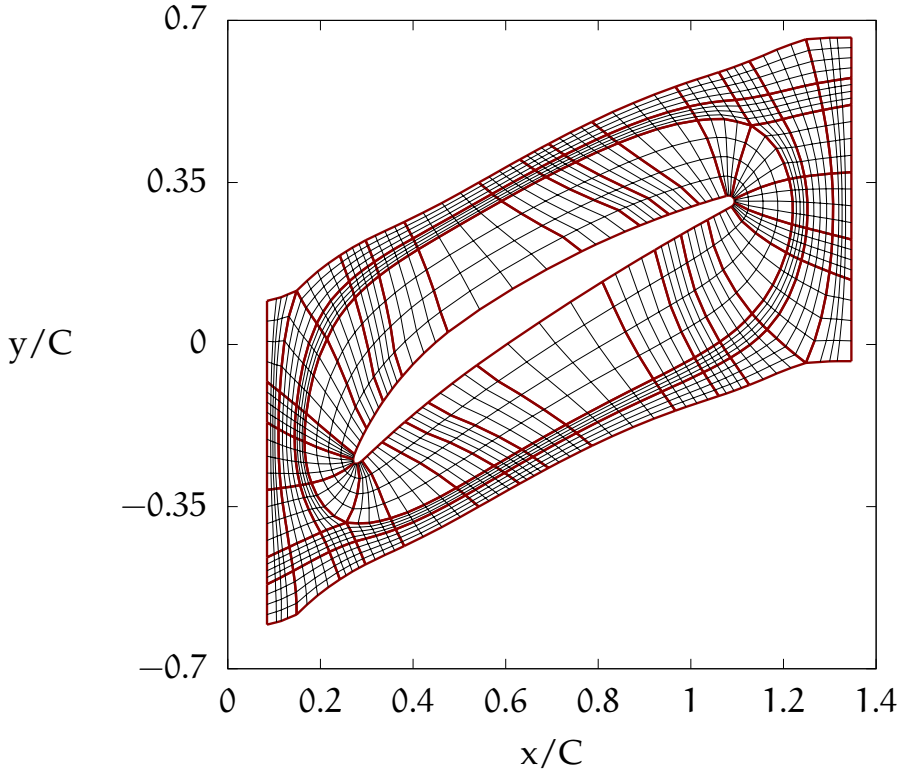


Figure 3: Initial mesh of compressor stator passage. Block boundaries marked by red lines.

main as possible. This is achieved through an iterative application of the seminal elliptic grid-generation equations of Thompson, Warsi and Mastin (TWM)[114]:

$$\mathbf{x} = f(\xi_1, \xi_2, \xi_2) \tag{37a}$$

$$a^i = \frac{\partial \xi_i}{\partial \mathbf{x}} \tag{37b}$$

$$a^{ij} = \frac{\partial \xi_i}{\partial \mathbf{x}} \frac{\partial \xi_j}{\partial \mathbf{x}} \tag{37c}$$

$$\tag{37d}$$

$$\begin{aligned} a^{11} \frac{\partial^2 \mathbf{x}}{\partial \xi_1 \partial \xi_1} + a^{22} \frac{\partial^2 \mathbf{x}}{\partial \xi_2 \partial \xi_2} + a^{33} \frac{\partial^2 \mathbf{x}}{\partial \xi_3 \partial \xi_3} + \\ 2a^{12} \frac{\partial^2 \mathbf{x}}{\partial \xi_1 \partial \xi_2} + 2a^{13} \frac{\partial^2 \mathbf{x}}{\partial \xi_1 \partial \xi_3} + 2a^{23} \frac{\partial^2 \mathbf{x}}{\partial \xi_2 \partial \xi_3} = \\ P^1 \frac{\partial \mathbf{x}}{\partial \xi_1} + P^2 \frac{\partial \mathbf{x}}{\partial \xi_2} + P^3 \frac{\partial \mathbf{x}}{\partial \xi_3} \end{aligned} \tag{38}$$

Due to the inherent diffusive and smoothing properties of elliptic operators, elliptic grid-generation systems have enjoyed widespread use in cases where the coordinates are specified over the entire domain boundary[118]. The TWM grid-generation system is based on a description of the grid-points in terms of three mutually-orthogonal curvilinear coordinates, ξ_1, ξ_2, ξ_3, as shown in Equation 37. In Equation 38, P^i represent the control functions that can be used to either attract or repel grid-lines relative to each other[118]. In the current work, the control functions are used to locally refine the grid near viscous-walls, e. g. the blade surface and the hub/tip end-walls.

Each successive application of Equation 38 yields a displacement vector, $\delta\mathbf{x}$, which is used to update the position of the grid-point in question. Surfaces representing domain boundaries are expressed as a function of two parametric coordinates, $\mathbf{s} = \binom{s1}{s2}$. Hence for grid-points lying on domain boundaries, $\delta\mathbf{x}$ is projected onto the corresponding surface in order to compute an update in terms of the parametric coordinates, i. e. $\delta\mathbf{s}$. This ensures a physically accurate description of the surface, regardless of however the grid-point distribution is modified. The surface projection method is illustrated in Figure 4.

Figure 5 shows the result of applying the smoothing operation to the initial mesh shown in Figure 3. Cell size varies very smoothly throughout the domain, the grid-lines are also nearly orthogonal throughout the domain and at the boundaries. The mesh shown in Figure 5 is also partitioned into blocks of equal size, and hence represents a perfect domain decomposition.

A better understanding of the capabilities of the mesh generator can be gained by examining a mesh used to conduct the simulations presented in Chapter 4. Figure 6 shows a radial cross-section of the compressor stator passage mesh. Cell-face areas very very smoothly throughout the mesh, and the grid-lines are nearly orthogonal everywhere. Turbomachinery blade passages are meshed using an H-O-H grid topology; the grid-lines immediately surrounding the aerofoil resemble an "O", whereas those in the remainder of the passage resemble an "H"[45]. In such a layout, the most challenging

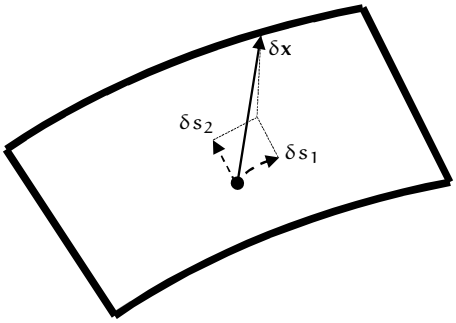


Figure 4: Grid-point displacements are projected on to the surface to compute updates for the parametric coordinates

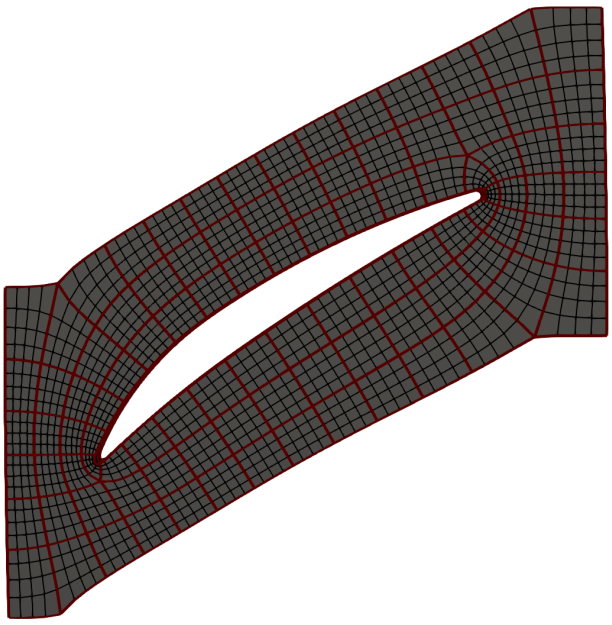


Figure 5: Smooth mesh of compressor stator passage. Block boundaries marked by red lines.

regions for any grid generator are the junction-points between the O-grid and the H-grid[118], marked with red circles in Figure 6. As seen in Figure 6, the quadrilaterals surrounding the junction-points are relatively free from distortion and the cell growth-rate around the junction-points is also very smooth.

Figure 7 shows a zoomed-in view of the mesh around the leading and trailing edges. The cell growth rate, 10% in the case shown, is very smooth from the blade surface out to the freestream. The grid-lines also remain orthogonal all the way throughout the boundary layer and down to the wall. It should be noted that in both Figure 6 and Figure 7, only every 4^{th} grid-point is shown; the true grid is too fine to visualise clearly.

A method by which grid-line orthogonality is quantified is the skewness, defined as the maximum cosine of the internal angles of a quadrilateral[128]. The optimum value of skewness is clearly 0, as it corresponds to a quadrilateral with all four edges perfectly orthogonal. The skewness for a production ready mesh is shown in Figure 8, and it is immediately clear that most of the grid is completely free of any skewness, especially the region around the blade surfaces. This is confirmed by Figure 9, which shows that approximately 95% of the cells in the domain are virtually free of any skew ($\leqslant 0.1$). Thompson estimated that as long as the internal angle is greater than 45^{o}, corresponding to a skewness value of 0.3, the error arising from skewness is no larger than that from unequal cell sizes[118]. Other than the junction points, regions with non-zero skewness are still under the threshold of 0.3; only 0.2% of cells suffering from skewness larger than 0.3.

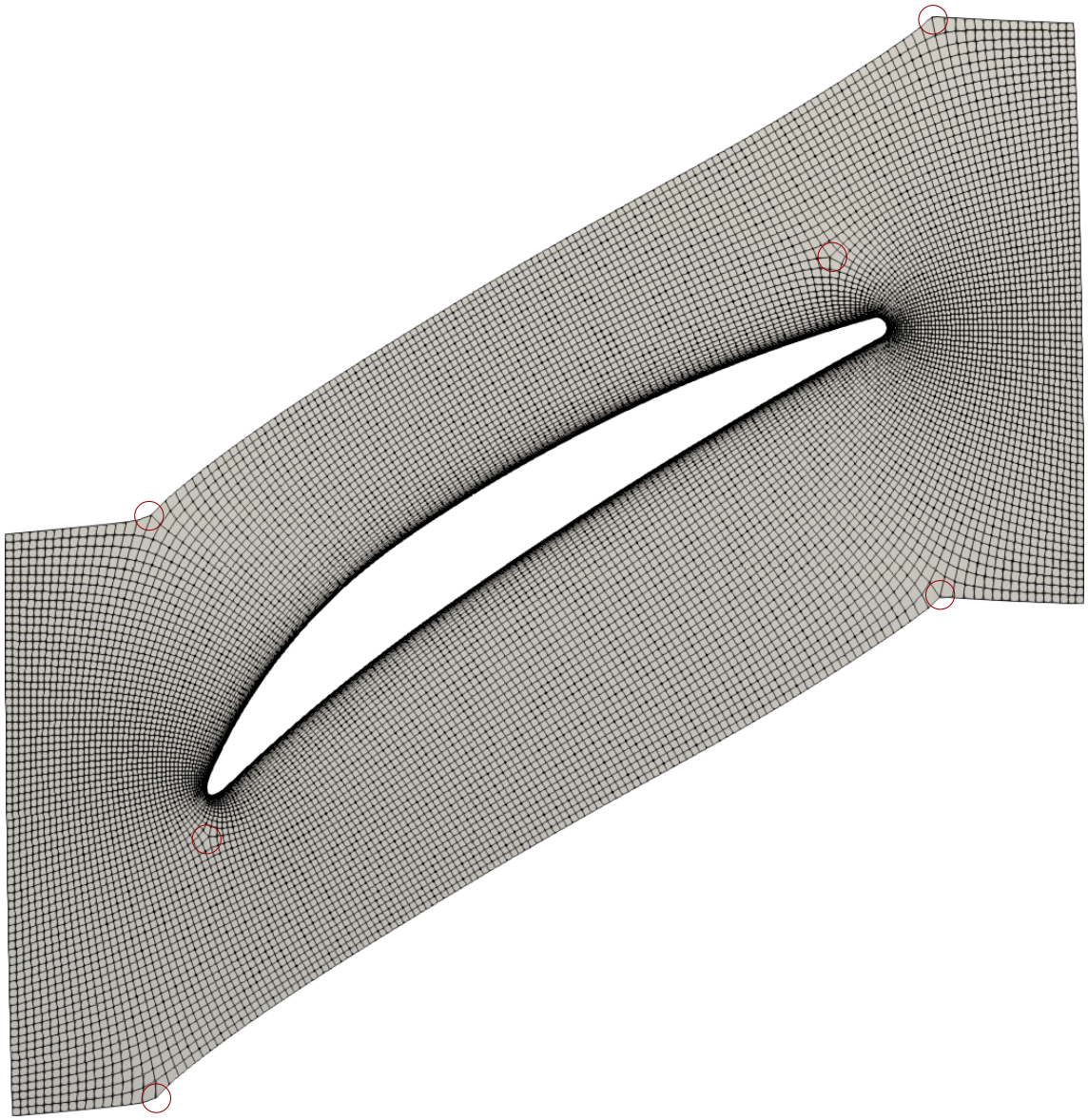
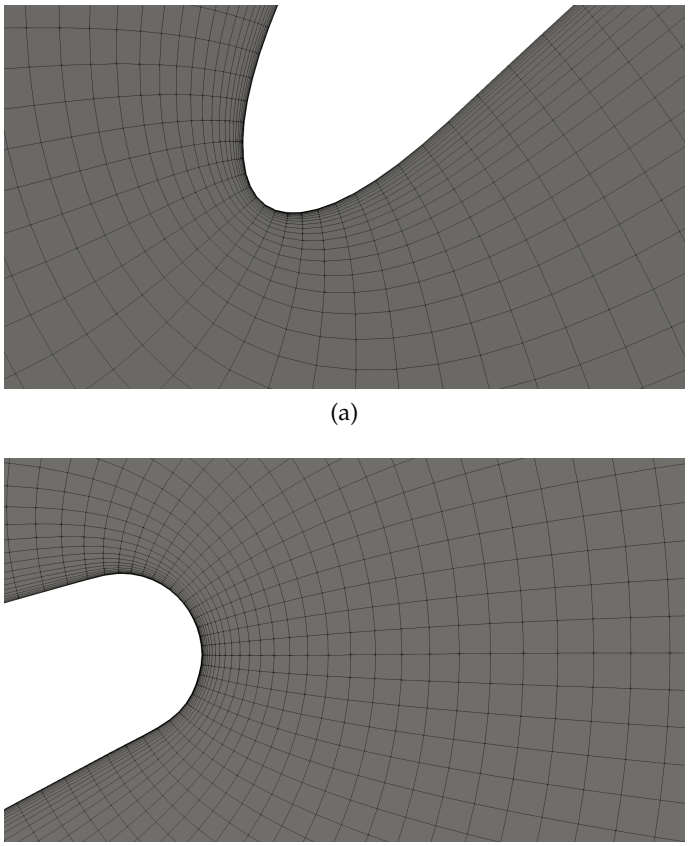


Figure 6: Production ready mesh of compressor stator passage. Junction-points are highlighted by red circles. Only every 4^{th} point has been plotted to make the grid-lines more visible.



(a)

(b)

Figure 7: Leading edge(a) and trailing edge(b) on production ready mesh of compressor stator passage. Only every 4^{th} point has been plotted to make grid-lines more visible.

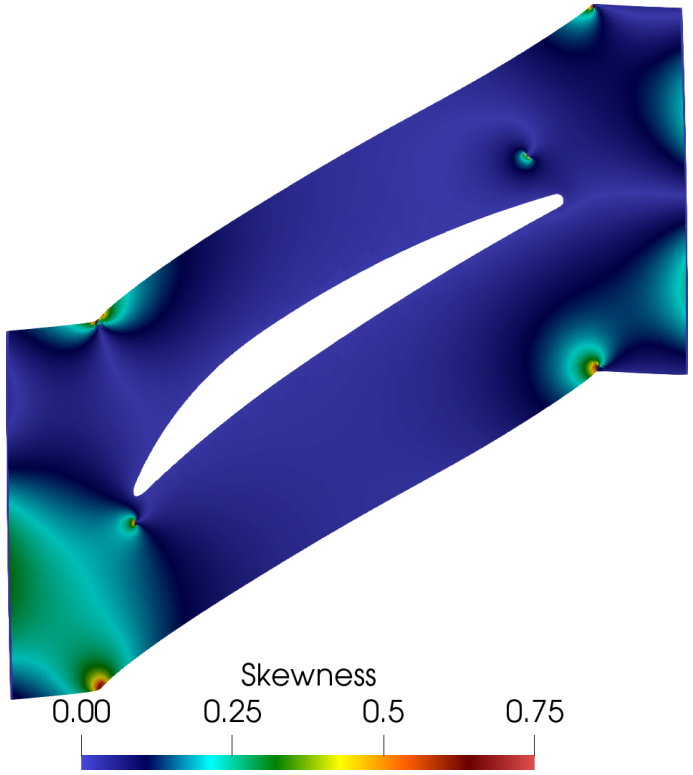


Figure 8: Skewness for production ready mesh of compressor stator passage.

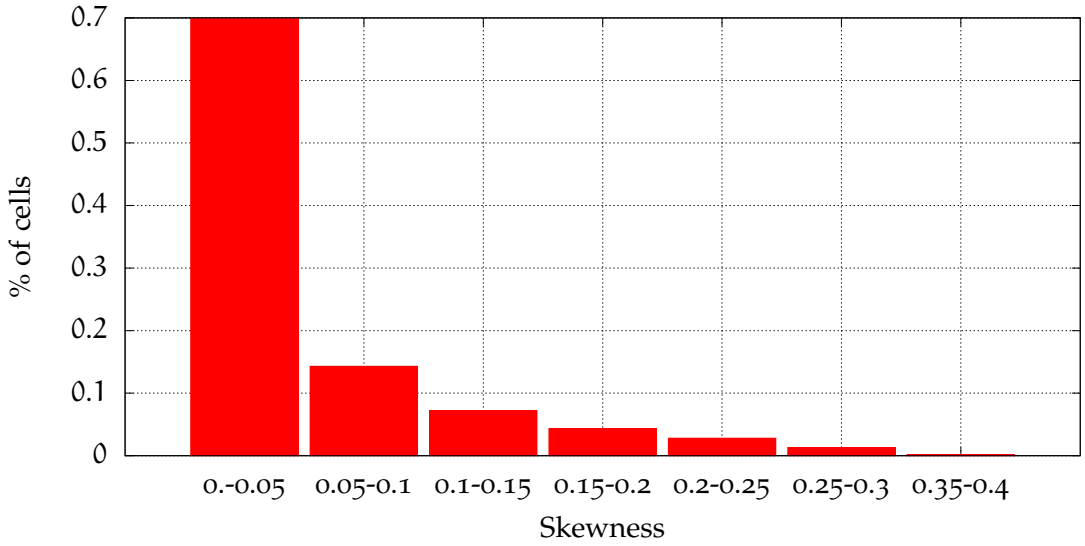


Figure 9: Skewness distribution for production ready mesh.

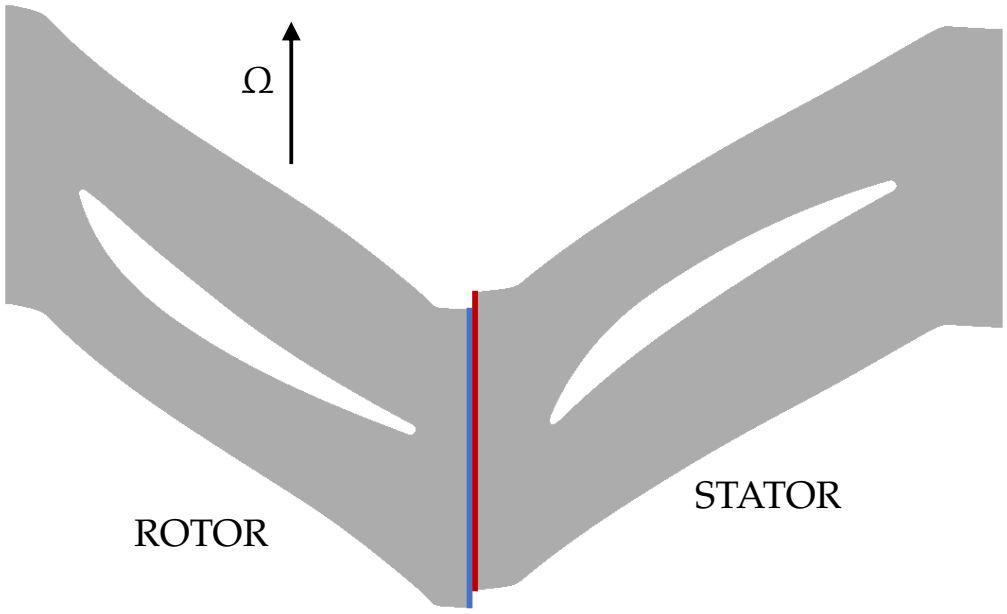


Figure 10: Radial cross-section of compressor stage simulation domain. The coloured lines mark the rotor-stator interface; rotor outlet is shown in blue, and stator inlet shown in red. The rotor row rotates at a speed of Ω, whereas the stator row is stationary.

2.6 Sliding plane

For unsteady simulations of turbomachinery stages, the widely accepted best practice is to use what is called the sliding-plane algorithm, sometimes also referred to as sliding-mesh. It comprises of meshing the rotor and stator passages independently, simulating each passage in its respective mesh, and updating the cell-connectivity as the passages rotate relative to each other. The principle is illustrated in Figure 10.

At each time-step, the motion of the rotor row causes the cells adjacent to the rotor-stator interface to move relative to each other, thereby potentially changing the cell-connectivity. The sliding-plane algorithm must thus perform two tasks; update the cell-connectivity across the rotor-stator interface and interpolate flow quantities based on the separation of the two matching cells.

Typically, modern CFD codes use a fast-search algorithm to identify the nearest neighbouring cells across the rotor-stator interface, e. g.Wang et al[131] use a kd-tree in their unsteady multi-stage compressor simulations. A kd-tree is a binary tree for storing k-dimensional data, and in the case of a two-dimensional sliding plane it can be shown to be of complexity $\mathcal{O}(n \log n)$, where n is the number of computational cells on each side of the sliding-plane[9].

In the case of massively parallel computations, such as those performed for the current work, each side of the sliding-plane could potentially be distributed across 10^2 message passing interface (MPI) ranks, and comprise of 10^4 cells. In such a computation, it would be extremely wasteful for all MPI ranks on the sliding-plane to share the coordinates of their cells, as communications are typically at least 3 orders of magnitudes slower than

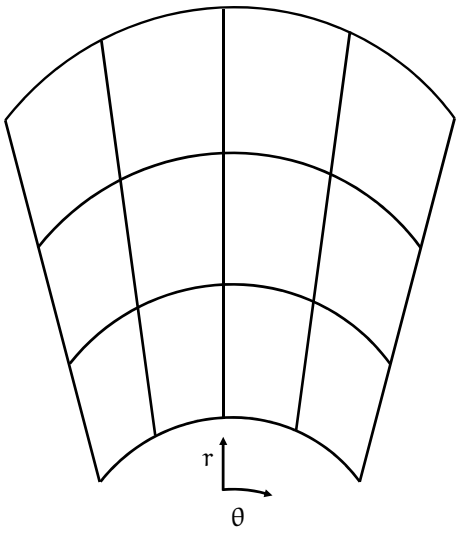


Figure 11: Typical block boundary arrangement at sliding plane

CPU computations[25]. Furthermore, requiring each MPI rank to hold a copy of the entire sliding-plane would lead to excessive memory demands.

In the case of a multi-block structured mesh, such as those used for the current work, the problem can be greatly simplified due to the fact that the block partitions at the sliding plane are likely to represent a relatively ordered two-dimensional grid in the radial and circumferential directions as shown in Figure 11.

The block boundaries can thus be mapped to two-dimensional (r and θ) intervals, and the sliding-plane algorithm can be simplified to computing and tracking the overlaps between two sets of intervals on opposing sides of the sliding-plane, i. e. the left and right hand sides (LHS and RHS). The remainder of this section explains the sliding plane algorithm step-by-step.

During the pre-processing step of a computation, the blocks and the MPI ranks participating in the sliding plane are identified. The bounds of all participating blocks are mapped onto two-dimensional intervals, as shown in Figure 11, and a copy is given to each MPI rank. The intervals are given a tag that defines whether they lie on the LHS or the RHS of the sliding plane. At the start of a computation, each MPI rank in the sliding plane will determine which intervals from the opposing side it shares a radial overlap with. If B is the number of blocks on one side of the sliding plane, this operation has a cost of $\mathcal{O}(B)$. As the relative motion of the blocks is only in the θ direction, the radial overlaps only have to be computed once. Having identified the radial overlaps, the next step is to determine which blocks overlap tangentially. This step is best explained with the aid of a minimum working example.

Figure 12 shows an illustration of tangentially overlapping intervals, with θ increasing from left to right. The LHS (blue lines) is moving whereas the RHS (red lines) is stationary. In order to emphasize the generality of the algorithm, the LHS has been constructed using three blocks and but the RHS with only two. The end-points of the intervals are numbered so that the left-bound of an interval always lies on an even numbered point, and the right-bound on an odd-numbered point: the left-bound of internal I_j is marked by point $2j$, and the right-bound by point $2j + 1$. The next task is to sort the point list

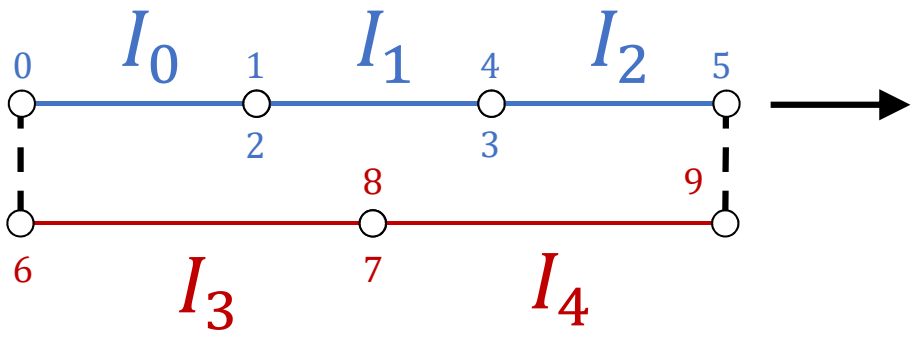


Figure 12: Illustration of tangentially overlapping intervals. Blue lines correpsond to the LHS of the sliding plane, and red lines coorespond to the RHS. Dotted black lines mark periodic computational domain bounds. θ is increasing from left to right.

in order of increasing θ. If N is the number of participating intervals, the cost of this operation is $\mathcal{O}(N \log 2N)$. For the diagram shown in Figure 12, $N = 5$ and its ordered points list is shown in Table 2.

Point #	Interval #	Sliding plane side
6	**3**	**R**
0	0	L
1	0	L
2	0	L
7	3	R
8	4	R
3	1	L
4	2	L
5	2	L
9	4	R
6	**3**	**R**

Table 2: Sorted point list corresponding to static intervals.

As Table 2 shows, the first and last point in the sorted list is the left-most point on the RHS of the sliding plane, i. e. the lower of the computational domain's periodic boundaries. These two points remain fixed as the list in Table 2 is updated.

Now that a sorted point has been obtained, the interval overlap list can be computed. This only needs to be done once at the start of a computation, and the procedure for doing so is very simple. Starting at the top of the sorted point list and moving through it point-by-point, whenever an even point is encountered, the interval it belongs to is

added to a stack. When arriving at an odd-point, its interval is removed from the stack. If intervals from the LHS and RHS ever happen to be on the stack simultaneously, they are added to each other's overlap lists. The overlap lists for the interval configuration in Figure 12 are given in Table 3.

Interval #	# of overlaps	Index of overlapping interval(s)
0	1	3
1	2	3, 4
2	1	4
3	2	0, 1
4	2	1, 2

Table 3: Overlap list corresponding to static intervals.

The interval overlap is essentially the communication pattern: each block will send MPI communications to the blocks in its interval overlap list. The cost of building the overlap lists is $\mathcal{O}(N)$. Having built the overlap list, only one task remains before the sliding plane algorithm can begin tracking the motion of the LHS.

The LHS moves relative to the RHS via a series of events. An event is defined as whenever a point on the LHS meets a point on the RHS. Whenever an event occurs, the location of the two points involved, and only those two, is swapped in the sorted point list. The event list is also sorted, in ascending order of the distance between the two points involved. Table 4 shows the event list corresponding to the intervals in Figure 12.

Event
5,9
1,7
2,7
3,9
4,9
0,7

Table 4: Event list for static intervals

The event list only has to be built once, and it incurs a cost proportional to $\mathcal{O}(N \log N)$. The start-up of the sliding plane algorithm is now complete. During the rest of the computation, the sliding plane algorithm will track the motion of the intervals and update the point, overlap and event list accordingly. The costs incurred so far have been:

1. Compute radial overlaps: $\mathcal{O}(B)$

2. Building ordered point list: $\mathcal{O}(N \log 2N)$
3. Building overlap list: $\mathcal{O}(N)$
4. Building and sorting events list: $\mathcal{O}(N \log N)$

The first event in Table 4 is a trivial one, and will result in point 5 and 9 being swapped. Whenever an event occurs, a search of the updated point list, at cost $\mathcal{O}(\log N)$, is carried out to determine the next nearest RHS point for the LHS point involved in the event. As such, the event list is never smaller than the number of LHS points. Swapping points 5 and 9 and performing a search of the point list reveals that point 6 is the next nearest point on the RHS. A new event, (5,6), is thus formed and placed in the event list, in order of increasing distance. This search also incurs a cost of $\mathcal{O}(\log N)$. The updated event list is shown in Table 5.

Event
5,6
1,7
2,7
3,9
4,9
0,7

Table 5: Updated event list after event (5,9).

When event (5,6) occurs, the position of points 5 and 6 is not swapped, because the lower-periodic bound of the RHS stays anchored at the top and bottom of the sorted point list. Whenever a LHS point reaches point 6, it is simply moved to the top of the sorted point list. Event (5,6) is of the odd-even type. Whenever an odd-even event occurs, a new overlap is created between the participating intervals: the event (2h+1,2k) creates a new overlap between $I_{(h-1)/2}, I_{k/2}$. New overlaps can be added to the overlap list in constant time. The next event to occur after (5,6) is (1,7), which will take place when a sufficient number of time-steps have passed for the intervals to be in the position shown in Figure 13.

After event (1,7) occurs, the next event is (2,7) which is of the even-odd type. When an even-odd event occurs, an overlap is destroyed between the participating intervals: the event (2h,2k+1) destroys the overlap between $I_{h/2}, I_{(k-1)/2}$. Destroying an overlap comes at a cost of $\mathcal{O}(M)$, where M is the number of overlaps for a particular interval. The updated point list, overlap list and event list after (2,7) has occurred are shown in Table 6, Table 7 and Table 8 respectively.

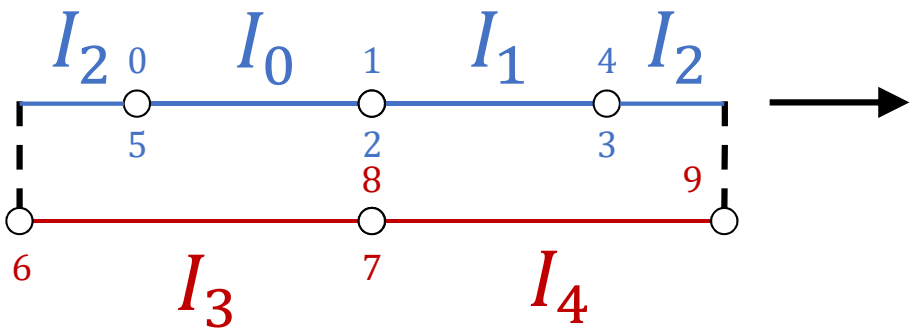


Figure 13: Position of intervals when event (1,7) occurs.

Point #	Interval #	Sliding plane side
6	**3**	**R**
5	2	L
0	0	L
7	3	R
1	0	L
2	0	L
8	4	R
3	1	L
4	2	L
9	4	R
6	**3**	**R**

Table 6: Sorted point list after event (2,7).

Interval #	# of overlaps	Index of overlapping interval(s)
0	1	3
1	1	4
2	2	4, 3
3	2	0, 2
4	2	1, 2

Table 7: Overlap list after event (2,7).

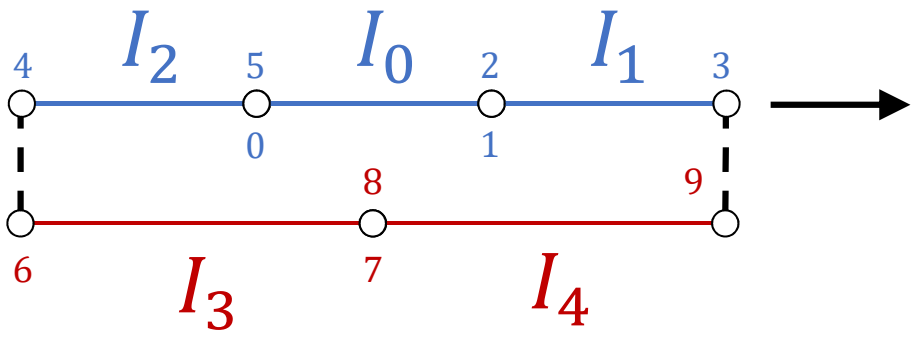


Figure 14: Position of intervals when event (3,9) occurs.

Event
1,8
2,8
3,9
4,9
0,7
5,6

Table 8: Updated event list after event (2,7).

The first two events in Table 8 are again trivial ones, and the next one requiring movement of the intervals is event (3,9). This will occur when the intervals are in the position shown in Figure 14.

The sliding plane algorithm thus carries on in this vein, by continuing to track events as the computation marches forward in time and updating the overlap lists accordingly. If the number of events per time-step is L, then the running cost of the sliding plane algorithm is at worst $\mathcal{O}(L(M + 2\log N))$.

The interval overlap list essentially defines the communication pattern across the sliding-plane; the blocks the overlapping intervals pertain to must exchange flow-variables with each other. Once the communicating partner(s) for each block has been determined, the final task is to determine which cells on the two block faces are nearest to each other. In the current implementation, a kd-tree of order $\mathcal{O}(n \log n)$ is used, where n represents the number of cells on a block face, typically 32×32.

3

Re_τ SCALING OF POD MODES

This chapter reports an investigation into the universality of the two-point velocity correlation tensor of plane-channel flow and its proper orthogonal decomposition (POD) modes. Not only can the POD modes of plane-channel flow be used in models relevant to computations of compressor passages, e. g. the specification of turbulence at the inlet of scale-resolving simulations, this study also provides an opportunity to test whether or not AU3X can match the two-point, second-order statistics of a direct numerical simulation (DNS) of plane-channel flow. As most validation studies focus only on single-point flow statistics such as Reynolds stresses and turbulent spectra, the research reported herein represents a very stringent test of the numerical methods of AU3X.

3.1 Introduction

One of the ways in which the academic community has endeavoured to make the prediction of turbulent flows a more tractable problem is to search for a set of universal mode shapes that permit a simplified statistical description of turbulent structures. These efforts can be traced all the way to the seminal work of Townsend[119] and Grant[39]. Both authors were computing two-point velocity correlations in canonical shear-flows, and in order to explain the shape of the correlations they theorized the existence of large-scale, organized turbulent motion, which they called coherent structures. For example, the transverse correlation in the wake of a circular cylinder was explained by proposing the existence of a large double-roller eddy whose rotational axes were aligned with the mean flow[120].

The presence of fundamental modes can also be seen in the measurements of Favre et al[4],[29]. Favre et al measured two-point and two-time correlations in zero pressure gradient flat-plate boundary layers. One of their key findings was that the time delayed two-point streamwise measurements remained correlated for very large separations (this result was also present in Grant's[39] measurements).

Many researchers subsequently employed conditional averaging techniques to study turbulent structures in more detail. Kline et al[60] were able to visualize fundamental modes corresponding to the spanwise hairpin vortex in the near-wall region. Moreover, the authors were also able to identify a mechanism of turbulent kinetic energy production, namely the rising up of low-speed streaks and "bursting" upon interaction with the outer flow. In a later publication[58], the authors observed that turbulent kinetic energy production occurs almost entirely due to "bursting" events in the region of $0 \leqslant y^+ \leqslant 100$, where $y^+ = \frac{y u_\tau}{\nu}$ and $u_\tau = \sqrt{\nu \left.\frac{d\overline{u}}{dy}\right|_{y=wall}}$. This description of near-wall turbulent structure and turbulent kinetic energy production was further validated by Blackwelder et al[7].

Although conditional averaging enjoyed success in visualizing fundamental modes of turbulent structures, it is a technique that is subject to a high degree of empiricism and

arbitrariness[7]. An alternative and more objective method for extracting modes from a turbulent flow field, one which requires no assumptions about the shape of the turbulent structures present[33], is Lumley's Proper Orthogonal Decomposition (POD)[73]. POD operates on the two-point and two-time velocity correlation tensor to identify the most energetic modes in a flow field. Physically speaking, POD modes are good indicators of the geometry of large scale, organized motion in turbulent flow field[74]. However, POD requires a full two-point and two-time correlation tensor, and therefore POD could not be thoroughly tested for approximately two decades after its introduction due to a lack of necessary experimental/computational data[85].

Moin[81] was the first to apply POD to a complete two-point correlation tensor (obtained from a Large Eddy Simulation of channel flow). Although Moin could only perform a two-dimensional POD, he was able to identify that the dominant eddy accounted for 64% of the total turbulent kinetic energy[81]. Arguably, the first complete application of POD was that carried out by Moin et al[85] on Kim et al's[59] direct numerical simulations (DNS) of plane channel flow.

Moin et al[85] attempted to identify the most energetic modes in turbulent plane channel flow at $Re_\tau = 180$. POD was applied to the time-averaged two-point velocity correlation tensor, allowing the authors to identify three dimensional modes of turbulent structures. Moreover, they were able to confirm that the most energetic POD mode corresponded to a spanwise hairpin vortex, very similar in form to that observed in the measurements of Kline et al[60].

Similar analyses of two-point velocity correlations have subsequently been conducted at higher Re_τ in order to study turbulent structures in greater detail. Del Alamo et al[20] analysed the scaling of one-dimensional and two-dimensional turbulent energy spectra in channel flows up to $Re_\tau = 1900$. Jimenez et al[54] analysed the two-point velocity correlation in zero pressure-gradient boundary layer flow, $Re_\tau \approx 450 - 700$, and channel flow, $Re_\tau \approx 550 - 950$. The authors were able to show a high degree of similarity in the large scale modes. More recently, Sillero et al[108] confirmed the scaling of large scale modes in boundary layers and channels from $Re_\tau \approx 950 - 2000$. The above examples offer the reader only a glimpse into the vast amount of research that has gone into understanding turbulent structures. To the best of the authors' knowledge however, the Re_τ scaling of the POD modes of the two-point correlation has not been studied extensively. This is arguably because of the expense associated with computing the full velocity two-point correlation tensor: due to its slow statistical convergence, samples of the flow-field need to be collected for very long separations in time. The POD modes correspond to the eigenvectors of the two-point correlation tensor - rescaled by the square-root of their respective eigenvalue - and represent a set of mutually orthogonal and mutually uncorrelated fields. The orthogonality property makes the set of POD modes an optimal basis for the representation of the fluctuating part of the flow-field[33]. As a result, the eigenvectors of the two-point correlation can be used in many modelling scenarios, with two examples being reduced-order modelling of turbulent flow[96] and synthetic turbulence generation at the inlet of spatially developing flows[23].

Chambers et al[12] first attempted to study the Re_τ scaling of the eigenvectors of the two-point velocity correlation. Due to computational constraints at the time, they were unable to solve the Navier-Stokes equations for high values of Re_τ and had to base their computations on a stochastically forced Burgers' equation. Their results showed

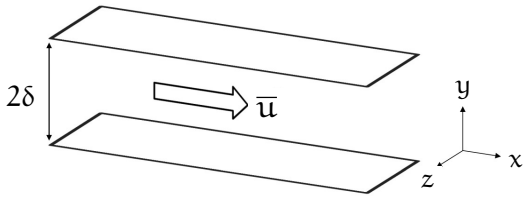


Figure 15: Plane channel flow schematic

the eigenvectors to be independent of Re_τ in the outer scales (i.e. $\frac{y}{\delta} \geqslant 0.2$), even for very high order eigenvectors. The inner scales on the other hand showed considerable dependence on Re_τ.

Liu et al[72] performed measurements using particle image velocimetry (PIV) on channel flows at $Re_\tau = 315$ and $Re_\tau = 1414$. For both these flows, a one-dimensional POD was performed on the two-point velocity correlation in the wall-normal direction. The authors were able to show that the eigenvalue spectrum and eigenvectors are largely independent of Re_τ in the outer scales. However, the modes extracted by POD in this case do not directly correlate to turbulent structures because they are only one-dimensional and lack length-scales in the streamwise and spanwise directions. Another shortcoming of this analysis was that it lacked the resolution necessary to resolve the flow very close to the wall, i.e. the inner scales.

Liu et al[71] repeated their analysis with a two-dimensional POD. However, even the POD modes from this analysis cannot be thought of as turbulent structures because they lack a length scale in the z (spanwise) direction. Moreover, the eigenvectors obtained from the two-dimensional POD do not appear to be independent of Re_τ. Finally, the data still lacks the resolution to study the inner scales.

The emphasis of this chapter is thus to study the Re_τ scaling of the POD eigenvalues and eigenvectors of the two-point velocity correlation tensor.

The two-point correlations are obtained from a database of Direct Numerical Simulations (DNS) of plane channel flow. The reader is therefore first presented with details about the DNS database used. Subsequently, a brief summary is given of the POD applied to channel flow, and the key features of the statistical techniques employed are discussed. Finally, an in-depth analysis is presented of the Re_τ scaling of the eigenvalues and eigenvectors of the two-point velocity correlation.

3.2 Numerical Methods

3.2.1 *DNS database*

The investigations in this chapter are based on direct simulations of plane channel flow using the incompressible Navier-Stokes equations. The numerical underpinnings of the solver can be found in the seminal paper of Kim et al[59].

Figure 15 shows a schematic of the plane channel flow simulations. The walls of the channel lie on the $y+$ and $y-$ boundaries, and are separated by a distance of 2δ. The bulk flow is in the x-direction. As the flow is homogeneous in the x and z directions, periodic boundary conditions are used in both these directions.

Table 9: Simulation parameters

Re_τ	$(L_x, L_y, L_z)/\delta$	Δx^+,Δy^+_{max},Δz^+	N_x, N_y, N_z	N_f	Tu_τ/δ
547	8π,2,4π	7.2,7.2,3.6	1536,257,1536	142	22
934	8π,2,3π	9.2,7.6,3.8	3072,385,2304	73	12

Two-point correlations were computed using the velocity fields from two simulations; $Re_\tau = 547$[19],[18] and $Re_\tau = 934$[20]. Details of both are given in Table 9.

In Table 9, L is the domain size and Δx^+,Δy^+,Δz^+ are the grid spacings in each direction in wall-units, i.e. $\Delta x^+ = \frac{x u_\tau}{\nu}$. N_f is the number of velocity fields used to compute the statistics and Tu_τ/δ is the non-dimensional time spanned by the statistics; all statistics shown in this article represent an average from $t = 0$ to $t = Tu_\tau/\delta$. The grid is uniform in the x and z directions but stretched in the y direction using a cosine distribution. N_x and N_z are the number of points in their respective cartesian directions, but the number of Fourier modes is given by de-aliasing using the $2/3^{rd}$ rule. N_y is the number of points and Chebychev modes in the wall-normal direction[19],[18]. It should be noted that for the $Re_\tau = 547$ case, the simulation was carried out using 257 Chebychev modes but in the present work the expansion to physical space was performed on to the same wall-normal grid as the $Re_\tau = 934$ case, i.e. 385 points. The motivation for doing so is explained in section Section 3.2.2.

3.2.2 *Two-point velocity correlation and the Proper Orthogonal Decomposition*

As stated in Section 3.1, POD can be applied to the two-point velocity correlation tensor to extract modes shapes of turbulent structures[74]. The aspects of POD most relevant to the current work are summarised in the following paragraphs.

To search for modes in a velocity field, a projection can be performed:

$$a = \int_0^{L_y} \psi(y) u(y)\, dy \tag{39}$$

In Equation 39, u is the velocity, ψ is a proposed mode, a its projection coefficient and L_y is the length of the domain over which the velocity signal is defined. The magnitude of the projection coefficient determines how closely ψ resembles the velocity field. In the case of turbulent flow, u and a are stochastic variables. Clearly, one would be more interested in ensemble-averaged values. Therefore, rather than searching for modes that yield the largest instantaneous value of a, it is more useful to maximise the mean-square of the projection coefficient (averaged over a large number of realisations of the flow). The modes that maximise the mean square of the projection coefficient are the eigenfunctions of the two-point velocity correlation. For a one-dimensional velocity field, this statement can be expressed as:

$$\int_0^{L_y} \overline{u(y)u^*(y')} f^{(n)}(y') dy' = \lambda^{(n)} f^{(n)}(y) \tag{40}$$

In Equation 40, $f_i^{(n)}$ is the n^{th} order eigenfunction, $\lambda^{(n)}$ its corresponding eigenvalue and $u(y)$ has been assumed to be a complex variable to preserve generality. The daunt-

ing task of computing three-dimensional eigenfunctions can be simplified with the realisation that in the directions of statistical homogeneity, the eigenfunctions of the two-point correlation are Fourier modes[74]. Thus if a Fourier transform is performed on the velocity field in the homogeneous directions *a priori*, the problem reduces to a series of decoupled one-dimensional eigenvalue problems at every streamwise and spanwise wavenumber pair, i.e. k_x and k_z:

$$\begin{aligned} \Phi_{ij}(k_x, k_z, y, y', t) &= \hat{u}'_i(k_x, k_z, y, t)\hat{u}'^{*}_j(k_x, k_z, y', t) \\ \overline{\Phi_{ij}}(k_x, k_z, y, y') &= \frac{1}{N_f}\sum_{n=1}^{N_t} \hat{u}'_i(k_x, k_z, y, t_n)\hat{u}'^{*}_j(k_x, k_z, y', t_n) \\ \int_0^{L_y} \overline{\Phi_{ij}} f_j^{(n)}(k_x, k_z, y')dy' &= \lambda^{(n)} f_i^{(n)}(k_x, k_z, y) \end{aligned} \tag{41}$$

A salient point to note here is that $\hat{u}_i(k_x, k_z, y)$ only contains information about the fluctuating component of the velocity field, and not the mean. Equation 41 can be converted to a Hermitian eigenvalue problem using the following transformation:

$$\sum_y \sum_{y'} D(y)\overline{\Phi_{ij}}(k_x, k_z, y, y')f_j^{*(n)}(k_x, k_z, y')D(y') \approx \lambda^{(n)} \sum_y D(y) f_i^{(n)}(k_x, k_z, y) \tag{42}$$

In Equation 42, $D(y)$ is a diagonal matrix that contains the appropriate weight factors to account for the non-uniform grid in the y-direction. $D(y)$ was set using the trapezium rule in the current work. Equation 42 now represents an eigenvalue problem of the form $A_{ij}f_j = \lambda f_i$, in which A_{ij} and is a Hermitian matrix. The CHEEV routine in the LAPACK library[6] was used to perform the inversion, and the eigenvectors are recovered by dividing the result by $D(y)$.

As the L.H.S of Equation 42 is a Hermitian, positive-definite matrix, the eigenvalues are always real and positive even though the eigenvectors are complex[36]. Physical considerations also require the eigenvalues to be real and positive, given that they represent the contribution of a particular mode to the total turbulent kinetic energy. It should be noted that the eigenvectors are orthonormal, and thus describe only the shape of the POD modes. Information about the turbulent kinetic energy contained in POD modes is obtained solely from the eigenvalues.

The eigenvalues of the two-point correlation represent contributions to the total turbulent kinetic energy. The number of eigenvalues extracted using Equation 42 is given by the number of points in the y-direction. Therefore if both simulations have the same number of points in the y-direction, then the eigenvalue indices will correspond to the same fractions of turbulent kinetic energy. This explains why the $Re_\tau = 547$ case was expanded onto the same grid in the y-direction as the $Re_\tau = 934$ case, as alluded to at the end of Section 3.2.1.

3.2.3 *Symmetry groups*

In order to improve the statistical convergence of the two-point velocity correlations, three symmetry groups can be exploited. Two of these symmetries arise from reflections about the centreline in the y and z directions[85]. The final symmetry arises from the

definition of Φ_{ij}. As Φ_{ij} is a Hermitian matrix, the complex conjugate of its transpose is an equally likely realisation[85]. These symmetries are expressed numerically as follows:

$$\Phi_{ij}(k_x, k_z, y, y') = \pm\Phi_{ij}(k_x, k_z, -y, -y') \tag{43a}$$
$$\Phi_{ij}(k_x, k_z, y, y') = \pm\Phi_{ij}(k_x, -k_z, y, y') \tag{43b}$$
$$\Phi_{ij}(k_x, k_z, y, y') = \Phi^*_{ji}(k_x, k_z, y, y') \tag{43c}$$

It should be noted that in Equation 43a the minus is applied when either $i = 2$ or $j = 2$ but not both. Similarly, for Equation 43b the minus sign is applied when either $i = 3$ or $j = 3$[85]. All three symmetry groups in Equation 43 were used to achieve a six-fold increase in the total number of samples made available in the DNS databases[19],[18],[20].

3.2.4 *Finite domain effects*

At $k_x = 0$ or $k_z = 0$, the instantaneous Fourier coefficients of the velocity field $\hat{u}'_i$ represent line averages in the statistically homogeneous directions. Homogeneity and ergodicity require $\hat{u}' = 0$ if u' is defined on a domain of infinite extent in the homogeneous directions. However due to the finite size of the computational domains the estimates of $\hat{u}'_i$ at $k_x = 0$ or $k_z = 0$ are not identically 0. Consequently, the eigenvalues of $\overline{\Phi_{ij}}$ at $k_x = 0$ or $k_z = 0$ could also be non-zero.

Thus in the case of finite domains, the eigenvalues at $k_z = 0$ or $k_x = 0$ can be thought to represent turbulent kinetic energy contained in structures larger than the domain[71], because the domain size represents the largest structure that can be represented by the numerical solution. Any energy that is contained in structures larger than the domain will be grouped into the $k_z = 0$ or $k_x = 0$ modes when a line average is applied over the domain.

Previous researchers, who have used the same DNS database as the current work, have also found the low-order modes to be influenced by the domain size. When studying the pre-multiplied streamwise spectra near the centre of the channel, Jimenez et al[53] found that the peaks occurred at wavelengths very close to the periodicity of the channel. Del Alamo et al[18] also remarked that the "dynamics of the first few Fourier modes are affected by the periodicity of the box". In a later publication, Del Alamo et al[19] estimated that as much as 20% of the streamwise turbulent kinetic energy and 10% of the spanwise turbulent kinetic energy was contained in structures larger than the numerical domain.

Caution should thus be exercised when interpreting the modes at $k_z = 0$ or $k_x = 0$, because they do not strictly represent the mean flow. Moreover, they are unlikely to represent the same quantity at different values of Re_τ as one has no information about the sizes or energy-content of the modes that were cut-off. More light can be shed on this phenomenon by examining the eigenvalue spectra.

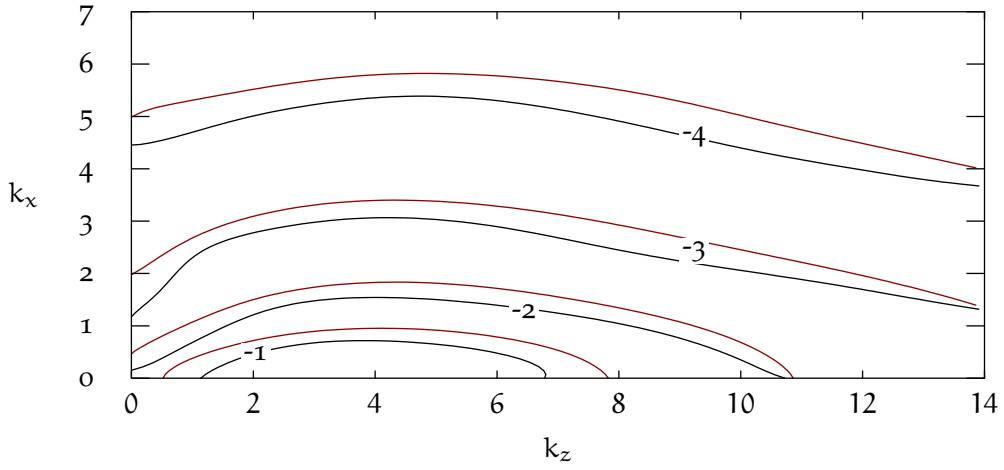


Figure 16: Contour plots of largest eigenvalue, i.e. $\ln\left(\frac{\lambda^{(0)}}{{u_\tau}^2}\right)$ across the k_x-k_z wavenumber space. —— $Re_\tau = 547$, —— $Re_\tau = 934$.

3.3 Two-point correlation POD modes

3.3.1 Re_τ *scaling of eigenvalues*

As explained in Section 3.2.2, the contribution of each POD mode to the turbulent kinetic energy is contained solely in the eigenvalues. Plotting an eigenvalue spectrum can thus help to understand how the turbulent kinetic energy is distributed across length-scales in the homogeneous directions. A two-dimensional spectrum of the most energetic eigenvalue is shown in Figure 16.

The eigenvalue spectrum shows a remarkably high degree of independence from Re_τ. Both spectra decay monotonically with increasing $k_x\delta$ but peak at approximately $k_z\delta = 3$. A notable feature of Figure 16 is that the magnitude of the eigenvalues decays very rapidly with increasing wavenumber, especially in the x-direction. Consequently, only a few modes would be needed to reproduce a significant fraction of the turbulent kinetic energy.

Figure 17 shows one-dimensional eigenvalue spectra along the axes of Figure 16, i.e. at lengthscales equal to the domain sizes. It is immediately clear that the three largest eigenvalues have non-negligible magnitude for the $k_x = 0$ and the $k_z = 0$ modes, at both values of Re_τ. Moreover, although the spectra at the two values of Re_τ converge as the wavenumber increases, they have very different magnitudes at $k = 0$. The zero modes thus do not represent like-for-like quantities at the two values of Re_τ. These observations are consistent with the arguments of Section 3.2.4. Therefore for the remainder of the paper, the Re_τ scaling of quantities at $k_x = 0$ and $k_z = 0$ will not be studied, as not enough information is present to draw firm conclusions about them.

Furthermore, based on the eigenvalue spectrum in Figure 16, it was decided to focus the Re_τ scaling study of the POD eigenvectors on modes in the region from $k_z\delta = 2$ to $k_z\delta = 6$ as these are the ones with the highest turbulent kinetic energy. Modes

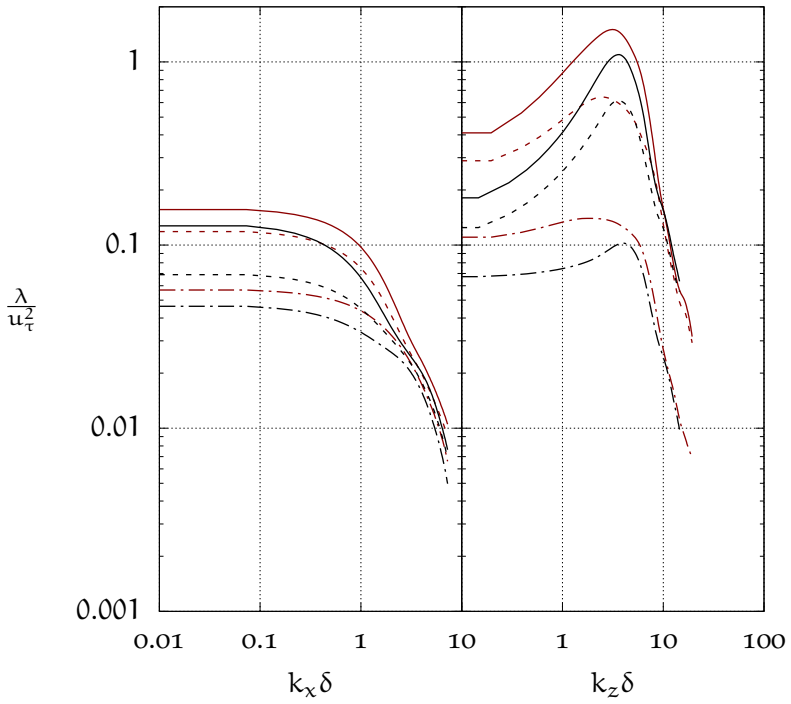


Figure 17: One-dimensional eigenvalue spectra. $k_z = 0$ for streamwise spectrum (left), $k_x = 0$ for spanwise spectrum (right).— $Re_\tau = 547$ — $Re_\tau = 934$. — $\lambda^{(0)}$ - - - $\lambda^{(1)}$ -.-. $\lambda^{(2)}$.

corresponding to small lengthscales, i.e. $k_z\delta = 12$, are also briefly examined for the sake of completeness.

3.3.2 *Two-point correlations and* Re_τ *scaling of eigenvectors*

Before comparing the POD eigenvectors across the two simulations, it could potentially be instructive to compare the two-point correlation tensors themselves. The tensors cannot however simply be compared at matching wavenumbers, but rather the same region of the k_x - k_z space has to be compared. The region of the k_x - k_z space represented by each mode is a function of the wavenumber resolution of the discrete Fourrier transform (DFT).

When performing a DFT, the frequency resolution is determined solely by the length of the signal. Similarly, the wavenumber resolution in the DFT of a velocity field is governed by the domain size, i.e. $\Delta k = 2\pi/L$. Given that the $Re_\tau = 547$ simulation has a larger domain in the spanwise direction (as shown in Table 9), it will have a finer wavenumber resolution in the z-direction and each mode will consequently represent a smaller region of the k_x - k_z space. Figure 18 plots some of the wavenumber pairs present in both the simulations. It is clear from Figure 18 that the modes for the $Re_\tau = 934$ case represent a larger region of the $k_x - k_z$ space. This can be corrected by including the relevant contributions from the neighbouring k_z modes.

The difference in $\Delta k_z\delta$ between the two simulations is $\frac{1}{6}$, i.e. one-third of the wavenumber resolution of the $Re_\tau = 547$ run. Therefore to represent the same area of the k_x -

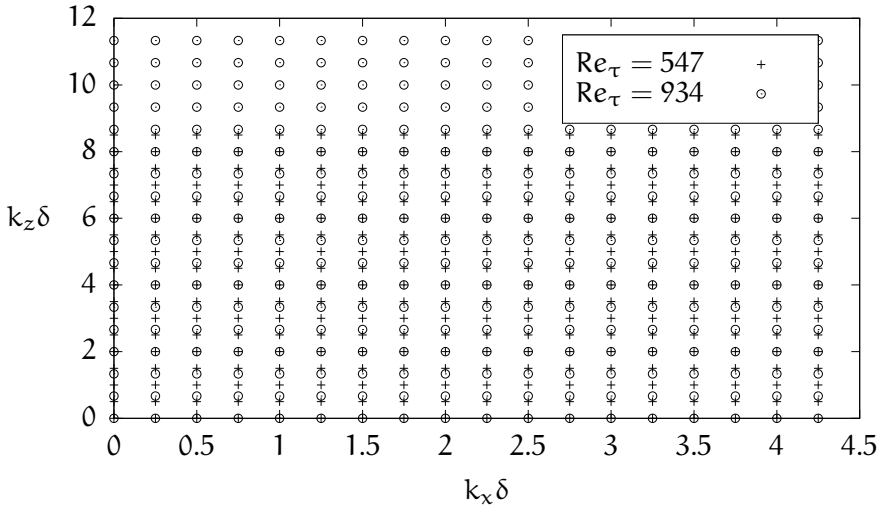


Figure 18: Non-dimensional wavenumbers in x and z directions

k_z space, turbulent kinetic energy corresponding to one-half of that fraction has to be taken from the neighbouring nodes.

The above assertion can be best understood with an example. As shown in Figure 18, all the modes at $k_z\delta = 2$ have the same wavenumbers in both simulations. In order to capture the same area of the k_x - k_z space, one-sixth of the turbulent kinetic energy from the $k_z\delta = 2.5$ and $k_z\delta = 1.5$ modes also needs to be included for the $Re_\tau = 547$ modes. This energy was included by performing the Chebychev expansion using one-sixth of the coefficients from the neighbouring modes, as shown in Equation 44.

$$\begin{aligned}\overline{\Phi_{ij}|_{k_x,k_z=2}} = T_k T_h \Bigg[& \overline{C_{ik}|_{k_x,k_z=2} C_{jh}|_{k_x,k_z=2}} + \\ & \frac{1}{6} \times \overline{C_{ik}|_{k_x,k_z=2.5} C_{jh}|_{k_x,k_z=2.5}} + \\ & \frac{1}{6} \times \overline{C_{ik}|_{k_x,k_z=1.5} C_{jh}|_{k_x,k_z=1.5}} \Bigg]\end{aligned} \tag{44}$$

In Equation 44, T_k is the k^{th}-order Chebychev polynomial and C_{ik} is the coefficient corresponding to the k^{th}-order polynomial for the i^{th} velocity component. Having applied the wavenumber space corrections, the resulting correlation contour plots are shown in Figure 19.

Figure 19 shows the two-point correlation contour plots for spanwise wavelengths of approximately 3δ and streamwise wavelengths of 24δ to 6δ. The shape of the contours can be used to infer qualitative features about the turbulent structures present at the wavelengths being examined. The $\overline{\hat{u}'\hat{u}'}$ contours show maximum correlation at zero separation and at a height of $y/\delta \approx 0.5$. It is likely that this high value of the correlation coefficient corresponds to the "longest scales" found by Del Alamo et al[18] at $y/\delta \approx 0.5$; one would expect modes with very long lengthscales to also possess large amounts of turbulent kinetic energy. Although it is weaker, the $\overline{\hat{u}'\hat{u}'}$ contours do retain a finite correlation right down to the wall.

On the contrary, the contours for the $\overline{\hat{v}'\hat{v}'}$ correlation do not extend all the way down to the wall; an obvious consequence of the zero-normal gradient imposed at the walls

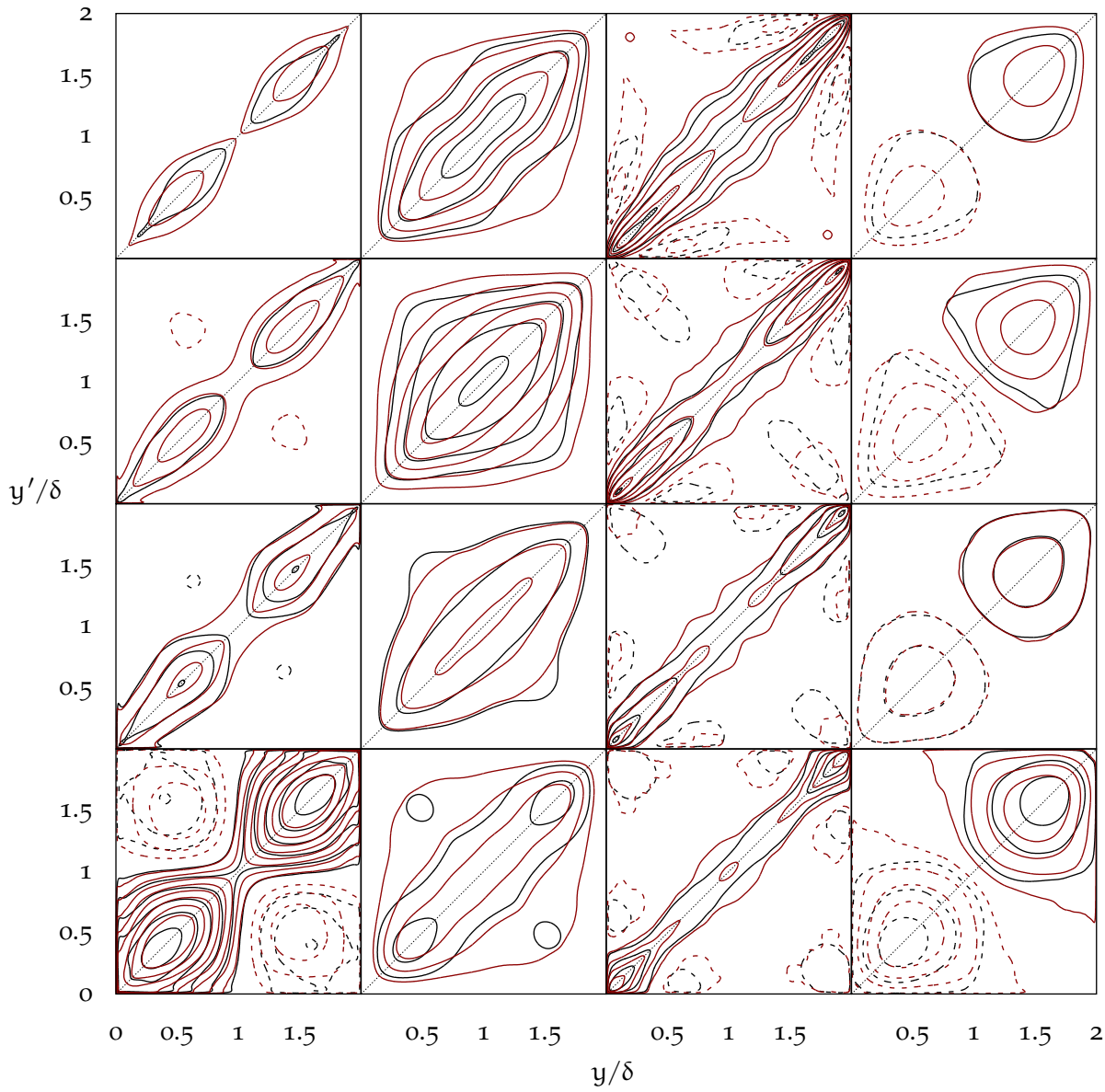


Figure 19: Contour plots of the real component of the two-point velocity correlation tensor, i.e. $Re(\overline{\Phi_{ij}})/u_\tau^2$. Left to right: $\overline{\hat{u}'\hat{u}'}, \overline{\hat{v}'\hat{v}'}, \overline{\hat{w}'\hat{w}'}, \overline{\hat{u}'\hat{v}'}$ at $k_z\delta = 2$ ($l_z \approx 3\delta$), $k_x\delta = 0.25 - 1$ increasing bottom-to-top ($l_x \approx 24\delta - 6\delta$). —— $Re_\tau = 547$ —— $Re_\tau = 934$ ····· $y = y'$. Contour levels: $\overline{\hat{u}'\hat{u}'} = -0.004 : 0.008, \overline{\hat{v}'\hat{v}'} = 0.00004 : 0.002, \overline{\hat{w}'\hat{w}'} = -0.0003 : 0.0009, \overline{\hat{u}'\hat{v}'} = -0.0007 : 0.0007$. Dashed lines represent negative values. $k_x\delta = 0$ are not shown, see section Section 3.2.4.

by mass continuity, i.e. $\frac{\partial v}{\partial y}|_{wall} = 0$. Arguably the most interesting feature of the $\overline{\hat{v}'\hat{v}'}$ contours is that not only is the correlation coefficient large for zero-separation at mid-channel, but it also remains significant for large *separations* at mid-channel. A large structure with its centre near the mid-channel producing momentum transfer across the $y = \delta$ plane could potentially explain the shape of the $\overline{\hat{v}'\hat{v}'}$ contour plots. Further evidence for such a structure can be seen in the $\overline{\hat{u}'\hat{v}'}$ correlations; the correlation coefficients remain significant at very large ($\approx \delta$) separations. It is possible that the correlations in Figure 19 correspond to the large, "inactive" and anisotropic scales proposed by Townsend[120]. The contours for the $\overline{\hat{w}'\hat{w}'}$ are also consistent with this hypothesis; Townsend hypothesized that the large anisotropic scales would contribute significantly to the wall-parallel turbulent intensities[120].

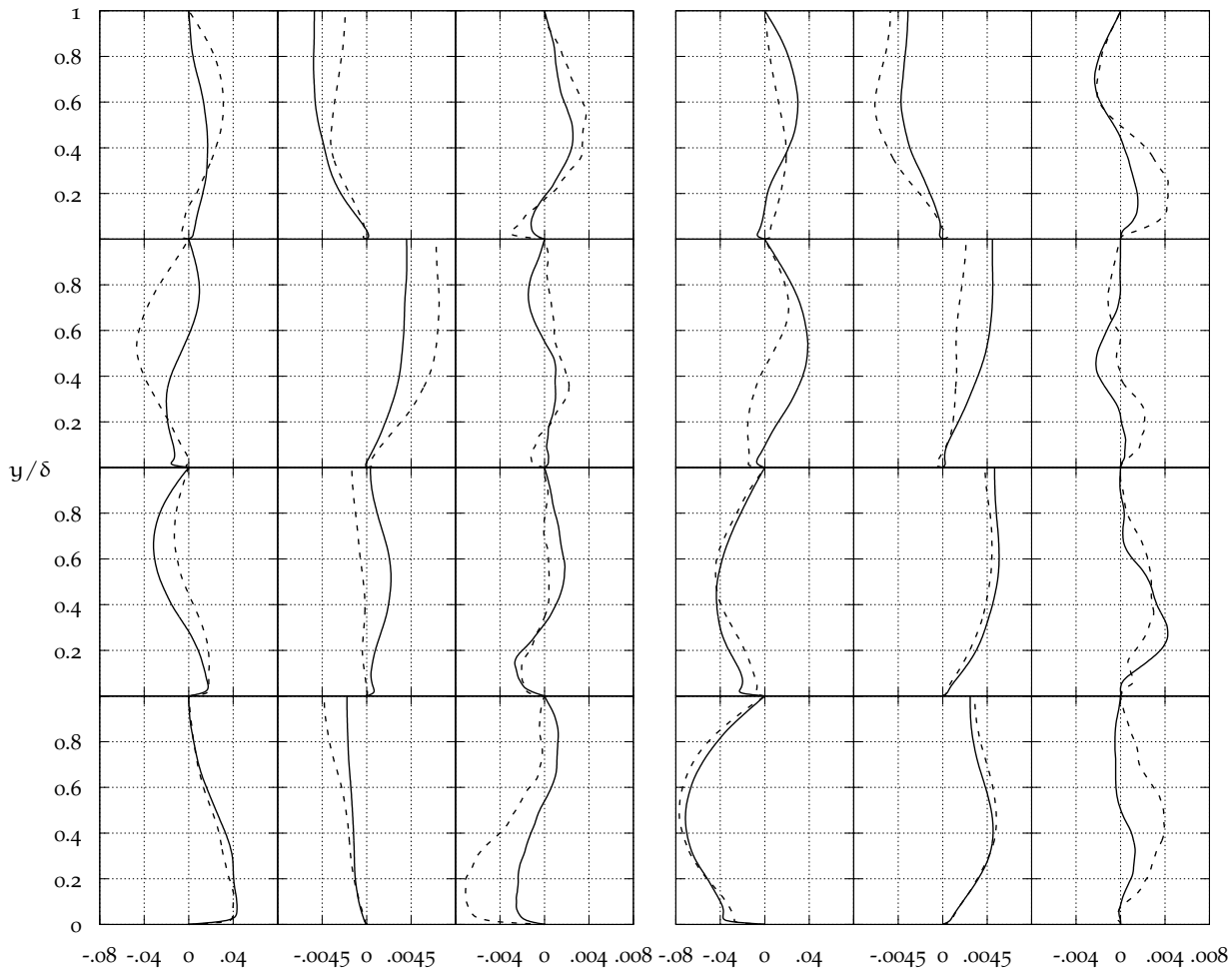
Although there is no clear consensus within the turbulence community on how Townsend's large modes scale, there is considerable evidence to show that they do not scale with inner units[16],[86],[20]. One may thus expect the eigenvectors of modes with such large lengthscales to also not scale with Re_τ. Surprisingly this is not the case, as the eigenvectors extracted from the two-point correlations in Figure 19 do exhibit a high-degree of Re_τ scaling.

Figure 20 shows the eigenvectors of the two-point correlation scaled with their respective eigenvalues, expressed mathematically as $\sqrt{\lambda^{(n)}} f_i^{(n)}$; this is the quantity that can be used in the generation of synthetic turbulent fields[74]. For brevity it will henceforth be denoted as $\xi_i^{(n)}$. Both the real and imaginary parts, especially those corresponding to $\hat{u}'$ and $\hat{v}'$ for $k_x\delta = 0.25$ and $k_x\delta = 0.5$, scale well with Re_τ. The eigenvectors generally only have one or less zero-crossings, again suggesting the presence of turbulent structures of similar wall-normal scale to δ.

Further insight into the Re_τ scaling of $\xi_i^{(n)}$ can be gained by separating the large and small modes, with respect to their lengthscales in the y-direction. Chebychev polynomials of increasing degree represent smaller and smaller wall-normal lengthscales[8]. These lengthscales can be estimated by computing two-point correlations using just the Chebychev polynomials of different orders, as shown in Figure 21. Figure 21 shows that the Chebychev polynomials up to 5^{th} order (6^{th} polynomial overall as the first one is 0^{th} order) remain correlated for distances of order δ. Therefore the 6^{th} polynomial can be used as a first approximation for the cut-off between large and small lengthscales. The large and small modes can be separated by performing Chebychev expansion shown in Equation 44 using only the desired modes. Figure 22 shows the eigenvectors obtained using the 6^{th} Chebychev polynomial and upwards, whereas Figure 23 shows the eigenvectors obtained from just the first five polynomials.

The modes in Figure 22 also scale very well with Re_τ. Moreover, the eigenvectors corresponding to $\hat{w}'$ also scale well, which was not the case when all the Chebychev polynomials had been used (Figure 20). As shown in Figure 23, the Re_τ scaling of the eigenvectors that comprise of just the first five Chebychev polynomials is not as consistent as the modes in Figure 22. This is to be expected; one would not expect u_τ to be the dominant velocity scale for modes with such large lengthscales in all three dimensions.

Figure 24 shows the POD modes at higher streamwise and spanwise wavenumbers, namely $k_z\delta = 4$ and $k_x\delta = 1.25$. Unlike the modes at $k_z\delta = 2$, the eigenvectors at $k_z\delta = 4$ comprising of all the Chebychev polynomials do not scale with u_τ. Neither



(a) $Re(\xi_i^{(0)})/u_\tau$ (b) $Im(\xi_i^{(0)})/u_\tau$

Figure 20: Real(left) and imaginary(right) components of scaled eigenvectors corresponding to the most energetic eigenvalue. $k_z\delta = 2$ ($l_z \approx 3\delta$) and $k_x\delta = 0.25 - 1$ ($l_x \approx 24\delta - 6\delta$). Left to right: $\overline{\hat{u}'}$,$\overline{\hat{v}'}$,$\overline{\hat{w}'}$.—— $Re_\tau = 547$ - - - $Re_\tau = 934$.

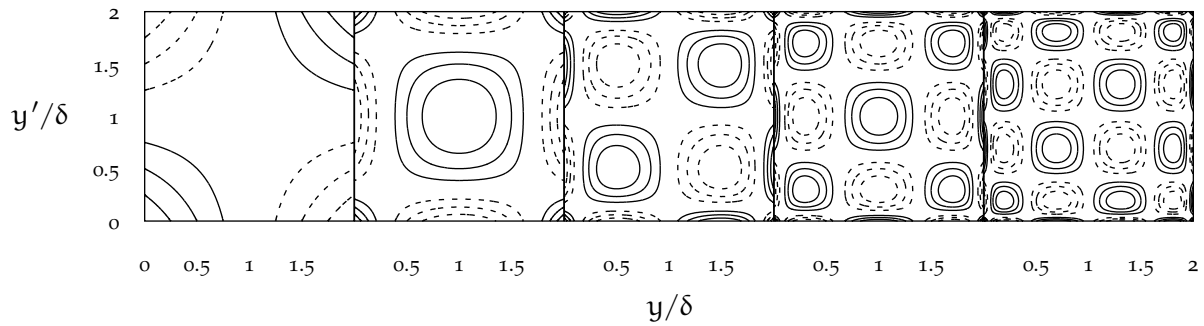
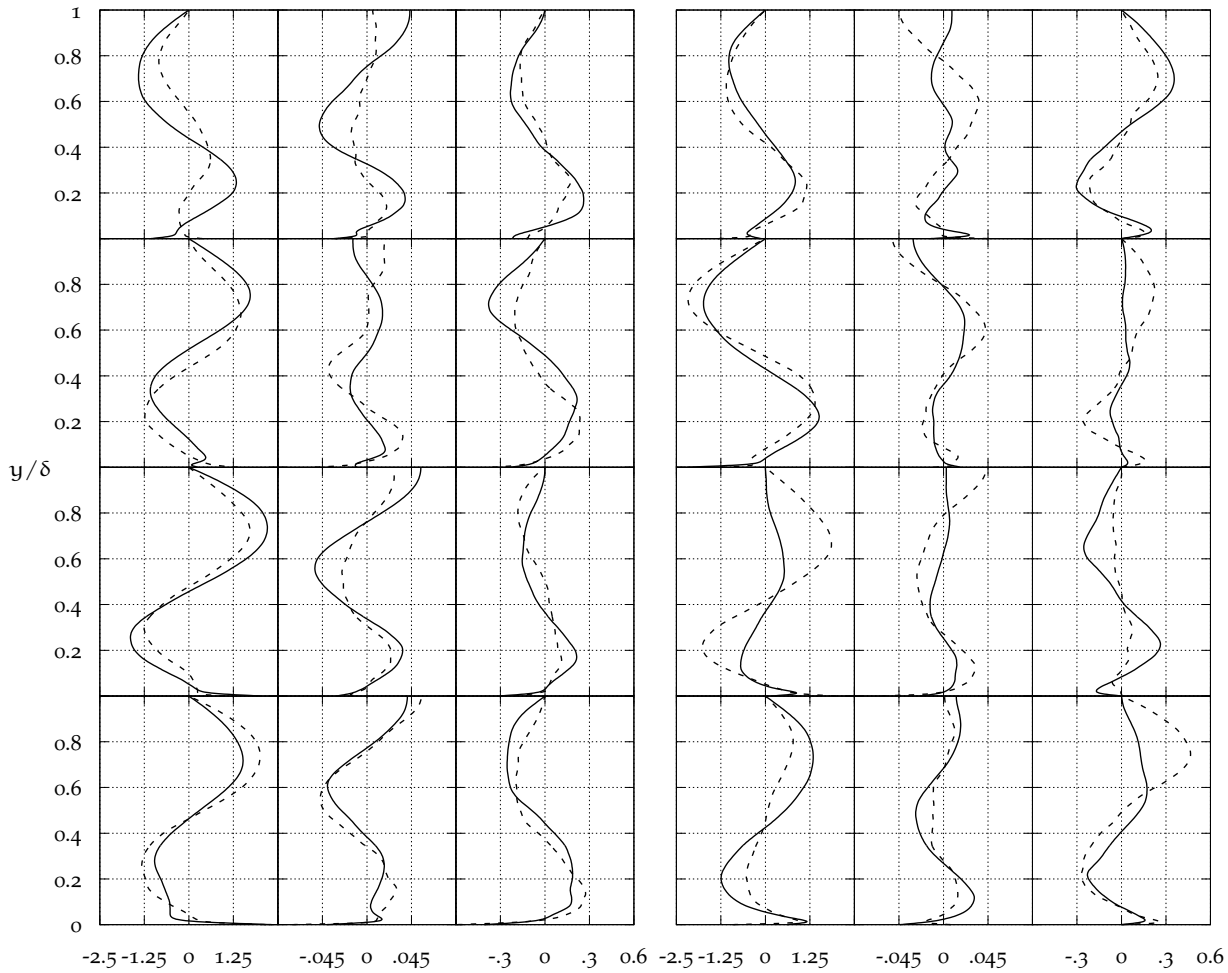
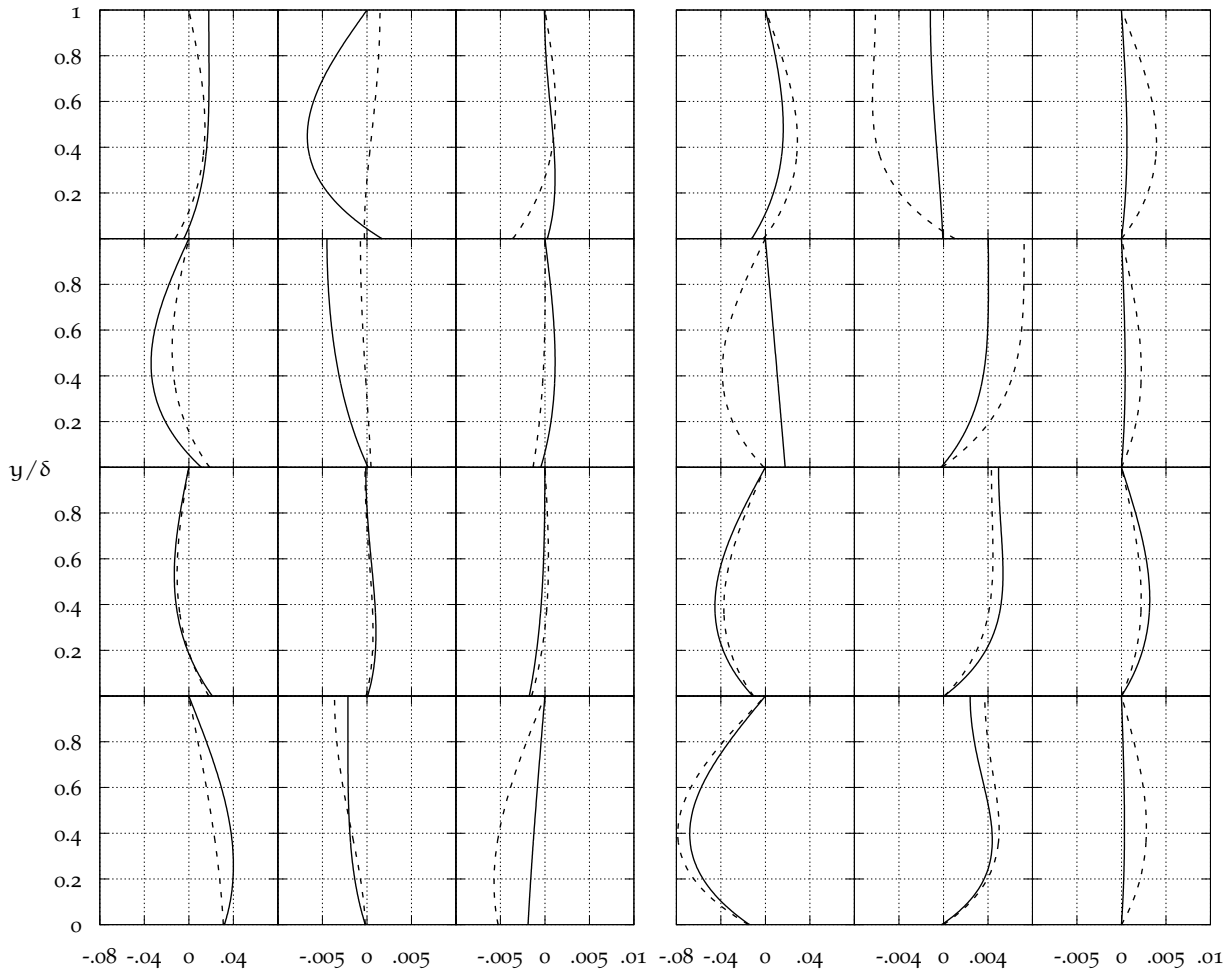


Figure 21: Two-point correlation contours of the Chebychev polynomials of 1^{st} to 5^{th} order (left to right). Dashed lines indicate negative values of the correlation coefficient.



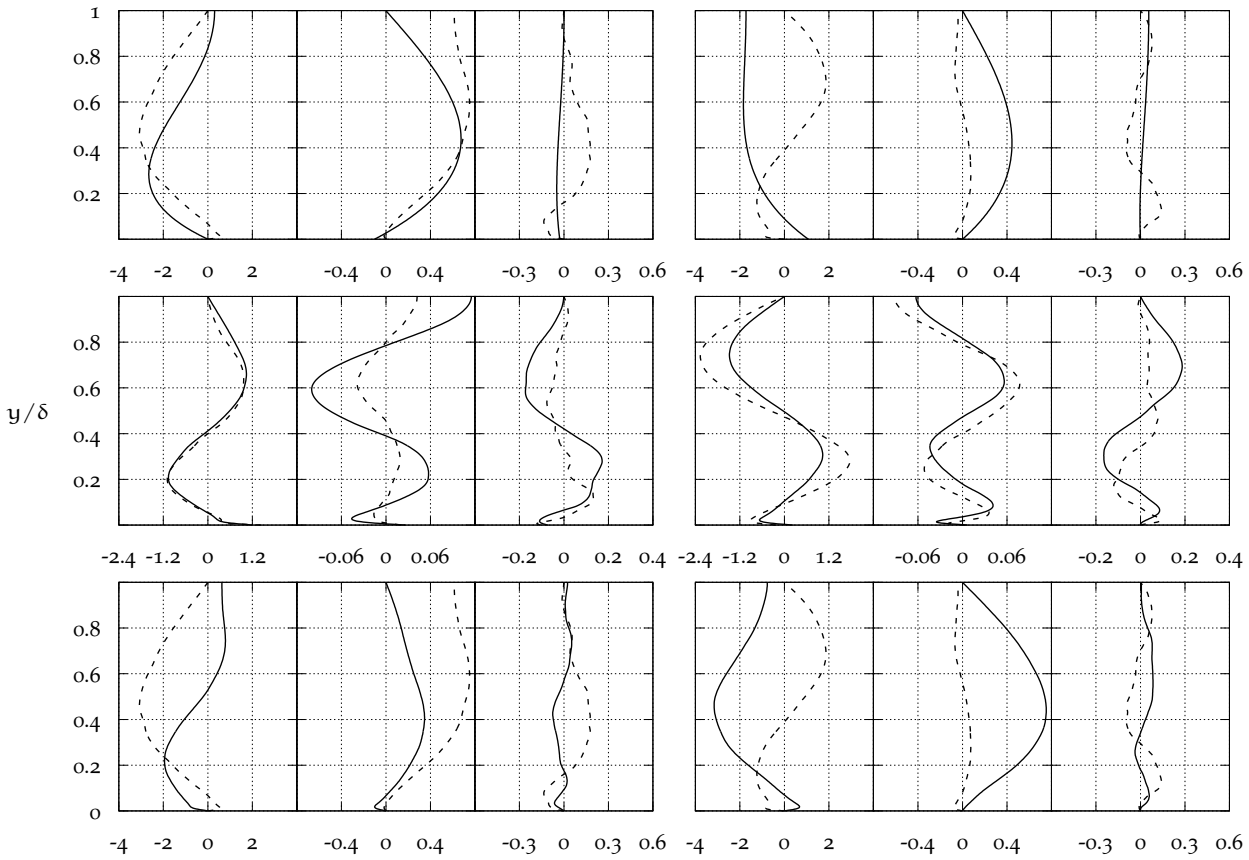
(a) $\mathrm{Re}(\xi_i^{(0)})/u_\tau$ (b) $\mathrm{Im}(\xi_i^{(0)})/u_\tau$

Figure 22: Real(left) and imaginary(right) components of scaled eigenvectors corresponding to the most energetic eigenvalue. The Chebychev expansion has been performed without the first five modes. $k_z\delta = 2$ ($l_z \approx 3\delta$) and $k_x\delta = 0.25 - 1$ ($l_x \approx 24\delta - 6\delta$). Left to right: $\overline{\hat{u}'}$,$\overline{\hat{v}'}$,$\overline{\hat{w}'}$.—— $Re_\tau = 547$ - - - $Re_\tau = 934$.



(a) $Re(\xi_i^{(0)})/u_\tau$ (b) $Im(\xi_i^{(0)})/u_\tau$

Figure 23: Real(left) and imaginary(right) components of scaled eigenvectors corresponding to the most energetic eigenvalue. The Chebychev expansion has been performed using only the first five modes. $k_z\delta = 2$ ($l_z \approx 3\delta$) and $k_x\delta = 0.25 - 1$ ($l_x \approx 24\delta - 6\delta$). Left to right: $\overline{\hat{u}'}$,$\overline{\hat{v}'}$,$\overline{\hat{w}'}$.—— $Re_\tau = 547$ - - - $Re_\tau = 934$.



(a) $\mathrm{Re}(\xi_i^{(0)})/u_\tau$ (b) $\mathrm{Im}(\xi_i^{(0)})/u_\tau$

Figure 24: Real(left) and imaginary(right) components of scaled eigenvectors corresponding to the most energetic eigenvalue. Bottom row corresponds to all Chebychev polynomials, middle row to 5^{th} mode and upwards and top row to just the first 5 modes. $k_z\delta = 4$ ($l_z \approx 1.75\delta$) and $k_x\delta = 1.25$ ($l_x \approx 5\delta$). Left to right: $\widehat{u}'$,$\widehat{v}'$,$\widehat{w}'$. —— $Re_\tau = 547$ - - - $Re_\tau = 934$.

do the eigenvectors corresponding to just the first 5 Chebychev polynomials. On the contrary, the modes constructed with the 6^{th} polynomial and upwards do exhibit near independence from Re_τ and almost collapse onto the same line when normalized by u_τ.

Figure 25 shows the eigenvectors at $k_z\delta = 6$ and $k_x\delta = 2.75$. These confirm the trends seen earlier, namely that the modes comprising of the 5^{th} order Chebychev polynomial and upwards exhibit near Re_τ independence. By contrast, the modes that use all the Chebychev polynomials, or just the first five, do not exhibit good Re_τ scaling.

The modes examined thus far all correspond to wavelengths in the x and z directions larger than δ. A more complete picture of the Re_τ scaling can be formed by examining modes with streamwise and spanwise lengthscales smaller than δ. Such modes are shown in Figure 26 and Figure 27.

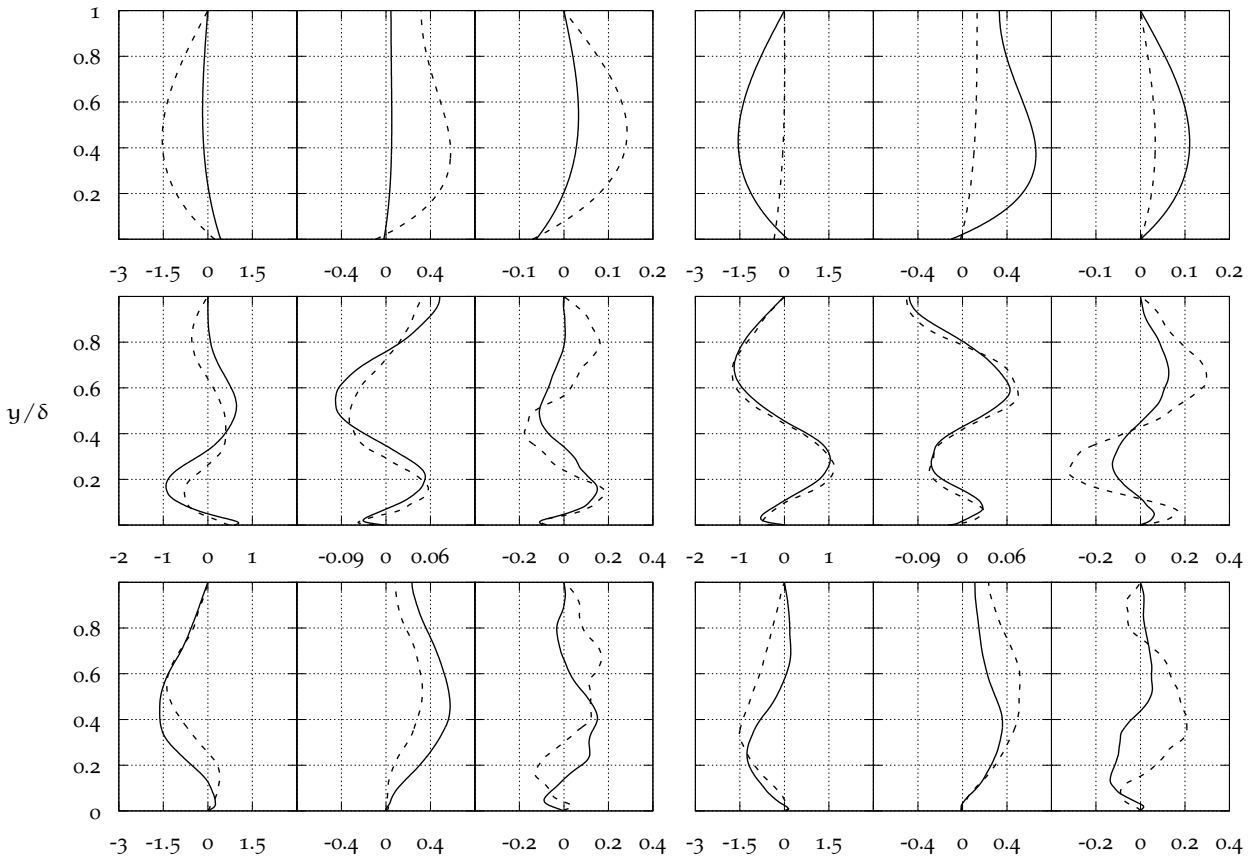
An interesting feature of Figure 26 and Figure 27 is that the modes with small wall-normal lengthscales (first two rows) corresponding to $\hat{w}'$ have not yet achieved full statistical convergence, whereas those of $\hat{u}'$ and $\hat{v}'$ have. A possible explanation could be that the mean-shear plays an important role in shaping the POD eigenvectors, and thus much longer averaging times are needed for small-scale modes in the directions of zero shear.

In terms of their Re_τ scaling, the modes in Figure 26 and Figure 27 are consistent with the general trends seen earlier: the best Re_τ scaling is obtained once the first five Chebychev modes are removed. There are however some notable departures from this trend that should be highlighted.

For modes corresponding to the largest spanwise wavelength, $k_z\delta = 2$, although the best Re_τ scaling is seen in Figure 22 when the first five Chebychev polynomials are removed, the large wall-normal length-scales do nevertheless show a high degree of scaling, as shown in Figure 20 and Figure 23. At $k_z\delta = 12$ (Figure 26 and Figure 27) the best Re_τ scaling is again seen in the middle row where the first five Chebychev modes have been removed. However in Figure 26, the modes corresponding to all the Chebychev modes (bottom row) scale remarkably well and in Figure 27, the first five Chebychev modes (top row) also exhibit a very high degree of Re_τ independence. The modes at $k_z\delta = 4$ and $k_z\delta = 6$ exhibit a much clearer distinction between the large and small wall-normal lengthscales: in Figure 24 and Figure 25, only the modes in the middle row, that have the first five Chebychev polynomials removed, exhibit good Re_τ scaling.

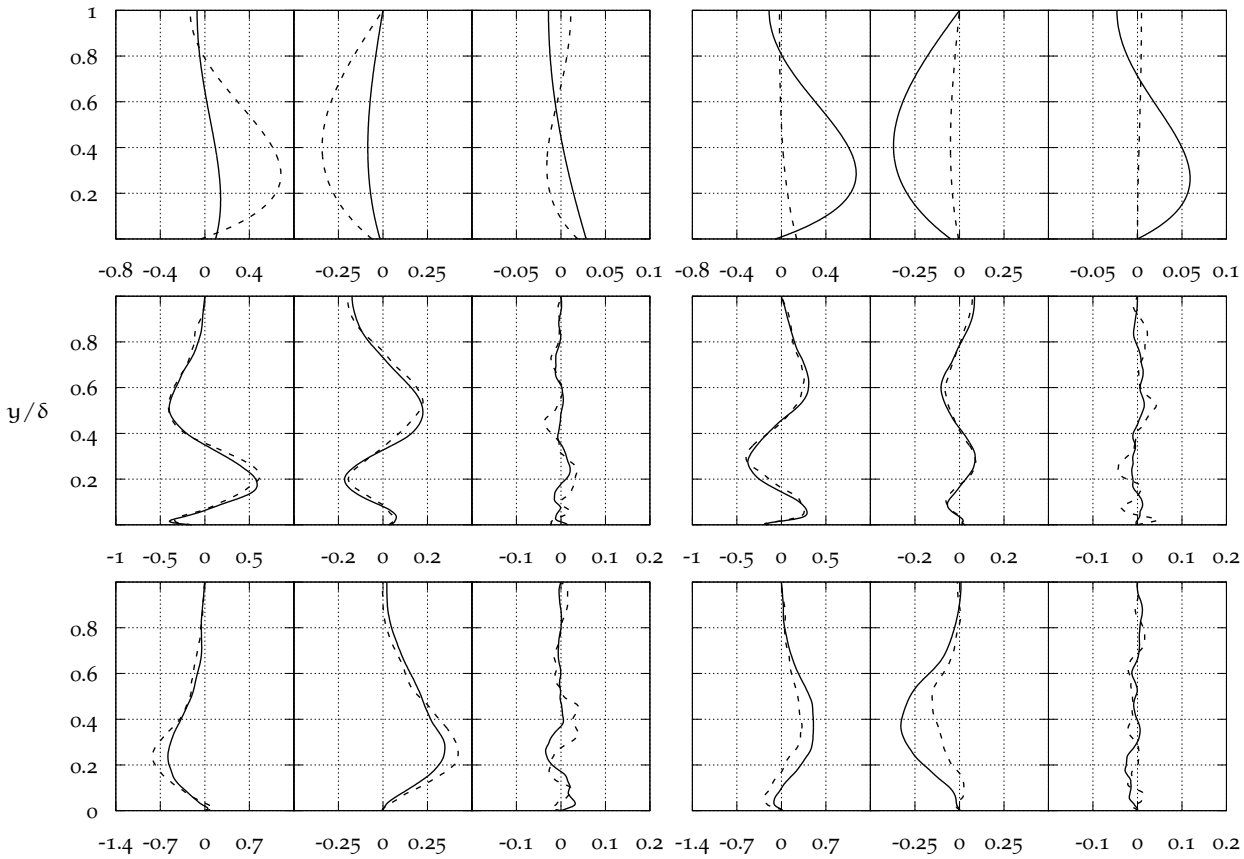
Thus the main finding of the Re_τ scaling analysis is that if the Chebychev modes corresponding to wall-normal length-scales larger than δ are neglected, the POD modes exhibit near complete Re_τ independence. While modes at some values of k_x and k_z do show reasonable scaling even if the low-order Chebychev polynomials are included, the best scaling is always achieved without the inclusion of the first five Chebychev modes, throughout the k_x-k_z space.

A noteworthy effect of removing the first five Chebychev polynomials is that the eigenvectors violate the no-slip condition, as seen in Figure 22, Figure 24, Figure 25, Figure 26 and Figure 27. As explained by Berkooz et al[33], the eigenfunctions produced by the POD must also satisfy the no-slip condition. The Chebychev polynomials however are always non-zero valued at the boundaries[8]. Therefore if the Chebychev expansion (equation Equation 44) is performed using only some of the modes, there is no guarantee that the amplitudes will cancel at the walls. Thus the violation of no-slip, in the



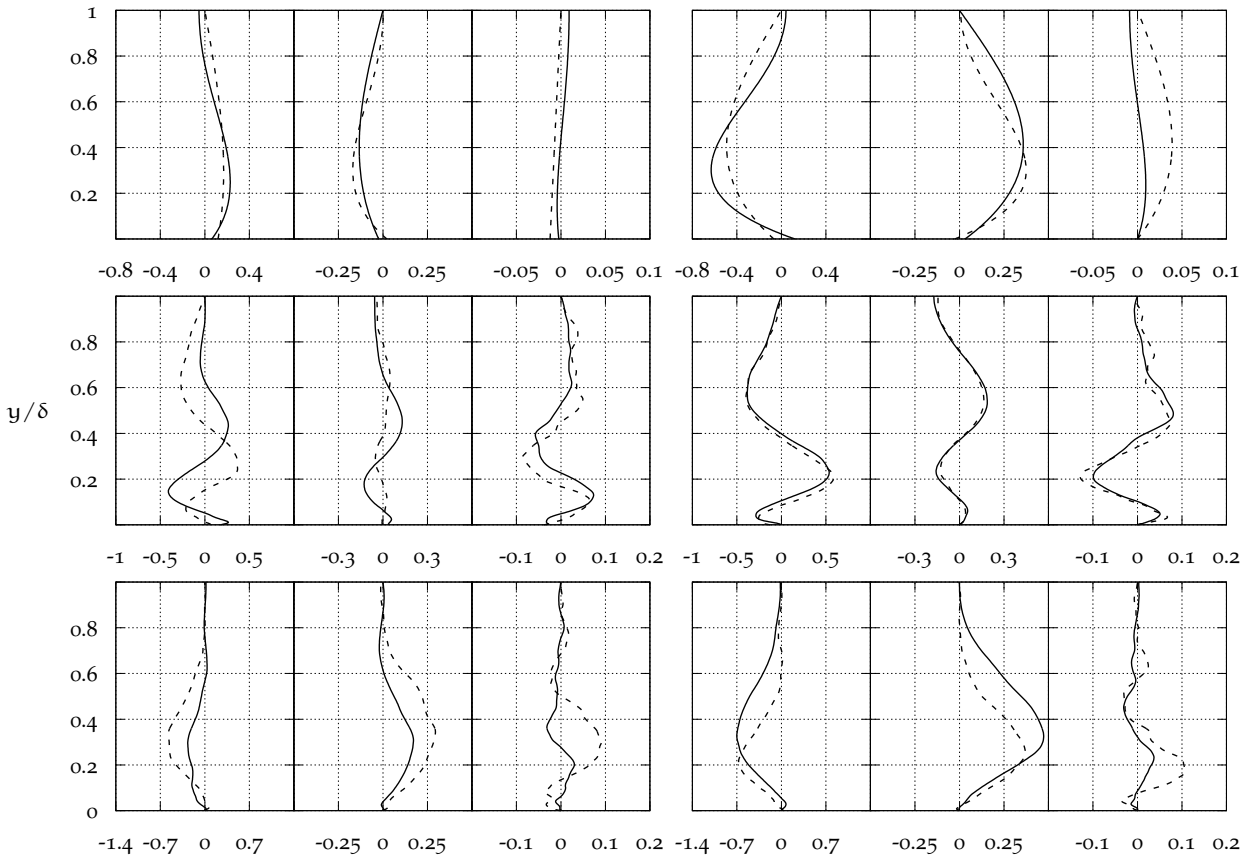
(a) $\mathrm{Re}(\xi_i^{(0)})/u_\tau$ (b) $\mathrm{Im}(\xi_i^{(0)})/u_\tau$

Figure 25: Real(left) and imaginary(right) components of scaled eigenvectors corresponding to the most energetic eigenvalue. Bottom row corresponds to all Chebychev polynomials, middle row to 5^{th} mode and upwards and top row to just the first 5 modes. $k_z\delta = 6$ ($l_z \approx 1\delta$) and $k_x\delta = 2.75$ ($l_x \approx 2\delta$). Left to right: $\widehat{u}'$,$\widehat{v}'$,$\widehat{w}'$. —— $Re_\tau = 547$ - - - $Re_\tau = 934$.



(a) $\mathrm{Re}(\xi_i^{(0)})/u_\tau$ (b) $\mathrm{Im}(\xi_i^{(0)})/u_\tau$

Figure 26: Real(left) and imaginary(right) components of scaled eigenvectors corresponding to the most energetic eigenvalue. Bottom row corresponds to all Chebychev polynomials, middle row to 5^{th} mode and upwards and top row to just the first 5 modes. $k_z\delta = 12$ ($l_z \approx 0.5\delta$) and $k_x\delta = 5.5$ ($l_x \approx \delta$). Left to right: $\widehat{u}'$,$\widehat{v}'$,$\widehat{w}'$. —— $Re_\tau = 547$ - - - $Re_\tau = 934$.



(a) $\mathrm{Re}(\xi_i^{(0)})/u_\tau$ (b) $\mathrm{Im}(\xi_i^{(0)})/u_\tau$

Figure 27: Real(left) and imaginary(right) components of scaled eigenvectors corresponding to the most energetic eigenvalue. Bottom row corresponds to all Chebychev polynomials, middle row to 5^{th} mode and upwards and top row to just the first 5 modes. $k_z\delta = 12$ ($l_z \approx 0.5\delta$) and $k_x\delta = 6$ ($l_x \approx \delta$). Left to right: $\widehat{u}'$,$\widehat{v}'$,$\widehat{w}'$. —— $Re_\tau = 547$ - - - $Re_\tau = 934$.

eigenvectors constructed from a truncated Chebychev expansion, is purely an artefact of the choice of orthonormal basis. In order to verify that the violation of no-slip is indeed not the manifestation of a physical phenomenon, an attempt can be made to recover the no-slip using a correction consisting of the first five Chebychev polynomials.

A corrected eigenvector can be defined as shown in equation Equation 45:

$$\tilde{\xi}_i = \xi_i + \xi_i'' \tag{45}$$

In Equation 45, $\tilde{\xi}_i$ is the corrected eigenvector, ξ_i the original eigenvector and ξ_i'' is the correction. $\tilde{\xi}_i$ and ξ_i'' are subject to the following constraints:

$$\xi_i'' = \sum_{j=0}^{j=4} T_j C_{ij} \tag{46a}$$

$$\tilde{\xi}_i(y = 0) = 0 \tag{46b}$$

$$\tilde{\xi}_i(y = 2\delta) = 0 \tag{46c}$$

$$min\left(\|\xi_i''\|^2\right) \tag{46d}$$

Equation 46 represents a typical constrained optimization problem, and the Chebychev coefficients in Equation 46a can be found using the method of Lagrange multipliers. This correction was tested for the eigenvectors at $k_z\delta = 2$ and the results are shown in Figure 28. As Figure 28 shows, the eigenvectors corrected for no-slip scale almost as well with Re_τ as the original eigenvectors in Figure 22 but now also satisfy the no-slip condition.

3.4 Reynolds-stress budget

In order to understand how the removal of the first five Chebychev modes would affect a synthesized flowfield, the terms comprising the Reynolds-stress budget can be examined. Its various terms can be defined as shown below[77]:

$$\text{Production rate : } P_{ij} = -\left(\overline{u_i' u_k'}\frac{\partial \overline{u}_j}{\partial x_k} + \overline{u_j' u_k'}\frac{\partial \overline{u}_i}{\partial x_k}\right) \tag{47a}$$

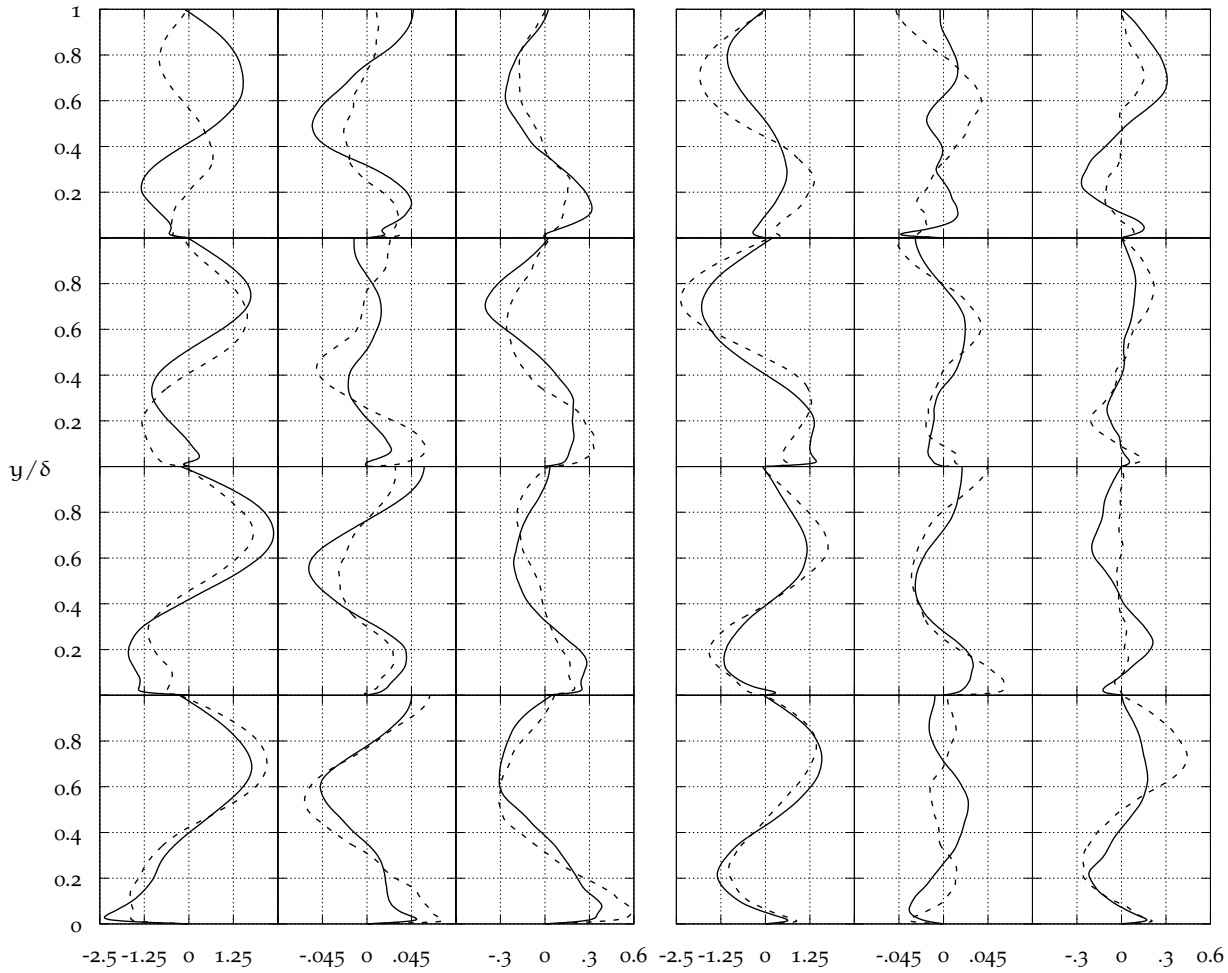
$$\text{Dissipation rate: } \epsilon_{ij} = 2\nu\overline{\frac{\partial u_i'}{\partial x_k}\frac{\partial u_j'}{\partial x_k}} \tag{47b}$$

$$\text{Turbulent transport rate: } T_{ij} = -\frac{\partial}{\partial x_k}\left(\overline{u_i' u_j' u_k'}\right) \tag{47c}$$

$$\text{Viscous diffusion rate: } D_{ij} = \nu\frac{\partial}{\partial x_k \partial x_k}\left(\overline{u_i' u_j'}\right) \tag{47d}$$

Figure 29 shows the Reynolds-stress $\overline{u'v'}$ and the terms comprising its budget. The Reynolds-stress budgets were computed by first performing an inverse Fourier transform over the entire k_x-k_z space, and subsequently averaging in the physical x and z directions.

By removing the first five Chebychev polynomials, the production term becomes non-zero at the wall. Viscous diffusion at the wall also becomes larger in magnitude and changes sign to become positive; the stress acts away from the wall rather than towards it. Turbulent transport also experiences a significant change; the peak at the start of the



(a) $\mathrm{Re}(\xi_i^{(0)})/u_\tau$ (b) $\mathrm{Im}(\xi_i^{(0)})/u_\tau$

Figure 28: Real(left) and imaginary(right) components of scaled eigenvectors corresponding to the most energetic eigenvalue. The Chebychev expansion has been performed using only the first five modes but the eigenvectors have been corrected in order to recover no-slip. $k_z\delta = 2$ ($l_z \approx 3\delta$) and $k_x\delta = 0.25 - 1$ ($l_x \approx 24\delta - 6\delta$). Left to right: $\widehat{u}'$,$\widehat{v}'$,$\widehat{w}'$.—— $Re_\tau = 547$ - - - $Re_\tau = 934$.

Table 10: Parameters of LES of plane channel flow at $Re_\tau = 1000$

Re_τ	$(L_x, L_y, L_z)/\delta$	Δx^+,Δy^+_{min},Δy^+_{max},Δz^+	N_x, N_y, N_z	N_f	Tu_τ/δ
1000	8π,2,4π	19.6,0.6,32.7,8.2	1280,96,1536	393	9

logarithmic region is markedly larger. The only notable feature of the dissipation is that it becomes negative between $y^+ = 10 - 12$ and essentially acts like a production term in that region.

The overall effect of the modified budget terms is almost a 50% drop in the peak of $\overline{u'v'}$ in the logarithmic region, but an increase in $\overline{u'v'}$ in the buffer and viscous layers as well as a non-zero value of $\overline{u'v'}$ at the wall.

The significant reduction in the magnitude of $\overline{u'v'}$ in the logarithmic region is consistent with the previous results. As the largest wall-normal structures only exist away from the wall and do carry significant energy, removing even a few can cause a significant drop in magnitude of the Reynolds-stress. In the budget terms, this is manifested as $\overline{u'v'}$ being transported away from the logarithmic region and towards the wall, i.e. the peak in T_{12}. This can perhaps explain the local maxima in $\overline{u'v'}$ in the buffer layer. Figure 29 thus suggests that the large wall-normal structures are instrumental in transporting $\overline{u'v'}$ from the wall to the logarithmic region.

3.5 Two-point correlations from Large Eddy Simulations

One of the avenues for extending the current work is to study the scaling of POD eigenvectors at even higher values of Re_τ or for larger numerical boxes. As a means to limit the cost of such calculations, they can be performed using Large Eddy Simulations (LES) rather than DNS. Such a calculation was performed at $Re_\tau = 1000$, the parameters for which are given in Table 10. Similar to the DNS database, the grid for the run in Table 10 is stretched in the y-direction using a cosine distribution and uniformly spaced in the x and z directions. N signifies cell counts, not node counts as was the case in Table 9.

AU3X was used to perform the LES computation. Figure 30 shows a comparison between the two-point velocity correlation computed using the LES run and that extracted from the DNS database at $Re_\tau = 934$. Despite the two being at nominally different values of Re_τ and the averaging time being shorter for the LES run, the contour plots are remarkably similar and the LES computation clearly contains the same turbulent structures as the DNS data.

The eigenvectors must also be compared before LES can be declared a credible tool for studying the Re_τ scaling of POD modes. As shown in Figure 31, the POD eigenvectors extracted from the LES data match those extracted from DNS extremely well. Moreover, the similarity exists for both the real and the imaginary parts of the modes corresponding to all three velocity components. The results of Figure 30 and Figure 31 are remarkable considering the LES computation represents at worst one-tenth of the computational expense of the DNS run.

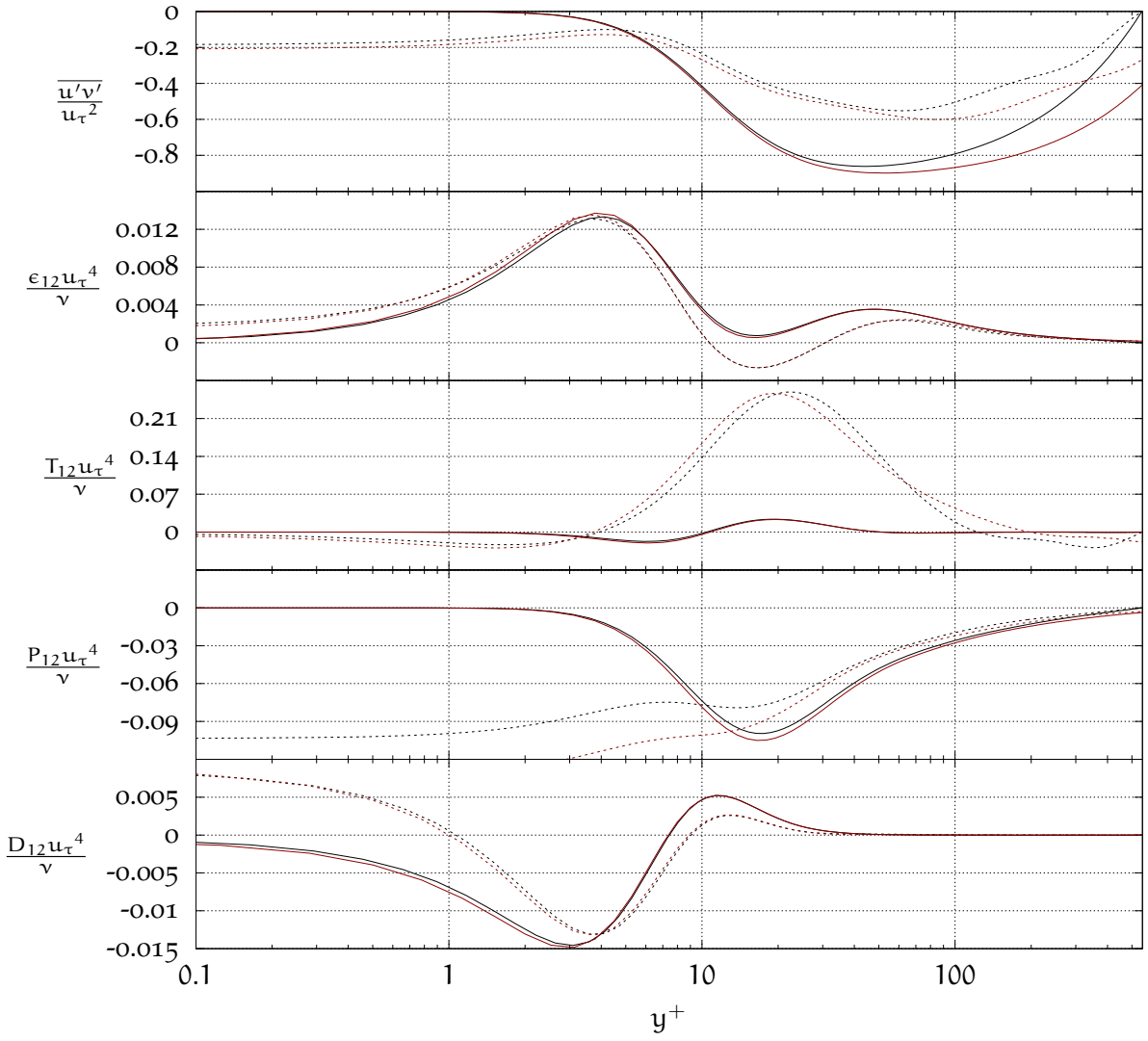


Figure 29: Budget terms of the Reynolds-stress $\overline{u'v'}$ from bottom to top: viscous diffusion (D_{12}), production (P_{12}), turbulent transport (T_{12}), dissipation rate (ϵ_{12}) and $\overline{u'v'}$.
—— $Re_\tau = 547$ —— $Re_\tau = 934$. Solid lines indicate all Chebychev polynomials whereas dashed lines mean exclusion of the first five.

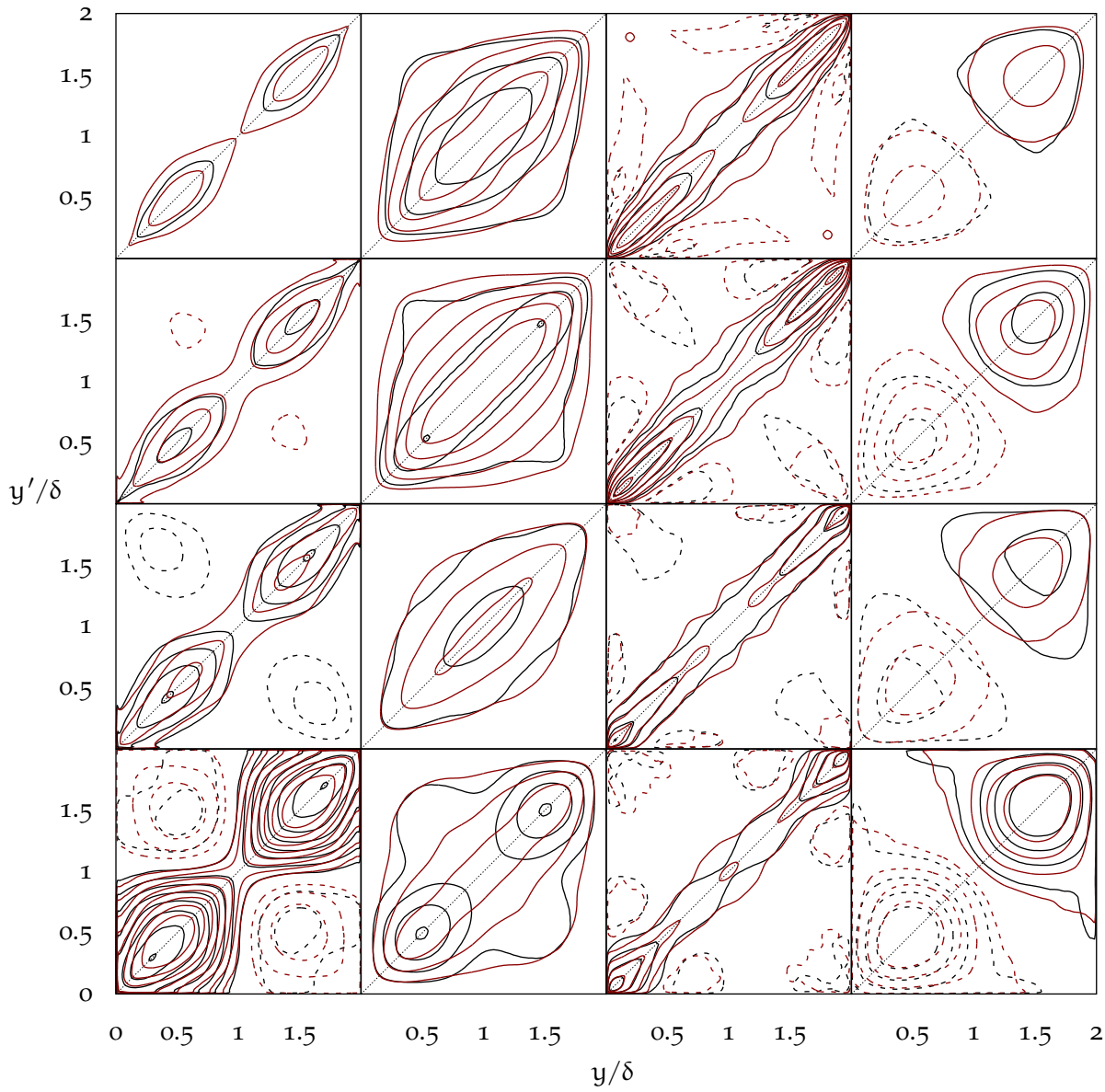
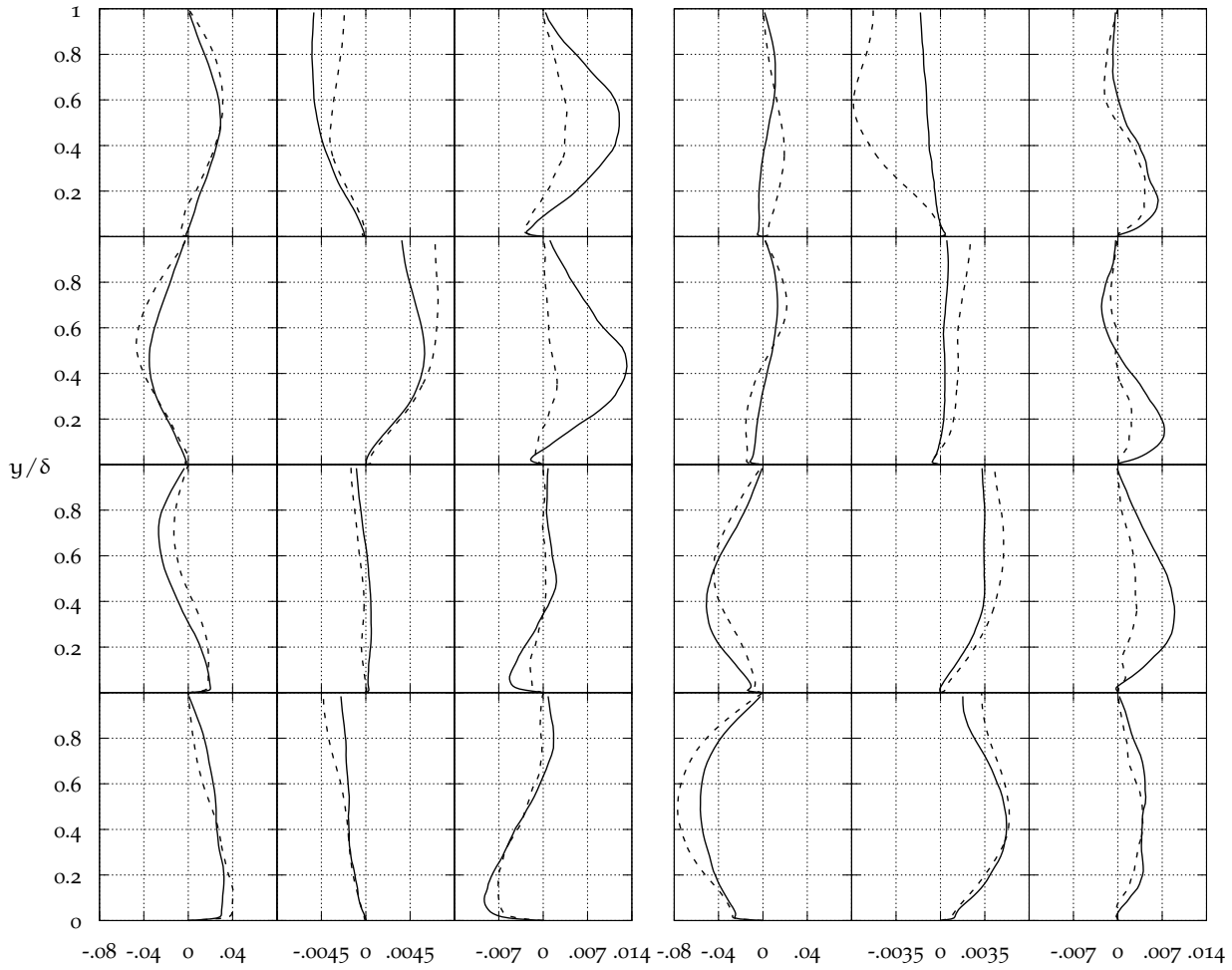


Figure 30: Contour plots of the real component of the two-point velocity correlation tensor, i.e. $Re(\overline{\Phi_{ij}})/u_\tau^2$, computed from LES. Left to right: $\overline{\hat{u}'\hat{u}'}, \overline{\hat{v}'\hat{v}'}, \overline{\hat{w}'\hat{w}'}, \overline{\hat{u}'\hat{v}'}$ at $k_z\delta = 2$ ($l_z \approx 3\delta$), $k_x\delta = 0.25 - 1$ increasing bottom-to-top ($l_x \approx 24\delta - 6\delta$). —— LES at $Re_\tau = 1000$ —— DNS at $Re_\tau = 934$ ····· $y = y'$. Contour levels: $\overline{\hat{u}'\hat{u}'} = -0.004 : 0.008, \overline{\hat{v}'\hat{v}'} = 0.00004 : 0.002, \overline{\hat{w}'\hat{w}'} = -0.0003 : 0.0009, \overline{\hat{u}'\hat{v}'} = -0.0007 : 0.0007$. Dashed lines represent negative values.



(a) $\mathrm{Re}(\xi_i^{(0)})/u_\tau$ (b) $\mathrm{Im}(\xi_i^{(0)})/u_\tau$

Figure 31: Real(left) and imaginary(right) components of scaled eigenvectors corresponding to the most energetic eigenvalue. $k_z\delta = 2$ ($l_z \approx 3\delta$) and $k_x\delta = 0.25 - 1$ ($l_x \approx 24\delta - 6\delta$). Left to right: $\widehat{u}'$,$\widehat{v}'$,$\widehat{w}'$.—— LES at $Re_\tau = 1000$ - - - DNS at $Re_\tau = 934$.

3.6 Conclusions

The current work analysed the POD eigenvectors and eigenvalues of the two-point velocity correlation tensor of plane channel flow at $Re_\tau = 547$ and $Re_\tau = 934$. The two-dimensional eigenvalue spectra showed a remarkable degree of similarity at the two values of Re_τ, even up to high wavenumbers where the magnitude had dropped significantly. The eigenvectors also exhibited near Re_τ independence, once they had been scaled to represent the same region of the $k_x - k_z$ space. At all the streamwise and spanwise lengthscales examined, the best Re_τ scaling is achieved without the inclusion of the first five Chebychev polynomials. It should be noted however that modes at some values of k_x and k_z do scale reasonably well even with the inclusion of the first five polynomials; the author is yet to find a pattern in the Re_τ scaling of POD eigenvectors constructed using the large Chebychev polynomials. The removal of the first five Chebychev polynomials also leads to a significant drop in the Reynolds-stress, $\overline{u'v'}$, in the buffer and logarithmic layers and an increase of $\overline{u'v'}$ in the viscous layer. These were attributed to the removal of large wall-normal structures that would transport $\overline{u'v'}$ from the centre of the channel to the wall.

The results of the current chapter suggest that a significant portion of the turbulent structures present in fully-developed channel flows possess a universal nature. Not only does this finding potentially offer an insight into the fundamental nature of wall-bounded turbulent flows, the scaling behaviour can also be used as the basis for models that attempt to generate synthetic turbulence. The digital-filters method of di Mare et al[23] generates synthetic turbulent flowfields by filtering stochastic signals, and the statistical information embedded within the synthetic field depends on the choice of filter coefficients: if the filter coefficients represent POD eigenvectors, then the resulting signals will contain all the information present in the corresponding two-point correlation. As the POD eigenvectors are expensive to compute, the ability to compute them once and subsequently rescale them could dramatically increase the applicability of methods such as that of di Mare et al[23].

A few key questions remain however before the current results can be applied to synthesizing turbulent velocity fields. The POD modes corresponding to large streamwise and spanwise wavelengths exhibit the best Re_τ scaling when the large wall-normal length-scales, i.e. the first five Chebychev polynomials, are removed. It is desirable to look for alternative scaling laws for these large wall-normal length-scales as they contribute significantly to the turbulent kinetic energy. If such a scaling law can be found, it will lead to more realistic synthesized turbulent velocity fields. Naturally, it would also be desirable to the test the scaling of the POD eigenvectors and eigenvalues across a wider range of Re_τ. Given that Section 3.5 showed AU3X can match the two-point correlations and POD modes of the DNS computations, it can be used to study the scaling at values of Re_τ that would be prohibitively high for DNS.

4

DETERMINISTIC AND REYNOLDS STRESSES IN COMPRESSOR PASSAGES

4.1 Introduction

Ever since Townsend's seminal categorisation of inhomogeneous shear flows into a mean field, large-eddy motion and a main turbulent motion[120], the turbulence community has sought to represent flows as a superposition of coherent structures and a "fine-gained" background, stochastic component. A subset of this field of research are flows where a large wave-like structure, pertaining to a narrow band or even a single frequency, interacts with both the mean field and the fine-grained turbulence. In such studies, a method is needed for extracting the organised wave motion. Hussain and Reynolds' triple decomposition[50] is commonly used:

$$f(\mathbf{x},t) = \bar{f}(\mathbf{x}) + \tilde{f}(\mathbf{x},t) + f'(\mathbf{x},t) \tag{48a}$$

$$\bar{f}(\mathbf{x}) = \lim_{T\to\infty} \frac{1}{T}\int_0^T f(\mathbf{x},t)\,dt \tag{48b}$$

$$\langle f(\mathbf{x},t)\rangle = \lim_{N\to\infty} \sum_{n=0}^{N} f(\mathbf{x},t+n\tau) \tag{48c}$$

$$\tilde{f}(\mathbf{x},t) = \langle f(\mathbf{x},t)\rangle - \bar{f}(\mathbf{x}) \tag{48d}$$

In equation 48c, $\langle\cdot\rangle$ denotes the phase-locked averaging operator and τ is the period of the organised wave. Hussain and Reynolds invoked the triple decomposition in the Navier-Stokes during their study of plane channel flow into which a sinusoidal disturbance was introduced[50]. The authors found that in determining the evolution of the organized wave, its interaction with the time-mean component of the flow was as important as the organized wave's interaction with the fluctuating component[97].

Although Reynolds and Hussain's experiment was based on an idealised configuration, the presence of a similar monochromatic wavelike structure interacting with both the fine-grained turbulence and the mean flow, has been observed in several naturally occurring free-shear flows[69]. Examples include clear-air turbulence in the atmosphere[10], the vertical mixing process in oceans[70] and aerodynamic sound generation from a free turbulent jet[76].

Flow in turbomachinery passages can also be interpreted as one that is undergoing large-scale periodic perturbations, due to passing upstream wakes as well potential effects from neighbouring blade rows. The effects of this periodic unsteadiness on the time-mean flow are interpreted as an additional stress, called the Deterministic stress (DS). The DS arises when the law of momentum conservation for the time-mean flow is derived, by invoking the triple decomposition in the Navier-Stokes equations and applying a phase-locked average and time-average. Equation 49 shows the time-mean flow

momentum conservation law for the case of incompressible flow. The DS is the last term on the RHS of Equation 49.

$$\frac{\partial \overline{u}_i}{\partial t} + \frac{\partial(\overline{u}_i \overline{u}_k)}{\partial x_k} = -\frac{1}{\rho}\frac{\partial \overline{P}}{\partial x_i} + \nu \frac{\partial^2 \overline{u}_i}{\partial x_k \partial x_k} - \frac{\partial(\overline{u_i' u_k'})}{\partial x_k} - \frac{\partial(\overline{\tilde{u}_i \tilde{u}_k})}{\partial x_k} \tag{49}$$

The study of the DS can be traced back to Evans' measurements[28] of unsteady flow at mid-span downstream of a compressor rotor. He found that the kinetic energy contained within the periodic unsteadiness, i. e. the Deterministic kinetic energy (DKE), to be of a similar magnitude to the turbulent kinetic energy (TKE) when the compressor was operating at its design point. As the working conditions approached the stall point though, the TKE became larger in magnitude.

The first attempt at modelling the DS was made by Adamczyk[1][3] when he created the average-passage system for steady computations of flow in turbomachinery passages. Within the average-passage approach, the DS was modelled as a time-averaged velocity correlation, and was estimated by iterative simulation of two neighbouring blade rows with the aim of obtaining a unique axisymmetric velocity distribution throughout the simulation. Adamczyk later also successfully used DS modelling to study wake recovery and mixing loss in compressor stages, two key determinants of the efficiency of a compressor stage[2].

Rhie developed an improved mixing plane model for steady-state turbomachinery passage computations based on the DS. In Rhie's model, domain boundaries of neighbouring passages overlap and the DS is applied in the overlap region to allow for azimuthally non-uniform yet continuous flow across the passage interface. When applied to a one and a half stage compressor computation, the DS was found to be greater than the Reynolds stress (RS) at the blade hub, smaller at the tip and of a similar magnitude at mid-span[99]. Hall also used a DS model in conjunction with the mixing plane approach to successfully predict the performance of a multi-stage research compressor[43][42].

The DS was first treated as a transported quantity in the work of van de Wall et al[126]. The authors derived the transport model by computing the product of u_j with the momentum conservation law for u_i and adding it to the product of u_i and the momentum conservation law for u_j. Subsequently, van de Wall et al decomposed the flow variables into a mean and a periodic component and performed a time-average; the authors did not perform a triple decomposition as their work was based on the phase-locked averaged Navier-Stokes equations[125]. The various terms of the DS transport law were then either solved directly, or modelled based on empirical correlations and physical reasoning.

The transport model of van de Wall et al did not specifically account for the interaction of the Reynolds and deterministic stress fields; the only influence of turbulence on the deterministic stresses was via the eddy viscosity in the viscous terms. The same shortcoming also exists in other DS transport models reported in literature[13][115].

As the DS field accounts for the effects of the periodic perturbations on the time-mean flow field, the RS field quantifies the effects of turbulence on the time-mean flow field. During the design process of aerodynamic devices, such as gas turbine compressors, the conventional practice is to only solve for the time-mean flow field using the Reynolds-averaged Navier-Stokes (RANS) equations, and to estimate the RS field using turbulence models. Due to the inherent complexity of the flow in compressor passages, such as the

presence of adverse pressure-gradients and periodic perturbations in the form of passing upstream wakes and potential effects from neighbouring blade-rows, turbulence models have enjoyed mixed success, even at design conditions[103]. This is especially true of computations of multi-stage compressors; the research of Wang et al shows that even state-of-the-art RANS turbulence models struggle to correctly predict the performance characteristics along the entire machine in a multi-stage compressor[130]. Moreover, when simulating compressors at off-design conditions, RANS computations have been known to even fail to converge[78].

Due to its potentially higher fidelity, some researchers have suggested that LES can be used instead of RANS during the design process of gas-turbine compressors, and have predicted that it will be computationally viable for simulating flows in multi-stage compressors by the year 2035[38]. Such projections however are based on the assumption of Moore's law continuing to hold true, whereas there is a growing body of evidence over the last decade suggesting it has ended[121]. As such, there is likely to be a continued need for improved RANS-based turbulence models for simulating flows in single and multi-stage compressors.

A necessary first step towards this is an investigation of the RS field in compressor passages. This has been an active field of research for a very long time, with the aim of both gaining a deeper physical insight and providing reference data for improved turbulence models.

An early example are the hot-wire measurements of Hah et al[41] in the wake of a compressor stator. The authors report profiles in the near and far wake region of both the Reynolds normal and shear stresses. Other early examples include the works of Deutsch and Zierke[21][22] and Dong and Cumpsty[26]. In both cases, the authors report profiles of the turbulence intensity in the blade surface boundary layers.

A more recent example of experimental investigations of the RS field in compressor passages are the particle image velocimetry measurements of Soranna et al[111][112]. The authors conducted their investigations on a low-speed research compressor, and plotted isocontours of the RS field near the blade surfaces and in the near-wake region. Michon et al[80] used laser doppler velocimetry to measure the RS field in a compressor passage operating near the stall point. Along with contour plots of the RS field, the authors also report blade surface boundary layer profiles. Jelly et al[52] used a rotated hot-wire technique to compute phase-averaged flow statistics in the near wake of a low-speed compressor stage. The authors found the RS to be of comparable magnitude to the DS.

In any flow, the behaviour of the RS field is entirely governed by the RS budget terms. Examining the turbomachinery literature reveals that the budget terms of the RS field in compressor passages have not been investigated extensively. For the case of experimental investigations, this is perhaps explained by the difficulty in measuring the RS budget terms. Not only would a three component measurement technique with fine spatial and temporal resolution be required, but the pressure fluctuations would also need to be known throughout the compressor passage.

Scale-resolving computations, such as direct numerical simulations (DNS) and large eddy simulations (LES), are another means of computing the RS budget terms. In the last ten years, there has been a marked increase in the use of scale-resolving simulations to study flow in compressor passages. Notable contributions to the literature

include studying loss prediction at off-design conditions[65], studying the influence of free-stream turbulence on laminar-to-turbulent transition[136], and studying the effect of axial gap in a compressor stage on loss[95]. To the best of the author's knowledge however, scale resolving simulations have not been used to study the RS budget terms in compressor passages.

The brief literature survey of the preceding paragraphs shows that although the DS and RS fields have been active fields of research for several decades, scale resolving simulations have not been used to study the stress fields and their budget terms in detail in compressor passages. Moreover, little is known about the interaction of the DS and RS fields. As argued by Sandberg et al, the push towards smaller and more power-dense turbomachines that rotate faster means that there will be a greater overlap of the frequencies of deterministic unsteadiness and the frequencies at which the bulk of turbulent kinetic energy production occurs[103]. Consequently, modern compressor designs will feature an increasingly stronger link between the DS and RS fields. Although it has been examined previously, most notably the PIV measurements of Uzol et al[124], the link between the DS and RS fields in compressor passages is not well understood.

In an effort to fill this knowledge gap, the current chapter reports a detailed investigation of the RS and DS fields in compressor passages. The research comprises of not only an analysis of the stress fields and their budget equations, but also of their interaction. The motivation for carrying out this research is to not only gain a deeper physical insight into the RS and DS fields, but also to provide a reference dataset for the creation of more accurate DS and RS transport models. Moreover, as a repeating stage is simulated in the current work, the data reported herein can be used to inform the creation of improved models for simulating multi-stage compressor geometries.

The chapter starts with a derivation of the DS and RS transport laws based on the triple decomposition. This is followed by a description of the repeating compressor stage LES runs used to conduct the research. Finally, the deterministic and Reynolds stress fields and their budgets are examined in detail throughout the compressor stage.

4.2 Deterministic and Reynolds stress transport laws

A dynamical equation governing the motion of an organised wave, i. e. the periodic unsteadiness in the flow, can be derived by first invoking the triple decomposition (Equation 48a) in the Navier-Stokes equations, performing a phase-locked and a time average and finally subtracting the time average from the phase-locked average. The result is shown in Equation 50.

$$\begin{aligned}\frac{\partial \tilde{u}_i}{\partial t} + \overline{u}_k \frac{\partial \tilde{u}_i}{\partial x_k} + \tilde{u}_k \frac{\partial \overline{u}_i}{\partial x_k} = &-\frac{1}{\rho}\frac{\partial \tilde{P}}{\partial x_i} + \nu \frac{\partial^2 \tilde{u}_i}{\partial x_k \partial x_k} \\ &+ \frac{\partial}{\partial x_k}\left(\overline{\tilde{u}_i \tilde{u}_k} - \tilde{u}_i \tilde{u}_k\right) - \frac{\partial}{\partial x_k}\left(\langle u_i' u_k' \rangle - \overline{u_i' u_k'}\right)\end{aligned} \tag{50}$$

Equation 51, which expresses the law of conservation of momentum for the fluctuating component of the flow, can be derived by subtracting Equation 50 and the time-mean flow momentum equation, Equation 49, from the Navier-Stokes equation.

$$\frac{\partial u_i'}{\partial t} + \overline{u}_k \frac{\partial u_i'}{\partial x_k} + \tilde{u}_k \frac{\partial u_i'}{\partial x_k} + u_k' \frac{\partial \overline{u}_i}{\partial x_k} + u_k' \frac{\partial \tilde{u}_i}{\partial x_k} = - \frac{1}{\rho}\frac{\partial P'}{\partial x_i} + \nu \frac{\partial^2 u_i'}{\partial x_k \partial x_k} + \frac{\partial}{\partial x_k}\left(\langle u_i' u_k' \rangle - u_i' u_k'\right) \tag{51}$$

The transport equation governing the Deterministic stress (DS) can be derived by computing the sum of the momentum equation for $\tilde{u}_i$ multiplied by $\tilde{u}_j$ and the momentum equation for $\tilde{u}_j$ multiplied by $\tilde{u}_i$, and then performing phase-locked and time averages. The transport law for the Reynolds stress (RS) can be computed with a similar manipulation of Equation 51. The results can be seen in Equation 52 and Equation 53.

$$\begin{aligned}\frac{D\left(\overline{\tilde{u}_i \tilde{u}_j}\right)}{Dt} =& - \overline{\tilde{u}_j \tilde{u}_k}\frac{\partial \overline{u}_i}{\partial x_k} - \overline{\tilde{u}_i \tilde{u}_k}\frac{\partial \overline{u}_j}{\partial x_k} - \frac{\partial}{\partial x_k}\left(\overline{\tilde{u}_i \tilde{u}_j \tilde{u}_k}\right) - \frac{1}{\rho}\overline{\tilde{u}_j \frac{\partial \tilde{P}}{\partial x_i}} - \frac{1}{\rho}\overline{\tilde{u}_i \frac{\partial \tilde{P}}{\partial x_j}} \\ &+ \nu \frac{\partial^2}{\partial x_k \partial x_k}\left(\overline{\tilde{u}_i \tilde{u}_j}\right) - 2\nu \overline{\frac{\partial \tilde{u}_i}{\partial x_k}\frac{\partial \tilde{u}_j}{\partial x_k}} \\ &+ \underbrace{\overline{\langle u_i' u_k' \rangle \frac{\partial \tilde{u}_j}{\partial x_k}} + \overline{\langle u_j' u_k' \rangle \frac{\partial \tilde{u}_i}{\partial x_k}}}_{\text{I}} \underbrace{- \frac{\partial}{\partial x_k}\left(\overline{\tilde{u}_j \langle u_i' u_k' \rangle}\right) - \frac{\partial}{\partial x_k}\left(\overline{\tilde{u}_i \langle u_j' u_k' \rangle}\right)}_{\text{II}}\end{aligned} \tag{52}$$

$$\begin{aligned}\frac{D\left(\overline{u_i' u_j'}\right)}{Dt} =& - \overline{u_j' u_k'}\frac{\partial \overline{u}_i}{\partial x_k} - \overline{u_i' u_k'}\frac{\partial \overline{u}_j}{\partial x_k} - \frac{\partial}{\partial x_k}\left(\overline{u_i' u_j' u_k'}\right) - \frac{1}{\rho}\overline{u_j' \frac{\partial P'}{\partial x_i}} - \frac{1}{\rho}\overline{u_i' \frac{\partial P'}{\partial x_j}} \\ &+ \nu \frac{\partial^2}{\partial x_k \partial x_k}\left(\overline{u_i' u_j'}\right) - 2\nu \overline{\frac{\partial u_i'}{\partial x_k}\frac{\partial u_j'}{\partial x_k}} \\ &\underbrace{- \overline{\langle u_i' u_k' \rangle \frac{\partial \tilde{u}_j}{\partial x_k}} - \overline{\langle u_j' u_k' \rangle \frac{\partial \tilde{u}_i}{\partial x_k}}}_{\text{-I}} \underbrace{- \frac{\partial}{\partial x_k}\left(\overline{\langle u_i' u_j' \rangle \tilde{u}_k}\right)}_{\text{III}}\end{aligned} \tag{53}$$

The operator on the LHS of Equation 52 and Equation 53 is the total derivative, i. e. $\frac{D\cdot}{Dt} = \frac{\partial \cdot}{\partial t} + \overline{u}_k \frac{\partial \cdot}{\partial x_k}$. The terms that encapsulate the interaction of the DS and RS fields have been highlighted. Term I appears in both Equation 52 and Equation 53 but with opposite signs. It can be thus be thought of as representing energy transfer from the DS field to turbulence, and will henceforth be referred to as turbulent dissipation of the DS or deterministic production of the RS, $\widetilde{D}_{ij}$. Term II represents the transport of DS by turbulence, i. e. turbulent diffusion, $\widetilde{\phi}_{ij}$. Term III represents transport of the RS due to deterministic fluctuations, and will be referred to as deterministic diffusion, ϕ_{ij}'.

The remaining budget terms in Equation 52 and Equation 53 correspond to the familiar budget terms shown in[77], and are summarized in Table 11.

Table 11: Reynolds stress and Deterministic stress budget terms

$\widetilde{P}_{ij}, P'_{ij}$	$-\overline{\tilde{u}_j\tilde{u}_k}\frac{\partial\overline{u}_i}{\partial x_k} - \overline{\tilde{u}_i\tilde{u}_k}\frac{\partial\overline{u}_j}{\partial x_k}, -\overline{u'_j u'_k}\frac{\partial\overline{u}_i}{\partial x_k} - \overline{u'_i u'_k}\frac{\partial\overline{u}_j}{\partial x_k}$	Mean-flow production rate
$\widetilde{T}_{ij}, T'_{ij}$	$\frac{\partial}{\partial x_k}\left(\overline{\tilde{u}_i\tilde{u}_j\tilde{u}_k}\right), \frac{\partial}{\partial x_k}\left(\overline{u'_i u'_j u'_k}\right)$	Deterministic/turbulent transport rate
$\widetilde{\Pi}_{ij}, \Pi'_{ij}$	$-\frac{1}{\rho}\overline{\tilde{u}_j\frac{\partial\tilde{P}}{\partial x_i}} - \frac{1}{\rho}\overline{\tilde{u}_i\frac{\partial\tilde{P}}{\partial x_j}}, -\frac{1}{\rho}\overline{u'_j\frac{\partial P'}{\partial x_i}} - \frac{1}{\rho}\overline{u'_i\frac{\partial P'}{\partial x_j}}$	Pressure-gradient velocity correlation
$\widetilde{V}_{ij}, V'_{ij}$	$\nu\frac{\partial^2}{\partial x_k\partial x_k}\left(\overline{\tilde{u}_i\tilde{u}_j}\right), \nu\frac{\partial^2}{\partial x_k\partial x_k}\left(\overline{u'_i u'_j}\right)$	Viscous diffusion rate
$\widetilde{\epsilon}_{ij}, \epsilon'_{ij}$	$-2\nu\overline{\frac{\partial\tilde{u}_i}{\partial x_k}\frac{\partial\tilde{u}_j}{\partial x_k}}, -2\nu\overline{\frac{\partial u'_i}{\partial x_k}\frac{\partial u'_j}{\partial x_k}}$	Viscous dissipation rate
$\widetilde{D}_{ij}$	$\overline{\langle u'_i u'_k\rangle\frac{\partial\tilde{u}_j}{\partial x_k}} + \overline{\langle u'_j u'_k\rangle\frac{\partial\tilde{u}_i}{\partial x_k}}$	Deterministic production rate / turbulent dissipation rate
$\widetilde{\Phi}_{ij}, \Phi'_{ij}$	$-\frac{\partial}{\partial x_k}\left(\overline{\tilde{u}_j\langle u'_i u'_k\rangle}\right) - \frac{\partial}{\partial x_k}\left(\overline{\tilde{u}_i\langle u'_j u'_k\rangle}\right), -\frac{\partial}{\partial x_k}\left(\overline{\langle u'_i u'_j\rangle\tilde{u}_k}\right)$	Turbulent/deterministic diffusion rate

4.3 Repeating compressor stage

A repeating compressor stage is one in which the velocity and stagnation pressure profiles at the stage inlet and outlet of the stage are very similar[48]. It is a naturally occurring phenomenon in the embedded stages of a multi-stage compressor, as reported by Smith[109] and Horlock and Denton[49]. A repeating stage is thus a very instructive test-case, as it allows a multi-stage environment to be simulated using a computation comprising of only two blade passages (rotor and stator). In the context of a scale-resolving simulation, a repeating stage computation has the added advantage of allowing physically realistic turbulent flowfields to be obtained without the use of any synthetic inflow turbulence generation methods. To the best of the authors' knowledge, the current work is the first example of a scale-resolving simulation of a repeating compressor stage.

The computational domain for a repeating stage consists of a rotor and stator passage, with a sliding plane (see Section 2.6) between the rotor exit and stator inlet, and another sliding plane between the stator outlet and rotor inlet. The setup is illustrated in Figure 32.

In each passage, the flow is computed in its respective frame of reference. Therefore, when velocities are exchanged across the sliding plane the relative frame speed has to be added to them. Moreover, flow variables must also be interpolated, based on the distance between each cell and its nearest neighbour across the sliding plane. A 2^{nd} order accurate scheme is used, as summarised in Equation 54:

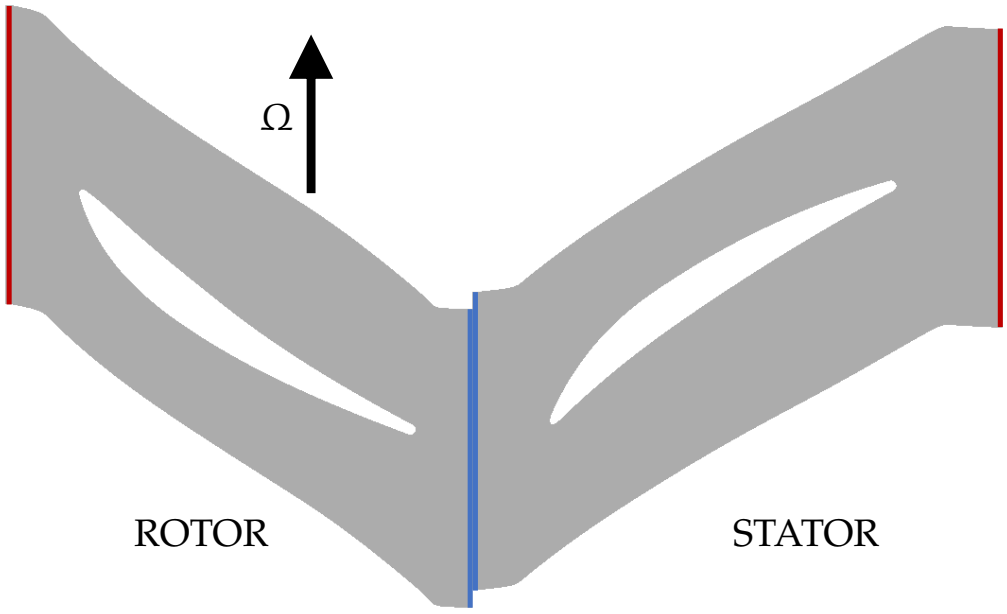


Figure 32: Repeating-stage computational domain. Coloured lines mark the positions of matching sliding planes. The rotor row rotates at a speed of Ω, whereas the stator row is stationary.

$$\left.\frac{\partial \mathbf{q}}{\partial \mathbf{x}}\right|_r = \left.\frac{\partial \mathbf{q}}{\partial \mathbf{x}}\right|_l \tag{54a}$$

$$\mathbf{q}_r = \mathbf{q}_l + (\mathbf{x}_r - \mathbf{x}_l) \cdot \left.\frac{\partial \mathbf{q}}{\partial \mathbf{x}}\right|_l \tag{54b}$$

$$\mathbf{q}_l = \mathbf{q}_r + (\mathbf{x}_l - \mathbf{x}_r) \cdot \left.\frac{\partial \mathbf{q}}{\partial \mathbf{x}}\right|_r \tag{54c}$$

The subscripts in Equation 54 denote quantities on the left and the right hand sides of the sliding plane. $\left.\frac{\partial \mathbf{q}}{\partial \mathbf{x}}\right|_r$ and $\left.\frac{\partial \mathbf{q}}{\partial \mathbf{x}}\right|_l$ are computed using the same 2^{nd} order accurate central-differencing scheme that is used to discretize the convection terms of the Navier-Stokes, as described in Section 2.2.

The truncation error associated with interpolating quantities across the sliding plane will inevitably lead to a small but finite difference in the mass-flow rate across the two sides of the sliding plane. This is corrected by explicitly enforcing mass continuity across the sliding plane; at each outer iteration, the total difference in mass flux across the sliding plane is distributed equally over its two sides. The pressure-correction is performed separately in each blade passage.

If the flow in a repeating stage is assumed to be reversible and adiabatic, a simple relationship between the work input to the flow and the static pressure rise can be derived.

$$\dot{Q} - \dot{W} = \dot{m}\Delta h_0 \tag{55a}$$

$$h_0 = h + \frac{1}{2}\rho u^2 \tag{55b}$$

$$T\Delta s = \Delta h - \frac{\Delta P}{\rho} \tag{55c}$$

In Equation 55a, the steady-state energy balance, $\dot{Q}$ represents heat addition, which is zero if the stage is assumed to be adiabatic. $\dot{W}$ is the shaft work done by the flow, and hence is negative if the machine does work on the flow and positive if the flow does work on the machine. Given that the flow has been assumed to be reversible, entropy generation is zero and $T\Delta s$ in Equation 55c (the second law of thermodynamics) is thus zero. As the velocity profiles at the entry and exit of the the stage are identical, the change in stagnation enthalpy is equal to the change in static enthalpy, i. e. $\Delta h_0 = \Delta h$. As a result, the work input can de related to static pressure rise as shown in Equation 56.

$$\dot{W} = -\frac{\dot{m}}{\rho}\Delta P \tag{56}$$

The repeating stage computations do however contain irreversibilities, namely the viscous dissipation of kinetic energy, and Equation 56 will not hold true. Therefore in the current work, Equation 56 is used as a first approximate for the value of the pressure gradient body force required to achieve a certain rate of shaft work input. Consequently, this value of the body force is adjusted via trial-and-error until the repeating stage is operating at the desired work, ψ, and flow coefficient, ϕ. It should be noted that this

trial-and-error is performed on a much coarser grid, formed by taking only every 4^{th} cell in each direction, and thus contains only $\frac{1}{64}$ of the total cells of the actual computations.

The geometry being used in the repeating stage computations is that of the Deverson compressor, a one and a half stage low-speed research compressor at the Whittle laboratory at the University of Cambridge[52, 134, 37]. The key features of the Deverson compressor are shown in Table 12.

Table 12: Deverson compressor[133]

Casing diameter(m)	0.762
Hub diameter(m)	0.6096
IGV count	49
True rotor blade count	51
True stator blade count	49
Adjusted rotor and stator blade count	50
Re based on rotor chord and mid-span blade speed	2.64×10^5
Rotor chord(m)	0.12
Mid-span stage reaction	51.6%

As seen in Table 12, the blade counts of the Deverson compressor have been adjusted to the same number of blades in the rotor and stator row. This is to allow simulations of a reduced section, in order to keep computational costs to a minimum. The true blade counts have no common factors and hence strictly would have required the whole annulus to be simulated.

The axial gap in the Deverson compressor between the rotor and the stator is 0.5 rotor chord lengths[133]. As it is essentially a 50% reaction stage, one would expect the amount of turning imparted to the flow to be the same in the rotor and stator. The repeating stage calculations were thus set up with the same axial gap between the stator trailing edge and rotor leading edge as that between the rotor trailing edge and stator leading edge. One of the runs however was computed with a reduced axial gap between the rotor and stator, in an attempt to study the effect this would have. This is highlighted in Table 13.

Another consequence of the 50% reaction stage is the same static pressure rise across the rotor and stator rows. The axial pressure gradient body force used to control the amount of work input to the flow was therefore set as the same value throughout the computational domain, rather than different values for the rotor and stator passages.

Three repeating stage computations have been run. All three were run at the same rotor rotational speed, and thus correspond to three different working points on a compressor speed line. The parameters for all the runs are summarized in Table 13.

When the repeating stage computations began, it was envisaged that many operating points on the same speed line would be computed. It was also decided to compute a

section corresponding to a quarter of the total span of the blade, so as to enable the computations to resolve large turbulent structures. As such, run 3 was the first computation performed. When it was however realized that the statistical convergence of the RS and DS budget terms was slower than expected (run 3 corresponds to a run-time of approximately 6 months), it was decided to perform the remainder of the computations on a much thinner slice. The domain sizes are discussed in further detail in Section 4.7.

Furthermore, as opposed to simulating the entire speed line, only two further operating points were computed, one corresponding to the nominal design point, and one representing a lower load coefficient. Computations at an operating point representing a higher work coefficient than the design point are underway, and will be reported in a future publication.

Table 13: Run parameters for repeating stage computations

Run #	$\phi = \frac{V_{ref}}{U_m}$	$\psi = \frac{\Delta h_0}{U_m^2}$	$Re_c = \frac{U_m c_R}{\nu}$	# cells	% span	Axial gap (mm)	# blade passes
1	0.507	0.422	2.65×10^5	33.8×10^6	5	60	70
2	0.729	0.204	2.65×10^5	33.8×10^6	5	60	32
3	0.767	0.036	2.65×10^5	157×10^6	25	40	28

In Table 13, V_{ref} is the average axial velocity at the rotor passage inlet, U_m the rotor speed at mid-span and c_R the true rotor chord.

After the computations were initialized, the flow coefficient was computed over a time period corresponding to five blade passes. When two consecutive estimates of the flow coefficient were sufficiently similar, the flow was considered to be statistically stationary and the collection of samples of the flowfield was started. The last column of Table 13 shows the number of blade-passes for which data was collected.

Samples of the flowfield were collected until the end of the time allocation for the DPhil. In the case of runs 2 and 3, the size of the sample set was not sufficiently large for achieving complete statistical convergence for the turbulent and deterministic kinetic energy budget terms. This is discussed further in Section 4.14.

4.4 Post-processing

Information is extracted from the simulations through the use of virtual probes. Probes can be used in isolation to extract data at a point, or can be grouped together to form lines or planes. An example of line probes normal to a blade surface, that can be used to extract boundary layer profiles, is shown in Figure 33. Flow variables are extracted from the simulation by first finding the nearest cell to a probe. The average, either time-mean or phase-locked, of the quantity in question is then computed at the nearest cell along with the average of its spatial derivative. Once the average is computed, a first-order Taylor series expansion is performed around the nearest cell, as shown in Equation 57, where x_i represents the location of the probe, x_i^0 the location of the nearest cell and q can represent any quantity that one may wish to compute. It should be noted that the expression shown in Equation 57 is valid for both time-mean and phase-locked average quantities.

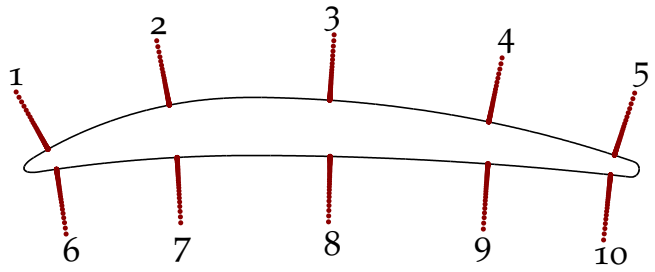


Figure 33: Probe locations relative to stator blade surface.

$$\overline{q(x_i)} \approx \overline{q(x_i^0)} + (x_i - x_i^0) \cdot \overline{\frac{\partial q}{\partial x_i}\Big|_{x^0}} \tag{57}$$

The line probes shown in Figure 33 are placed at 5%, 25%, 50%, 75% and 95% of the arclength of their respective side of the blade, and are used to extract boundary layer profiles.

4.5 Grid refinement

In order to express the grid spacings in inner coordinates, an estimate of the friction velocity, u_τ, is needed. An average value of u_τ was computed around the blade at mid-span as shown in Equation 58a, in which $\oint$ represents a circular line integral along the camber line of the blade and n_j is the blade surface normal vector.

$$u_\tau = \sqrt{\frac{1}{\rho}\frac{\oint \sqrt{\overline{\tau}_{ij} n_j \overline{\tau}_{ik} n_k}\, ds}{\oint ds}} \tag{58a}$$

$$\overline{\tau}_{ij} = \frac{1}{2}\mu\left(\frac{\partial \overline{u}_i}{\partial x_j} + \frac{\partial \overline{u}_j}{\partial x_i}\right) \tag{58b}$$

The average value of u_τ computed in each of the three runs using Equation 58a is shown in Table 14. The stator in run 3 had the highest average u_τ, which is to be expected given it was operating at the highest flow coefficient. Since the same numerical grid was used for all three computations, and the same block layout and refinement parameters were used to generate the rotor and stator passage grids, examining the stator 3 grid in inner coordinates is sufficient for judging the grid refinement levels.

Table 14: Average u_τ values around blade at mid-span

Run #	ψ	Stator u_τ (ms^{-1})	Rotor u_τ (ms^{-1})
1	0.422	1.72	1.72
2	0.204	2.20	2.16
3	0.036	2.61	2.56

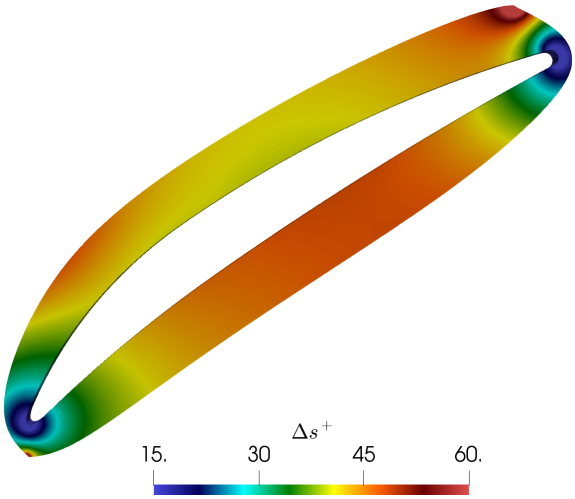


Figure 34: Streamwise grid-spacing in inner coordinates at mid-span for run 3 stator.

Figure 34 shows that around the blade surface, the streamwise grid-spacing is finest at the blade edges, and coarsest near mid-chord on the pressure side. At all points however, it is less than 50 wall units. It should be noted that the values of u_τ quoted in Table 14 are likely to overestimate u_τ at mid-chord and the trailing edge, and underestimate u_τ near the leading edge.

As Figure 35 shows, the wall-normal grid-spacing stays below 1 for a considerable distance away from the wall. The average value of the nearest cell to the blade is $\Delta n^+ \approx 0.4$, and grows at a rate no larger than 10%. The spanwise grid-spacing was constant throughout the domain at $\Delta r^+ \approx 20$.

Piomelli and Balaras set the following grid-spacing requirements for a wall-resolved LES[91] in the streamwise, wall-normal and spanwise directions: $\Delta s^+ \leqslant 100$, $\Delta n^+ \leqslant 1$, $\Delta r^+ \leqslant 20$. In their LES computations of a compressor blade at design and off-design incidences, Legget et al[65] report the following levels of refinement: $\Delta s^+ \approx 15-20$, $\Delta n^+ \approx 1.5$, $\Delta r^+ \approx 12-22$. Therefore, the level of grid-refinement shown in Figure 34 and Figure 35 is within the recommendations of Piomelli and Balaras. The grid resolution of Legget et al in the streamwise direction is however much finer than the recommendations of Piomelli and Balaras. For the $\psi = 0.036$ case in the current work, the streamwise grid-refinement matches that of Legget et al at the leading and trailing edges, but is coarser on the rest of the blade surface. The difference in the streamwise grid-refinement will be smaller for the $\psi = 0.204$ case, and the $\psi = 0.422$ will be essentially in line with the streamwise refinement levels of Legget et al. It should be noted

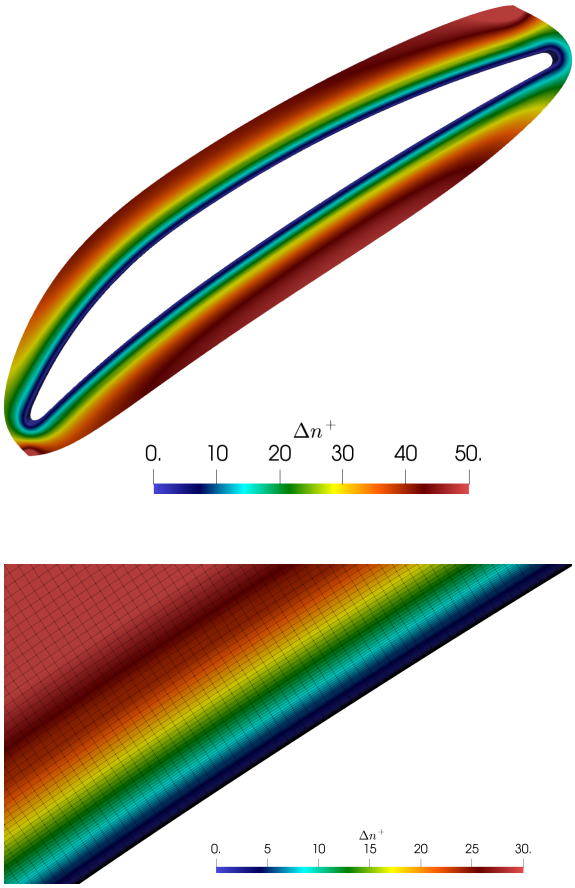


Figure 35: Top: Wall-normal grid-spacing in inner coordinates at mid-span for run 3 stator. Bottom: zoomed in view of grid-lines near mid-chord on the suction side.

however that the wall-normal grid-resolution of the computations reported herein is finer than that of Legget et al, in all three test cases.

4.6 Subgrid-scale kinetic energy

In the current implementation of LES, as explained in Section 2.1.1, the local grid-spacing defines the cut-off wavenumber above which the turbulence is modelled. As such, the spatial resolution of the grid determines the proportion of the turbulent kinetic spectrum resolved by the computation. Verifying that the majority of the turbulent kinetic energy spectrum is resolved is thus an important component of assessing the grid-refinement level.

This can be evaluated by comparing the subgrid-scale kinetic energy, q^2_{SGS}, to the resolved turbulent kinetic energy. q^2_{SGS} essentially represents the trace of the subgrid-scale stress tensor. However as Section 2.4 explained, in an incompressible flow the subgrid-scale model in the solver only accounts for the deviatoric component of the subgrid-scale stress tensor. A separate model is thus needed to estimate q^2_{SGS}.

Moin et al's model, which is also based on the Germano identity, can be used[83]:

$$q^2_{SGS} = 2C_I\Delta^2|\overline{S}|^2 \tag{59a}$$

$$C_I = \frac{1}{2}\frac{\overline{\widehat{u_k u_k}} - \overline{\widehat{u}}_k\overline{\widehat{u}}_k}{\widehat{\Delta}^2|\overline{\widehat{S}}|^2 - \overline{\widehat{\Delta^2|S|^2}}} \tag{59b}$$

The proportionality constant in Equation 59a is evaluated in a similar manner to C_s in the dynamic subgrid-scale model (see Section 2.4). A test filter-width, $\widehat{\Delta}$, can be defined by including the adjacent cells in each direction. Therefore, $\widehat{\Delta} \approx 3\Delta$. The operator $\widehat{\cdot}$ in Equation 59b thus represents test-filtered quantities, whereas $\overline{\cdot}$ indicates a time-average.

Figure 36 compares the resolved turbulent kinetic energy to q^2_{SGS} for run 1 ($\psi = 0.422$). Only the stator passage is shown as the plot for the rotor passage is very similar. Given that q^2_{SGS} is at least two orders of magnitude smaller than the turbulent kinetic energy throughout Figure 36, the computational grid can be deemed fine enough to resolve the majority of the turbulent kinetic energy spectrum.

It should be noted that the magnitude of q^2_{SGS} has only been computed for run 1, due to the slow statistical convergence of q^2_{SGS} and run 1 containing the longest time history of flowfields. Nevertheless, given that the same grid was used for run 2, and almost identical grid-refinement levels were used in run 3, it can safely be assumed that q^2_{SGS} would be similarly small for the other two computations.

4.7 Integral lengthscales

As listed in Table 13, runs 1 and 2, at $\psi = 0.422$ and $\psi = 0.204$ respectively, were computed on a domain corresponding to a 5% section of the total span of the Deverson compressor. Run 3, at $\psi = 0.036$, represents a 25% section of the total span. Although this decision was made purely on the grounds of minimising computational expense, the gathered data can nevertheless be used to assess whether or not the domain size was sufficient for reproducing large turbulent structures.

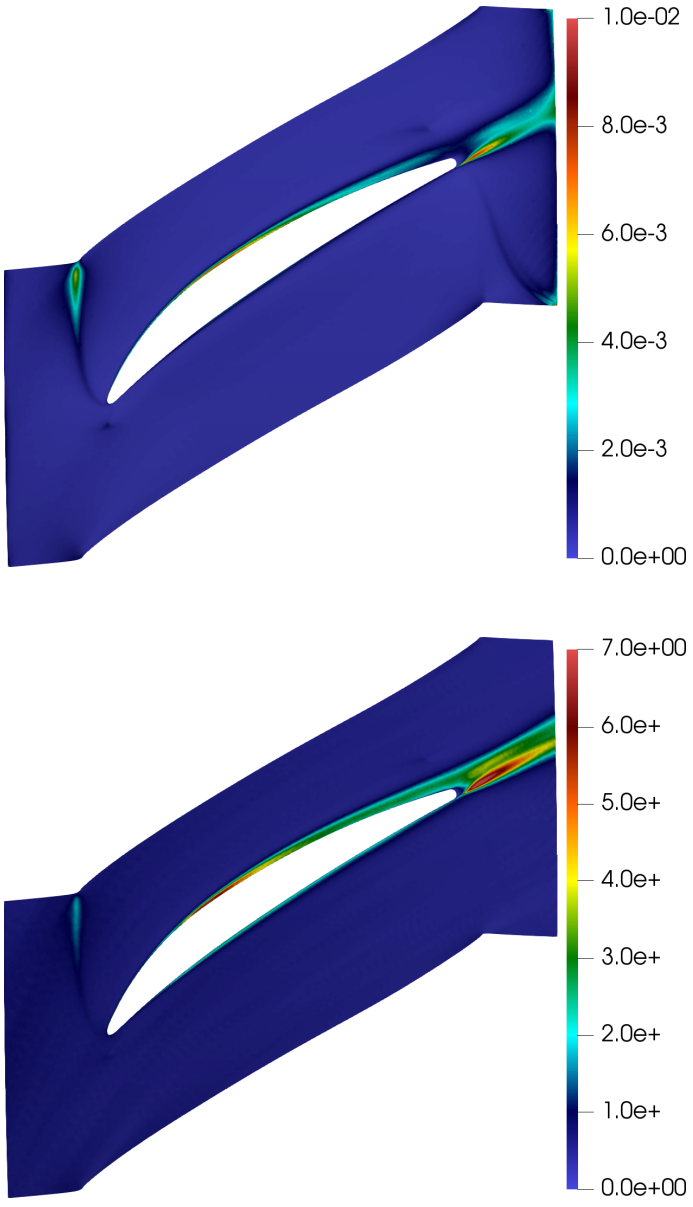


Figure 36: Top: q^2_{SGS}/u^2_τ. Bottom: $\frac{1}{2}\overline{u'_i u'_i}/u^2_\tau$. Both plots have been normalized using the global u_τ values reported in Table 14. Both plots correspond to mid-span of the stator passage at $\psi = 0.422$.

The criteria developed by Moin and Kim[84] can be used to perform this analysis. In their LES of plane-channel flow, Moin and Kim state that the domain must be at least twice as long as the integral length scale of the flow. Crucially, the authors assert that this assessment does not necessarily have to be performed *a priori*; the computed integral lengthscale can be compared to the domain length[84].

The integral lengthscale can be approximated by first computing the autocorrelation function, $\rho(\tau)$, at a suitable point in the domain. In the current work, the autocorrelation function was computed at mid-passage and mid-span at the stator passage inlet and outlet. $\rho(\tau)$ is defined as shown in Equation 60a[117].

$$\rho(\tau) = \frac{\overline{u'(t)u'(t+\tau)}}{\overline{u'(t)u'(t)}} \tag{60a}$$

$$T_\tau = \int_0^\infty \rho(\tau)\,d\tau \tag{60b}$$

Once the autocorrelation function is known, it can be integrated to compute the integral timescale, T_τ, as shown in Equation 60b. T_τ can then be converted to an integral lengthscale, L_τ, using Taylor's hypothesis of frozen turbulence[116] and the time-mean velocity. The integral lengthscales computed at the passage inlet and outlet are given in Table 15 for all three runs:

Table 15: Integral lengthscales at stator passage inlet and outlet for all three runs.

Run #	ψ	Domain height (mm)	$L_{\tau,in}$ (mm)	$L_{\tau,out}$ (mm)
1	0.422	7.62	1.544	1.02
2	0.204	7.62	2.687	0.545
3	0.036	38.1	10	11

Table 15 shows that all three of the computations reported herein satisfy the Moin and Kim criteria for domain size. Interestingly, the integral lengthscales in run 3 are significantly larger than those of runs 1 and 2. This is consistent with the elevated levels of TKE seen in run 3 at the passage inlet and outlet (see Section 4.10).

For flows containing regions of separation, a commonly used criterion for assessing the domain size is that of von Terzi[127]. In simulations of compressor passages, the von Terzi criterion can be interpreted to mean that the domain size in the spanwise direction must be four times as large as the boundary layer displacement thickness in the separation bubble[55]. In the current work, runs 2 and 3 contain regions of separated flow. In run 2, the displacement thickness in the separation bubble is 25% of the spanwise domain size. In run 3, it is 10%. The current computations thus also satisfy the von Terzi criterion for domain size.

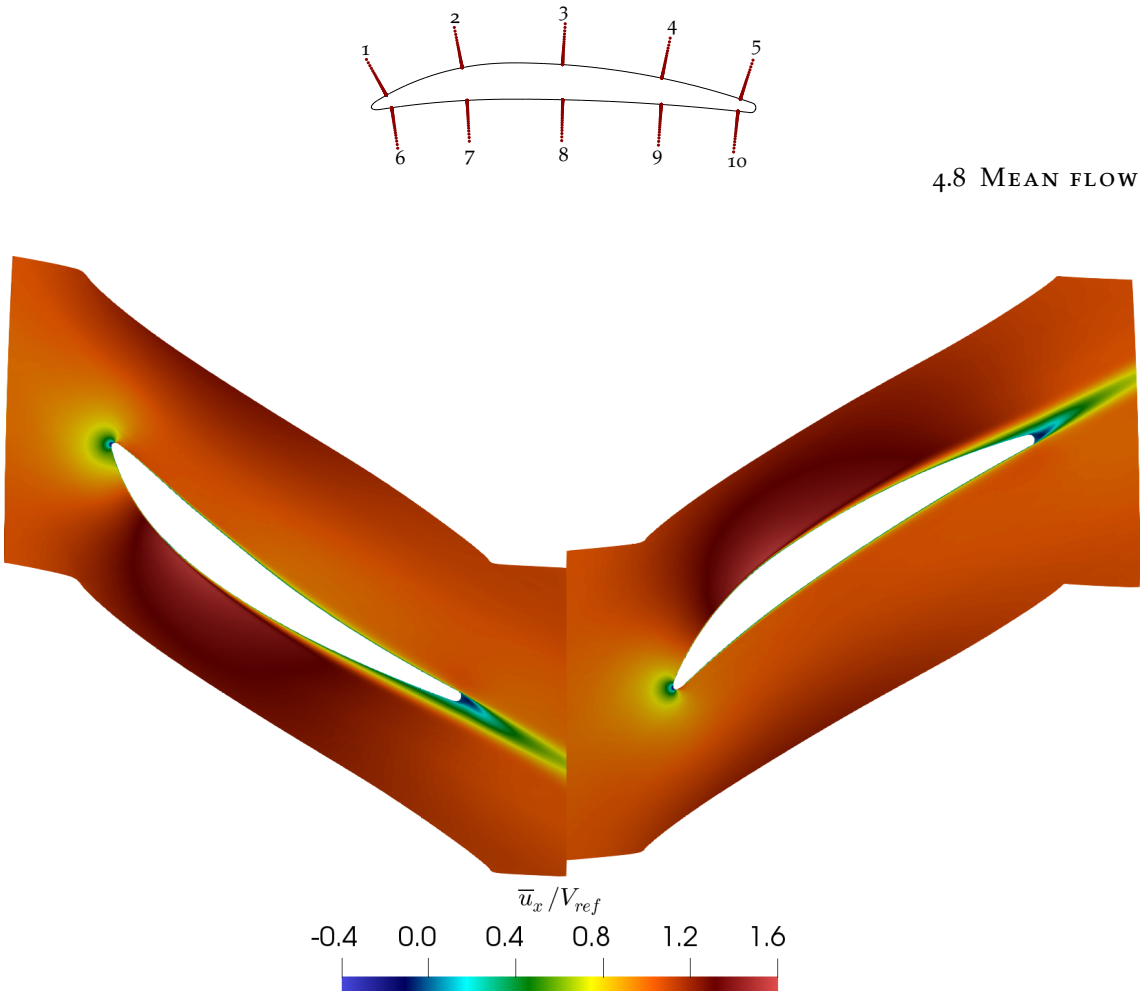


Figure 37: Axial velocity contours at mid-span for run 1 ($\psi = 0.422$). Normalized by V_{ref} i.e. velocity used to compute flow coefficient.

4.8 Mean flow

The time-mean axial velocity for run 1 is shown in Figure 37, which represents the design point of the Deverson compressor[133]. In each blade passage, the velocity has been plotted in its respective frame of reference. The stagnation point for both the rotor and stator is on the pressure side of the blade, explaining the positive incidence quoted in Table 16. The flow remains attached to the blade surfaces on both the pressure and suction sides. Peak suction appears to occur approximately one-third of a chord length downstream of the leading edge, after which the adverse pressure gradient causes the flow to decelerate and the boundary layer to grow visibly. A noteworthy feature of Figure 37 is the similarity of the flowfield in the rotor and stator passages; this is to be expected in an essentially 50% reaction stage. The wake profiles of run 1 are shown in Figure 38. The wake profiles were computed using an azimuthal line probe placed at the passage exit at mid-span. The time-averaged velocity profiles were then rotated so as to to align them with the angle of the blade trailing edge. The rotor wake exhibits a higher momentum deficit than the stator wake, which shows an almost flat velocity profile outside of the negative jet region. It should also be noted that as a result of positive incidence, both the wake profiles are offset towards the suction side relative to the trailing edge.

Further insight into the mean-flow can be gleaned by examining the blade boundary layers. These can be computed using the line probes shown in Figure 33, placed at 5%, 25%, 50%, 75% and 95% of the suction and pressure side surfaces (see Section 4.4). A copy of Figure 33 has also been included in the document header so as to assist

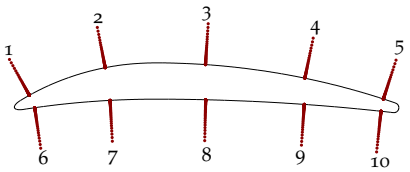


Table 16: Mean-flow incidence angles

Run #	Rotor	Stator
1	5.4	7.4
2	-9.4	-8.4
3	-16.3	-18.4

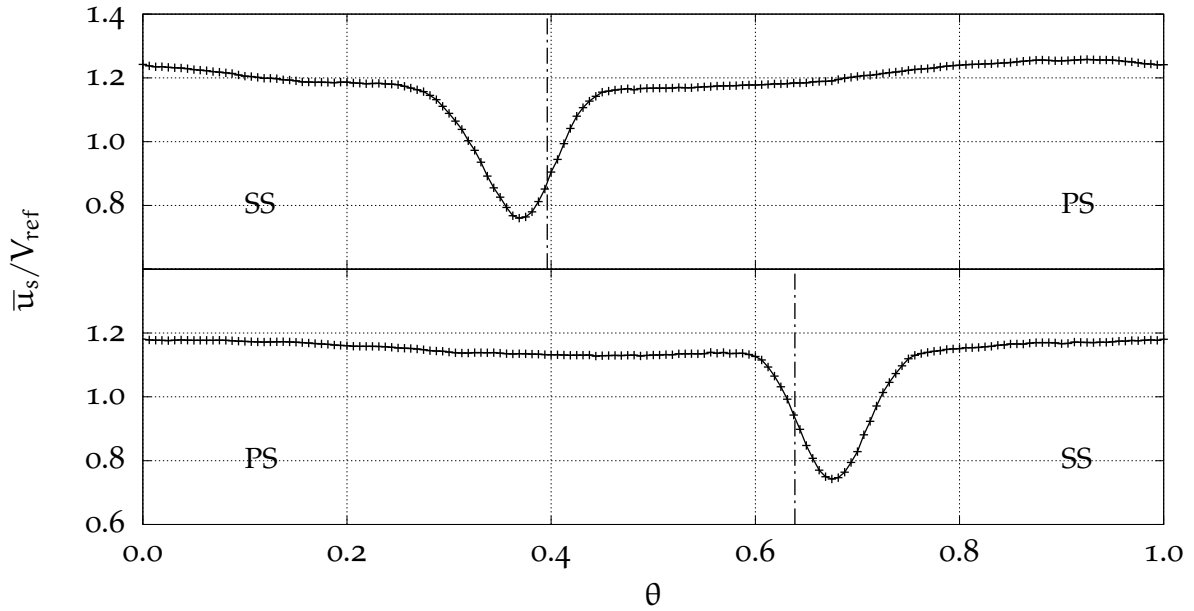


Figure 38: Wake profiles for run 1 ($\psi = 0.422$) plotted in a coordinate system aligned with the blade trailing edge. X-axis is normalized by domain bounds. Top plot is for rotor row, bottom plot for stator row. Dash-dotted line marks the location of the blade trailing edge projected to the passage outlet.

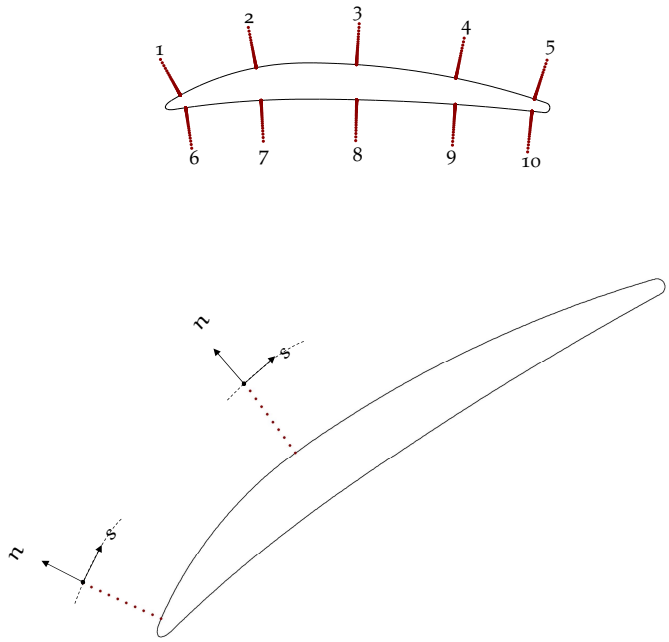


Figure 39: Rotated coordinate system for boundary layer line plots.

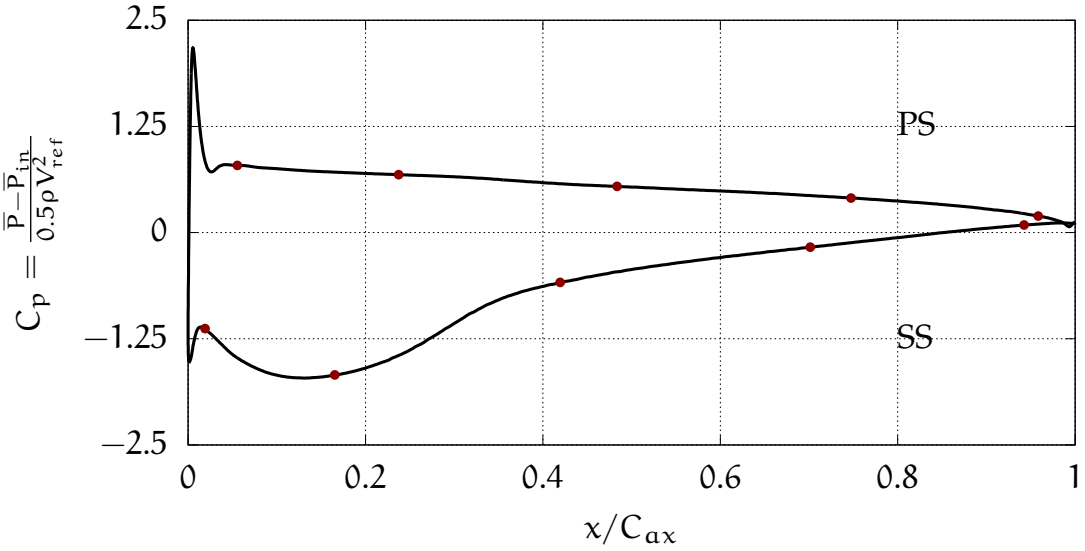
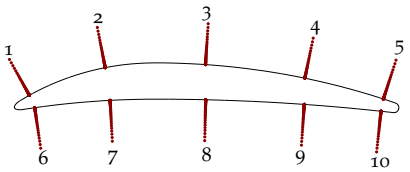


Figure 40: Pressure coefficient distribution around run 1 stator ($\psi = 0.422$) at mid-span, as a fuction of the axial position along the blade. $\overline{P}_{in}$ is the azimuthally averaged pressure at the passage inlet. Red dots mark the location of boundary layer probes.

the reader in understanding the boundary layer profiles shown hereafter. Rather than plotting the velocities in cartesian coordinates however, it is more insightful to rotate them as illustrated in Figure 39. In the rotated coordinate system , the streamwise direction, s, is aligned with the time-mean flow at the freestream end of the probe, the normal direction, n, is perpendicular to the blade surface and the spanwise direction, w, is orthogonal to both the s and n directions. All boundary layer plots will henceforth be plotted using the rotated coordinate system shown in Figure 39.

In order to better understand the boundary layer profiles, it is worth determining the local pressure-gradient, as well as the local skin-friction. The pressure coefficient around the stator blade at mid-span is shown in Figure 40, and the skin-friction coefficient in Figure 41.

It should be noted that Figure 41 plots the streamwise component of the wall-shear stress:



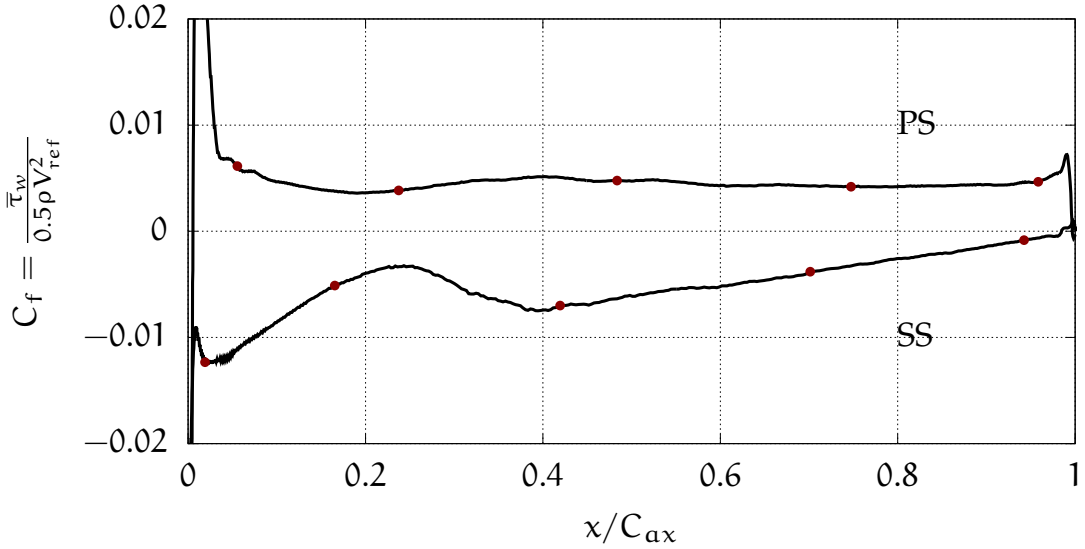


Figure 41: Skin-friction coefficient distribution around run 1 stator ($\psi = 0.422$) at mid-span, as a fuction of the axial position along the blade. Red dots mark the location of boundary layer probes.

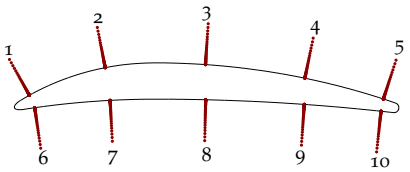
$$\overline{\tau}_w = \overline{\tau}_{ij} n_j l_i \tag{61}$$

In Equation 61, l_i is the unit vector parallel to the blade-surface. Boundary layer profiles for the streamwise velocity in outer and inner coordinates for the stator in run 1 are shown in Figure 42 and Figure 43 respectively.

The first probes on both the pressure and suction sides show a local velocity peak close to the wall. On the pressure side, the velocity recovers away from the wall whereas on the suction side the freestream velocity remains lower than the near-wall peak. The skin friction is also very high at the first probe, which can be seen clearly in Figure 41 and supported by the low values of $\overline{u}_s/u_\tau$ at probes 1 and 6 in Figure 43. At the second probe on the suction side, the boundary layer does not exhibit the typical characteristics of a turbulent boundary layer and appears transitional. It does however appear to have become turbulent by the third probe, with a narrow logarithmic layer developing at probe 3 and 4.

On the suction side of the blade, the boundary layer is operating under an adverse pressure-gradient from probes 2-5, as shown by Figure 40. The adverse pressure-gradient also manifests itself in the increased "wake" component in the outer region of the boundary layer profiles at probes 3-5, similar to the profiles computed by Spalart et al[113]. At probe 5, the profile no longer resembles that of a typical turbulent boundary layer, and is close to the point of separation. This assertion is supported by the profile at probe 5 corresponding to the largest value of the boundary layer shape factor, H.

It should be noted that in order to compute the boundary layer shape factor, the conventional definition of the displacement thickness, δ^*, and momentum thickness, θ^*, cannot be used. The conventional definition assumes $\overline{u}_s$ tends to a constant as the distance from the wall tends to infinity. Due to the fact that compressor blades act to turn the flow, the above assumption does not hold true in the current flowfield. As such,



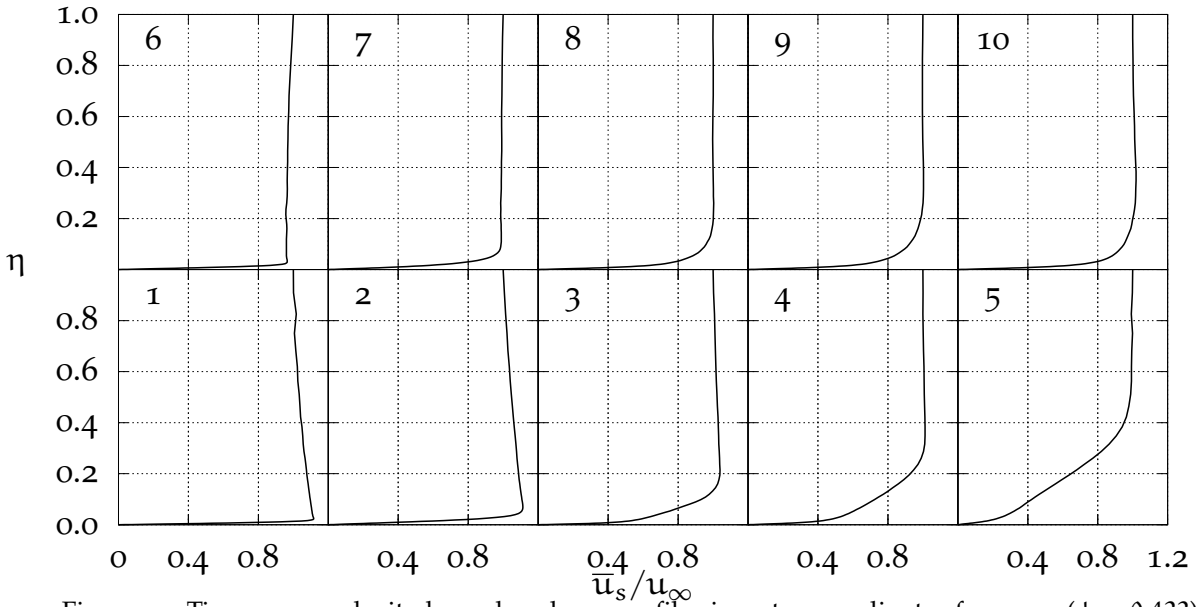


Figure 42: Time-mean velocity boundary layer profiles in outer coordinates for run 1 ($\psi = 0.422$) stator. Normalized by the streamwise velocity at the freestream end of the probe. Probe number shown in the top-left corner.

Spalart et al's modified definitions of the integral boundary layer quantities must be used[113].

$$U_{ref} = -\int_0^\infty \frac{\partial \overline{u}_s}{\partial \eta} d\eta \tag{62a}$$

$$\delta^* = -\frac{1}{U_{ref}} \int_0^\infty \eta \frac{\partial \overline{u}_s}{\partial \eta} d\eta \tag{62b}$$

$$\theta^* = \frac{2}{U_{ref}^2} \int_0^\infty \eta \Big[\int_0^\eta \frac{\partial \overline{u}_s}{\partial \eta'} d\eta' \Big] \frac{\partial \overline{u}_s}{\partial \eta} d\eta - \delta^* \tag{62c}$$

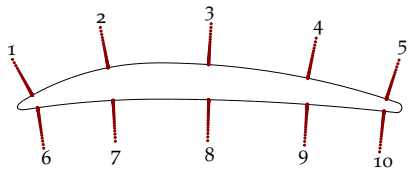
$$H = \frac{\delta^*}{\theta^*} \tag{62d}$$

On the pressure side of the blade, the boundary layers are operating under a favourable pressure gradient, as shown by the pressure-coefficient distribution in Figure 40. The favourable pressure gradient increases markedly from probes 9 to 10, and as expected, this is accompanied by a drop in the shape-factor from probes 9 to 10.

At first glance, one may interpret the boundary layer profiles on the pressure side of the blade as displaying laminar characteristics. This is however not the case, and the profiles from probes 8-10 are very similar to typical turbulent boundary layer profiles in favourable pressure gradients. This can be verified by a comparison to boundary layer profiles reported in literature.

A common non-dimensional method of relating the local pressure-gradient to the local wall shear-stress is $\beta = \frac{\delta^*}{\overline{\tau}_w} \frac{\partial \overline{p}}{\partial s}$. For the profiles shown in Figure 43, $\beta = -0.21$ at probe 8 and $\beta = -0.36$ at probe 9. Figure 44 shows a comparison of the profiles at probes 8 and 9 with that computed by Spalart et al at $\beta \approx -0.3$[113].

As shown in Figure 44, the boundary layer profiles at profiles at probes 8 and 9 match that of Spalart et al very well in the inner part of the boundary layer, up to $\eta^+ \approx 200$.



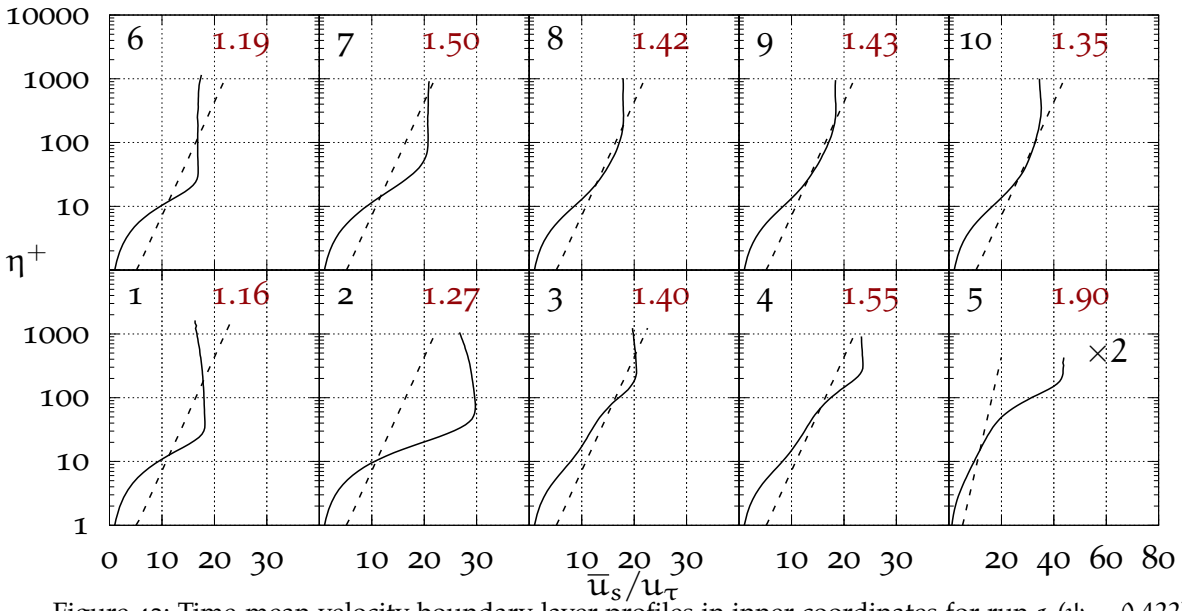


Figure 43: Time-mean velocity boundary layer profiles in inner coordinates for run 1 ($\psi = 0.422$) stator. Normalized by local u_τ. - - - $u^+ = \frac{1}{\kappa}\log\eta^+ + C$, $\kappa = 0.41$ $C = 5.2$. Probe number shown in the top-left corner. Boundary layer shape-factor written in red.

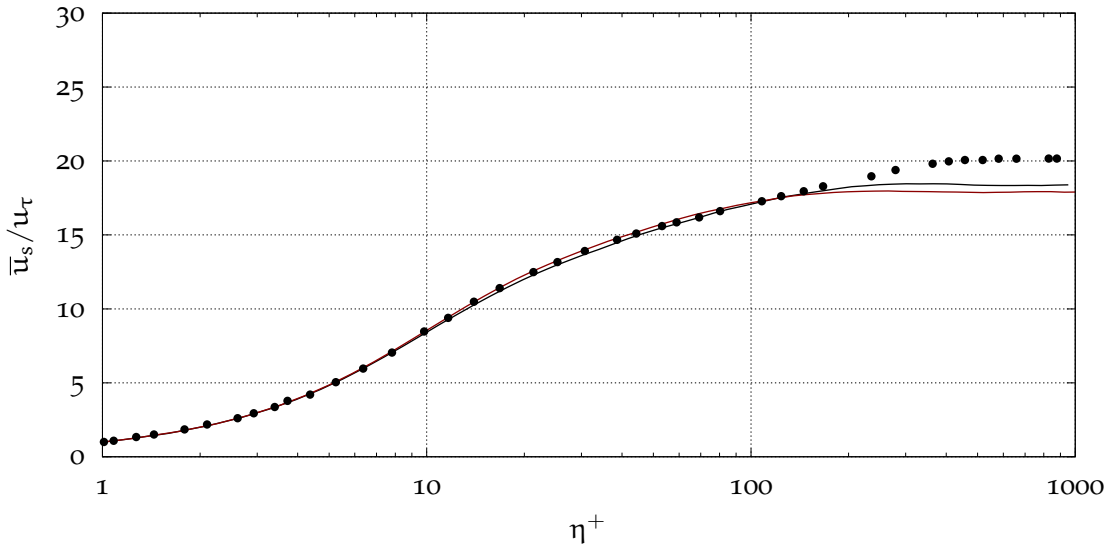


Figure 44: Time-mean velocity boundary layer profiles in inner coordinates for run 1 ($\psi = 0.422$) stator. Normalized by local u_τ. ● Spalart et al —— Probe 9 —— Probe 8.

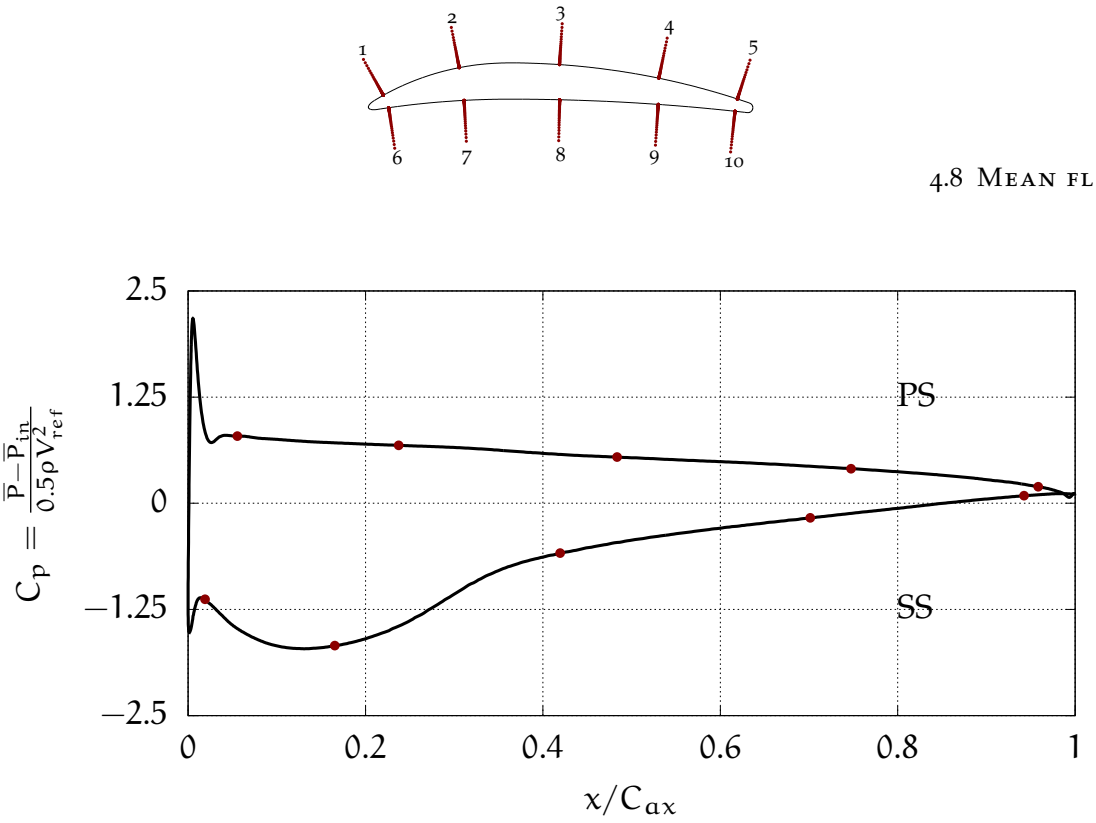


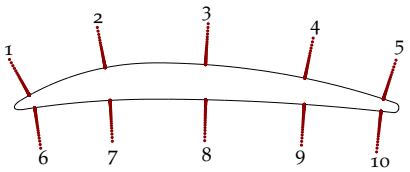
Figure 45: Pressure coefficient distribution around run 1 rotor ($\psi = 0.422$) at mid-span, as a fuction of the axial position along the blade. $\overline{P}_{in}$ is the azimuthally averaged pressure at the passage inlet. Red dots mark the location of boundary layer probes.

As the outer part of the boundary layer is not expected to scale with u_τ[11], the lack of agreement above $\eta^+ \approx 200$ is of no concern.

Figure 45 and Figure 46 show the pressure and skin-friction distributions around the rotor blade for run 1, respectively, and Figure 47 and Figure 48 show the boundary layer profiles in outer and inner coordinates, respectively. As the data shows, the distributions of C_p and C_f as well as the blade surface boundary layer profiles in the rotor and stator passage are so similar that any comments made about the stator also apply to the rotor.

A contour plot for the axial velocity at mid-span for run 2 is shown in Figure 49. Run 2 represents a significantly lower load coefficient than the design point, and it is immediately clear how different the velocity field is from run 1. The flow coefficient in run 2 is higher than that of run 1, and thus it is no surprise that the peak axial velocity is also higher. Moreover, the peak velocity occurs at the leading edge in run 2, as opposed to mid-chord on the suction surface. This is a direct consequence of the negative incidence, see Table 16. As the stagnation point is on the suction side, the flow has to turn all the way around the leading edge, leading to high local acceleration. The negative incidence also creates a separation bubble, which persists for approximately 10% of the blade chord, as confirmed by the skin-friction distribution in Figure 50. It should also be noted that the flow is again very similar in the rotor and stator passages.

In Figure 49, the boundary layer on the pressure side of the blade is visibly thicker than that on the suction side. This increased momentum deficit is carried through to the wakes as well; the wake velocity profile in Figure 51 takes longer to recover to the freestream value on the pressure side than it does on the suction side. Unlike the wake profiles of run 1, those of run 2 do not show an offset towards the trailing edge. The stator wake profile is centred around the trailing edge, whereas the rotor wake profile is offset slightly towards the trailing edge, most likely due to the rotor blade operating at a greater negative incidence, see Table 16.



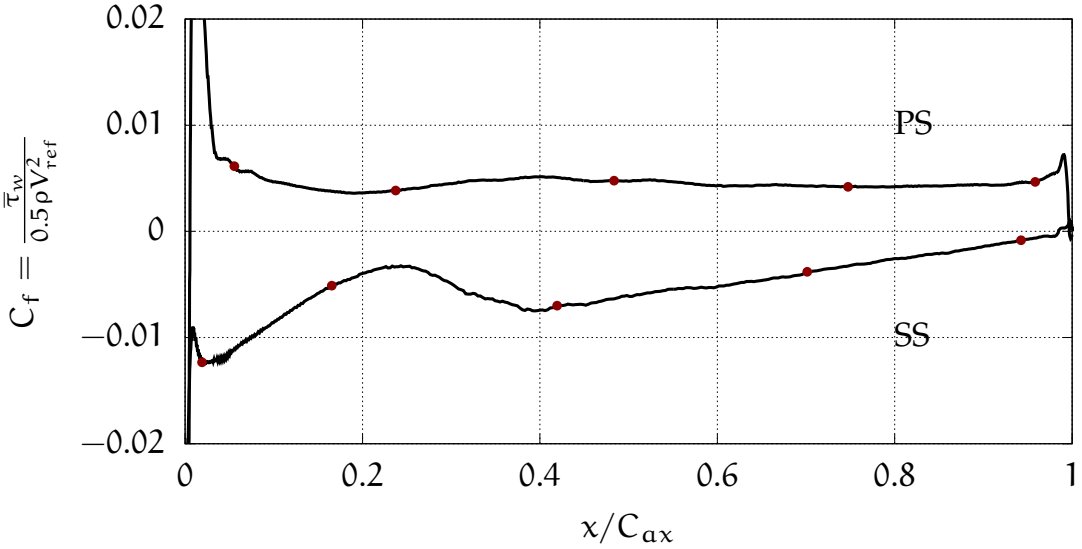


Figure 46: Skin-friction coefficient distribution around run 1 rotor ($\psi = 0.422$) at mid-span, as a fuction of the axial position along the blade. Red dots mark the location of boundary layer probes.

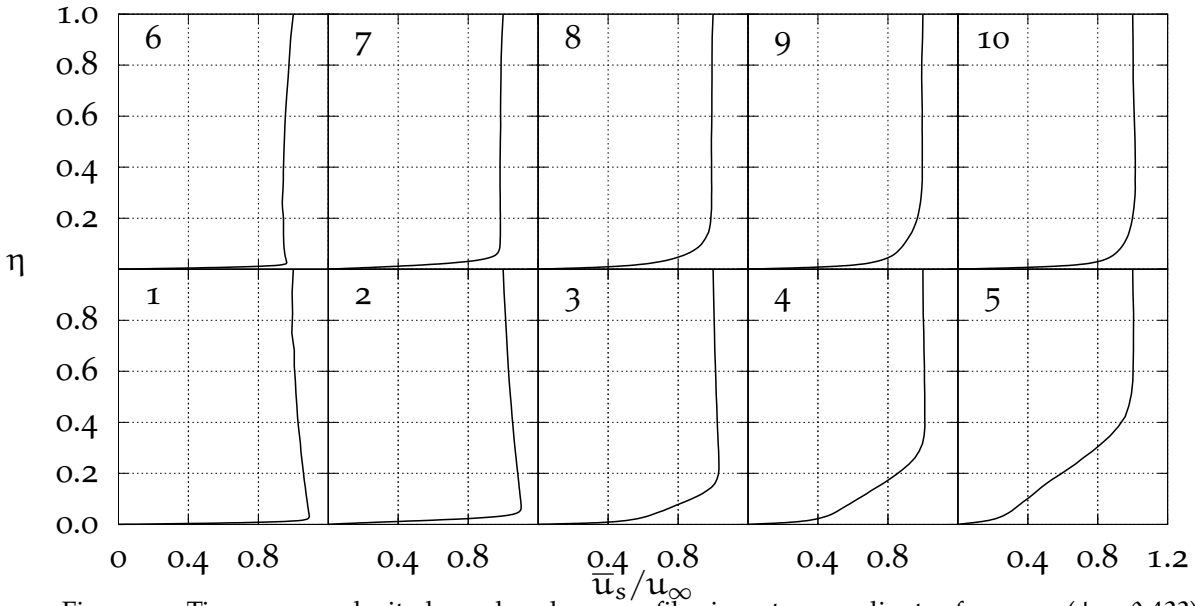
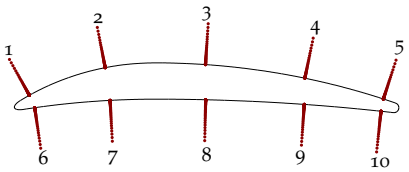


Figure 47: Time-mean velocity boundary layer profiles in outer coordinates for run 1 ($\psi = 0.422$) rotor. Normalized by streamwise velocity at the freestream end of the probe. Probe number shown in the top-left corner.



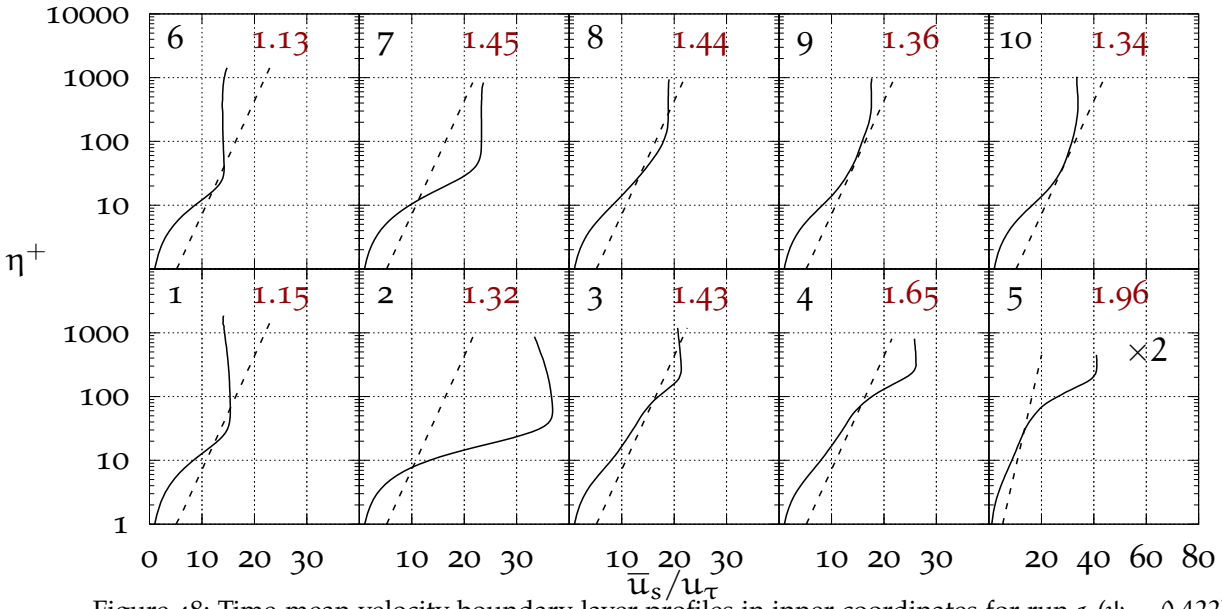


Figure 48: Time-mean velocity boundary layer profiles in inner coordinates for run 1 ($\psi = 0.422$) rotor. Normalized by local u_τ. --- $u^+ = \frac{1}{\kappa}\log\eta^+ + C$, $\kappa = 0.41$ $C = 5.2$. Probe number shown in the top-left corner. Boundary layer shape-factor written in red.

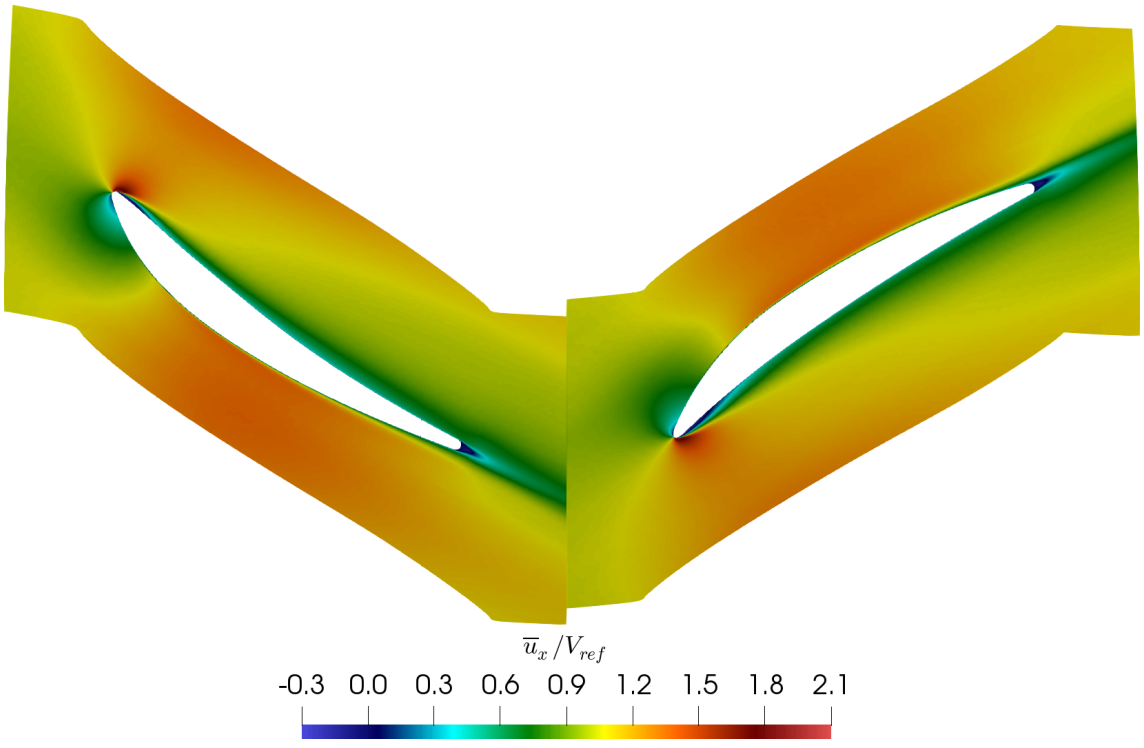
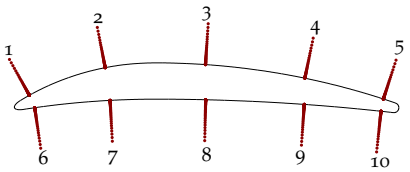


Figure 49: Axial velocity contours at mid-span for run 2 ($\psi = 0.204$). Normalized by V_{ref}.



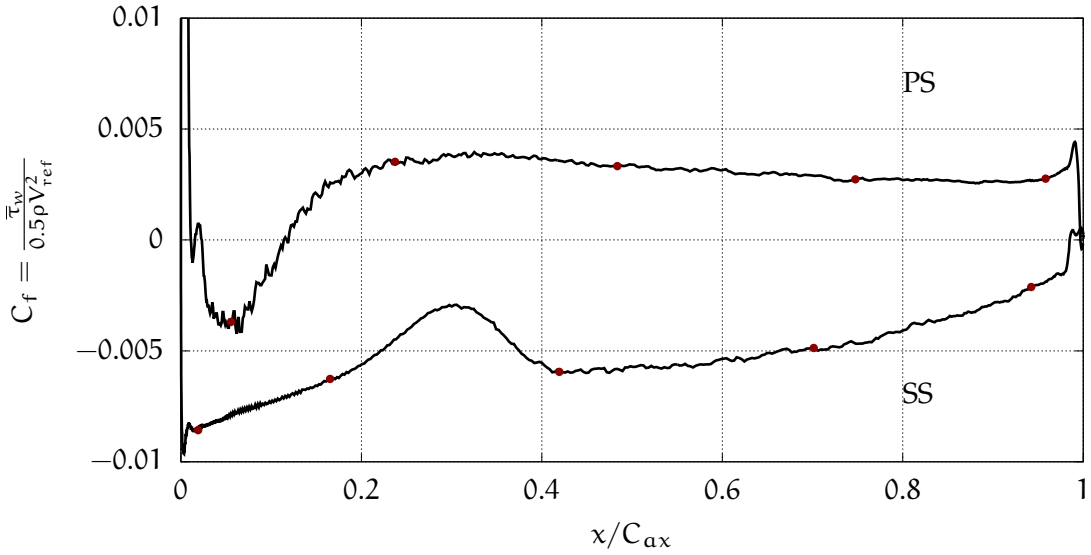


Figure 50: Skin-friction coefficient distribution around run 2 stator ($\psi = 0.204$) at mid-span, as a fuction of the axial position along the blade. Red dots mark the location of boundary layer probes.

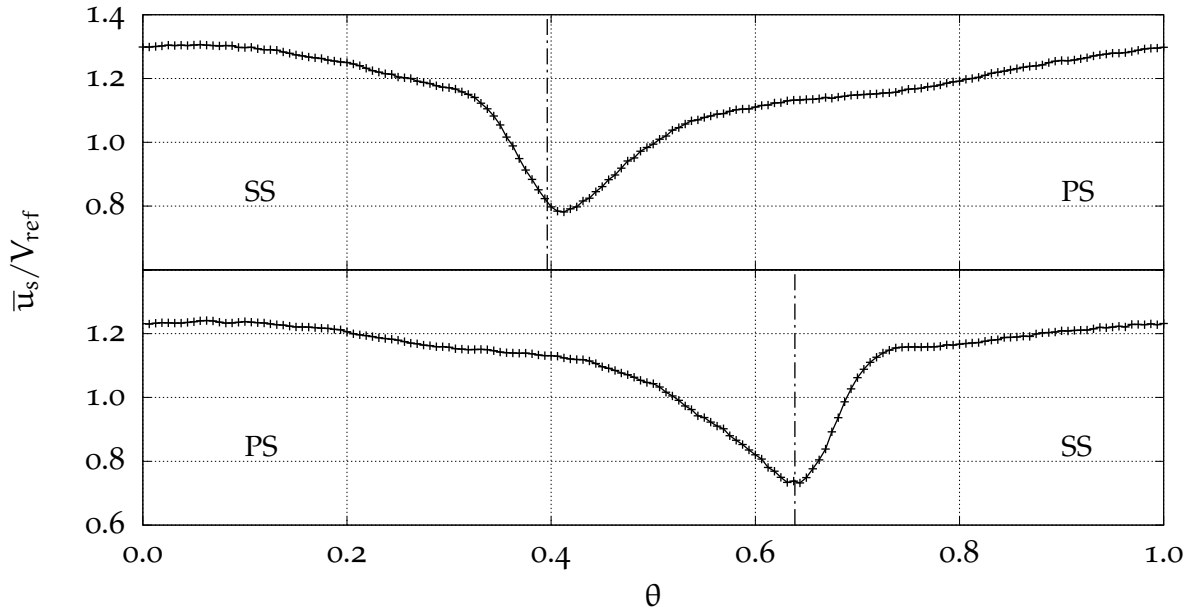
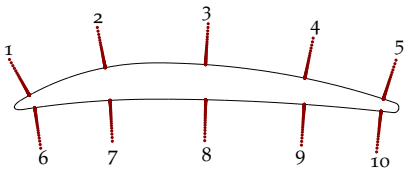


Figure 51: Wake profiles for run 2 ($\psi = 0.204$). X-axis is normalized by domain bounds. Top plot is for rotor row, bottom plot for stator row. Dash-dotted line marks the location of the blade trailing edge projected to the passage outlet.



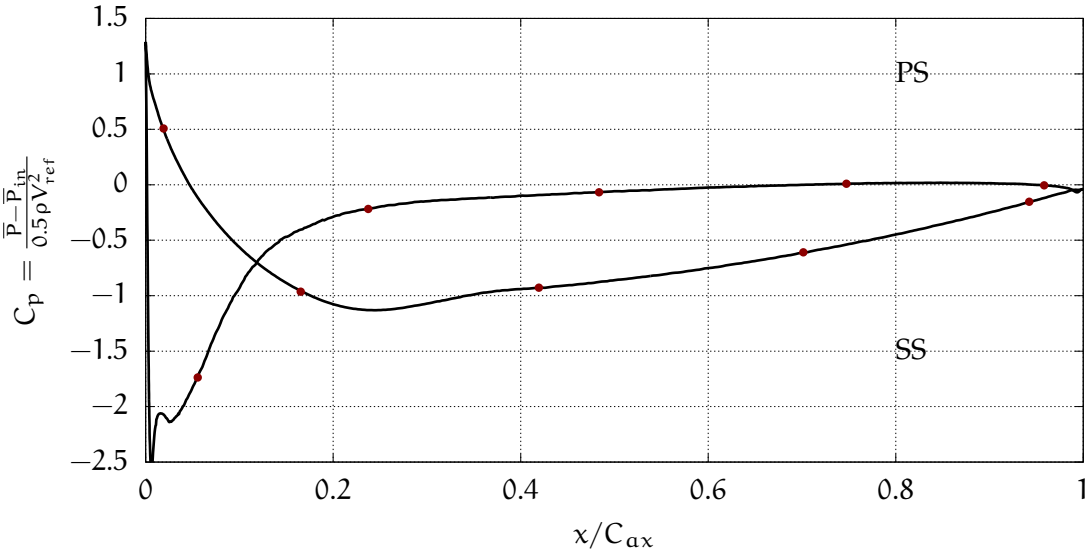


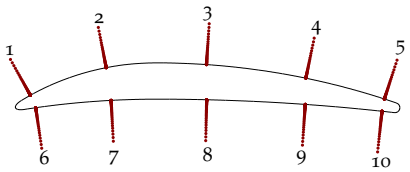
Figure 52: Pressure coefficient distribution around run 2 stator ($\psi = 0.204$) at mid-span, as a fuction of the axial position along the blade. $\overline{P}_{in}$ is the azimuthally averaged pressure at the passage inlet. Red dots mark the location of boundary layer probes.

Figure 52 shows the C_p distribution around the stator blade in run 2. Whereas run 1 featured a favourable pressure-gradient along the pressure side, run 2 shows an adverse pressure gradient all along the pressure side, other than at the very end (probe 10). The suction side of the stator blade in run 2 is now experiencing a favourable pressure-gradient at the first two probes, as opposed to just the first probe in run 1.

The boundary layer profiles for run 2 shown in Figure 53 show a greater momentum deficit on the pressure side than the suction side. Moreover, the pressure side separation bubble at probe 6 appears to cause the boundary layer to transition. The profile at probe 7 in Figure 54 shows a distinct logarithmic layer that persists until probe 9. At probe 10, the boundary layer is operating under a strong favourable pressure-gradient, hence the large in shape-factor as compared to probe 9. Interestingly, although an adverse pressure-gradient persists from probes 6-9, the shape factor continues to drop. This suggests the boundary layer on the pressure side is still recovering from the separation bubble.

The suction side boundary layer starts with a very strong favourable pressure-gradient, which gradually turns into an adverse pressure-gradient as one moves down the chord. This is accompanied by a gradually increasing shape-factor, as shown in Figure 54. Boundary layers profiles have only been shown for the stator blade because the flow-field is again very similar for both blade passages.

Figure 55 shows axial velocity contours for run 3. The flowfield is an exaggerated version of that of run 2, with a much larger pressure side separation bubble that persists for approximately 20% of the chord, as shown in Figure 56. Furthermore, this is the only case in which the flow appears to be noticeably different between the rotor and stator, most likely due to the different axial gaps, see Table 13. The boundary layer on the suction side appears very thin all along the length of the blade. On the pressure side,



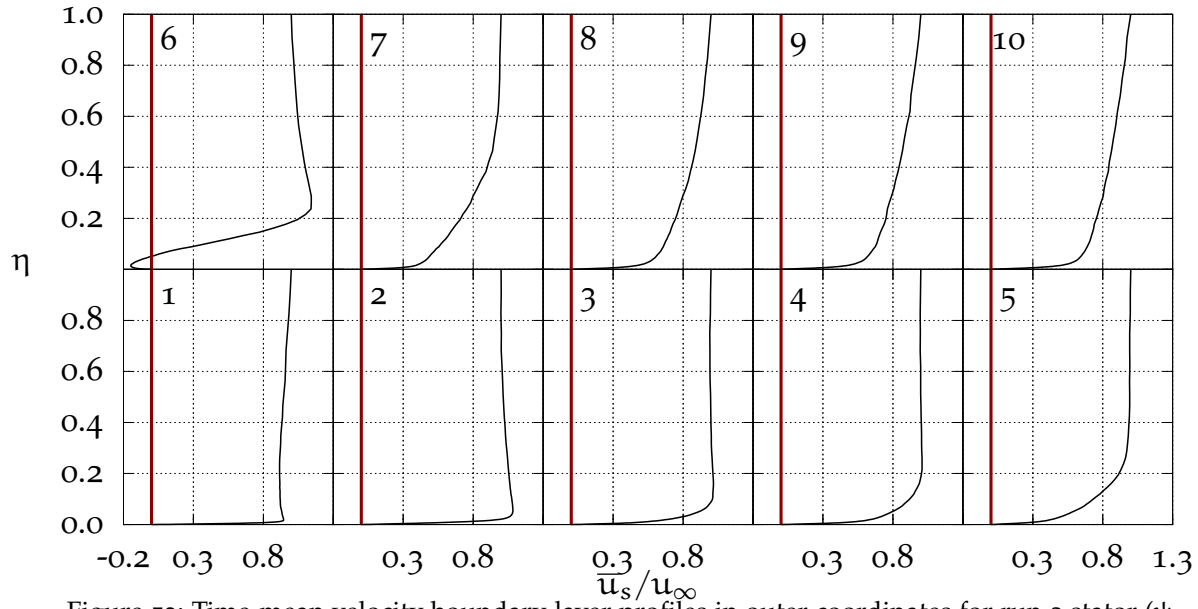


Figure 53: Time-mean velocity boundary layer profiles in outer coordinates for run 2 stator ($\psi = 0.204$). Normalized by the streamwise velocity at the freestream end of the probe. Red line marks $\overline{u}_s = 0$. Probe number shown in the top-left corner.

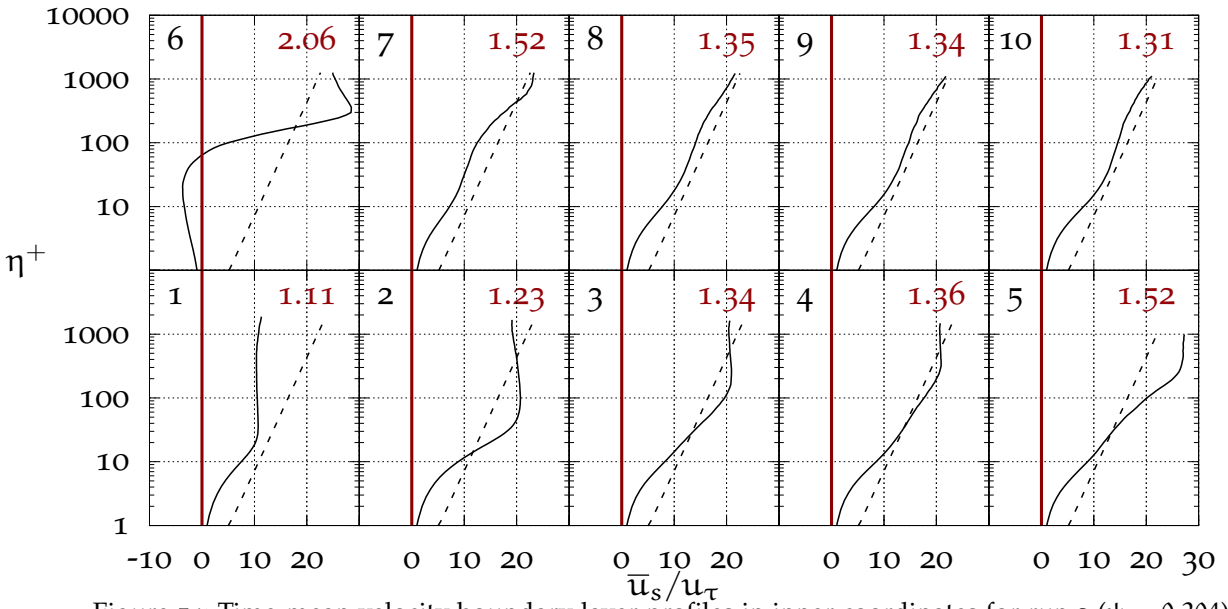


Figure 54: Time-mean velocity boundary layer profiles in inner coordinates for run 2 ($\psi = 0.204$) stator. Normalized by local u_τ. - - - $u^+ = \frac{1}{\kappa}\log\eta^+ + C$, $\kappa = 0.41$ $C = 5.2$. Red line marks $\overline{u}_s = 0$. Probe number shown in the top-left corner. Boundary layer shape-factor written in red.

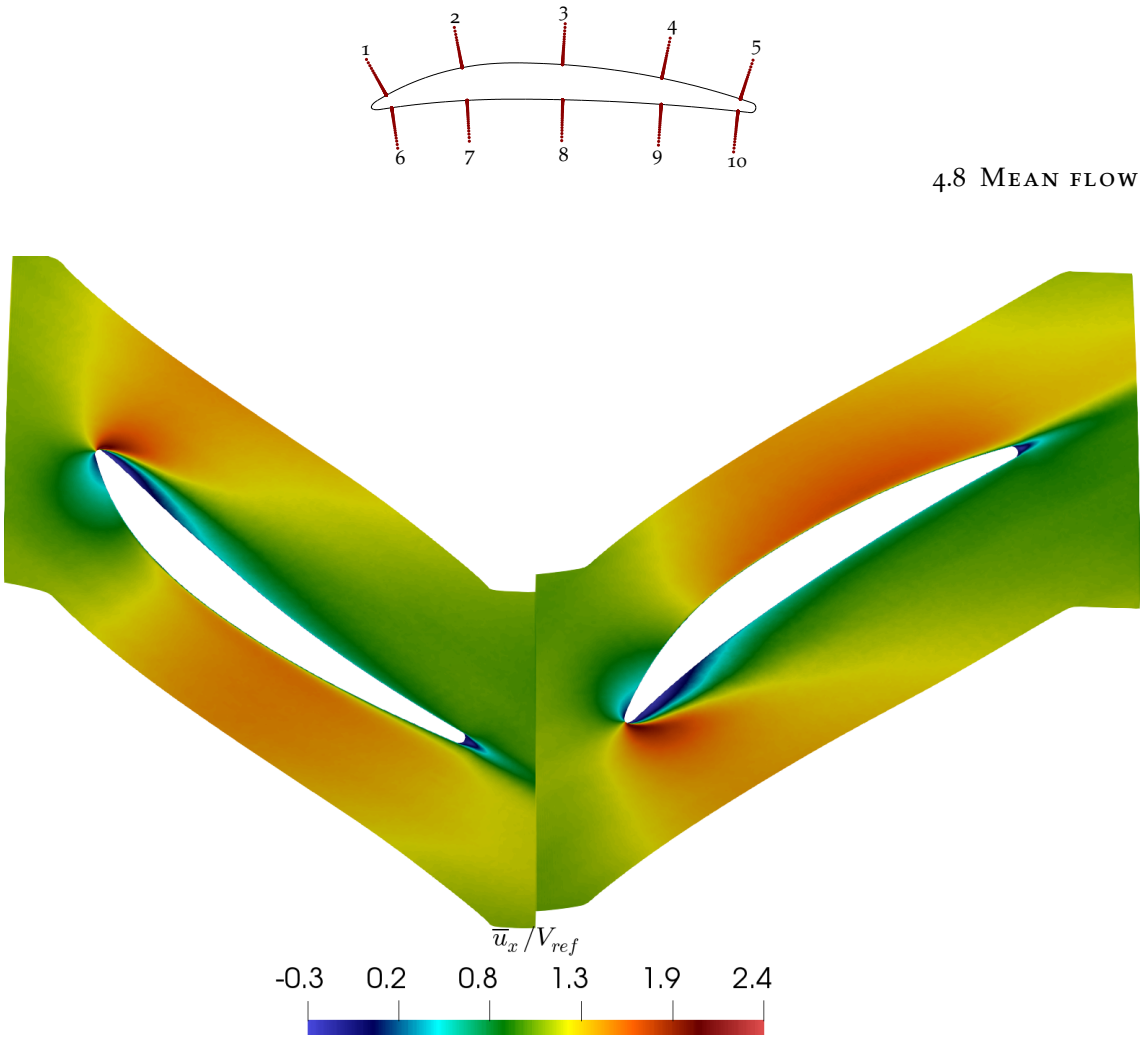


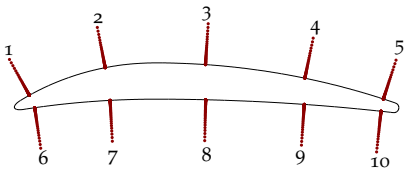
Figure 55: Axial velocity contours at mid-span for run 3 ($\psi = 0.036$). Normalized by V_{ref}.

the separation bubble significantly disrupts the flow, and the axial velocity remains well below that on the suction side.

Figure 57 shows the true extent of the effect of the pressure side separation bubble on the flow. Neither the stator nor the rotor blade wake on the pressure side recover to a freestream value, resulting in significant blockage. The wake profiles also show that the effects of the separation bubble are more pronounced for the stator, as it shows no discernible negative jet region.

Figure 58 shows the C_p distribution around the blade for run 3. It is largely very similar to that of run 2 in Figure 52, except for the fact that the favourable pressure-gradient on the suction side now persists until probe 3, as opposed to probe 2.

Figure 59 shows the suction side boundary layer remains very thin. In contrast to run 2, Figure 60 shows that the shape-factor drops from probe 1 to probe 2, suggesting a strong favourable pressure-gradient in the early chord region on the suction side in run 3. Consequently, the shape-factor on the suction side consistently remains below those of run 2, and the profiles never develop a fully-turbulent appearance. The pressure side separation bubble in run 3 has a similar effect to that in run 2; it causes the boundary layer to transition, with a distinct but narrow logarithmic layer visible up to probe 9.



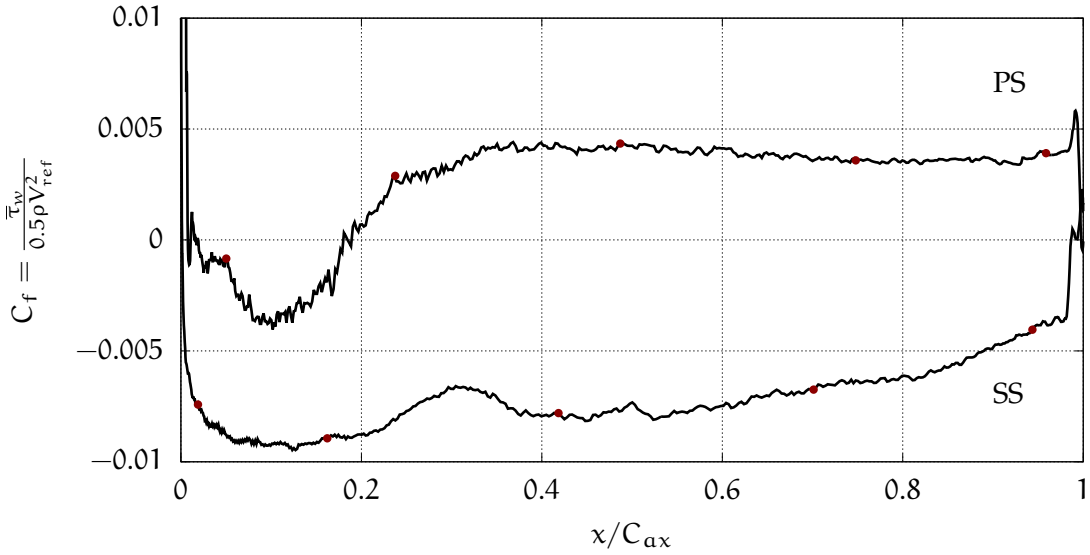


Figure 56: Skin-friction coefficient distribution around run 3 stator ($\psi = 0.036$) at mid-span, as a fuction of the axial position along the blade. Red dots mark the location of boundary layer probes.

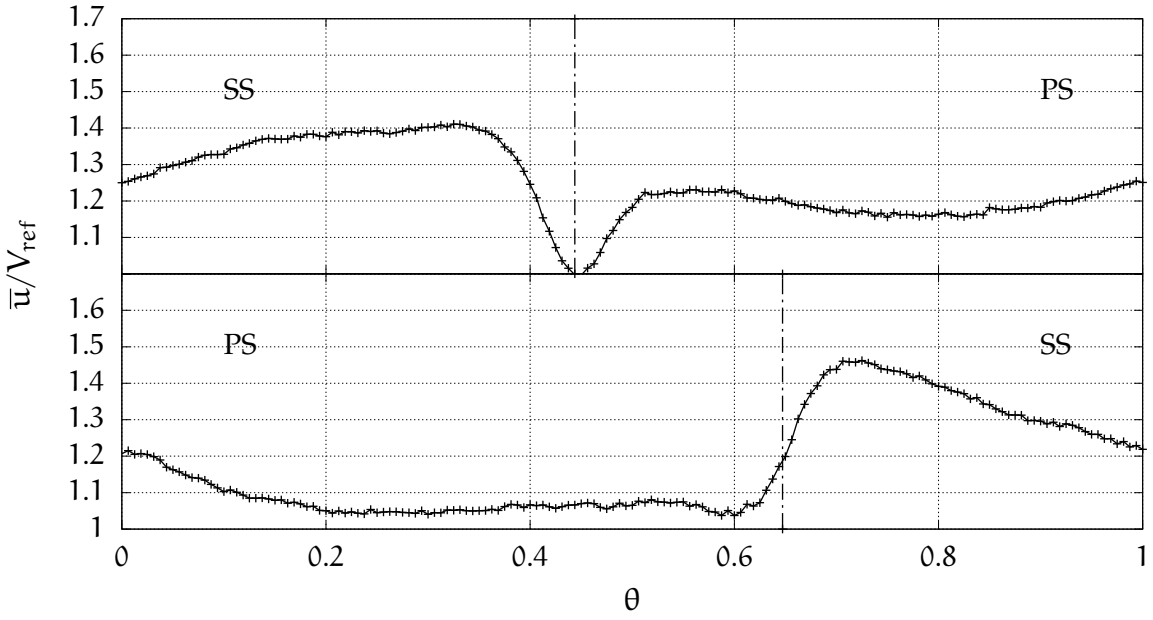
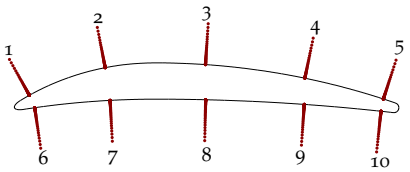


Figure 57: Wake profiles for run 3 ($\psi = 0.036$). X-axis is normalized by domain bounds. Top plot is for rotor row, bottom plot for stator row. Dash-dotted line marks the location of the blade trailing edge projected to the passage outlet.



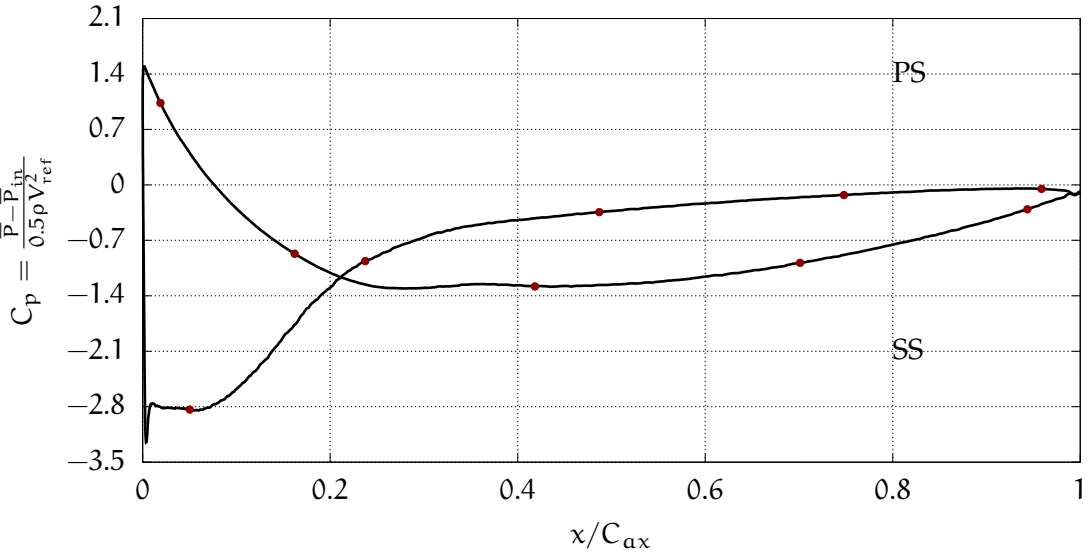


Figure 58: Pressure coefficient distribution around run 3 stator ($\psi = 0.036$) at mid-span, as a fuction of the axial position along the blade. $\overline{P}_{in}$ is the azimuthally averaged pressure at the passage inlet. Red dots mark the location of boundary layer probes.

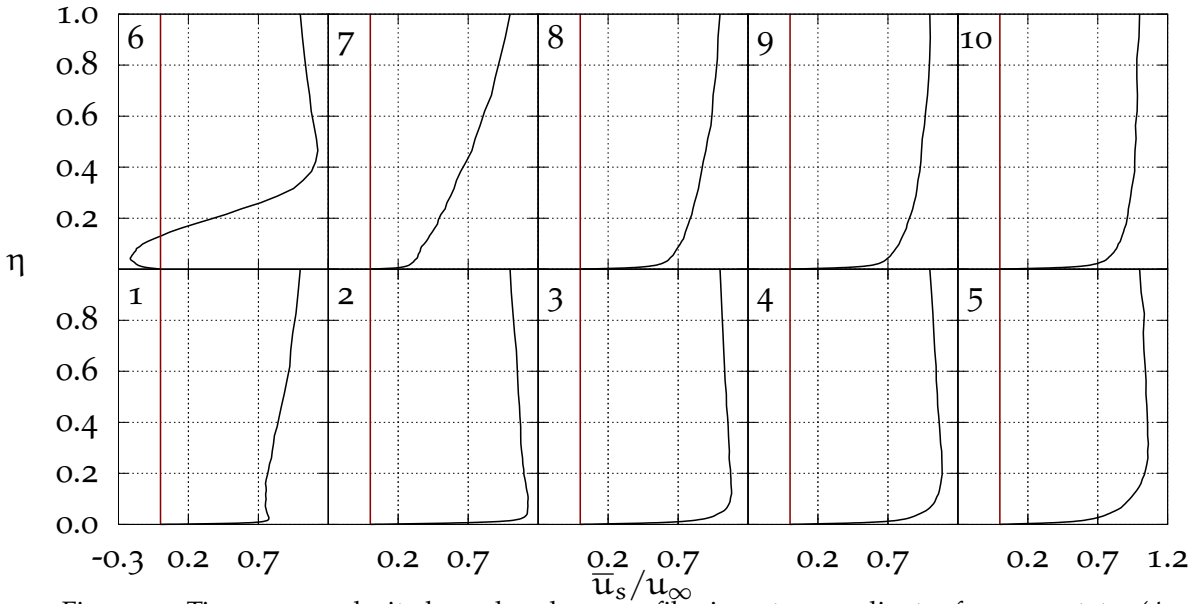
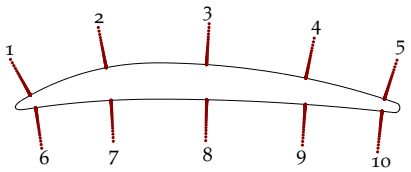


Figure 59: Time-mean velocity boundary layer profiles in outer coordinates for run 3 stator ($\psi = 0.036$). Normalized by the streamwise velocity at the freestream end of the probe. Red line marks $\overline{u}_s = 0$. Probe number shown in top-left corner.



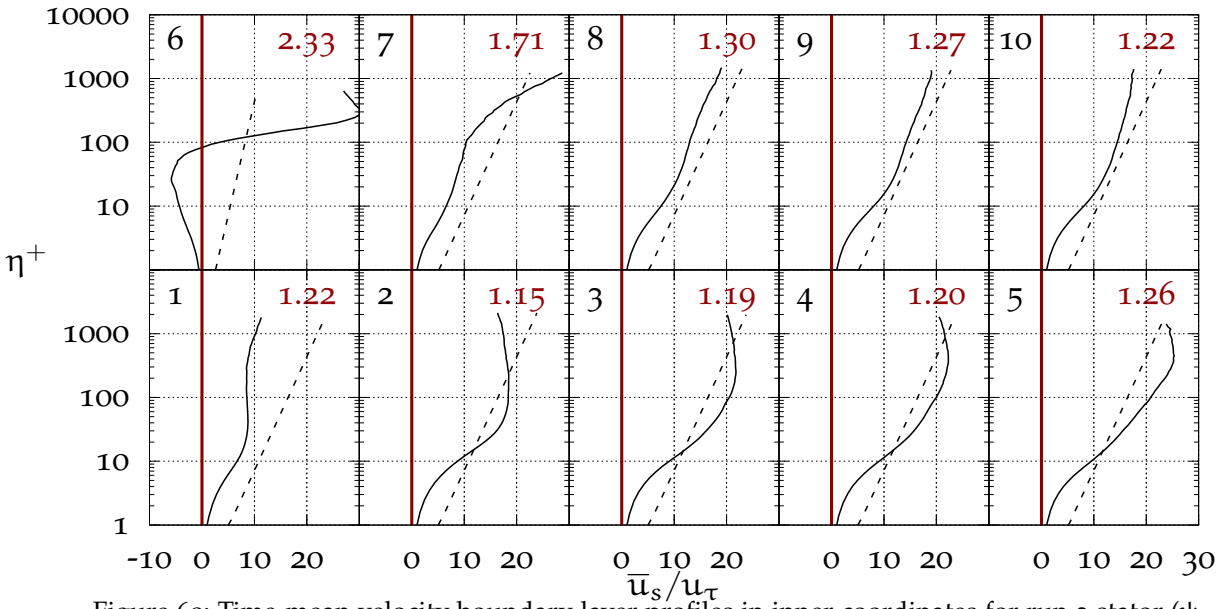
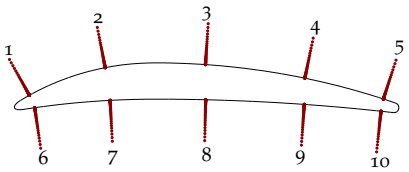


Figure 60: Time-mean velocity boundary layer profiles in inner coordinates for run 3 stator ($\psi = 0.036$). Normalized by local u_τ. - - - $u^+ = \frac{1}{\kappa}\log\eta^+ + C$, $\kappa = 0.41$ $C = 5.2$. Red line marks $\overline{u}_s = 0$. Probe number shown in top-left corner. Boundary layer shape-factor written in red.



4.9 Unsteady flow

The periodic nature of the flow can be understood by extracting the organized unsteady motion, by first computing a phase-locked average and subtracting the time-average from that, i. e. $\tilde{u}$ in Equation 48d. The phase-locked average is performed over the time taken for the rotor blade to traverse one blade-pitch, i. e. complete one blade-pass. Figure 61 plots $\tilde{u}$ at four different points of the blade-pass period for run 1.

As a wake shed by an upstream blade is convected through the passage, one end of it will lie on the suction side surface, and the other on the pressure side. Consequently, the wake will be "chopped"[110] as the suction side end travels faster than the pressure side end. An example of this is clearly visible in Figure 61. In the topmost plot of Figure 61, an upstream wake has just passed the stator leading edge. By the next picture, which represents a step forward in time of one-quarter of the blade-pass period, the suction side end of the wake has visibly travelled further than the pressure side end.

Due to one end of the wake travelling faster than the other, it will be elongated, and tilted clockwise in the rotor row and counter-clockwise in the stator row. Following the reasoning of Smith, Kelvin's circulation theorem implies that as the wake is stretched, its velocity deficit must be attenuated[110]. As this attenuated wake is eventually mixed out by viscosity, it will incur a smaller mixing loss than the original wake. This is the mechanism behind wake recovery in compressors[126]. The wake mixing is clearly seen in Figure 61, as the wake velocity contours progressively turn into a lighter shade of blue as they move through the passage.

The discontinuous nature of Figure 61 across the rotor-stator interface also merits discussion. The quantity plotted in Figure 61 is the periodic perturbation around the mean flow. The motivation behind plotting $\widetilde{u}_x$ as opposed to $\langle u_x \rangle$ is to examine the evolution of periodic perturbations, i. e. passing upstream wakes, as they move through the blade passage. As such, one would expect the magnitude of the perturbation to be the greatest at the passage inlet, and to attenuate gradually as the wake is mixed out by viscosity and stretched due to the blade turning the flow. Therefore, the discontinuous appearance of Figure 61 across the rotor-stator interface is to be expected.

The above hypothesis can be verified by plotting the phase-averaged velocity. As Figure 62 shows, $\langle u_x \rangle$ is continuous across the rotor-stator interface. However by not removing $\overline{u}_x$, it is much harder to see how upstream wakes are modified as they pass through a blade passage.

Figure 63 plots the organized unsteady component of the axial velocity for run 2. As the rotor rotational speed is the same for all the runs, but the flow coefficient is greater in the second run than the first, run 2 is operating at a lower reduced frequency as compared to run 1. Proof of this is seen in the fact that whereas four wakes are visible in each passage in Figure 61, only three can be found in each passage in Figure 63. The unsteady separation bubble near the leading edge on the pressure side is most clearly visible in plots 2 and 4. The separation bubble clearly varies a lot throughout the blade-pass cycle, and is thus likely to correspond to high levels of deterministic stress.

Another notable feature of Figure 63 can be seen in the stator passage in plot 2. The rotor wake entering the stator passage is clearly visible and is marked by dark blue contours. It however appears to be connected another to another fainter wake just ahead of it. This is in fact the remnant of the stator wake that passed along the pressure side of

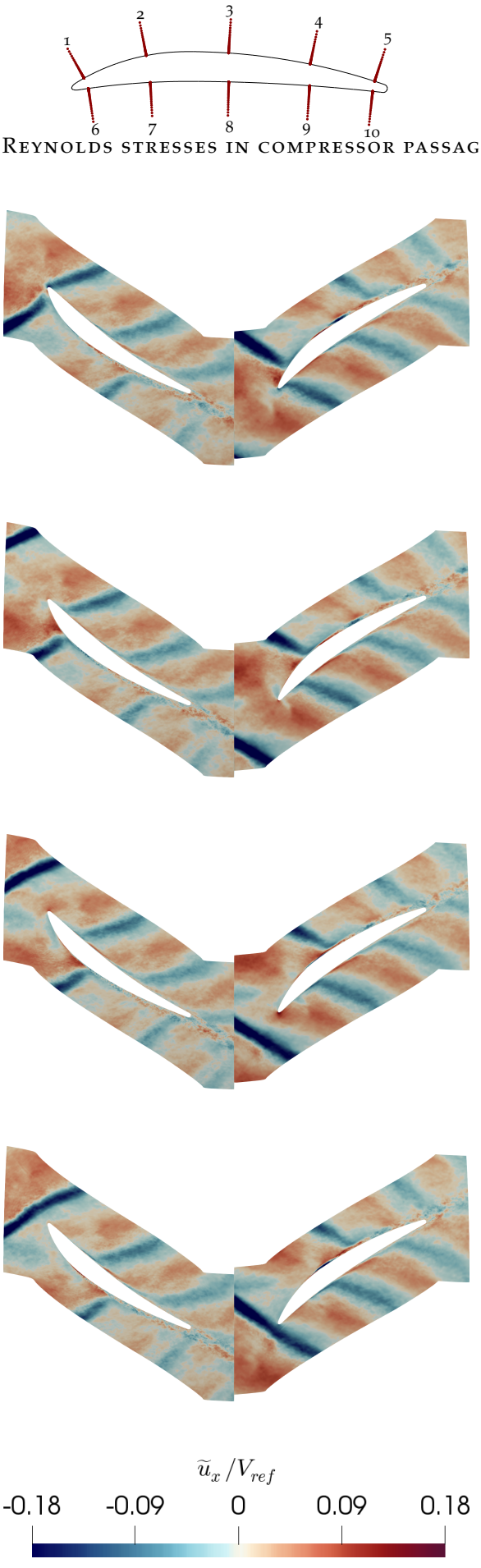
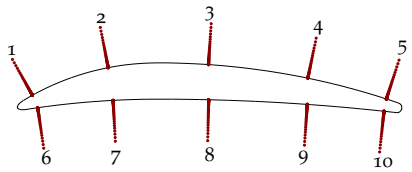


Figure 61: Organized unsteady component of axial velocity plotted at 0%, 25%, 50% and 75%, from top to bottom, of the blade pass period for run 1 ($\psi = 0.422$). Normalized by V_{ref}.



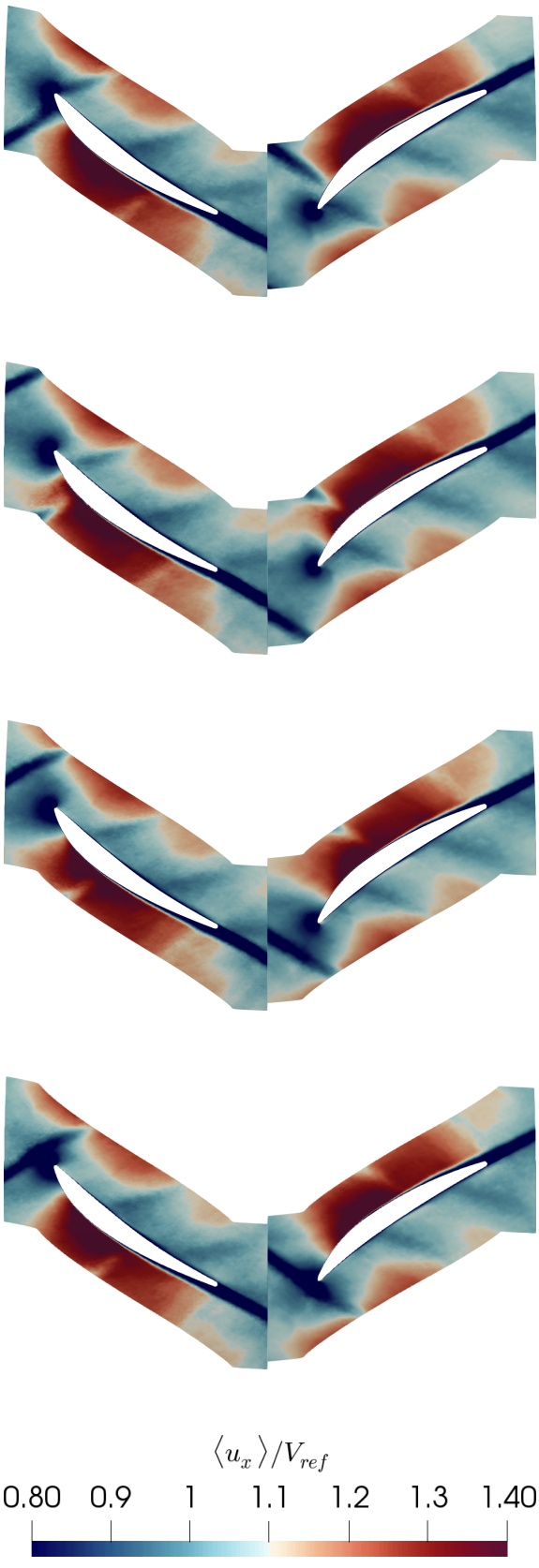
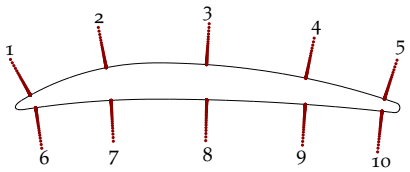


Figure 62: Phase-locked averaged axial velocity plotted at 0%, 25%, 50% and 75%, from top to bottom, of the blade pass period for run 1 ($\psi = 0.422$). Normalized by V_{ref}.



the rotor blade; the stator wake passes through the entire rotor passage and reappears at the stator passage inlet. The same phenomenon is also occurring in run 1, but it is more prominent in run 2 because the lower work coefficient means the wakes undergo less rotation and stretching, and the higher flow coefficient means they spend less time in the passage giving the blade less time to modify the incoming wakes.

The most prominent feature of Figure 64 is that the wakes are not as easily discernible as they were in run 1 and run 2. Figure 57 showed that the pressure side separation bubble results in a stator wake profile without a discernible negative jet region. The rotor wake profile also features a less pronounced negative jet region than runs 1 and 2. As these wakes are then convected to the downstream passage, they appear to be wider and with a smaller velocity deficit relative to the background flow as compared to the wakes seen in Figure 61 and Figure 63. Similar to run 2, the pressure side separation bubble in Figure 64 also appears to be highly phase-dependent. A final noteworthy remark is that run 3 is operating at an even lower reduced frequency than run 2, and hence only two wakes can be seen in a blade passage at any given time.

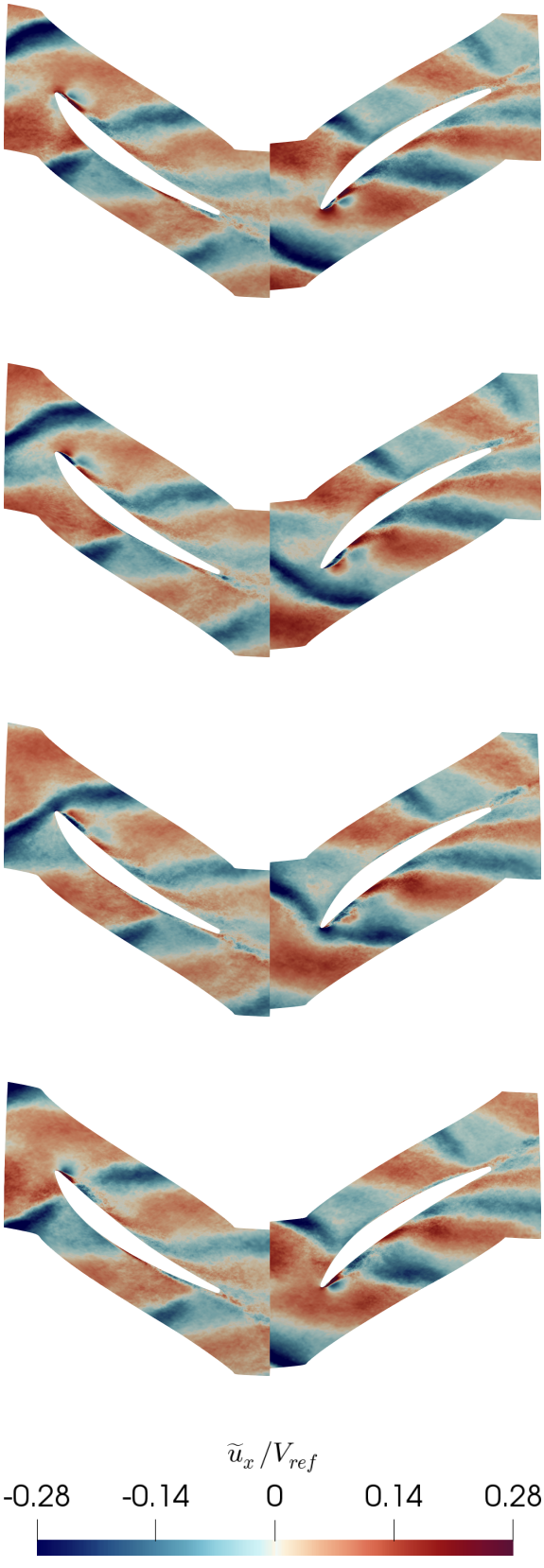


Figure 63: Organized unsteady component of axial velocity plotted at 0%, 25%, 50% and 75%, from top to bottom, of the blade pass period for run 2 ($\psi = 0.204$). Normalized by V_{ref}.

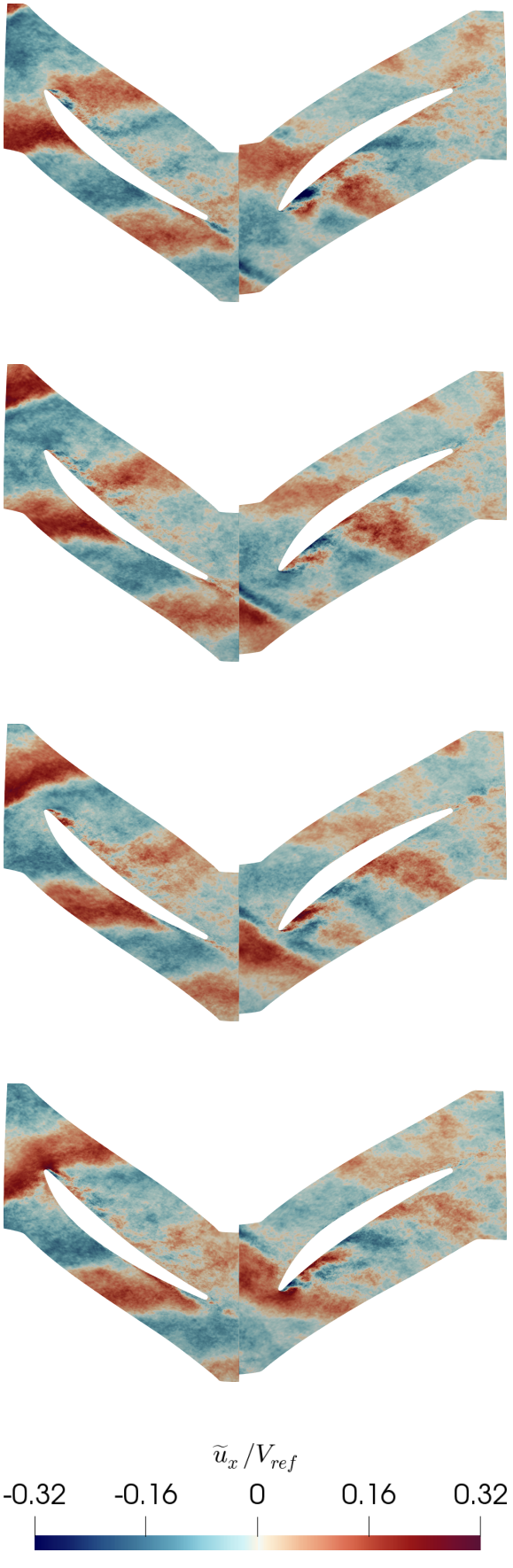
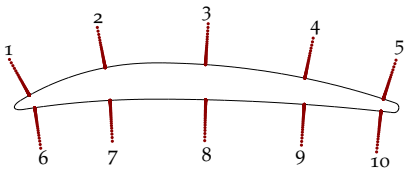


Figure 64: Organized unsteady component of axial velocity plotted at 0%, 25%, 50% and 75%, from top to bottom, of the blade pass period for run 3 ($\psi = 0.036$). Normalized by V_{ref}.



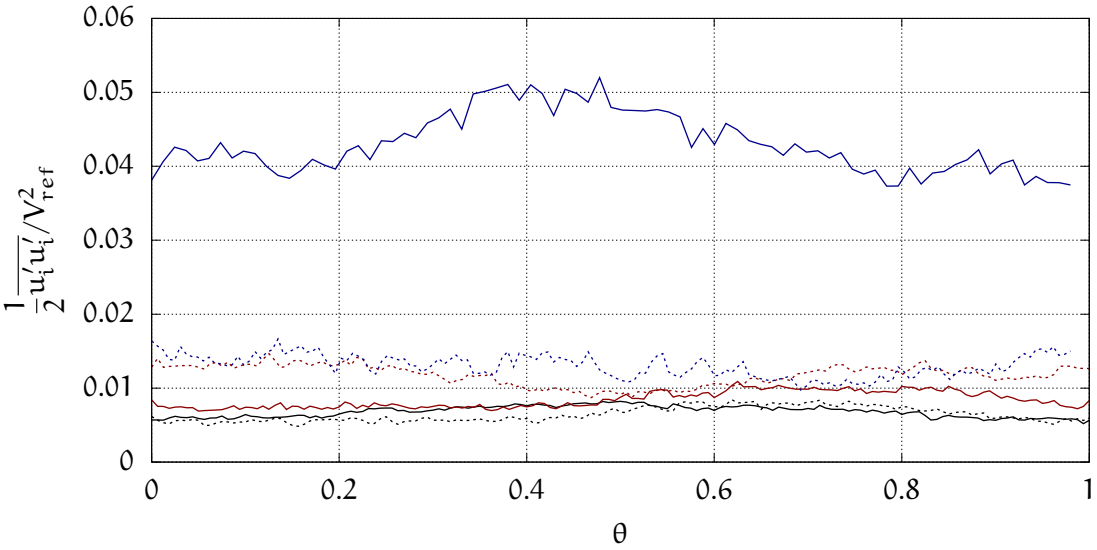


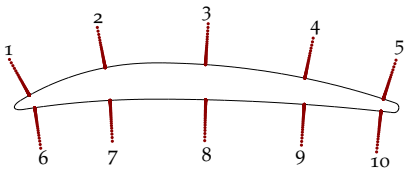
Figure 65: Stator passage inlet profiles of TKE and DKE at mid-span. —— TKE run 1 ····· DKE run 1 ($\psi = 0.422$), —— TKE run 2 ····· DKE run 2 ($\psi = 0.204$), —— TKE run 3 ····· DKE run 3 ($\psi = 0.036$).

4.10 Reynolds and deterministic stress - inlet and outlet profiles

The turbulent kinetic energy (TKE), $\frac{1}{2}\overline{u_i'u_i'}$, and deterministic kinetic energy (DKE), $\frac{1}{2}\overline{\tilde{u}_i\tilde{u}_i}$, profiles at the stator inlet passage at mid-span, extracted using an azimuthal line probe similar to the one used for the wake profiles in Section 4.8, are shown in Figure 65. The inlet profiles have been normalised by the u_τ given in Table 14.

Figure 65 shows that in run 1, the TKE and DKE are very similar at the stator passage inlet. In run 2 however, although they remain comparable in magnitude, the DKE is consistently larger than the TKE. This is corrobated by Evans' measurements of TKE and DKE in a compressor rotor's wake, which showed an increasing DKE as the flow coefficient was increased[28]. However run 3 is a departure from this trend, which shows that TKE is at least twice the magnitude of DKE across the entire inlet passage. As the dominant flow feature of run 3 is the pressure side separation bubble, it is likely that the elevated levels of TKE are due to the flow separation. Evans' data also showed that TKE was significantly greater than DKE when the compressor was operating near-stall[28], supporting the hypothesis that the TKE is larger in the presence of significant separation.

Figure 66 shows the TKE and DKE profiles at the outlet of the stator passage. The DKE profiles show no discernible peak at the region corresponding to the trailing edge, and the level of DKE across the passage is very similar for all three runs. For run 1, the TKE peak is very sharp and falls away quickly to mid-passage levels, where TKE and DKE are of essentially the same magnitude. For run 2, the peak falls away quickly on the suction side of the blade, and is again very similar in magnitude to the DKE. On the pressure side of the blade, the TKE does not fall away quickly and stays elevated above the mid-passage level for a considerable distance. Run 3 shows an even more



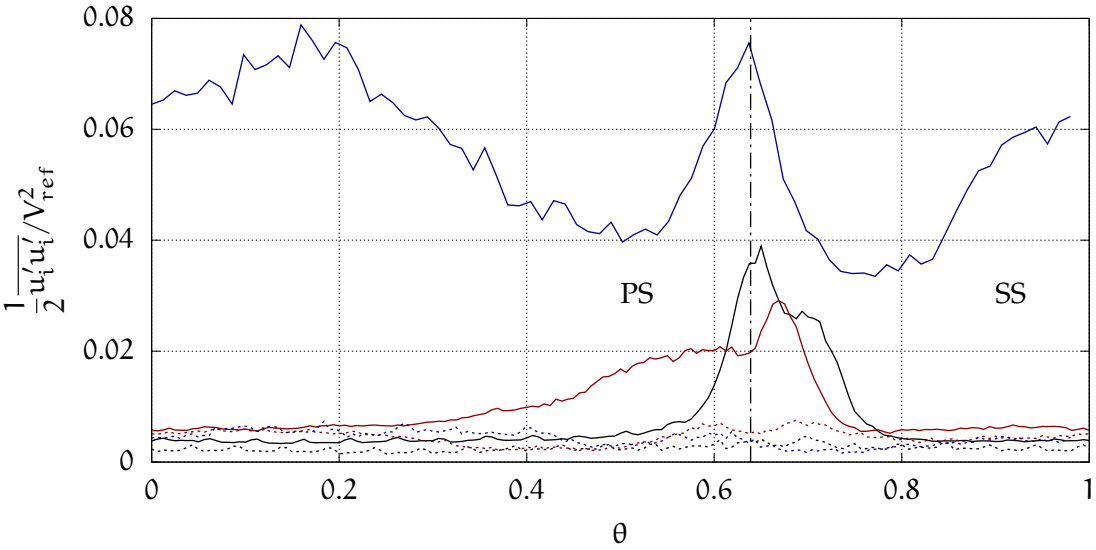


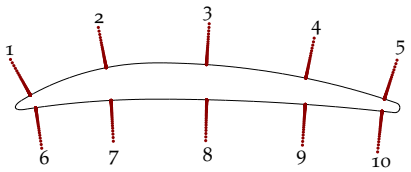
Figure 66: Stator passage outlet profiles of TKE and DKE at mid-span. —— TKE run 1 ····· DKE run 1 ($\psi = 0.422$), —— TKE run 2 ····· DKE run 2 ($\psi = 0.204$), —— TKE run 3 ····· DKE run 3 ($\psi = 0.036$). Dash-dotted line marks the location of the blade trailing edge projected to the passage outlet.

exaggerated version of the same phenomenon, with the TKE levels on the pressure side even exceeding those at the trailing edge peak. Figure 66 thus shows that operating at negative incidence creates elevated levels of TKE in the side of the wake corresponding to the blade pressure side.

It should be noted that the elevated levels of TKE in run 3 in both Figure 65 and Figure 66 are indeed genuine, and not simply an artefact of the normalization procedure; the flow-coefficient and thus V_{ref} is largest in run 3.

Inlet profiles for the Reynolds, $\overline{u_s' u_n'}$, and deterministic, $\overline{\tilde{u}_s \tilde{u}_n}$, shear stress are shown in Figure 67 and Figure 68 respectively. For the stresses at the inlet, the streamwise direction is rotated to be aligned with the leading edge metal angle. Concomitantly, the streamwise direction for the stresses at the outlet is aligned with the trailing edge metal angle. At the stator inlet, the Reynolds shear stress for runs 1 and 2 is essentially zero across the entire passage width. The deterministic shear stress however is significant at the passage inlet. This is most clearly seen in the profile of $\overline{\tilde{u}_s \tilde{u}_n}$ for run 2, which is zero at the region corresponding to the rotor trailing edge but very large everywhere else. In run 3, both the Reynolds and deterministic shear stress are non-zero throughout the passage width and are similar in magnitude.

At the passage outlet, the Reynolds shear stress profiles in Figure 68 for both runs 1 and 2 exhibit the expected profile in the near-wake region of an airfoil as reported by Hah et al[41]: zero across most of the pitch with a sharp dual peak around the region corresponding to the trailing edge. The Reynolds shear stress profile shows the same trend as the TKE in run 2, and takes longer to decay to zero on the pressure side of the blade. The $\overline{u_s' u_n'}$ profile for run 3 also shows a peak at the trailing edge, but it is uni-directional. A noteworthy feature of the Reynolds shear stress profiles is that as the



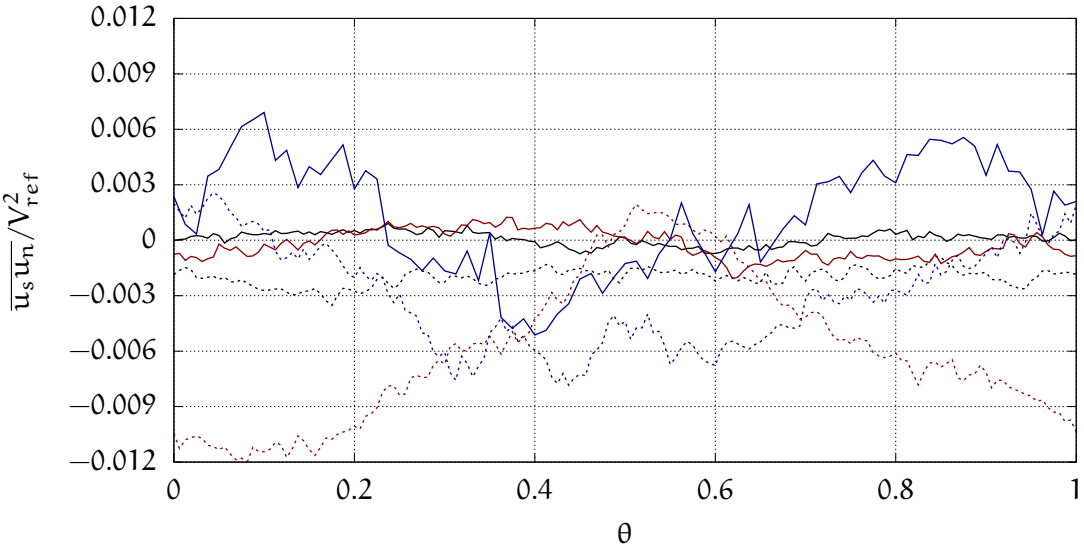


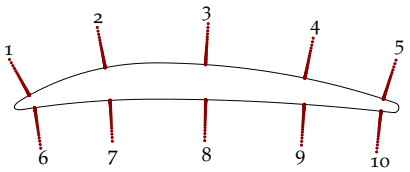
Figure 67: Stator passage inlet profiles of Reynolds and deterministic shear stress. —— $\overline{u_s' u_n'}/u_\tau^2$ run 1 ····· $\overline{\tilde{u}_s \tilde{u}_n}/u_\tau^2$ run 1 ($\psi = 0.422$), —— $\overline{u_s' u_n'}/u_\tau^2$ run 2 ····· $\overline{\tilde{u}_s \tilde{u}_n}/u_\tau^2$ run 2 ($\psi = 0.204$), —— $\overline{u_s' u_n'}/u_\tau^2$ run 3 ····· $\overline{\tilde{u}_s \tilde{u}_n}/u_\tau^2$ run 3 ($\psi = 0.036$).

angle of incidence decreases from runs 1 to 3, the peak of $\overline{u_s' u_n'}$ occurs at a lower value of θ.

The deterministic shear stress profile at the passage outlet for run 1 in Figure 68 appears to be zero throughout the passage width. In the case of run 3, $\overline{\tilde{u}_s \tilde{u}_n}$ is non-zero for parts of the passage width but it shows no peak the trailing edge and is much smaller than the Reynolds shear stress. The profile for $\overline{\tilde{u}_s \tilde{u}_n}$ for run 2 is again much smaller than the Reynolds shear stress, but it does exhibit a noticeable peak at the trailing edge.

Jelly et al measured turbulent and deterministic statistics in the Deverson compressor, operating close to its design point, downstream of the stator blade[52]. Although a repeating stage computation using modified blade counts does not truly represent the operating conditions of the Deverson compressor, the data reported in[52] can still be compared qualitatively to the current results.

Jelly et al compared the phase-locked averaged Reynolds shear stress, $\langle u_s' u_n' \rangle$, and the unsteady deterministic shear stress, $\tilde{u}_s \tilde{u}_n$. The authors found that while the two stresses had similar peak magnitudes throughout the blade-pass cycle, the deterministic shear stress varied considerably more than the Reynolds shear stress[52]. The Reynolds shear stress in Figure 69 also undergoes very little variation throughout the blade-pass cycle. The deterministic shear stress varies considerably, ranging from zero throughout the passage to being a of a similar magnitude to the Reynolds shear stress. Interestingly, only the negative peak of $\tilde{u}_s \tilde{u}_n$ reaches a similar value to $\langle u_s' u_n' \rangle$, suggesting the deterministic shear stress does not exhibit the same dual-peak reported by Hah et al for the Reynolds shear stress[41].



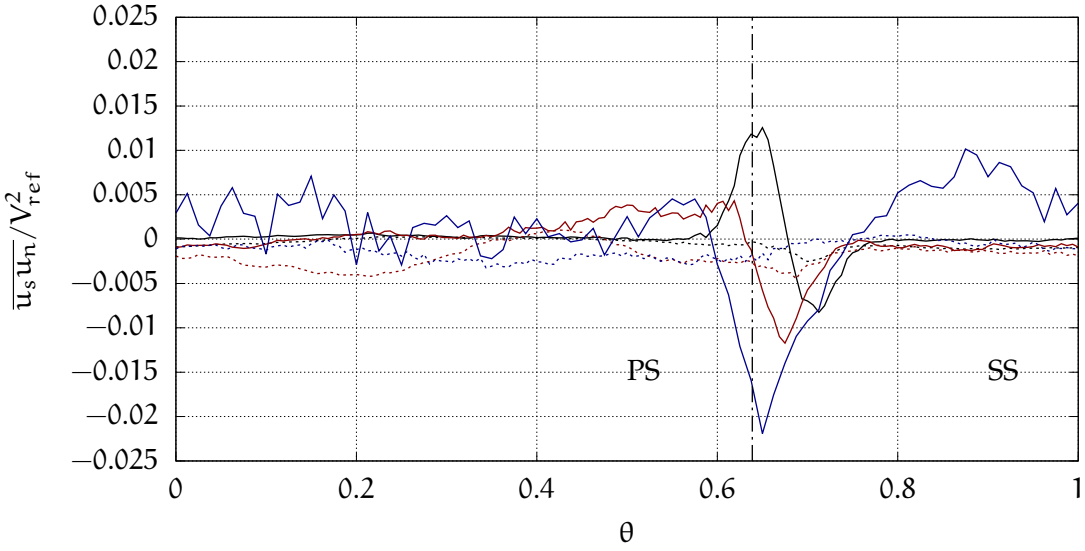


Figure 68: Stator passage outlet profiles of Reynolds and deterministic shear stress. —— $\overline{u_s' u_n'}/u_\tau^2$ run 1 ····· $\overline{\tilde{u}_s \tilde{u}_n}/u_\tau^2$ run 1 ($\psi = 0.422$), —— $\overline{u_s' u_n'}/u_\tau^2$ run 2 ····· $\overline{\tilde{u}_s \tilde{u}_n}/u_\tau^2$ run 2 ($\psi = 0.204$), —— $\overline{u_s' u_n'}/u_\tau^2$ run 3 ····· $\overline{\tilde{u}_s \tilde{u}_n}/u_\tau^2$ run 3 ($\psi = 0.036$). Dash-dotted line marks the location of the blade trailing edge projected to the passage outlet.

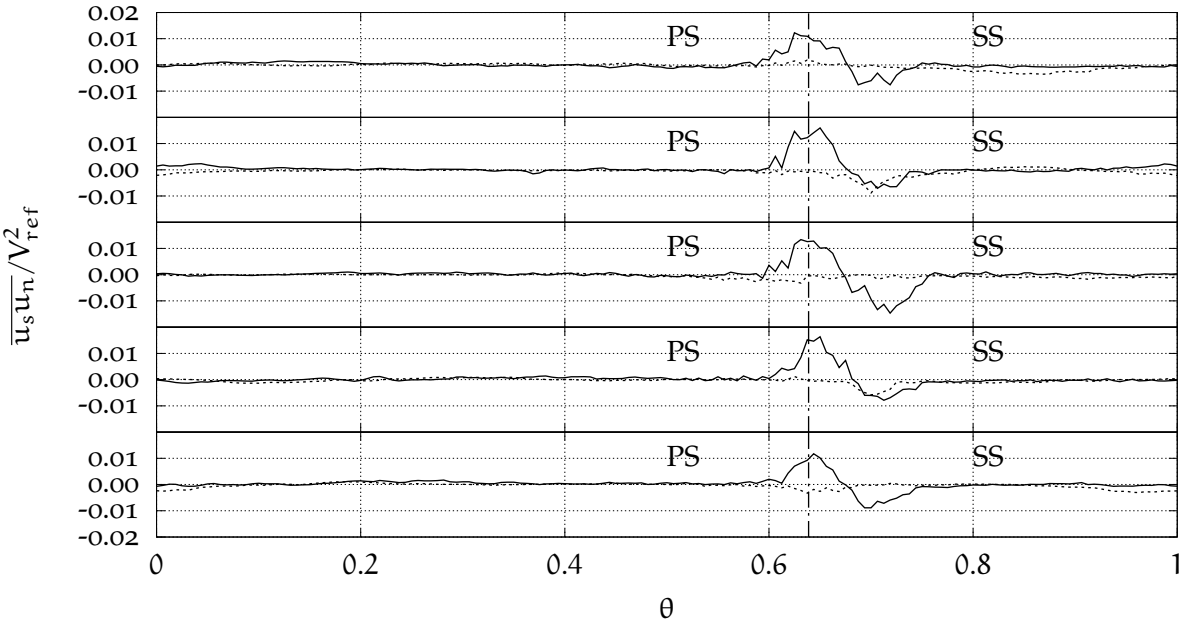


Figure 69: Stator passage outlet profiles of Reynolds and deterministic shear stress at 0%, 20%, 40%, 60% and 80% of the blade-pass cycle, time increasing from bottom to top. —— $\langle u_s' u_n' \rangle / u_\tau^2$ run 1 ····· $\tilde{u}_s \tilde{u}_n / u_\tau^2$ run 1 ($\psi = 0.422$). Dash-dotted line marks location of the blade trailing edge projected to the passage outlet.

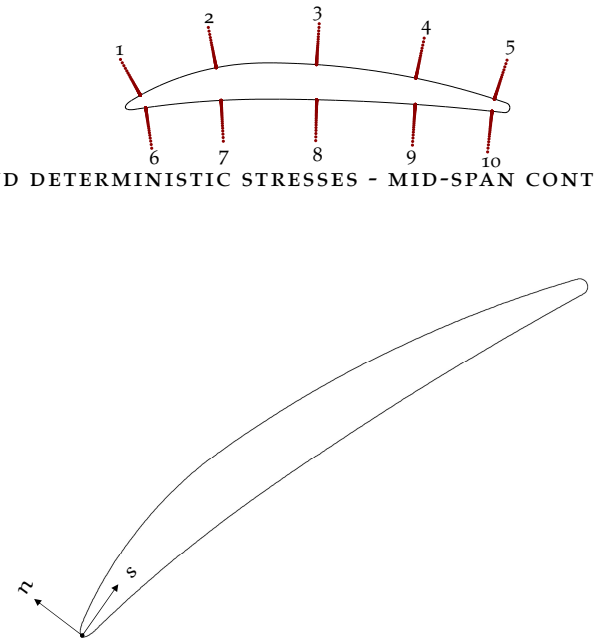


Figure 70: Coordinate system aligned with the mean-flow at the inlet of the passage.

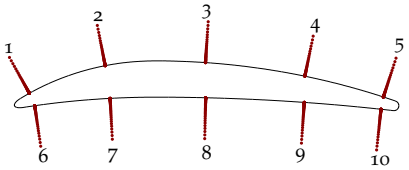
4.11 Reynolds and deterministic stresses - mid-span contours and boundary layer profiles

Contour-plots at mid-span of the six components of the RS tensor (it is symmetric) are shown in Figure 71 for run 1. In order to highlight how the stresses develop through the blade passage, they have been plotted in a coordinate system aligned with the azimuthally averaged mean flow direction at the passage inlet. An example of such a coordinate system is illustrated in Figure 70 for the case of zero incidence. It should be noted that u_θ, rather than u_y, is rotated to form u_n; a transformation of Cartesian to cylindrical coordinates is performed prior to the rotation illustrated in Figure 70.

The regions where the Reynolds normal stresses, and hence the TKE, are the highest are the momentum boundary layers, most clearly visible on the suction side of the blade, in the trailing edge separation region and in the wake. Peak $\overline{u'_s u'_s}$, $\overline{u'_n u'_n}$ and $\overline{u'_r u'_r}$ occur near mid-chord on the suction surface, near probe 3 in Figure 72. This approximately coincides with the point at which the blade curvature switches from convex to concave. The Reynolds stresses are also large in the wake region. Interestingly, there is a small gap between the blade trailing edge and the region of elevated Reynolds stresses in the wake. This suggests that it is the wake mixing that creates the high levels of Reynolds stresses as opposed to the trailing edge separation.

It should be noted that whereas the mid-span contour plots in Figure 71 have been normalized using the blade-averaged u_τ values reported in Table 14, the blade boundary layer profiles in Figure 72 are normalized with the local value of u_τ. As such, the high values of the Reynolds stresses at probe 5 in Figure 72 are purely due to a small u_τ because the flow locally is near the point of separation. It is worth remembering that like all the other boundary layer profile plots shown in the current chapter, the profiles of the RS tensor shown in Figure 72 are plotted in the transformed coordinate system illustrated in Figure 39.

The profiles of the Reynolds normal stresses on the later stages of the suction side in Figure 72, probes 3 to 5, qualitatively match the expected profiles of adverse pressure gradient boundary layer flows, as shown in the work of Spalart et al[113] and Nagano et al[87]. $\overline{u'_s u'_s}$ has a pronounced peak near the wall at $\eta^+ \approx 10$. After this peak, the stress drops slightly but remains significant until $\eta^+ \approx 10$, after which it drops away



rapidly. The largest adverse pressure gradient occurs at probe 5, and here the maximum value of $\overline{u'_s u'_s}$ occurs at $\eta^+ = 100$. This feature was also visible in the results of Nagano et al at large adverse pressure gradients[87]. $\overline{u'_w u'_w}$ and $\overline{u'_n u'_n}$ also match the expected profiles, and feature a rounded profile, devoid of a sharp peak, with the maximum value occurring near $\eta^+ = 100$. The profiles on the pressure side of the blade match those of boundary layers operating in favourable pressure gradients, as seen in[113]. These are characterized by a sharp peak at $\eta^+ \approx 20$, and the profile falling away rapidly at either side of it.

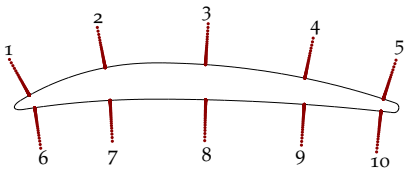
The Reynolds shear stresses are also most active in the momentum boundary layer and wake region, with $\overline{u'_s u'_n}$ showing a discernible dual peak in the blade wake region. The boundary layer plots extracted at probes 3 to 5 also match Nagano et al's[87] profiles of the Reynolds shear stress in an adverse pressure gradient boundary layer. The peak occurs much further away from the wall, at $\eta^+ \approx 100$, compared to $\overline{u'_s u'_s}$, and the Reynolds shear stress rapidly goes down to zero after the peak. Moreover, Nagano et al found the peak of $\overline{u'_s u'_n}$ moved away from the wall with an increasing pressure gradient[87], which is also the case when comparing the Reynolds shear stress profiles between probes 3 and 4. An interesting feature of the boundary layer profiles is that on the suction side of the blade, $\overline{u'_s u'_n}$ is the only significant shear stress, but on the pressure side $\overline{u'_s u'_w}$ and $\overline{u'_s u'_n}$ are equal in magnitude up until $\eta^+ = 10$ at probes 8, 9 and 10.

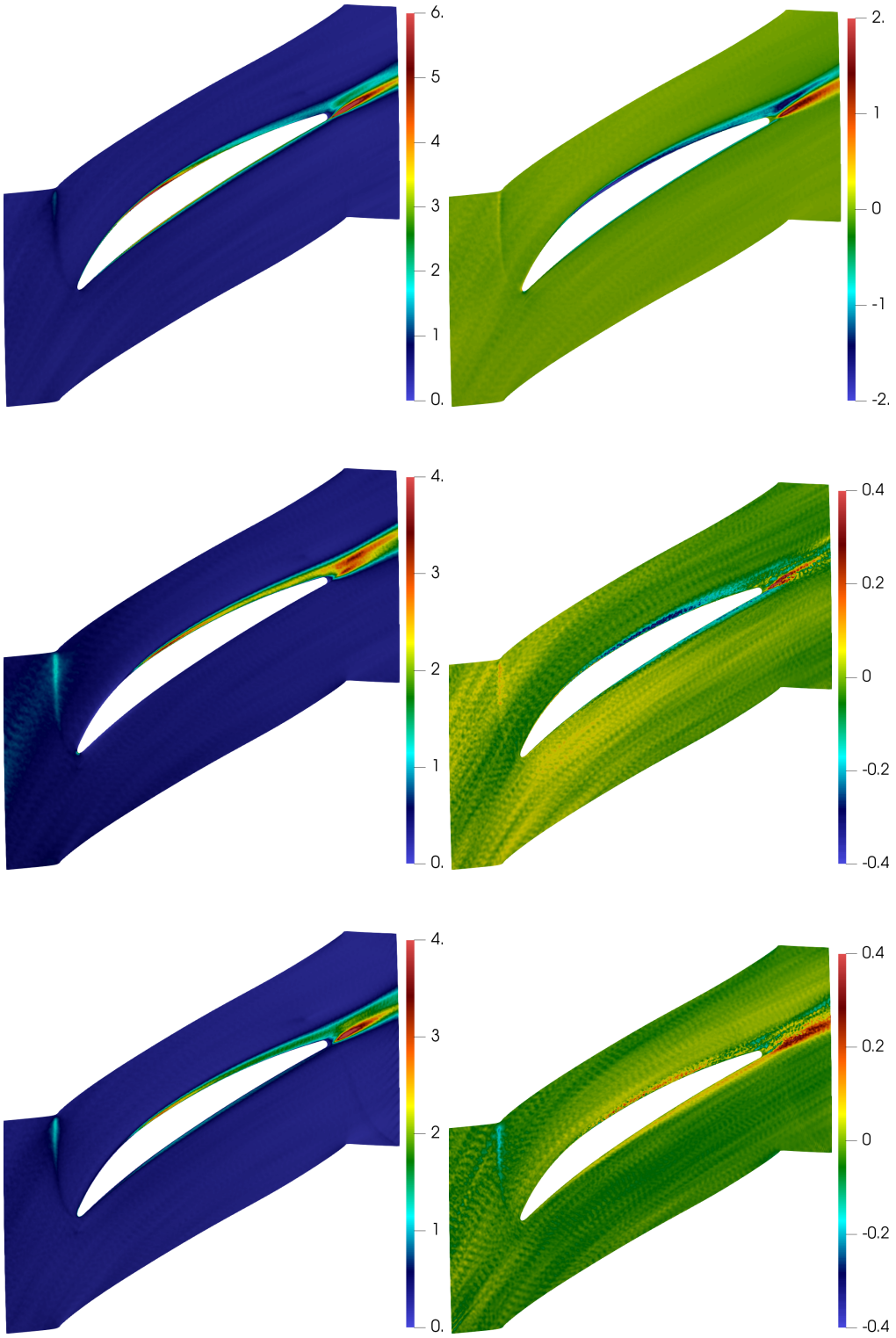
The DS component contour plots in Figure 73 and boundary layer plots in Figure 74 show a markedly different behaviour to the RS components. Whereas the Reynolds normal stresses were most active in the suction side momentum boundary layer, the deterministic normal stresses appear to rapidly attenuate where the momentum boundary layer begins to grow. This can also be seen in the boundary layer plots in Figure 74. At probe 2, $\overline{\tilde{u}_s \tilde{u}_s}$ shows a sharp dip at $\eta^+ = 20$, whereas $\overline{u'_s u'_s}$ peaked at $\eta^+ = 20$ at probe 2 in Figure 72. The same feature can also be seen at $\eta^+ = 20$ in the profiles of $\overline{\tilde{u}_s \tilde{u}_s}$ and $\overline{u'_s u'_s}$ at probe 7 on the pressure side. Probe 3 also shows $\overline{\tilde{u}_s \tilde{u}_s}$ peaking at $\eta^+ = 100$, at which point $\overline{u'_s u'_s}$ begins to drop away. It should be noted that the large values of the deterministic stress at probe 5 in Figure 74 are purely due to the low level of u_τ there.

The contour plots in Figure 73 also show that all six components of the DS tensor show a clearly distinguishable peak around mid-chord on the suction surface, where the curvature switches from concave to convex. Most of the RS tensor components were also significant here, suggesting a region where the two stress fields interact.

Figure 73 also shows that the elevated levels of DKE at the passage inlet seen in Figure 65 were almost entirely due to $\overline{\tilde{u}_n \tilde{u}_n}$. Interestingly, $\overline{\tilde{u}_n \tilde{u}_n}$ drops away very quickly downstream of the passage inlet and is zero in all the boundary layer profiles in Figure 74. Other interesting features of Figure 73 are the dual peaks of $\overline{\tilde{u}_s \tilde{u}_n}$ at the blade leading edge, and the fact that $\overline{\tilde{u}_n \tilde{u}_r}$ is small in magnitude but active over the entire blade passage.

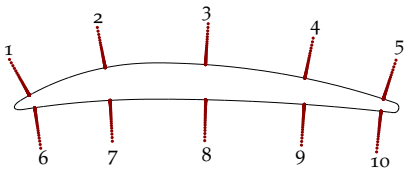
The DS contour plots in Figure 73 corroborate the findings of Uzol et al[124]. In their PIV measurements at mid span of a low-speed compressor operating at its design point, Uzol et al found that the DKE was large at the stator passage inlet, but decayed rapidly around the blade, similar to $\overline{\tilde{u}_n \tilde{u}_n}$ in Figure 73. As for the deterministic shear stress $\overline{\tilde{u}_s \tilde{u}_n}$, Uzol et al measured much lower levels on the pressure side as compared to the passage inlet, but on the suction side $\overline{\tilde{u}_s \tilde{u}_n}$ remained significant outside of the immedi-





$\overline{u_s' u_s'}$	$\overline{u_s' u_n'}$
$\overline{u_n' u_n'}$	$\overline{u_s' u_r'}$
$\overline{u_r' u_r'}$	$\overline{u_n' u_r'}$

Figure 71: Contour plots at mid-span of components of the RS tensor for run 1 stator ($\psi = 0.422$). Coordinate system aligned with the mean-flow at passage inlet. Normalized by global u_τ^2.



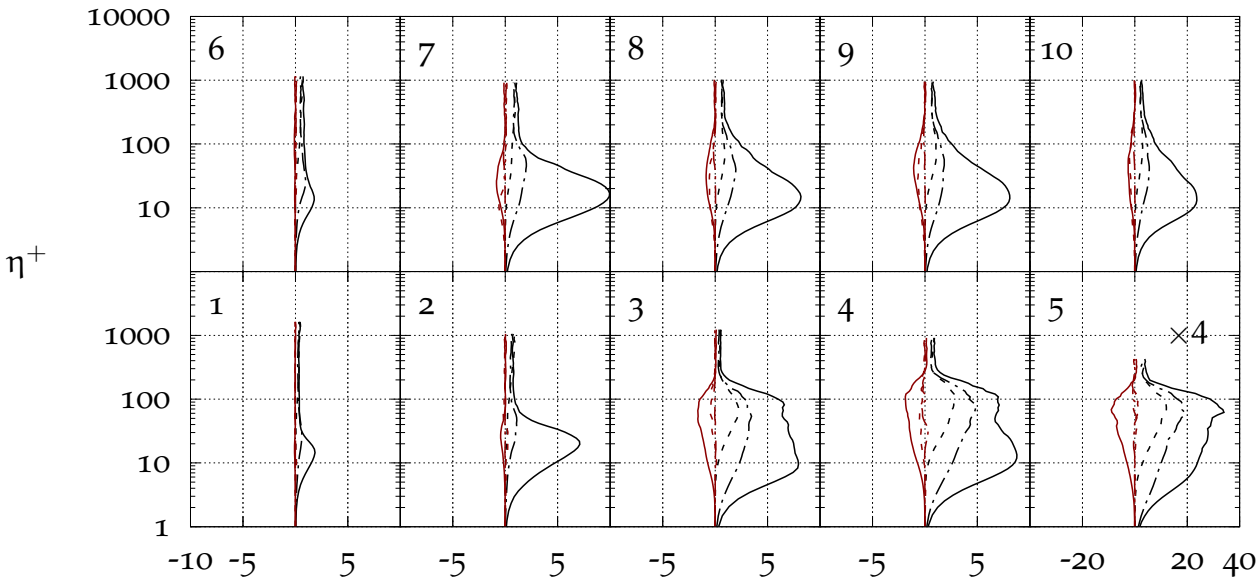


Figure 72: RS boundary layer profiles in inner coordinates for run 1 stator ($\psi = 0.422$). Normalized by local u_τ. —— $\overline{u_s' u_s'}/u_\tau^2$ - - - $\overline{u_n' u_n'}/u_\tau^2$ -·- $\overline{u_w' u_w'}/u_\tau^2$ —— $\overline{u_s' u_n'}/u_\tau^2$ - - - $\overline{u_s' u_w'}/u_\tau^2$ -·- $\overline{u_n' u_w'}/u_\tau^2$. Probe number in top-left corner.

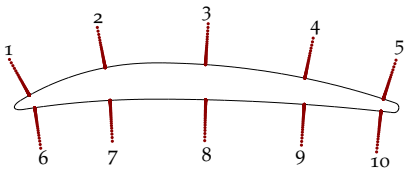
ate vicinity of the blade[124]. The same features can also be seen in the $\overline{\tilde{u}_s \tilde{u}_n}$ contours in Figure 73, except for the fact that in the current results, $\overline{\tilde{u}_s \tilde{u}_n}$ is only significant over the initial part of the suction side surface.

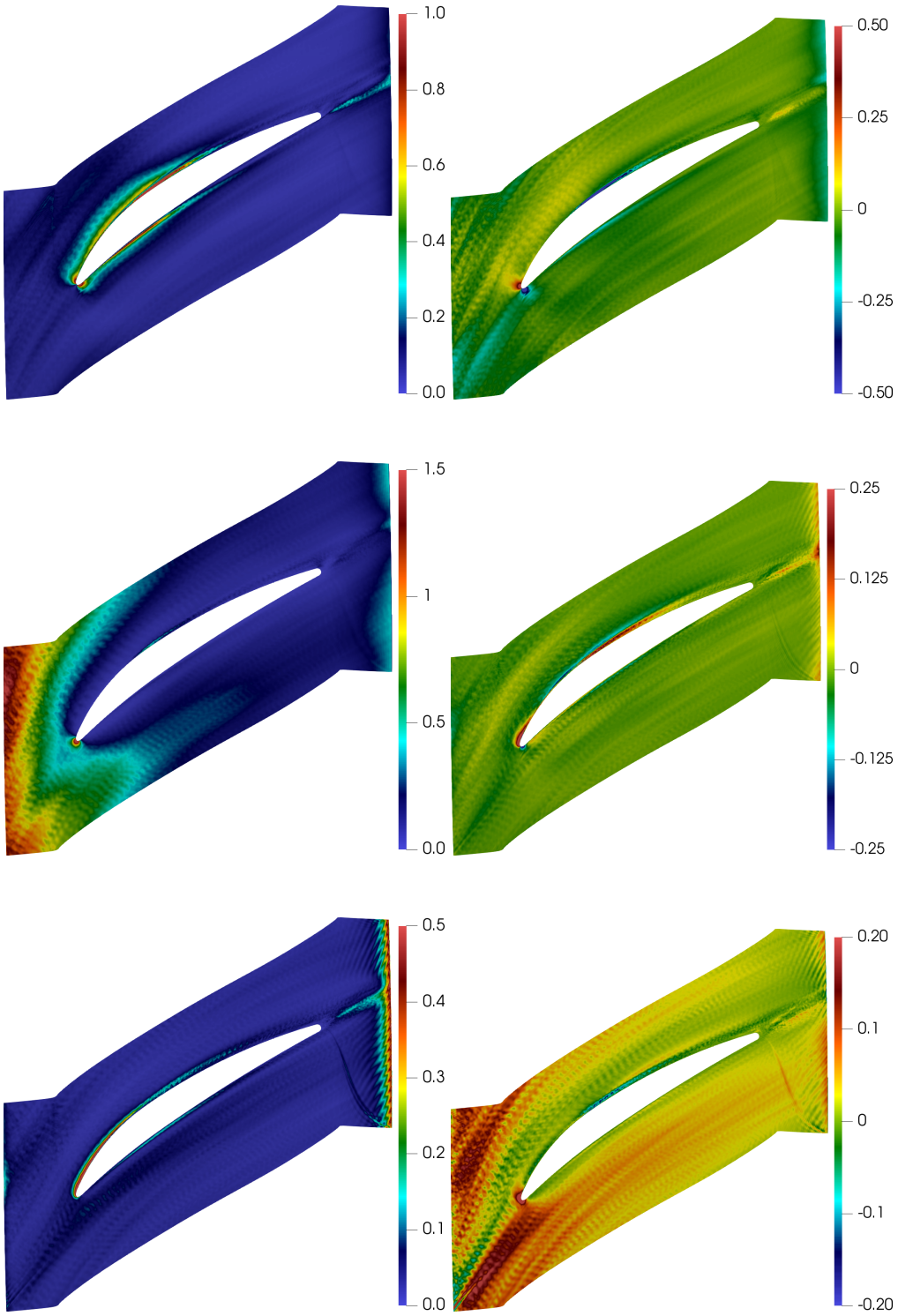
The RS component contour plots at mid-span for run 2 are shown in Figure 75. Whereas in run 1 the Reynolds normal stresses were largest on the suction side of the blade, in run 2 they are largest on the pressure side. The levels of RS are highest in the pressure side separation bubble, but remain significant over the entire pressure side surface. The Reynolds stresses are also large in the wake.

Interestingly, the first Reynolds shear stress, $\overline{u_s' u_n'}$, is as active in the suction side boundary layer in run 2 as it was in run 1. The second Reynolds shear stress, $\overline{u_s' u_r'}$, is also noteworthy because although the largest values do indeed occur in the pressure side separation bubble, $\overline{u_s' u_r'}$ is non-zero over almost the entirety of the suction side passage. This was not the case in run 1. Finally, both $\overline{u_s' u_r'}$ and $\overline{u_n' u_r'}$ show dual-peaks in the pressure side separation bubble, whereas $\overline{u_s' u_n'}$ shows a uni-directional peak.

Another notable feature of Figure 75 is the elevated level of $\overline{u_s' u_n'}$ at the flow stagnation point, which extends to the edge of the domain. A similar feature was visible in Figure 71, but it was weaker and the line extending from the leading edge to the edge of the domain was curved. The fact that the shape of this feature differs between runs, coupled with the elevated levels at the flow stagnation point in Figure 75 suggests that this feature is a consequence of the upstream wake interacting with the leading edge and front part of the blade.

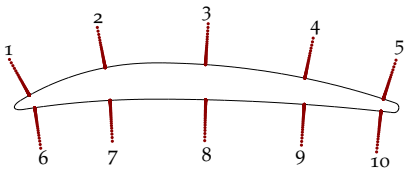
The suction side boundary layer plots in Figure 76 reveal profiles corresponding to a weaker adverse pressure gradient than those for run 1. This is most easily visible in the profiles for $\overline{u_s' u_s'}$ from probes 3 to 5, which drop at a faster rate from $\eta^+ = 10$ to $\eta^+ = 100$ than those in Figure 72. The RS profiles at the first pressure side probe in





$\widetilde{\overline{u}_s\widetilde{u}_s}$	$\widetilde{\overline{u}_s\widetilde{u}_n}$
$\widetilde{\overline{u}_n\widetilde{u}_n}$	$\widetilde{\overline{u}_s\widetilde{u}_r}$
$\widetilde{\overline{u}_r\widetilde{u}_r}$	$\widetilde{\overline{u}_n\widetilde{u}_r}$

Figure 73: Contour plots at mid-span of components of the DS tensor for run 1 stator ($\psi = 0.422$). Coordinate system aligned with the mean-flow at passage inlet. Normalized by global u_τ^2.



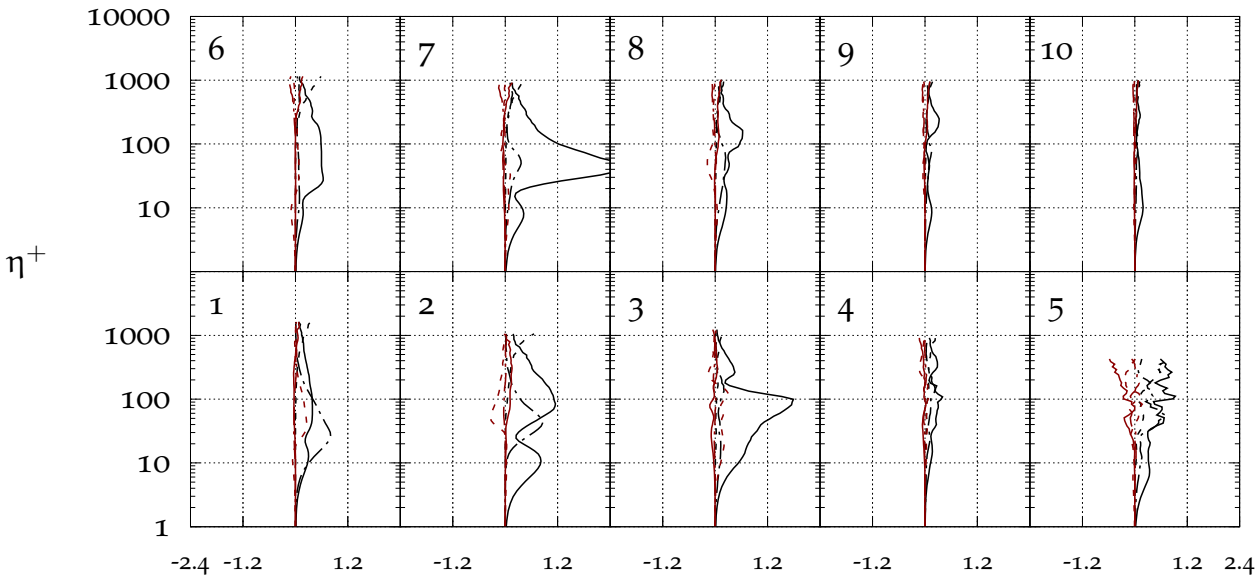


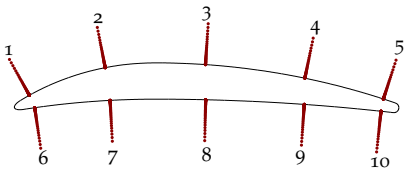
Figure 74: DS boundary layer profiles in inner coordinates for run 1 stator ($\psi = 0.422$). Normalized by local u_τ. —— $\overline{\tilde{u}_s\tilde{u}_s}/u_\tau^2$ - - - $\overline{\tilde{u}_n\tilde{u}_n}/u_\tau^2$ -·-·- $\overline{\tilde{u}_w\tilde{u}_w}/u_\tau^2$ —— $\overline{\tilde{u}_s\tilde{u}_n}/u_\tau^2$ - - - $\overline{\tilde{u}_s\tilde{u}_w}/u_\tau^2$ -·-·- $\overline{\tilde{u}_n\tilde{u}_w}/u_\tau^2$. Probe number in top-left corner.

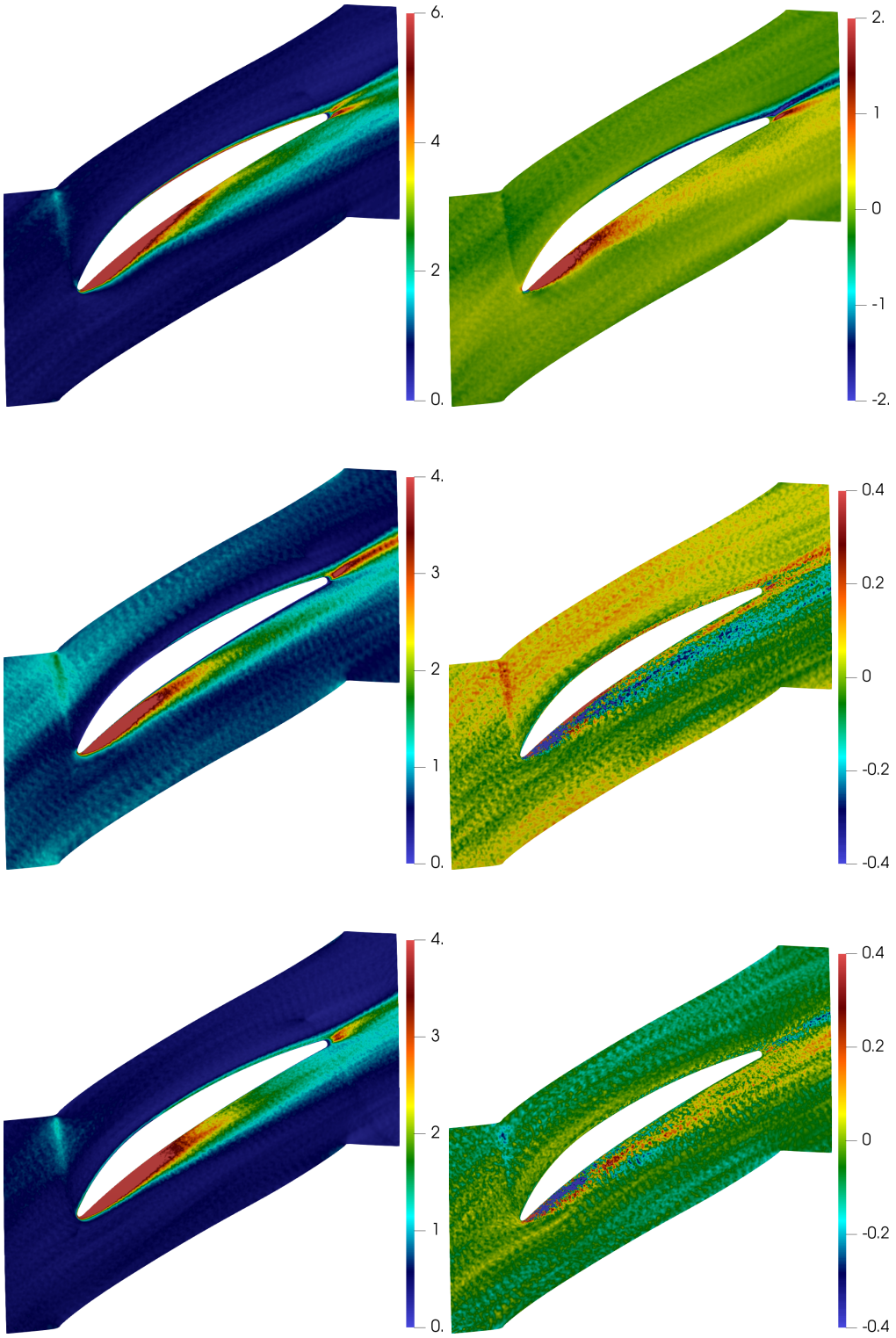
run 2 have a similar structure to those at probe 5 in run 1, and both boundary layers are operating under a large adverse pressure gradient. All three of the Reynolds normal stresses, as well as $\overline{u_s'u_n'}$, peak between $\eta^+ = 100 - 200$. The adverse pressure gradient persists until probe 9. At probe 10, where the boundary layer is operating under a favourable pressure gradient, there is a drop in the Reynolds stresses above $\eta^+ = 10$, and the profiles begin to develop a sharper peak.

Figure 77 shows that the deterministic stresses in run 2 are generally much larger than in run 1. $\overline{\tilde{u}_s\tilde{u}_s}$ shows the same elevated levels on the front of the suction side surface. It is missing however the peak value of $\overline{\tilde{u}_s\tilde{u}_s}$ at mid-chord on the suction side. On the pressure side however, $\overline{\tilde{u}_s\tilde{u}_s}$ is much larger than in run 1. The high levels of $\overline{\tilde{u}_s\tilde{u}_s}$ appear to originate from the separation bubble. Figure 77 also shows that the behaviour of $\overline{\tilde{u}_r\tilde{u}_r}$ on the suction side in run 2 is similar to that in run 1, but the levels of $\overline{\tilde{u}_r\tilde{u}_r}$ on the pressure side are greater than in run 1.

The behaviour of $\overline{\tilde{u}_n\tilde{u}_n}$ is noticeably different in run 2 as compared to run 1. In run 2, $\overline{\tilde{u}_n\tilde{u}_n}$ remains significant outside the immediate vicinity of the blade throughout the entire passage, whereas in run 1 this was only the case in the front half of the passage. Moreover, in Figure 73 the only part of the blade surface where $\overline{\tilde{u}_n\tilde{u}_n}$ was active was the leading edge of the blade, whereas Figure 77 also shows significant levels of $\overline{\tilde{u}_n\tilde{u}_n}$ in the pressure side separation bubble.

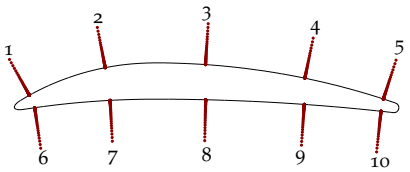
$\overline{\tilde{u}_s\tilde{u}_n}$ in Figure 77 shows the same dual peak around the blade leading edge as it did in Figure 73, but the magnitude is greater. The leading edge peak on the pressure side is followed by an even larger and opposite signed peak in the separation bubble. $\overline{\tilde{u}_s\tilde{u}_n}$ is also very large at the passage inlet, as was seen in Figure 67. $\overline{\tilde{u}_s\tilde{u}_r}$ shows the same peak near the leading edge on the suction side as run 1, but whereas the peak was localized in run 1, in run 2 it extends over the front half of the blade surface. The third deterministic





$\overline{u_s' u_s'}$	$\overline{u_s' u_n'}$
$\overline{u_n' u_n'}$	$\overline{u_s' u_r'}$
$\overline{u_r' u_r'}$	$\overline{u_n' u_r'}$

Figure 75: Contour plots at mid-span of components of the RS tensor for run 2 stator ($\psi = 0.204$). Coordinate system aligned with the mean-flow at passage inlet. Normalized by global u_τ^2.



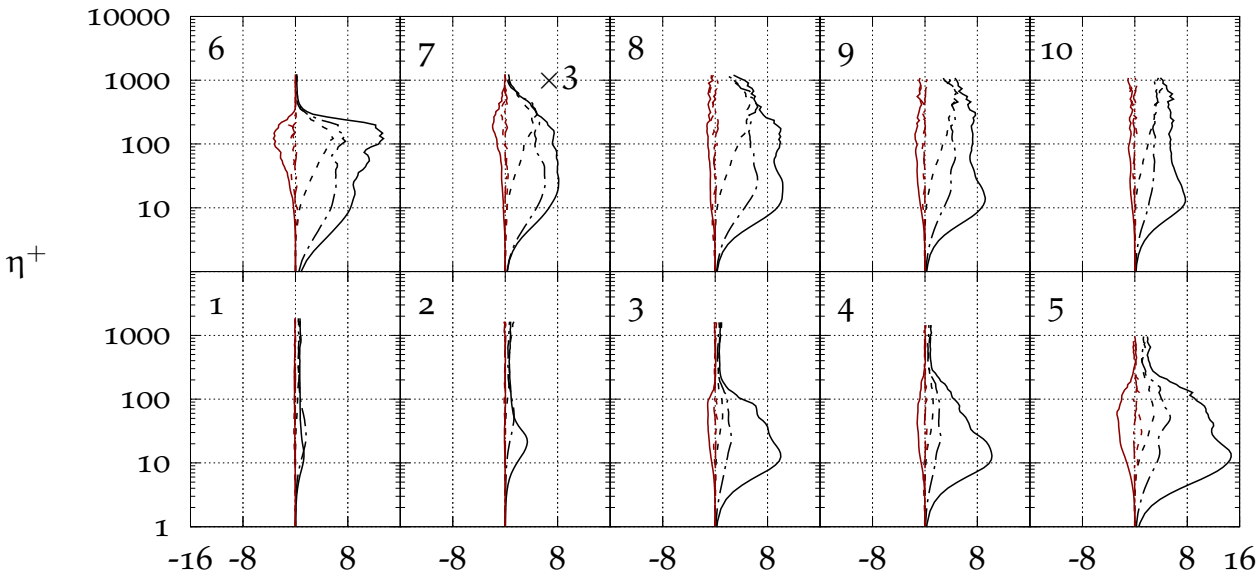


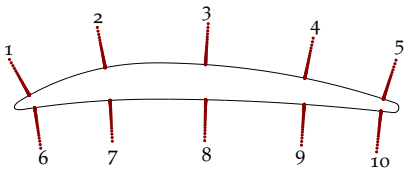
Figure 76: RS boundary layer profiles in inner coordinates for run 2 stator ($\psi = 0.204$). Normalized by local u_τ. — $\overline{u'_s u'_s}/u_\tau^2$ - - - $\overline{u'_n u'_n}/u_\tau^2$ -·- $\overline{u'_w u'_w}/u_\tau^2$ — $\overline{u'_s u'_n}/u_\tau^2$ - - - $\overline{u'_s u'_w}/u_\tau^2$ -·- $\overline{u'_n u'_w}/u_\tau^2$. Probe number in top-left corner.

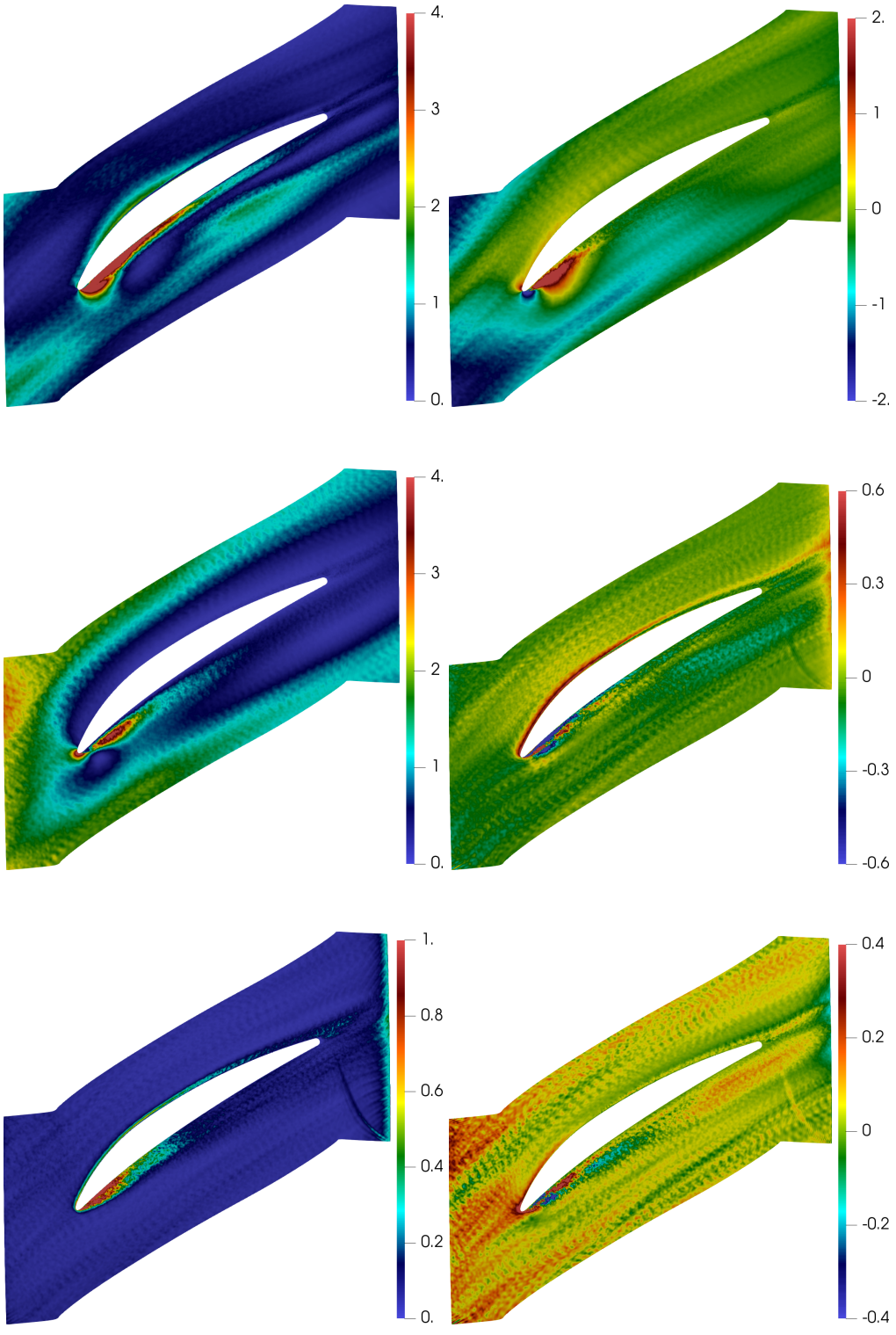
shear stress, $\overline{\tilde{u}_n \tilde{u}_r}$, is again non-zero throughout almost the entire blade passage, just like it was in run 1.

The DS boundary layer profiles in Figure 78 confirm the higher levels of activity in run 2. Moreover, the DS profiles often appear to peak at the same location as the RS profiles in Figure 76, which was seldom the case in run 1. On the suction side of the blade, the DS profiles are only significant from probes 1 to 3, similar to Figure 74. At probe 2 in Figure 78, $\overline{\tilde{u}_s \tilde{u}_s}$ peaks at $\eta^+ \approx 100$, whereas $\overline{u'_s u'_s}$ at probe 2 peaks at $\eta^+ = 20$. At probe 3, $\overline{\tilde{u}_s \tilde{u}_s}$ peaks at $\eta^+ = 10$, the same location of the peak in the corresponding Reynolds stress. However $\overline{\tilde{u}_s \tilde{u}_s}$ drops away very quickly above $\eta^+ = 10$, whereas $\overline{u'_s u'_s}$ stays significant until $\eta^+ = 100$. Interestingly, as the streamwise Reynolds normal stress attenuates above $\eta^+ = 100$, the streamwise deterministic normal stress grows. Another noteworthy feature of the DS profiles from probes 1 to 3 are the rising levels of $\overline{\tilde{u}_n \tilde{u}_n}$ as the freestream is approached.

Probes 6 to 10 in Figure 78 show much greater levels of deterministic stresses than the pressure side probes in run 1 (Figure 74, where only probe 7 showed any significant activity). In probe 6, both $\overline{\tilde{u}_s \tilde{u}_s}$ and $\overline{\tilde{u}_s \tilde{u}_n}$ show large and localized peaks at $\eta^+ \approx 200$, the same location where the corresponding RS profiles peaked in Figure 76. $\overline{\tilde{u}_s \tilde{u}_s}$ remains elevated throughout the rest of the pressure side of the blade, but never develops the near-wall peak at $\eta^+ = 10$ that the Reynolds stresses developed. The profiles of $\overline{\tilde{u}_s \tilde{u}_s}$ from probe 7 onwards also exhibit a pronounced dip at $\eta^+ = 500$, before rising quickly near the end of the probe. $\overline{\tilde{u}_n \tilde{u}_n}$ is also significant at this location, but it doesn't show any dips and just builds monotonically towards the freestream end of the probe.

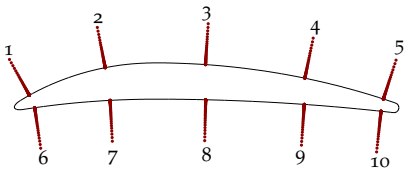
As Figure 79 and Figure 80 show, the Reynolds stresses in run 3 are dominated by the pressure side separation bubble to an even greater extent than in run 2. The peak value of all three Reynolds normal stresses occurs at probe 6 at $\eta^+ = 200$. At the downstream





$\widetilde{\overline{u}_s\widetilde{u}_s}$	$\widetilde{\overline{u}_s\widetilde{u}_n}$
$\widetilde{\overline{u}_n\widetilde{u}_n}$	$\widetilde{\overline{u}_s\widetilde{u}_r}$
$\widetilde{\overline{u}_r\widetilde{u}_r}$	$\widetilde{\overline{u}_n\widetilde{u}_r}$

Figure 77: Contour plots at mid-span of components of the DS tensor for run 2 stator ($\psi = 0.204$). Coordinate system aligned with the mean-flow at passage inlet. Normalized by global u_τ^2.



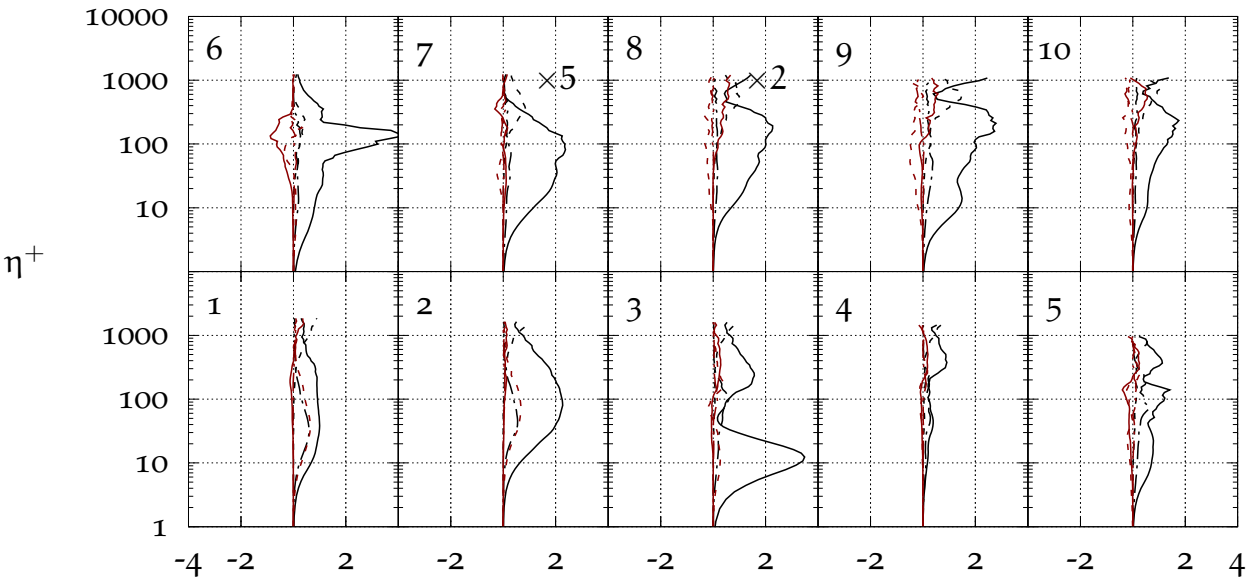


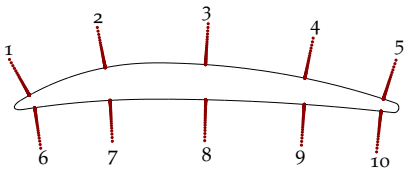
Figure 78: DS boundary layer profiles in inner coordinates for run 2 stator ($\psi = 0.204$). Normalized by local u_τ. —— $\overline{\tilde{u}_s\tilde{u}_s}/u_\tau^2$ - - - $\overline{\tilde{u}_n\tilde{u}_n}/u_\tau^2$ -·- $\overline{\tilde{u}_w\tilde{u}_w}/u_\tau^2$ —— $\overline{\tilde{u}_s\tilde{u}_n}/u_\tau^2$ - - - $\overline{\tilde{u}_s\tilde{u}_w}/u_\tau^2$ -·- $\overline{\tilde{u}_n\tilde{u}_w}/u_\tau^2$. Probe number in top-left corner.

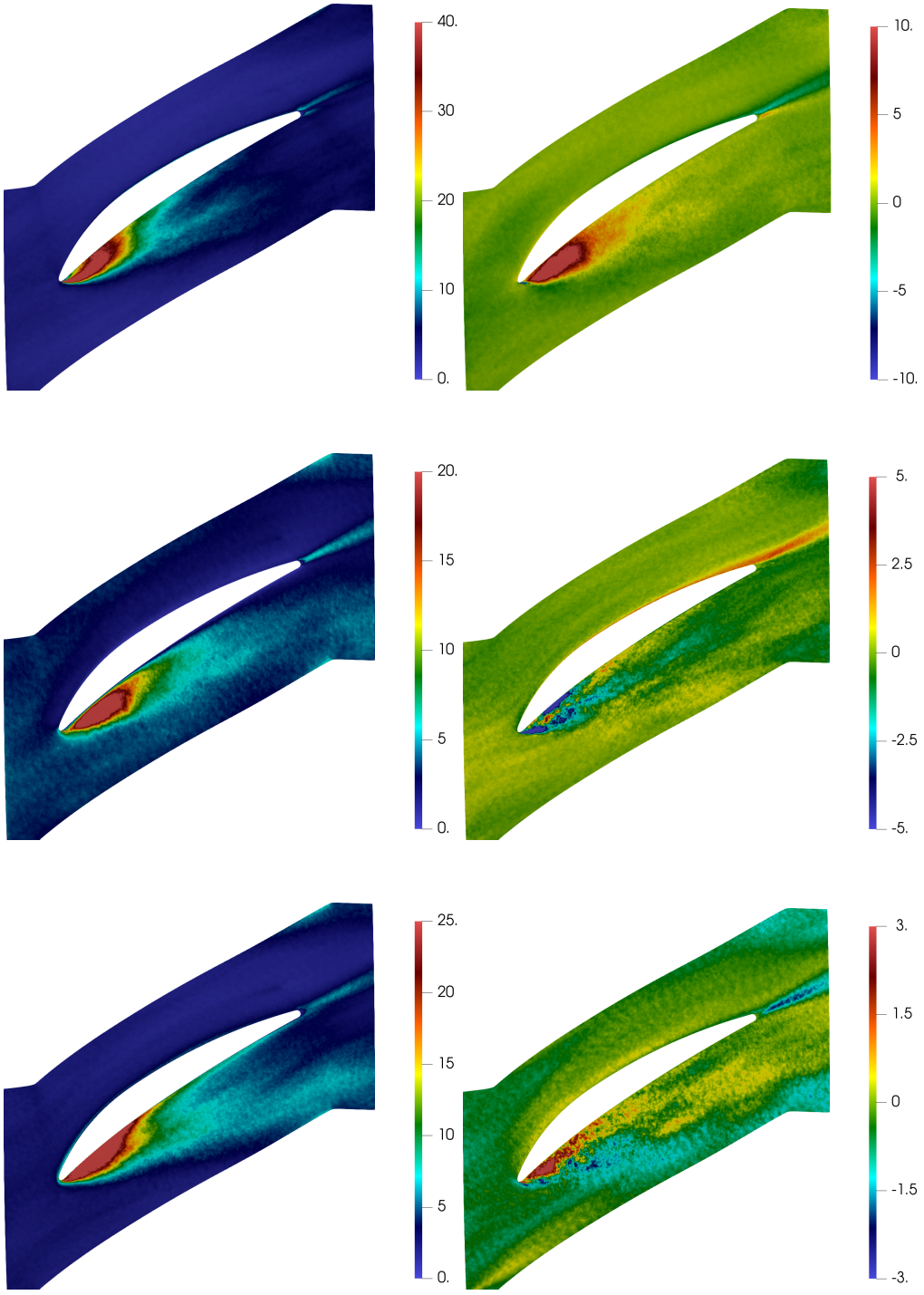
probes on the pressure side, the profiles do not resemble the RS boundary layer profiles seen so far. From probes 7 to 10 in Figure 80, $\overline{u'_w u'_w}$ is as large as $\overline{u'_s u'_s}$, and both of them stay significant until the freestream, rather than dropping away above $\eta^+ = 100$ as has been the case previously in regions of the blade surface operating under an adverse pressure gradient. As for $\overline{u'_n u'_n}$, from probes 7 to 10 it develops no peak within the boundary layer and grows monotonically as the freestream is approached. It should be noted that the high levels of the Reynolds normal stresses in the separation bubble in Figure 79 are the likely source for the high TKE levels seen at the passage inlet and outlet in Section 4.10; TKE is generated in the separation bubble and transported downstream.

An interesting feature of the suction side boundary layer profiles are the elevated levels of $\overline{u'_s u'_w}$ at probes 4 and 5, which was not the case in runs 1 and 2. These elevated levels of $\overline{u'_s u'_r}$ are also visible in Figure 79 on the second half of the suction side surface. Figure 75 also shows elevated positive levels of $\overline{u'_s u'_r}$ on the blade suction side in run 2, but much weaker than run 3. Figure 71 however shows negative values of $\overline{u'_s u'_r}$ on the blade suction side surface in run 1. In runs 2 and 3, $\overline{u'_n u'_r}$ is negative in the blade wake whereas in run 1 it is positive. The angle of incidence thus seems to have a significant influence on the behaviour of the second and third Reynolds shear stresses on the latter part of the blade surface and in the blade wake.

The pressure side separation bubble in run 3 was shown to vary a lot throughout the blade-pass cycle in Figure 64. It is thus of no surprise to see the highest levels of deterministic stress in run 3 occur in the separation bubble; all six components of the DS tensor show significant activity there.

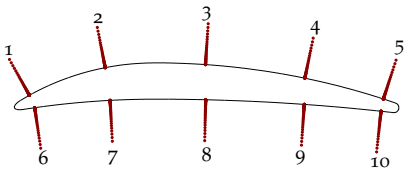
On the suction side of the blade, $\overline{\tilde{u}_w\tilde{u}_w}$ is the most active component of the DS tensor, as seen in the boundary layer plots in Figure 82. $\overline{\tilde{u}_w\tilde{u}_w}$, along with $\overline{\tilde{u}_s\tilde{u}_s}$, is also large on the first three probes on the pressure side. However whereas the streamwise component peaks close to the wall, $\eta^+ = 10$, the spanwise component peaks closer to $\eta^+ = 100$.





$\overline{u'_s u'_s}$	$\overline{u'_s u'_n}$
$\overline{u'_n u'_n}$	$\overline{u'_s u'_r}$
$\overline{u'_r u'_r}$	$\overline{u'_n u'_r}$

Figure 79: Contour plots at mid-span of components of the RS tensor for run 3 stator ($\psi = 0.036$). Coordinate system aligned with the mean-flow at passage inlet. Normalized by global u_τ^2.



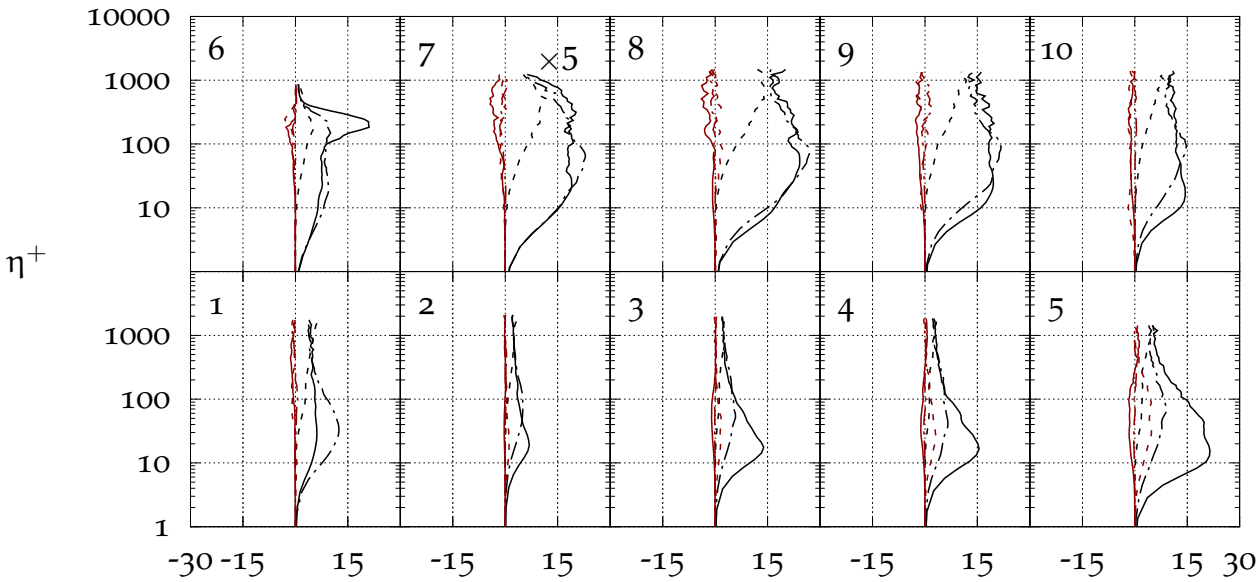
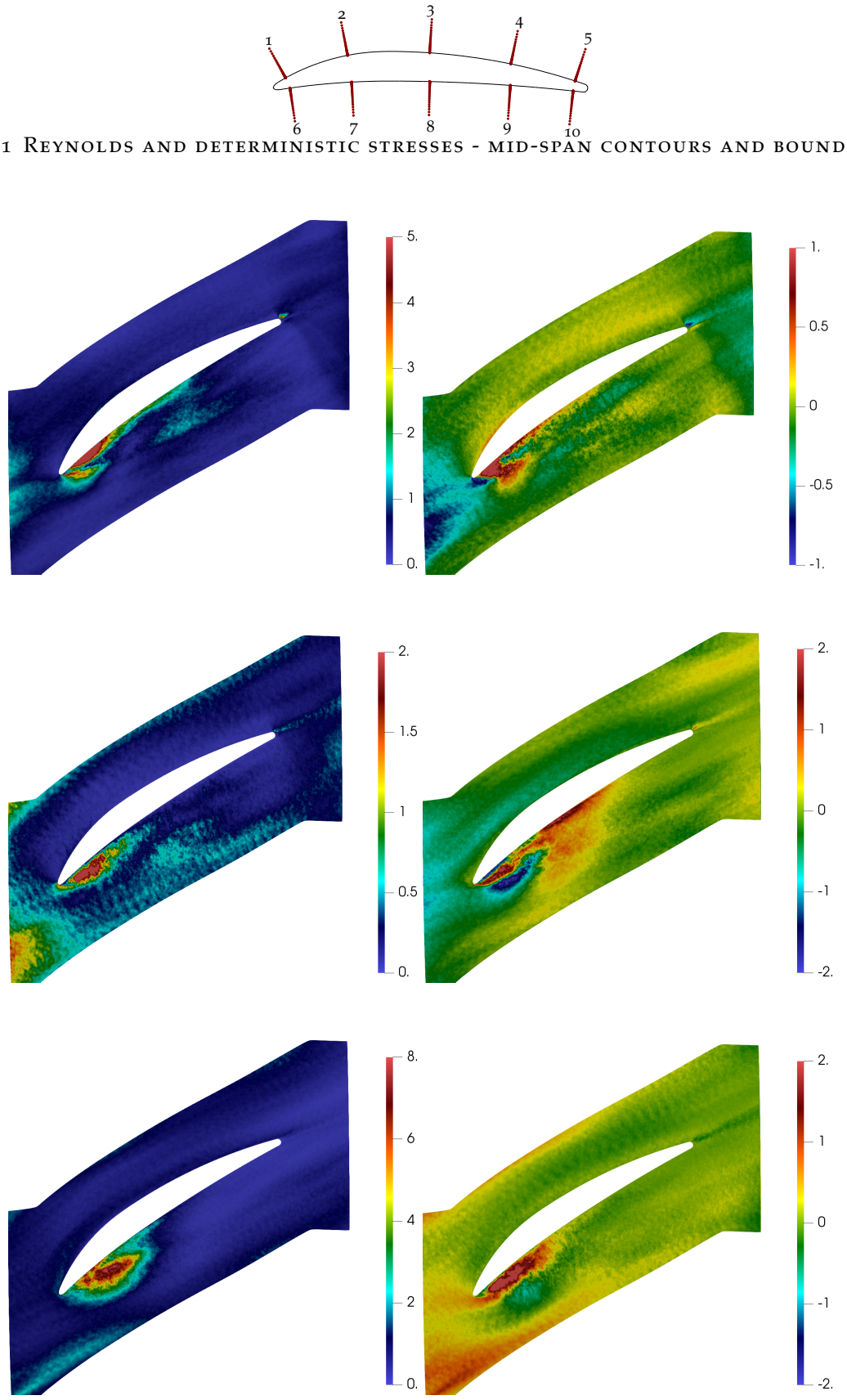


Figure 80: RS boundary layer profiles in inner coordinates for run 3 stator ($\psi = 0.036$). Normalized by local u_τ. — $\overline{u_s' u_s'}/u_\tau^2$ - - - $\overline{u_n' u_n'}/u_\tau^2$ -·- $\overline{u_w' u_w'}/u_\tau^2$ — $\overline{u_s' u_n'}/u_\tau^2$ - - - $\overline{u_s' u_w'}/u_\tau^2$ -·- $\overline{u_n' u_w'}/u_\tau^2$. Probe number in top-left corner.

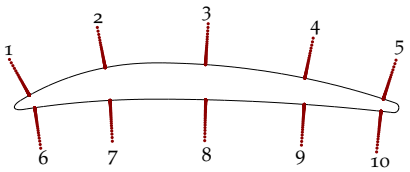
The most notable feature in the contour plots of $\overline{\tilde{u}_n \tilde{u}_n}$ in Figure 81 are the low levels at the passage inlet towards the suction side. This is reversed from the previous two runs, which showed higher levels of $\overline{\tilde{u}_n \tilde{u}_n}$ at the passage inlet on the suction side. A likely cause for this is the high level of blockage seen in the rotor blade wake in Figure 57.

The deterministic shear stresses are also most active in the separation bubble in Figure 81, but the largest component is $\overline{\tilde{u}_s \tilde{u}_r}$ rather than $\overline{\tilde{u}_s \tilde{u}_n}$. This is also clearly visible in the boundary layer plots in Figure 82 at probes 6 and 7. $\overline{\tilde{u}_s \tilde{u}_n}$ is also missing the dual-peak at the leading edge that was present in the first two runs. Finally, in Figure 73 and Figure 77 the third deterministic shear stress, $\overline{\tilde{u}_n \tilde{u}_r}$, was non-zero throughout essentially the entire passage. This is no longer the case in run 3, as Figure 81 shows.



$\widetilde{\overline{u}_s\widetilde{u}_s}$	$\widetilde{\overline{u}_s\widetilde{u}_n}$
$\widetilde{\overline{u}_n\widetilde{u}_n}$	$\widetilde{\overline{u}_s\widetilde{u}_r}$
$\widetilde{\overline{u}_r\widetilde{u}_r}$	$\widetilde{\overline{u}_n\widetilde{u}_r}$

Figure 81: Contour plots at mid-span of components of the DS tensor for run 3 stator ($\psi = 0.036$). Coordinate system aligned with the mean-flow at passage inlet. Normalized by global u_τ^2.



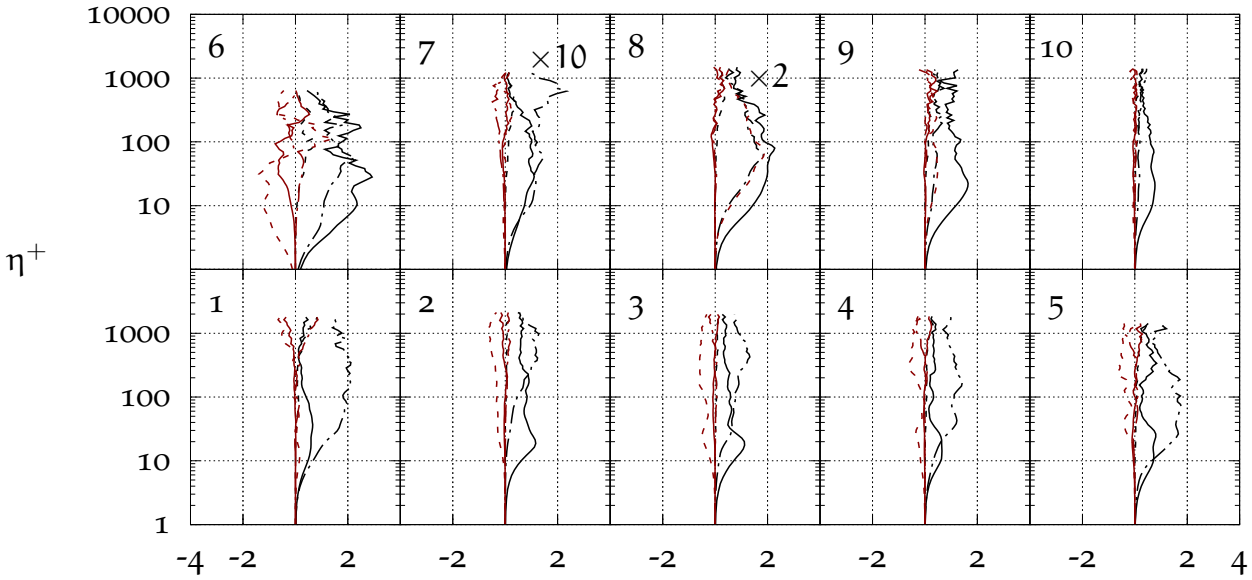
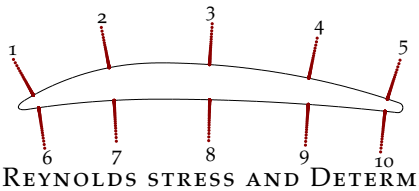


Figure 82: DS boundary layer profiles in inner coordinates for run 3 stator ($\psi = 0.036$). Normalized by local u_τ. —— $\overline{\tilde{u}_s\tilde{u}_s}/u_\tau^2$ - - - $\overline{\tilde{u}_n\tilde{u}_n}/u_\tau^2$ -·- $\overline{\tilde{u}_w\tilde{u}_w}/u_\tau^2$ —— $\overline{\tilde{u}_s\tilde{u}_n}/u_\tau^2$ - - - $\overline{\tilde{u}_s\tilde{u}_w}/u_\tau^2$ -·- $\overline{\tilde{u}_n\tilde{u}_w}/u_\tau^2$. Probe number in top-left corner.



4.12 Reynolds stress and Deterministic stress divergence

As Equation 49 shows, the divergence of the Reynolds and deterministic stress tensors determines their contributions to the momentum balance. Figure 83 shows contour plots of the RS and DS tensor divergence for run 1 at mid-span in the stator passage. The sign convention chosen means that positive contours indicate a positive contribution to the momentum balance.

All three components of the RS divergence, in the s, n, r directions, are largest in the blade wake, but also show elevated levels in the blade momentum boundary layers. The streamwise and normal components of the RS divergence generally appear much larger than the radial component. A non-zero contour extending from the leading edge to the domain boundary is visible, a feature also seen in the Reynolds stress contours in Section 4.11.

The RS and DS divergence contours in Figure 83 have been plotted using the same scale to allow for an easier comparison. On the whole, the components of the DS divergence are much smaller than those of the RS divergence. The leading edge of the blade is a noticeable exception, as both the streamwise and normal components of the DS divergence are large here, whereas components of the RS divergence are not. Another is the passage inlet, where the normal DS divergence appears to be larger than any of the RS divergence components.

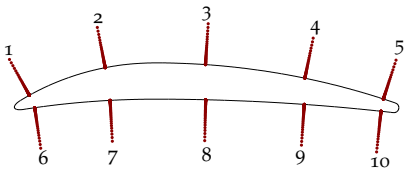
The RS divergence components in run 2 shown in Figure 84 show much greater levels of activity in the pressure side boundary layer due to the negative incidence. Indeed, all three components of the RS divergence are most active in the pressure side separation bubble. However, perhaps the most important aspect of Figure 84 is the increased magnitude of components of the DS divergence.

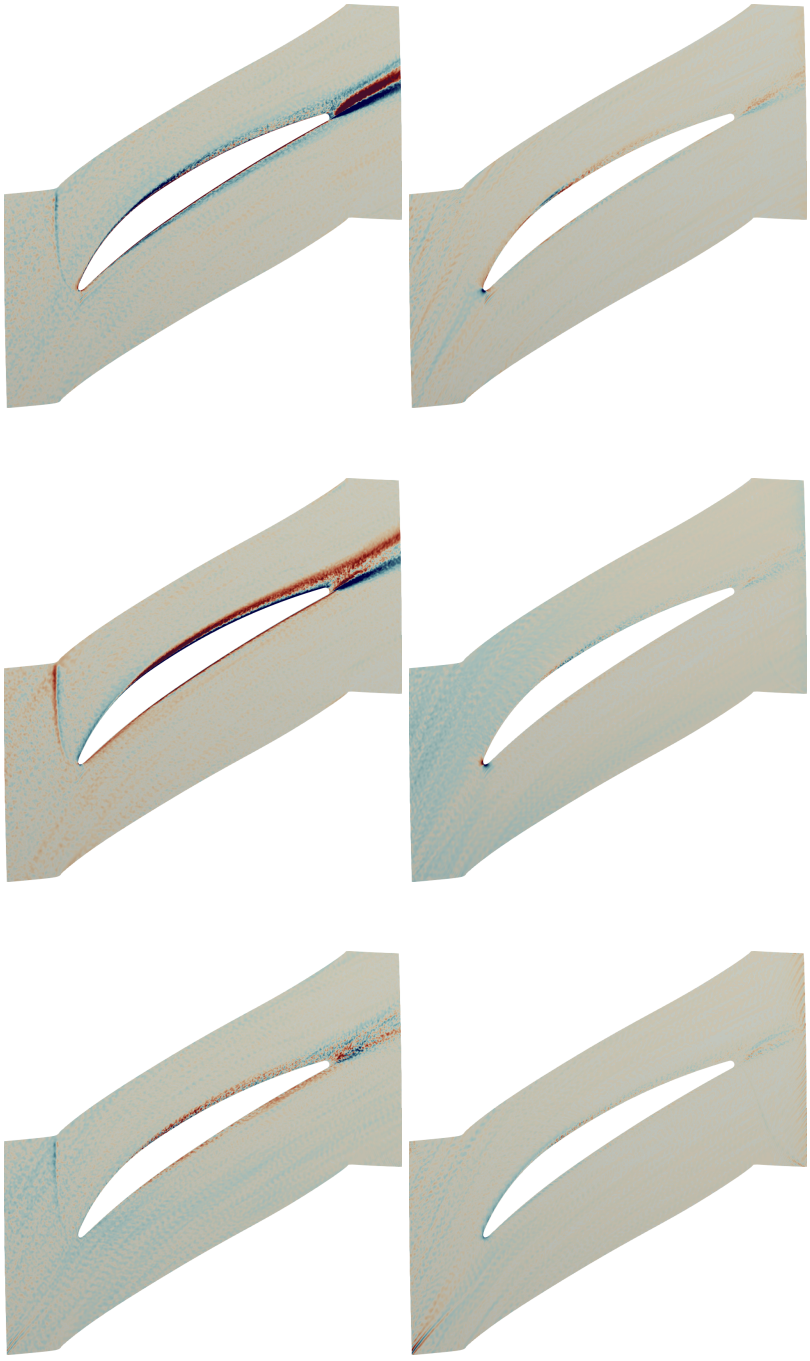
The streamwise DS divergence appears as large as the streamwise RS divergence at the blade leading edge and in the initial stages of the separation bubble. The normal component of the DS divergence is also large in the separation bubble. It also shows a peak at the flow stagnation point, which is missing in the normal RS divergence. The normal component of the DS divergence is also significant at the passage inlet, and exhibits elevated levels in the freestream all the way through the passage.

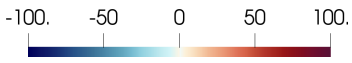
The radial DS divergence is again large in the separation bubble, but appears much smaller than the radial RS divergence. It should also be remarked that of all the quantities examined so far, the stress divergence appears the list statistically converged. This is the reason why boundary layer profiles have not been examined, as they have not yet converged to a sufficient degree. Nevertheless, the contour plots at mid-span do enable a qualitative comparison of the relative influences of the deterministic and Reynolds stress fields on the time-mean momentum.

Figure 85 shows that the RS divergence components in run 3 are much larger than those seen previously, and the separation bubble is again the dominant region of activity. Unlike run 2 however, the DS divergence components are virtually negligible in the separation bubble as compared to the RS divergence. The most likely reason for this is the Reynolds stresses generally being much larger than the deterministic stresses, as was seen in the wake profiles in Section 4.10 and the mid-span contours in Section 4.11.

The results of the current section show that while the RS divergence is generally larger than the DS divergence, there are regions of the flow where the DS divergence plays a







$-\frac{\partial\left(\overline{u_s' u_j'}\right)}{\partial x_j}$	$-\frac{\partial\left(\overline{\widetilde{u}_s \widetilde{u}_j}\right)}{\partial x_j}$
$-\frac{\partial\left(\overline{u_n' u_j'}\right)}{\partial x_j}$	$-\frac{\partial\left(\overline{\widetilde{u}_n \widetilde{u}_j}\right)}{\partial x_j}$
$-\frac{\partial\left(\overline{u_r' u_j'}\right)}{\partial x_j}$	$-\frac{\partial\left(\overline{\widetilde{u}_r \widetilde{u}_j}\right)}{\partial x_j}$

Figure 83: Contour plots at mid-span of components of the RS divergence and DS divergence for run 1 stator ($\psi = 0.422$). Coordinate system aligned with the mean-flow at passage inlet. Normalized by c/u_τ^2, using global u_τ.

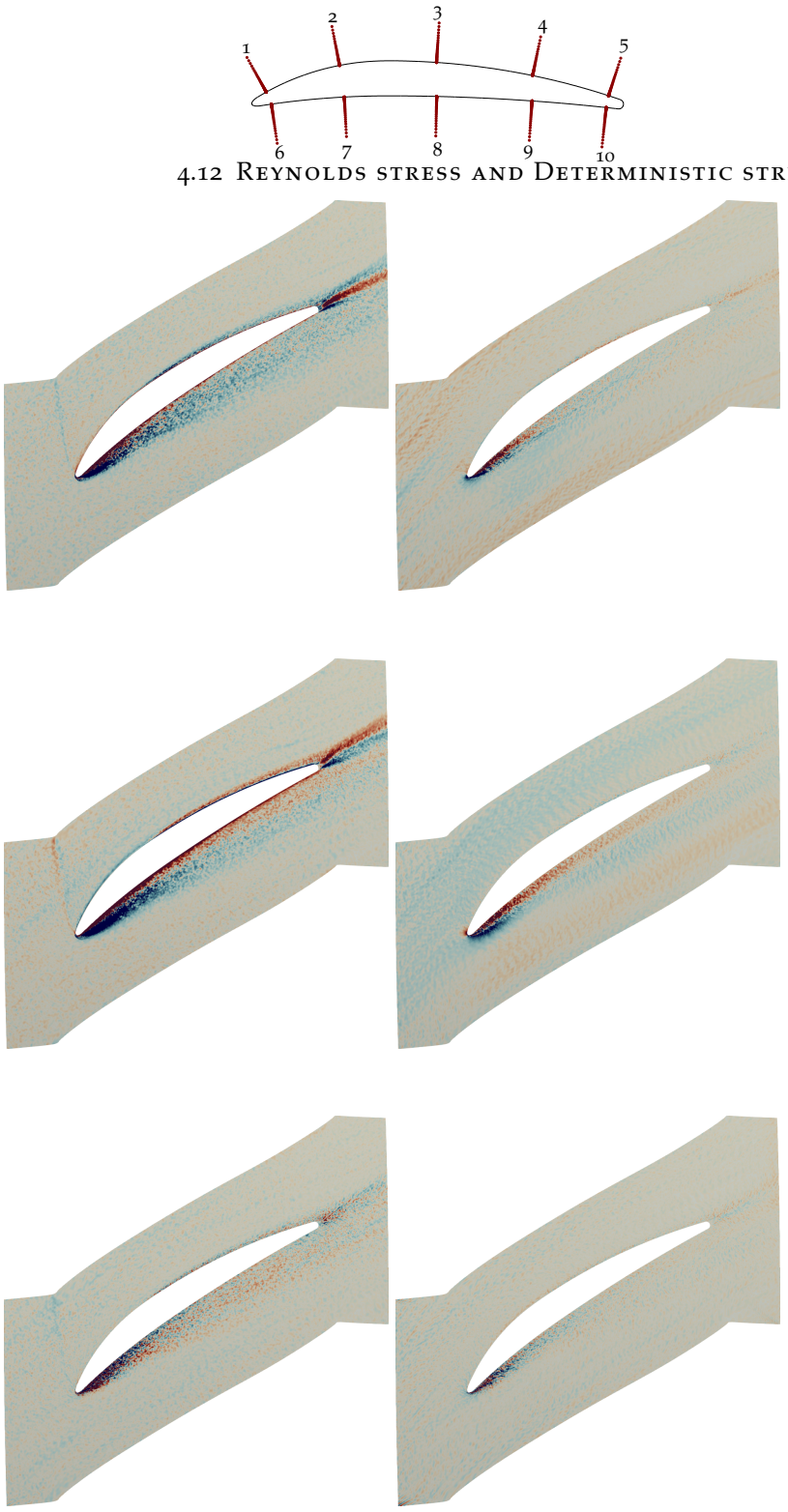
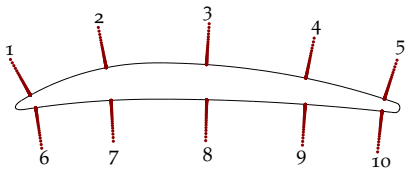
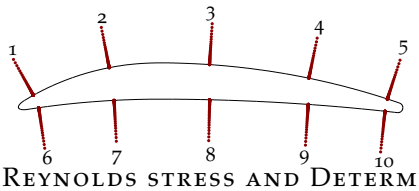
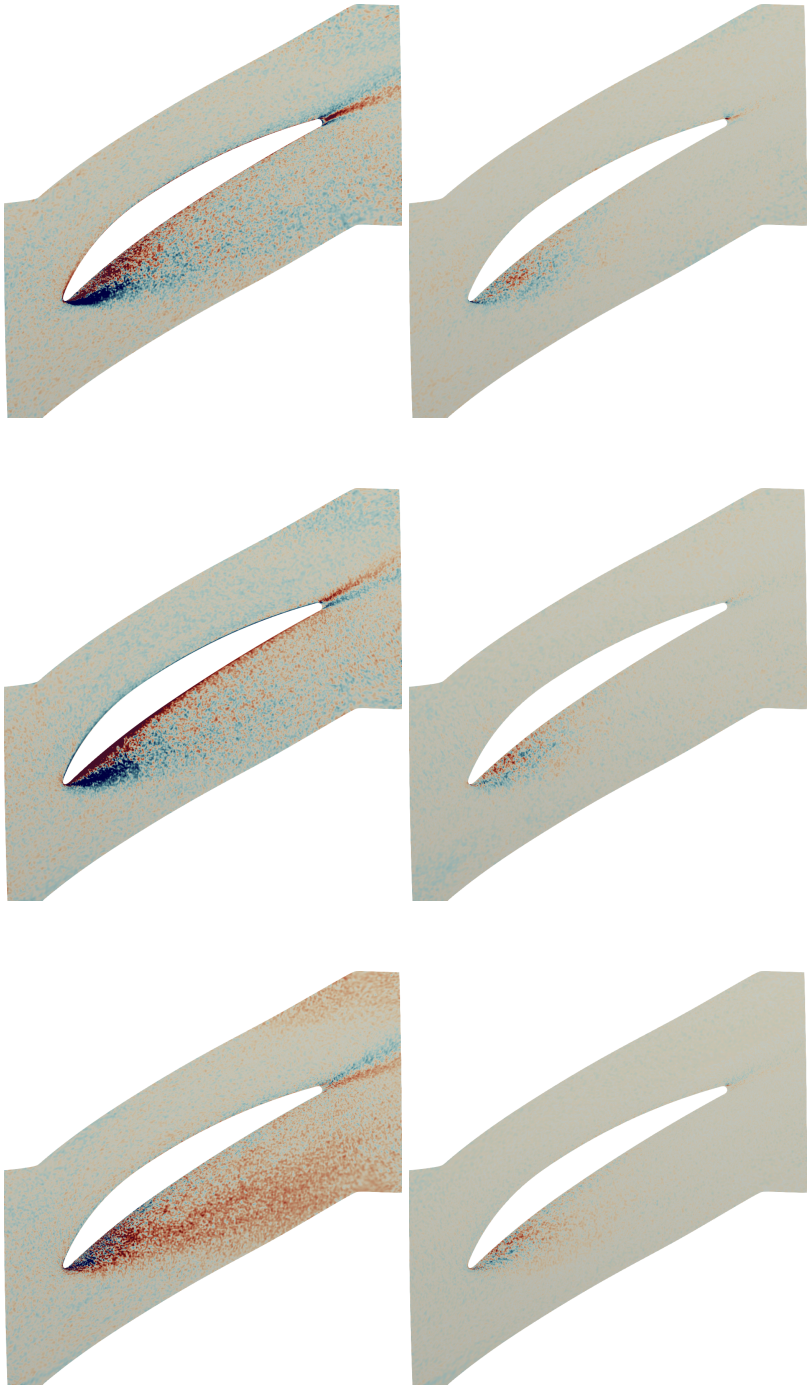


Figure 84: Contour plots at mid-span of components of the RS divergence and DS divergence for run 2 stator ($\psi = 0.204$). Coordinate system aligned with the mean-flow at passage inlet. Normalized by c/u_τ^2, using global u_τ.



significant role in the momentum balance. In run 1, which represents the compressor design point, the DS divergence was large at the passage inlet and blade leading edge. In run 2, the DS divergence was also significant in the pressure side separation bubble, which is a large phase-dependent unsteady flow feature. Although run 3 features an even larger separation bubble than run 2, the Reynolds stresses are very large and the DS divergence is negligible in comparison.

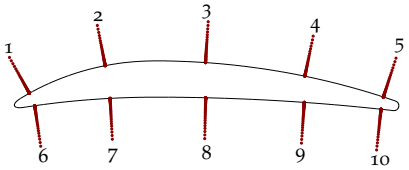






$-\frac{\partial\left(\overline{u_s' u_j'}\right)}{\partial x_j}$	$-\frac{\partial\left(\overline{\widetilde{u}_s \widetilde{u}_j}\right)}{\partial x_j}$
$-\frac{\partial\left(\overline{u_n' u_j'}\right)}{\partial x_j}$	$-\frac{\partial\left(\overline{\widetilde{u}_n \widetilde{u}_j}\right)}{\partial x_j}$
$-\frac{\partial\left(\overline{u_\tau' u_j'}\right)}{\partial x_j}$	$-\frac{\partial\left(\overline{\widetilde{u}_\tau \widetilde{u}_j}\right)}{\partial x_j}$

Figure 85: Contour plots at mid-span of components of the RS divergence and DS divergence for run 3 stator ($\psi = 0.036$). Coordinate system aligned with the mean-flow at passage inlet. Normalized by c/u_τ^2, using global u_τ.



4.13 REYNOLDS AND DETERMINISTIC STRESS BUDGETS

In order to understand the mechanisms responsible for the creation, destruction, or transportation of the Reynolds and deterministic stress fields, one can examine the terms comprising their budget. The derivation of the budget terms was shown in Section 4.2, and they have been listed again in Table 17 for the reader's convenience.

Table 17: Reynolds stress and Deterministic stress budget terms

$\widetilde{P}_{ij}, P'_{ij}$	$-\overline{\tilde{u}_j\tilde{u}_k}\frac{\partial\overline{u}_i}{\partial x_k} - \overline{\tilde{u}_i\tilde{u}_k}\frac{\partial\overline{u}_j}{\partial x_k}, -\overline{u'_j u'_k}\frac{\partial\overline{u}_i}{\partial x_k} - \overline{u'_i u'_k}\frac{\partial\overline{u}_j}{\partial x_k}$	Mean-flow production rate
$\widetilde{T}_{ij}, T'_{ij}$	$\frac{\partial}{\partial x_k}\left(\overline{\tilde{u}_i\tilde{u}_j\tilde{u}_k}\right), \frac{\partial}{\partial x_k}\left(\overline{u'_i u'_j u'_k}\right)$	Deterministic/turbulent transport rate
$\widetilde{\Pi}_{ij}, \Pi'_{ij}$	$-\frac{1}{\rho}\overline{\tilde{u}_j\frac{\partial\tilde{P}}{\partial x_i}} - \frac{1}{\rho}\overline{\tilde{u}_i\frac{\partial\tilde{P}}{\partial x_j}}, -\frac{1}{\rho}\overline{u'_j\frac{\partial P'}{\partial x_i}} - \frac{1}{\rho}\overline{u'_i\frac{\partial P'}{\partial x_j}}$	Pressure-gradient velocity correlation
$\widetilde{V}_{ij}, V'_{ij}$	$\nu\frac{\partial^2}{\partial x_k\partial x_k}\left(\overline{\tilde{u}_i\tilde{u}_j}\right), \nu\frac{\partial^2}{\partial x_k\partial x_k}\left(\overline{u'_i u'_j}\right)$	Viscous diffusion rate
$\widetilde{\epsilon}_{ij}, \epsilon'_{ij}$	$-2\nu\overline{\frac{\partial\tilde{u}_i}{\partial x_k}\frac{\partial\tilde{u}_j}{\partial x_k}}, -2\nu\overline{\frac{\partial u'_i}{\partial x_k}\frac{\partial u'_j}{\partial x_k}}$	Viscous dissipation rate
$\widetilde{D}_{ij}$	$\overline{\langle u'_i u'_k\rangle\frac{\partial\tilde{u}_j}{\partial x_k}} + \overline{\langle u'_j u'_k\rangle\frac{\partial\tilde{u}_i}{\partial x_k}}$	Deterministic production rate / turbulent dissipation rate
$\widetilde{\Phi}_{ij}, \Phi'_{ij}$	$-\frac{\partial}{\partial x_k}\left(\overline{\tilde{u}_j\langle u'_i u'_k\rangle}\right) - \frac{\partial}{\partial x_k}\left(\overline{\tilde{u}_i\langle u'_j u'_k\rangle}\right), -\frac{\partial}{\partial x_k}\left(\overline{\langle u'_i u'_j\rangle\tilde{u}_k}\right)$	Turbulent/deterministic diffusion rate

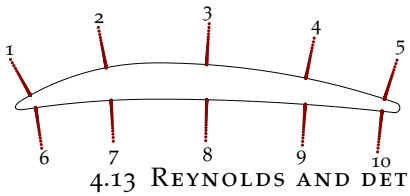
As Section 4.11 showed, the normal stresses and the first shear stress were the most active components of both the Reynolds and deterministic stress tensors throughout most of the stator passage in all three runs. As such, Section 4.13.1 discusses the budget terms of the turbulent and deterministic kinetic energy, and Section 4.13.2 does the same for the first Reynolds and deterministic shear stress.

4.13.1 *Kinetic energy budget*

4.13.1.1 *Turbulent kinetic energy budget*

Figure 86 shows contour plots at mid-span of the turbulent kinetic energy (TKE) budget terms. The three most active terms in the TKE budget for run 1 are the mean-flow production rate, viscous dissipation rate and turbulent transport rate, sometimes also known as the triple correlation. All three are mostly active in the blade momentum boundary layers and the wake.

On both sides of the blade, the boundary layer plots in Figure 87 show that the viscous diffusion acts to transport the turbulent kinetic energy into the viscous sub-layer where it is dissipated. At most locations, this effect is larger than the viscous dissipation rate. The mean-flow production rate is positive in most of the domain, indicating a net transfer of energy from the time-mean field to the turbulence. At the leading edge of the blade



however, the mean-flow production rate is negative. For the mean-flow production rate to be positive, the Reynolds stress tensor must be negatively proportional to the time-mean strain rate, i. e. Boussinesq's hypothesis: $\overline{u_i' u_j'} \propto -(\frac{\partial \overline{u}_i}{\partial x_j} + \frac{\partial \overline{u}_j}{\partial x_i})$. Figure 86 shows that near the leading edge of the blade, Boussinesq's hypothesis does not hold true and there is a transfer of energy from the turbulence to the time-mean flow. In the boundary layer plots in Figure 87 however, P'_{ii} is positive at all locations. P'_{ii} tends to peak around $\eta^+ = 10$ and it falls away sharply either side of the peak. Two notable exceptions are probes 4 and 5, where the mean-flow production rate is still significant at $\eta^+ \approx 100$. The mean-flow production rate is therefore the likely cause of the high values of the Reynolds normal stresses at $\eta^+ = 100$ in adverse pressure-gradient boundary layers. An interesting contrast between the blade surface boundary layers is that on the suction side, the triple-correlation is large at all five probes in the viscous sub-layer. From probes 6-10 on the pressure side however, T'_{ii} is not significant anywhere.

Figure 87 also shows the profile of the TKE. This is done to highlight the role that mean-flow convection plays. The main utility of the TKE profiles for the current purpose is their shape, rather than their magnitude. If their is little correlation between the shape of the TKE profile and the sum of the other budget terms, the mean-flow convection rate must be significant. Following this line of reasoning, the mean-flow convection rate thus clearly plays an important role in the TKE budget over the latter half of the suction side surface, i. e. from probes 3-5.

Another source term in the TKE budget is the deterministic production rate, $\widetilde{D}_{ii}$, which signifies the rate of kinetic energy transfer from the deterministic to the Reynolds stress field. $\widetilde{D}_{ii}$ is weakly positive at the passage inlet, indicating a transfer of energy from the organized unsteady field to turbulence. According to the contour plots in Figure 86, $\widetilde{D}_{ii}$ also appears to be significant near mid-chord on the suction side surface. However an examination of the boundary layer profiles of the budget terms in Figure 87 reveals that the deterministic production rate is much smaller than the other budget terms. The deterministic diffusion rate, Φ'_{ii}, whilst also being active at the passage inlet, does not play much of a role in the TKE budget in the blade boundary layers. Figure 87 thus reveals that in the blade surface boundary layers, the DS field does not play a significant role in the TKE budget.

As the contour plots show, the pressure-gradient velocity term exhibits a dual-peak around the leading edge; it acts like a production term at the leading edge and a destruction term immediately after it on both sides of the blade. Although Figure 86 suggests elevated levels of Π'_{ii} on the suction side surface, Figure 87 reveals that Π'_{ii} plays a minimal role in the TKE budget in the blade boundary layers.

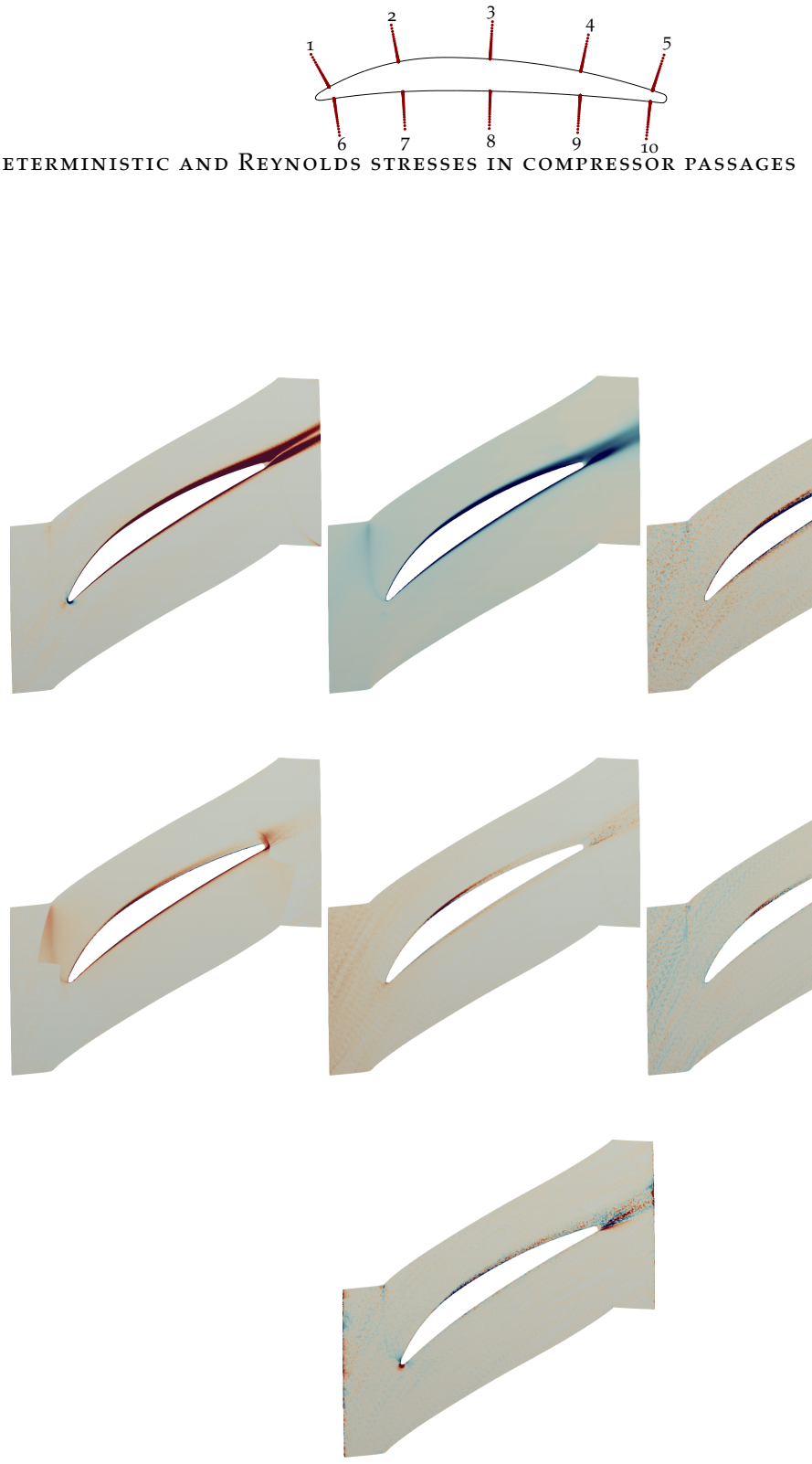
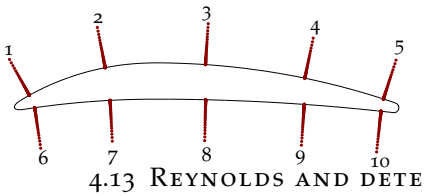


Figure 86: TKE budget terms for run 1 stator ($\psi = 0.422$). Normalized by u_τ^4/ν, using the global u_τ.



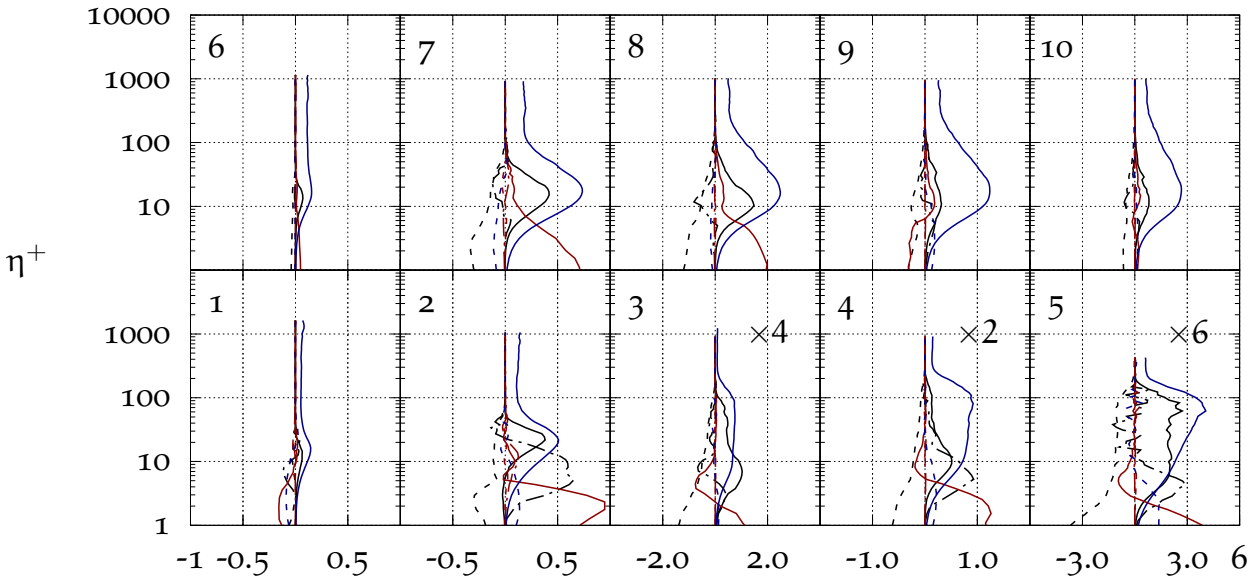
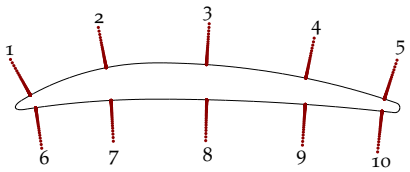


Figure 87: TKE budget terms in inner coordinates for run 1 ($\psi = 0.422$). Normalized by local u_τ.— $\frac{\nu}{u_\tau^4}P'_{ii}$ - - - $\frac{\nu}{u_\tau^4}\epsilon'_{ii}$ -·- $\frac{\nu}{u_\tau^4}T'_{ii}$ — $\frac{\nu}{u_\tau^4}V'_{ii}$ - - - $\frac{\nu}{u_\tau^4}\widetilde{D}_{ii}$ -·- $\frac{\nu}{u_\tau^4}\Phi'_{ii}$ - - - $\frac{\nu}{u_\tau^4}\Pi'_{ii}$ — $\frac{1}{16u_\tau^2}\overline{u'_i u'_i}$. Probe number in top-left corner.



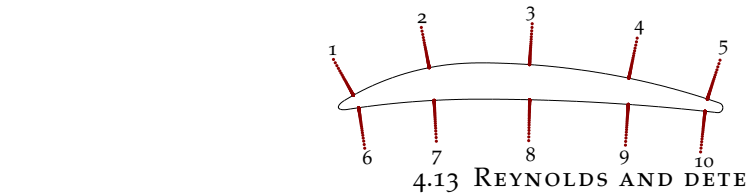
As was the case with the Reynolds stresses, the TKE budget terms are all very large in the pressure side separation bubble, as Figure 88 shows. Figure 89 also shows that the pressure side separation bubble creates very high levels of viscous dissipation and diffusion in the viscous sub-layer. These high levels persist until probe 8.

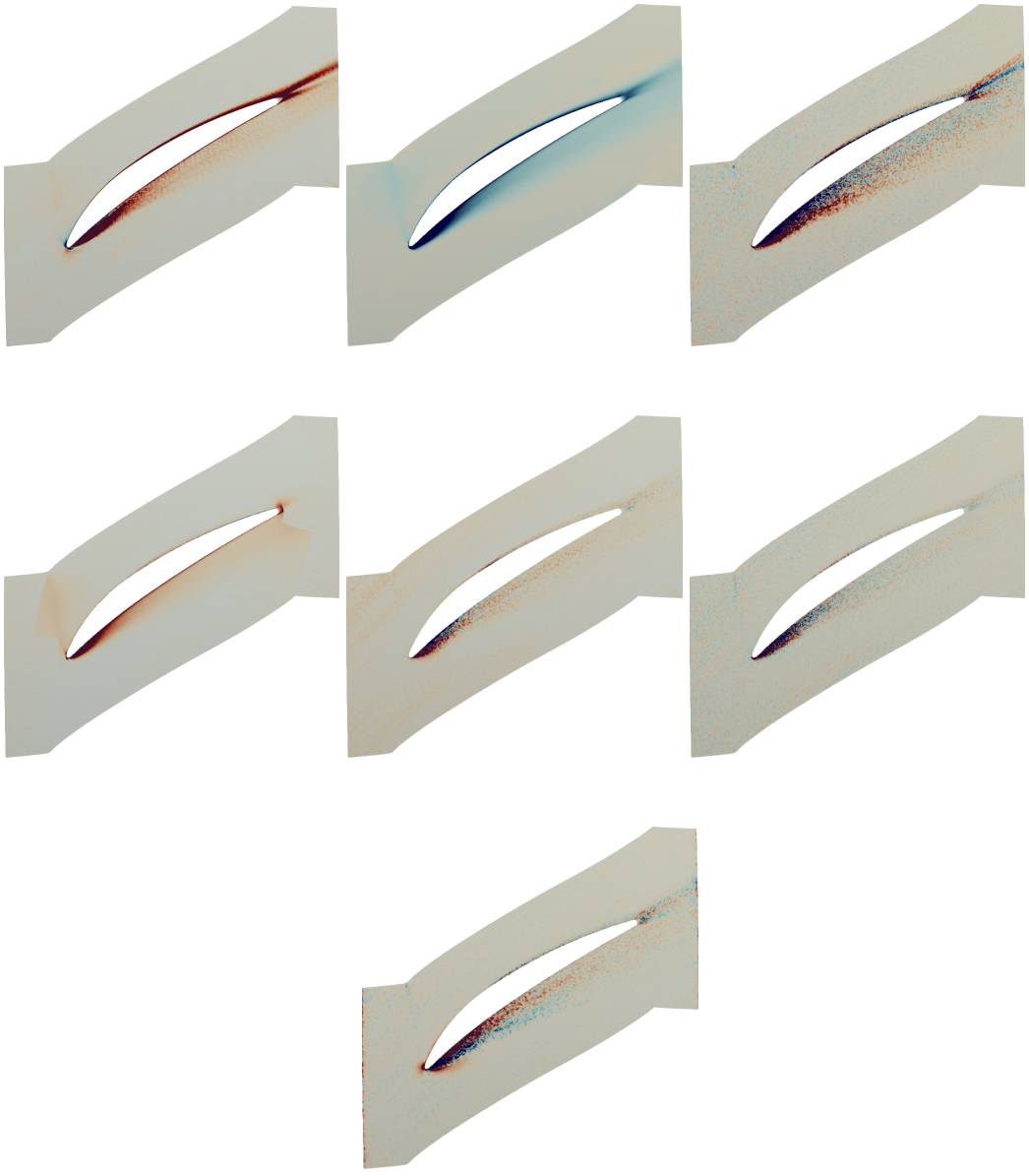
The turbulent diffusion rate is also very large in the pressure side separation bubble; T'_{ii} is significant at probe 6 throughout the boundary layer. At probe 6, the mean-flow production rate is only large around $\eta^+ = 100$; this is where the majority of the generation of TKE by the mean-flow is occurring. At this distance away from the wall, the turbulent transport rate acts like a large sink term, and acts to transport the TKE generated by the separation bubble towards the wall. Interestingly, the pressure-gradient velocity term also acts like a sink term in the separation bubble. As the TKE profiles from probes 7-10 show, the most dominant budget term at these locations is mean-flow convection. The separation bubble thus creates a lot of TKE, which is then convected by the mean-flow over the pressure side of the blade.

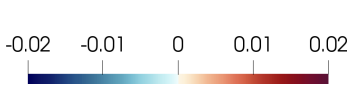
Although the deterministic production rate, $\widetilde{D}_{ii}$, is very small at probe 6, the deterministic diffusion rate, Φ'_{ii}, is significant up to $\eta^+ = 100$. Similar to the turbulent fluctuations then, deterministic fluctuations also act to transport the TKE produced in the separation bubble closer to the wall. Interestingly, the deterministic terms are not as large at the passage inlet of run 2 as they were in run 1.

On the suction side of the blade in run 2, only probes 3-5 are operating under an adverse pressure-gradient, and these are the only probes where the TKE budget terms are active. The trends here are largely the same as in run 1: the viscous diffusion rate acts to transport TKE away from $\eta^+ = 10$ and down to the wall. T'_{ii} is again large and positive around $\eta^+ = 10$, and the mean-flow production rate is significant from around $\eta^+ = 10 - 100$. The deterministic transport rate is as large as the viscous diffusion and dissipation rates at $\eta^+ = 10$ at probe 3, which was not the case in run 1. Similar to run 1, the mean-flow convection rate is large above $\eta^+ = 10$ at probes 3-5.

Finally, it is worth noting that similar to run 1, the mean-flow production rate in run 2 is also negative at the leading edge, as shown by Figure 88.

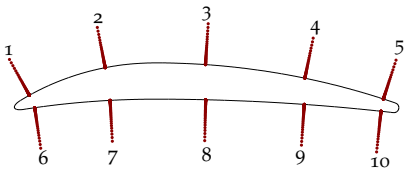






P'_{ij}	ϵ'_{ij}	T'_{ij}
V'_{ij}	D'_{ij}	Φ'_{ij}
	Π'_{ij}	

Figure 88: TKE budget terms for run 2 stator ($\psi = 0.204$). Normalized by u_τ^4/ν, using the global u_τ.



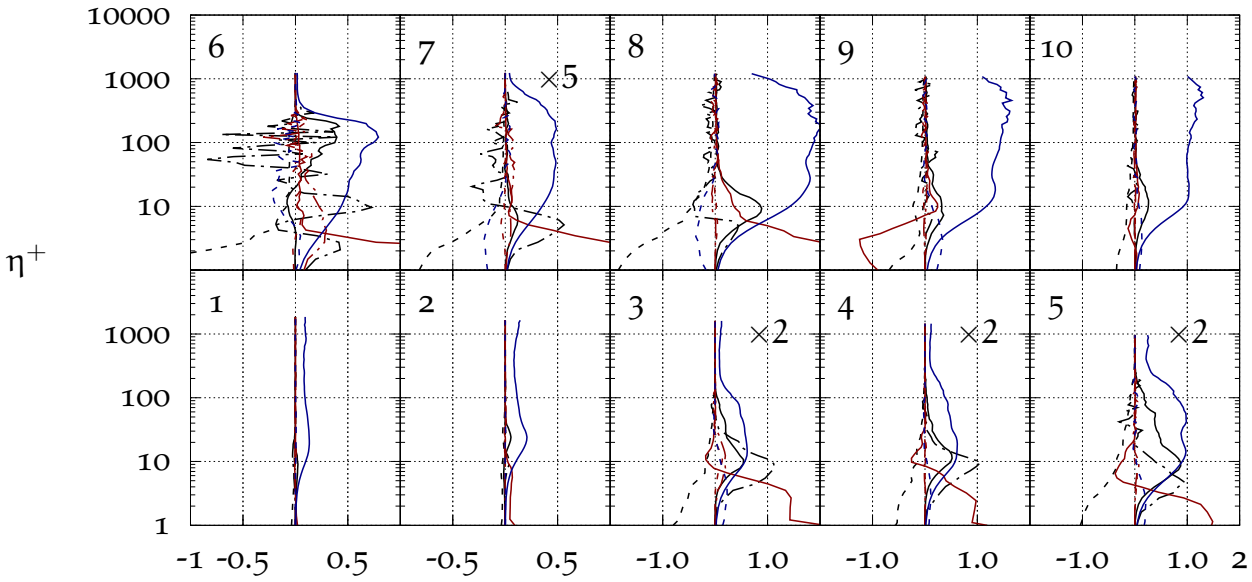
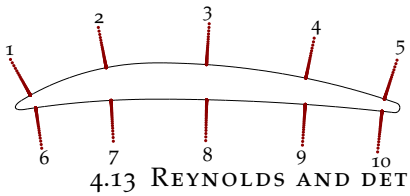


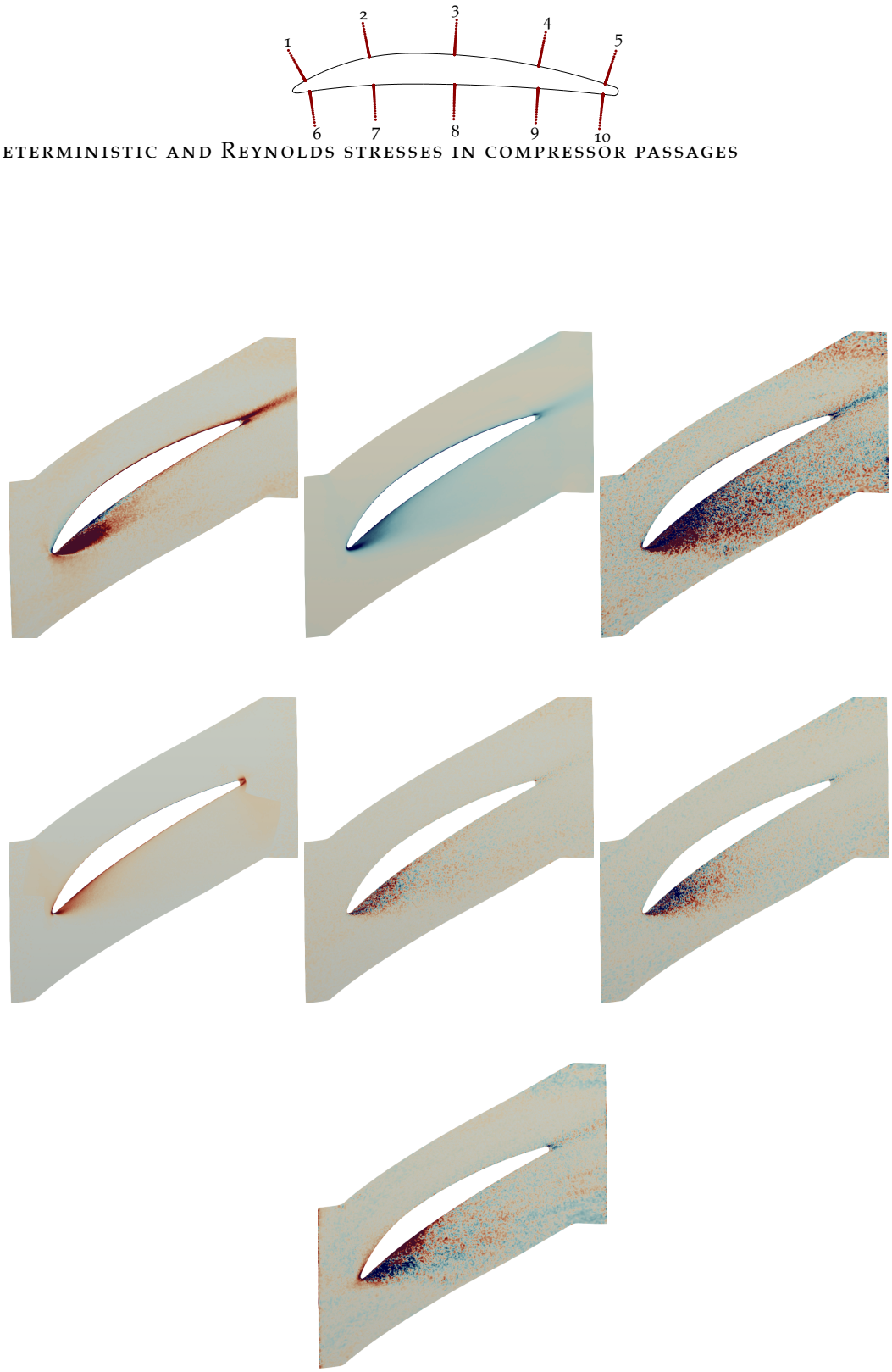
Figure 89: TKE budget terms in inner coordinates for run 2 ($\psi = 0.204$). Normalized by local u_τ.— $\frac{\nu}{u_\tau^4}P'_{ii}$ - - - $\frac{\nu}{u_\tau^4}\epsilon'_{ii}$ -·- $\frac{\nu}{u_\tau^4}T'_{ii}$ — $\frac{\nu}{u_\tau^4}V'_{ii}$ - - - $\frac{\nu}{u_\tau^4}\widetilde{D}_{ii}$ -·- $\frac{\nu}{u_\tau^4}\Phi'_{ii}$ - - - $\frac{\nu}{u_\tau^4}\Pi'_{ii}$ — $\frac{1}{40u_\tau^2}\overline{u'_i u'_i}$. Probe number in top-left corner.



Similar to run 2, Figure 91 shows that the TKE budget terms are most active in run 3 in the pressure side separation bubble. The mean-flow production rate again peaks around $\eta^+ = 200$, and the turbulent fluctuations act to transport it down the boundary layer. A difference to run 2 however is that whereas T'_{ii} was positive in the viscous sub-layer at probe 6, in Figure 91 it is negative. Perhaps this is to balance the pressure-gradient velocity correlation; Π'_{ii} is a significant TKE source at probe 6 in the viscous sub-layer. It carries on being a significant source term in the viscous sub-layer all along the pressure side. As the profiles from probes 7 to 10 in Figure 91 shown, the mean-flow convection of TKE is large along the pressure side of the blade.

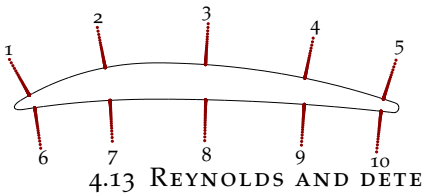
In fact, the freestream region in run 3 is generally characterized by high levels of TKE, as shown by Figure 79 and Figure 66. It is thus of no surprise to see the mean-flow convection to also play a significant role in all the suction side boundary layer profiles. Other than the mean-flow convection rate, the suction side boundary layers from probes 3-5 show the mean-flow production rate and turbulent transport rate are also significant above $\eta^+ = 10$. The turbulent transport rate is always negative, and is thus acting to transport TKE down to the region where dissipation is active. Such profiles of T'_{ii} in the suction side boundary layer are only visible in run 3. This is perhaps the reason why the profiles of $\overline{u'_s u'_s}$ from probes 3-5 in Figure 80 do not show a second peak around $\eta^+ = 100$, which is usually a feature of adverse pressure-gradient boundary layers.

In runs 1 and 2, the mean-flow production rate was negative at the leading edge and this is also the case in run 3. Furthermore, in run 3 the mean-flow production rate is also negative from $\eta^+ \approx 5 - 50$ at probe 7, i. e. immediately after the pressure side separation bubble.



P'_{ij}	ϵ'_{ij}	T'_{ij}
V'_{ij}	D'_{ij}	Φ'_{ij}
	Π'_{ij}	

Figure 90: TKE budget terms for run 3 stator ($\psi = 0.036$). Normalized by u_τ^4/ν, using the global u_τ.



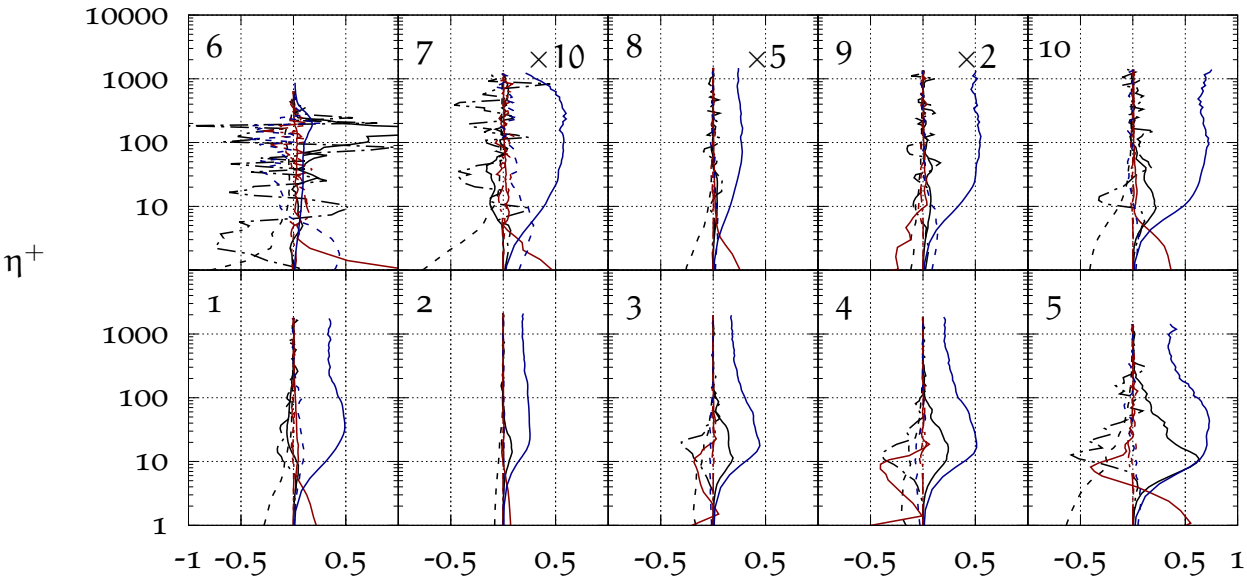
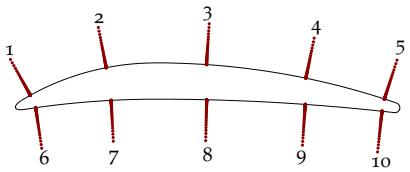


Figure 91: TKE budget terms in inner coordinates for run 3 ($\psi = 0.036$). Normalized by local u_τ.— $\frac{\nu}{u_\tau^4}P'_{ii}$ - - - $\frac{\nu}{u_\tau^4}\epsilon'_{ii}$ -·- $\frac{\nu}{u_\tau^4}T'_{ii}$ — $\frac{\nu}{u_\tau^4}V'_{ii}$ - - $\frac{\nu}{u_\tau^4}\widetilde{D}_{ii}$ -·- $\frac{\nu}{u_\tau^4}\Phi'_{ii}$ - - $\frac{\nu}{u_\tau^4}\Pi'_{ii}$ — $\frac{1}{40u_\tau^2}\overline{u'_i u'_i}$. Probe number in top-left corner.



4.13.1.2 *Deterministic kinetic energy budget*

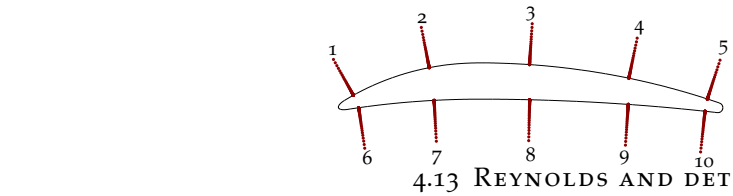
The deterministic kinetic energy budget terms for run 1 in Figure 92 exhibit a markedly different behaviour from those of the turbulent kinetic energy. The clearest example is the significantly reduced levels of activity in the blade momentum boundary layers. The only noticeable activity in the boundary layers corresponds to around the mid-chord on the suction surface, approximately in the region where the blade curvature changes from convex to concave.

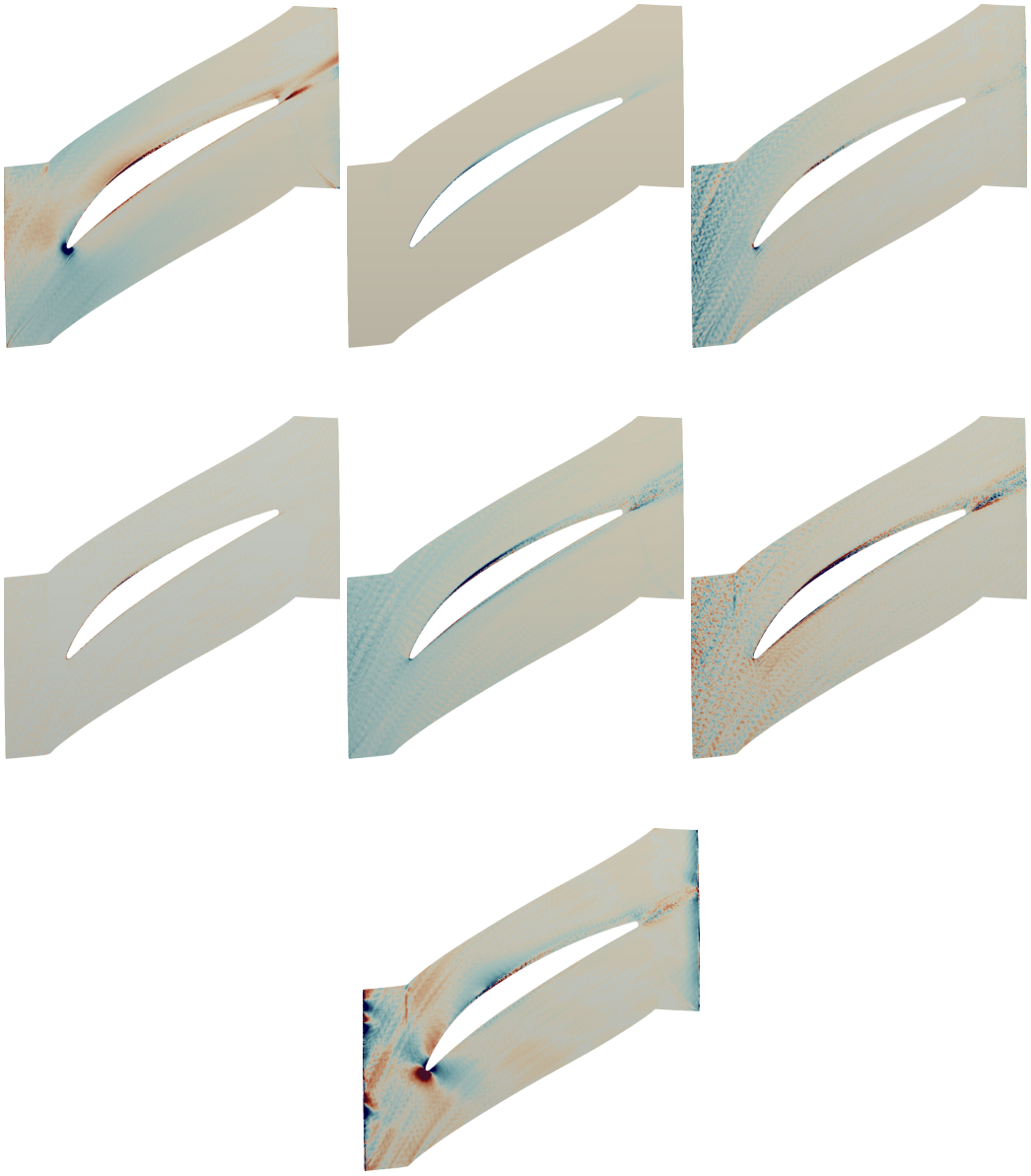
Another difference to the TKE budget contour plots is the increased activity at the passage inlet. The deterministic transport rate, $\widetilde{T}_{ii}$, is negative at the passage inlet and so is $\widetilde{D}_{ii}$; the DKE is being dissipated to turbulence at the passage inlet. The mean-flow production rate is negative at the passage inlet on the pressure side of the blade, signifying a transfer of energy from the deterministic fluctuations to the time-mean flow. Similar to the TKE mean-flow production rate, $\widetilde{P}_{ii}$ is also negative at the blade leading edge, but in this case over a larger region.

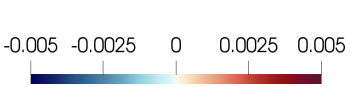
The most prominent feature of Figure 93 is the dominant role the Reynolds stresses play in the DKE budget in the blade boundary layers. The turbulent diffusion rate, $\widetilde{\Phi}_{ii}$, represents the rate at which Reynolds stresses transport deterministic fluctuations. $\widetilde{D}_{ii}$ represents the rate at which Reynold stresses create or destroy DKE. The role of $\widetilde{D}_{ii}$ is most clearly seen in probes 3 to 5. Here, it is acting like a dissipation term in the viscous sub-layer, in the place of the insignificant viscous dissipation term, $\widetilde{\epsilon}_{ii}$. $\widetilde{\Phi}_{ii}$ is positive in the viscous sub-layer from probes 3 to 5, and is thus acting to transport DKE to the viscous-sublayer where it is dissipated by turbulence.

It should be noted that at most of the probes in Figure 93, the profiles of $\frac{1}{2}\overline{\tilde{u}_i\tilde{u}_i}$ above the viscous sub-layer suggest that the mean-flow convection also plays a significant role in the DKE budget. A notable exception is probe 5, where the profile of $\frac{1}{2}\overline{\tilde{u}_i\tilde{u}_i}$ appears to be heavily influenced by $\widetilde{P}_{ii}$. As a very large adverse pressure-gradient is present at probe 5, this suggests regions of strong adverse pressure gradients are regions of significant DKE production.

The behaviour of the pressure-gradient velocity term in the DKE budget also merits discussion. $\widetilde{\Pi}_{ii}$ shows a very large positive peak at the blade leading edge, followed by two symmetrically positioned significant negative peaks on either side of the blade. The elevated levels on the blade suction side surface are also visible in Figure 93 at probe 5. As for the elevated levels of $\widetilde{\Pi}_{ii}$ at the inlet and outlet of the passage, these are most likely an artefact of performing the pressure-correction separately in the rotor and stator passages.

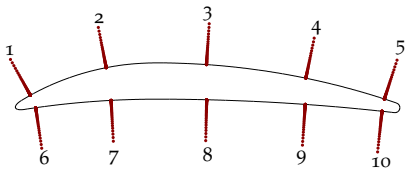






$\widetilde{P}_{ij}$	$\widetilde{\epsilon}_{ij}$	$\widetilde{T}_{ij}$
$\widetilde{V}_{ij}$	$\widetilde{D}_{ij}$	$\widetilde{\Phi}_{ij}$
	$\widetilde{\Pi}_{ij}$	

Figure 92: DKE budget terms for run 1 stator ($\psi = 0.422$). Normalized by u_τ^4/ν, using the global u_τ.



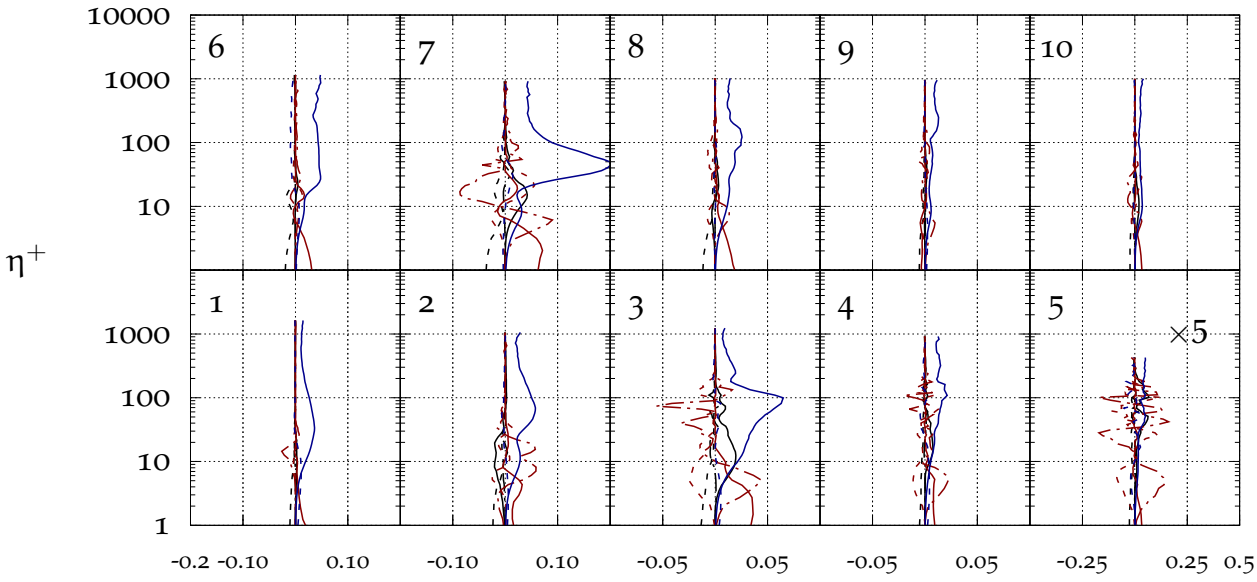


Figure 93: DKE budget terms in inner coordinates for run 1 ($\psi = 0.422$). Normalized by local u_τ.— $\frac{\nu}{u_\tau^4}\widetilde{P}_{ii}$ - - - $\frac{\nu}{u_\tau^4}\widetilde{\epsilon}_{ii}$ -·- $\frac{\nu}{u_\tau^4}\widetilde{T}_{ii}$ — $\frac{\nu}{u_\tau^4}\widetilde{V}_{ii}$ - - - $\frac{\nu}{u_\tau^4}\widetilde{D}_{ii}$ -·- $\frac{\nu}{u_\tau^4}\widetilde{\Phi}_{ii}$ - - - $\frac{\nu}{u_\tau^4}\widetilde{\Pi}_{ii}$ — $\frac{1}{30u_\tau^2}\overline{\tilde{u}_i\tilde{u}_i}$. Probe number in top-left corner.

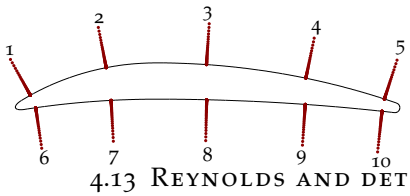


Figure 73 and Figure 77 showed that the deterministic stresses were larger in run 2 than run 1. It is thus of no surprise to see a greater level of activity in the DKE budget terms of run 2 in Figure 94. The behaviour of the DKE budget in the pressure side separation bubble is perhaps best understood by examining the boundary layer profiles at probes 6 and 7 in Figure 95.

The largest production term at probe 6 is $\widetilde{P}_{ii}$, and is most active above $\eta^+ = 100$. In the same region, the pressure-gradient velocity correlation and $\widetilde{D}_{ii}$ act as sink terms. The turbulent diffusion rate also acts to transport DKE away from regions of high production. In the viscous sub-layer, $\widetilde{\Phi}_{ii}$ acts like a very large sink term. At probe 7, the mean-flow and the turbulent fluctuations act to remove DKE, and the pressure-gradient fluctuations add DKE. Downstream of the separation bubble however, as was the case in the TKE budget, the dominant budget term is mean-flow convection. Large amounts of DKE is generated in the pressure side separation bubble, and is convected by the mean-flow. This is clearly seen in the profiles of $\frac{1}{2}\overline{\tilde{u}_i\tilde{u}_i}$ from probes 7 to 10, which suggest mean-flow convection to be the dominant term.

Similar to run 1, the mean-flow production rate is again negative at the leading edge, but the negative region is much larger. The boundary layer profiles on the suction side at probes 3-5 show the same influence of turbulence as in the DKE budget of run 1; turbulent fluctuations transport DKE to the viscous sub-layer, which the turbulence then acts to dissipate.

The pressure-gradient velocity term in Figure 94 shows the same dipole like peaks around the leading edge that it did in run 1. However the contours are no longer symmetric around the leading edge. The behaviour of the pressure-gradient velocity correlation around the blade leading edge in Figure 92 and Figure 94 matches the observations of Charbonnier et al[13]. Their unsteady simulations of a low-speed turbine also showed that the pressure-gradient velocity correlation exhibited dipole like peaks around the leading edge, as well as the large blocks of alternating sign on the blade suction surface. Interestingly, Charbonnier et al[13] also saw unphysical artefacts at the rotor-stator interface. The authors attributed these effects to their choice of boundary conditions, which they did not explain in the publication.

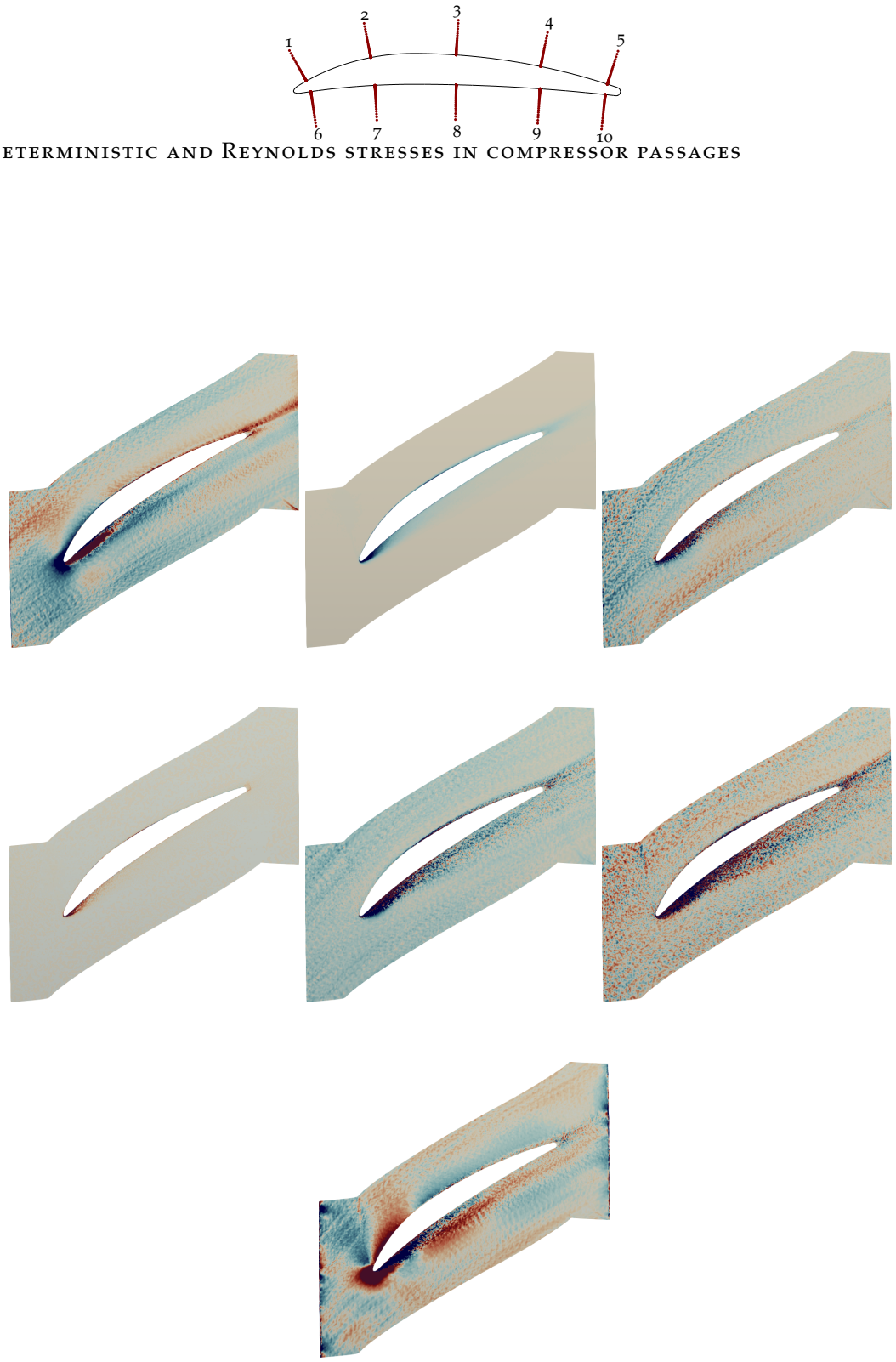
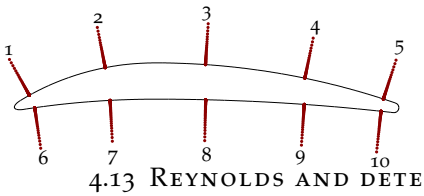


Figure 94: DKE budget terms for run 2 stator ($\psi = 0.204$). Normalized by u_τ^4/ν, using the global u_τ.



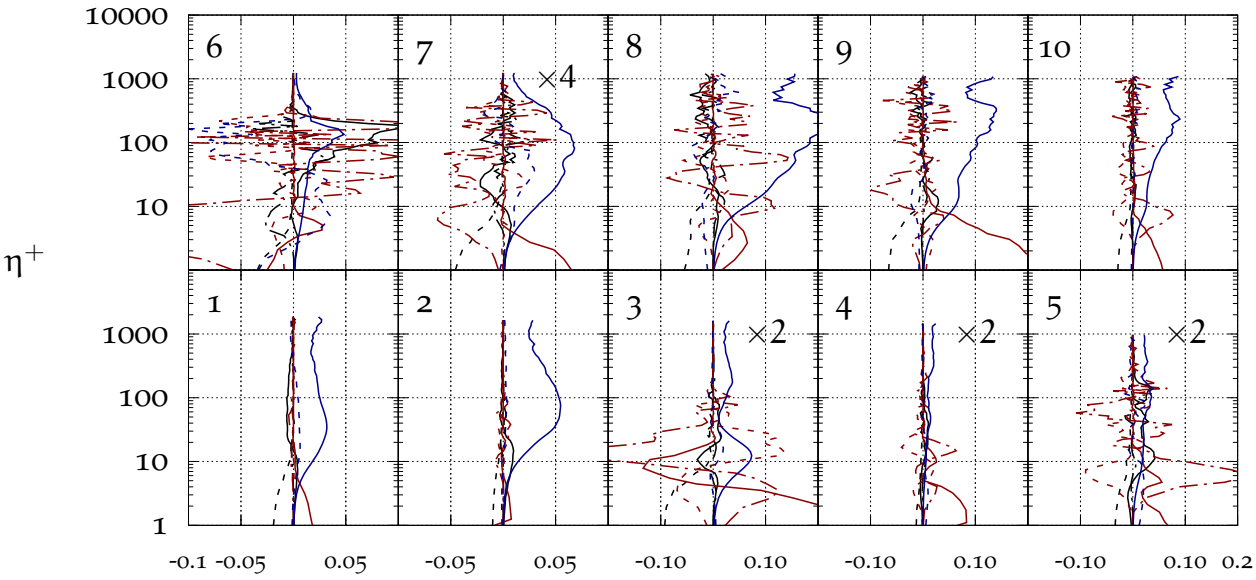
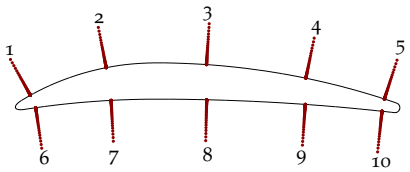


Figure 95: DKE budget terms in inner coordinates for run 2 ($\psi = 0.204$). Normalized by local u_τ.— $\frac{\nu}{u_\tau^4}\widetilde{P}_{ii}$ - - - $\frac{\nu}{u_\tau^4}\widetilde{\epsilon}_{ii}$ -·- $\frac{\nu}{u_\tau^4}\widetilde{T}_{ii}$ — $\frac{\nu}{u_\tau^4}\widetilde{V}_{ii}$ - - - $\frac{\nu}{u_\tau^4}\widetilde{D}_{ii}$ -·- $\frac{\nu}{u_\tau^4}\widetilde{\Phi}_{ii}$ - - - $\frac{\nu}{u_\tau^4}\widetilde{\Pi}_{ii}$ — $\frac{1}{50u_\tau^2}\overline{\tilde{u}_i\tilde{u}_i}$. Probe number in top-left corner.



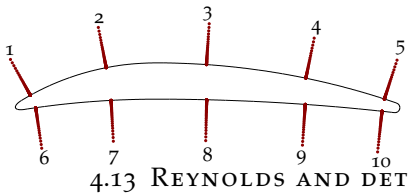
The DKE budget terms for run 3 are dominated by the pressure side separation bubble to an even larger extent than those in run 2, as shown in Figure 96. The boundary layer plots in Figure 97 also show that the turbulent terms play an even bigger role in the DKE budget than they did in run 2.

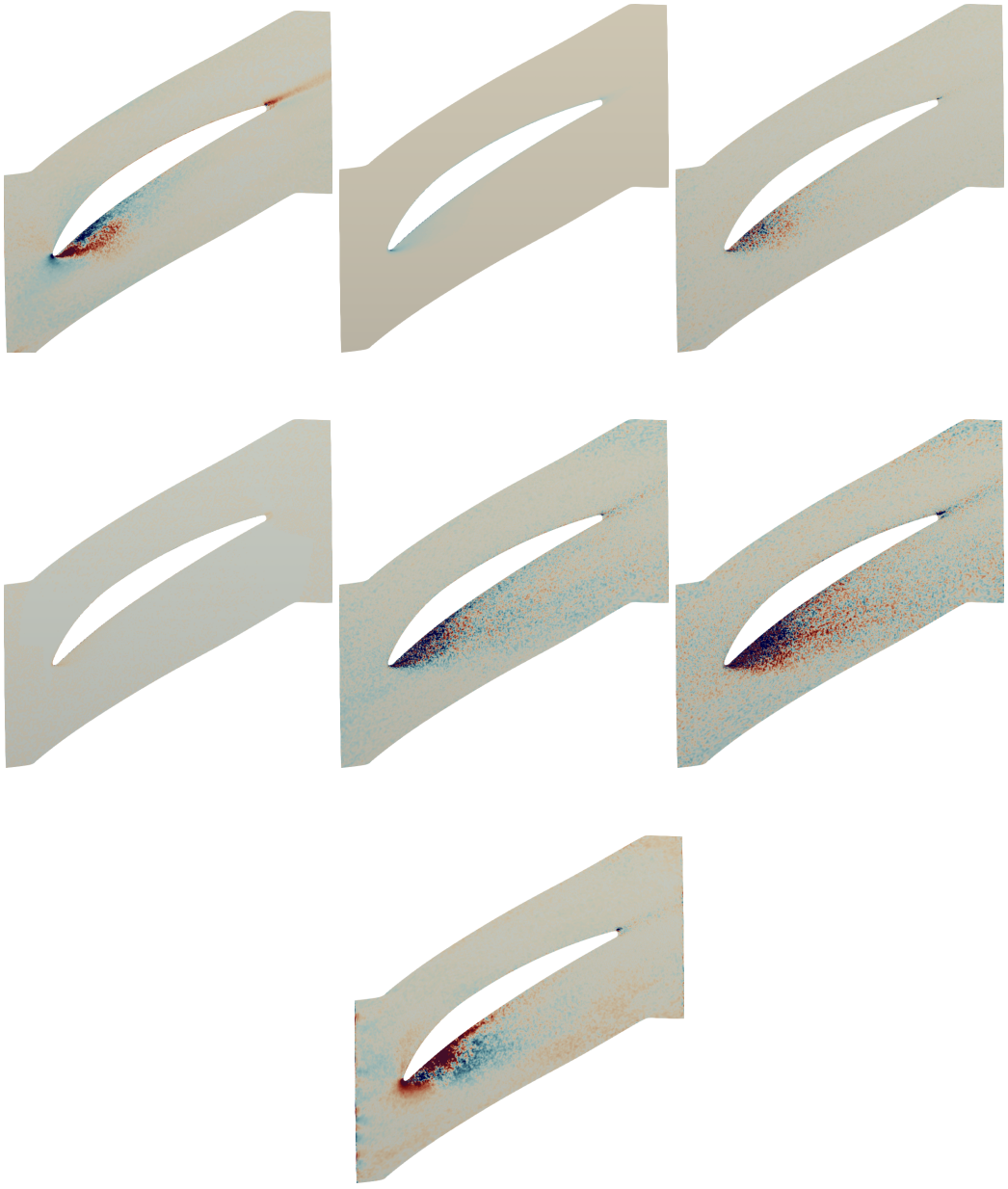
The overall trends however are largely the same as run 2. At probe 6, the mean-flow production rate acts as a large source term at $\eta^+ = 100$, and $\widetilde{\Pi}_{ii}$ acts as a destruction term. At probe 7, the mean-flow production rate in negative throughout the boundary layer, whereas the pressure-gradient velocity correlation is now a source term, all the way from the wall to $\eta^+ = 300$. Just like in run 2, the profiles of DKE at probes 7-10 in Figure 97 show that the mean-flow convection rate is the dominant term.

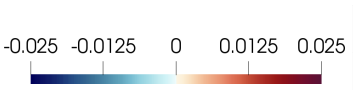
Figure 97 does nonetheless show some key differences to run 2. At probe 6, the deterministic transport rate, $\widetilde{T}_{ii}$, is also significant in the region of $\eta^+ = 5 - 30$, and is acting to transport DKE from the mean-flow production region down to the wall. This is the first and only instance where $\widetilde{T}_{ii}$ is significant in the blade surface boundary layers. $\widetilde{T}_{ii}$ was also significant at the passage inlet in both runs 1 and 2. In their derivation of a transport model for the Deterministic stresses, Van de Wall et al neglected the tripe correlation term, $\widetilde{T}_{ij}$. The authors did so on the grounds that their DS transport model was focused on studying mixing losses in axial turbomachinery passages, and the mixing loss is proportional to the square of the perturbation around the mean flow[125]. The deterministic stress therefore is proportional to the leading term in the mixing loss analysis, and the authors felt the triple-correlation would be a higher-order effect and could be neglected. The current results however show that at all three working points that were simulated, the triple correlation term cannot be neglected in the deterministic kinetic energy budget.

In Uzol et al's measurements, the authors found that the dissipation of deterministic kinetic energy by Reynolds stresses, i. e. $\widetilde{D}_{ii}$, was most active in the trajectory of the tip-vortex[124]. The authors attributed the high levels to the tip-vortex trajectory being characterized by large, phase-dependent unsteady perturbations about the time-mean flow. The high levels of $\widetilde{D}_{ii}$ in Figure 96 and Figure 97, as well as those at probe 6 in run 2 (Figure 95), are thus consistent with the measurements of Uzol et al.

Another obvious difference between runs 2 and 3 is the pressure-gradient velocity term, which no longer exhibits the dipole-like peaks at the leading edge. This leads one to the conclusion that the behaviour of $\widetilde{\Pi}_{ii}$ seen in Figure 92 and Figure 94 only occurs in a compressor operating close to its nominal design point.

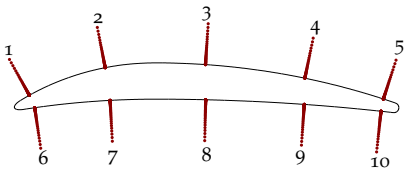






$\widetilde{P}_{ij}$	$\widetilde{\epsilon}_{ij}$	$\widetilde{T}_{ij}$
$\widetilde{V}_{ij}$	$\widetilde{D}_{ij}$	$\widetilde{\Phi}_{ij}$
	$\widetilde{\Pi}_{ij}$	

Figure 96: DKE budget terms for run 3 stator ($\psi = 0.036$). Normalized by u_τ^4/ν, using the global u_τ.



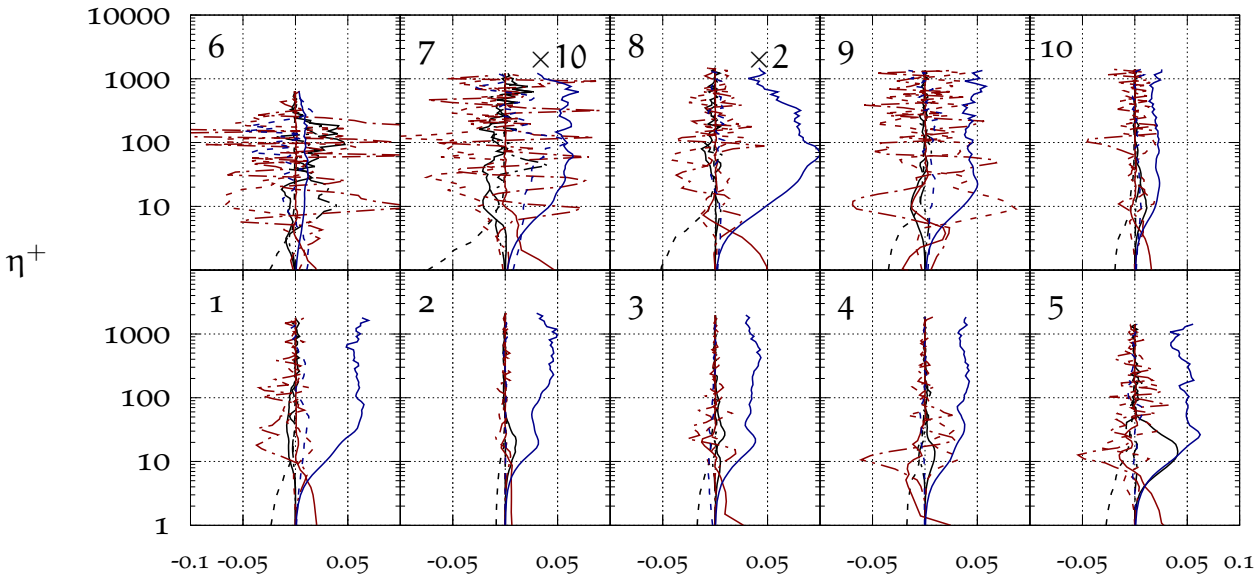
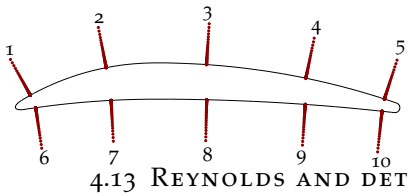


Figure 97: DKE budget terms in inner coordinates for run 3 ($\psi = 0.036$). Normalized by local u_τ.— $\frac{\nu}{u_\tau^4}\widetilde{P}_{ii}$ - - - $\frac{\nu}{u_\tau^4}\widetilde{\epsilon}_{ii}$ -·- $\frac{\nu}{u_\tau^4}\widetilde{T}_{ii}$ — $\frac{\nu}{u_\tau^4}\widetilde{V}_{ii}$ - - - $\frac{\nu}{u_\tau^4}\widetilde{D}_{ii}$ -·- $\frac{\nu}{u_\tau^4}\widetilde{\Phi}_{ii}$ - - - $\frac{\nu}{u_\tau^4}\widetilde{\Pi}_{ii}$ — $\frac{1}{40u_\tau^2}\overline{\tilde{u}_i\tilde{u}_i}$. Probe number in top-left corner.



4.13.2 *Shear stress budgets*

4.13.2.1 *Reynolds shear stress*

As Figure 98 shows, the largest terms in the Reynolds shear stress budget are the mean-flow production rate, turbulent transport rate and the pressure-gradient velocity correlation. In contrast to the TKE budget, the viscous dissipation rate is much less significant in the Reynolds shear stress budget. The pressure-velocity correlation on the other hand is a lot larger than it was in the TKE budget.

These conclusions are also supported by the boundary layer profiles in Figure 99. At probe 3, the dominant source term is P'_{sn}, and Π'_{sn} and T'_{sn} act as sink terms. Although the mean-flow production rate peaks at $\eta^+ = 10$, the Reynolds shear stress at probe 3 in Figure 72 does not peak until $\eta^+ = 100$. This is because the turbulent transport rate is also large around $\eta^+ = 10$, and acts to transport $\overline{u'_s u'_n}$ away from where it is being produced. At probe 4, T'_{sn} diminishes at $\eta^+ = 10$ but Π'_{sn} grows, with the effect that the peak of $\overline{u'_s u'_n}$ still occurs at $\eta^+ = 100$. By the final probe on the suction side, both the sink and source terms develop large peaks around $\eta^+ = 100$.

On the pressure side of the blade, the boundary layer plots show that the largest source term is again the mean-flow production rate. As the boundary layers are now operating in a favourable pressure gradient, P'_{sn} peaks around $\eta^+ = 20$, and falls away rapidly either side of it. Π'_{sn} also acts like a dissipation term in the pressure side boundary layers, but is of a noticeably smaller magnitude than the mean-flow production rate.

An interesting feature of the boundary layer profiles in Figure 99 is the reduced influence of the mean-flow convection rate; the profiles of $\overline{u'_s u'_n}$ correspond well to the sum of the other budget terms.

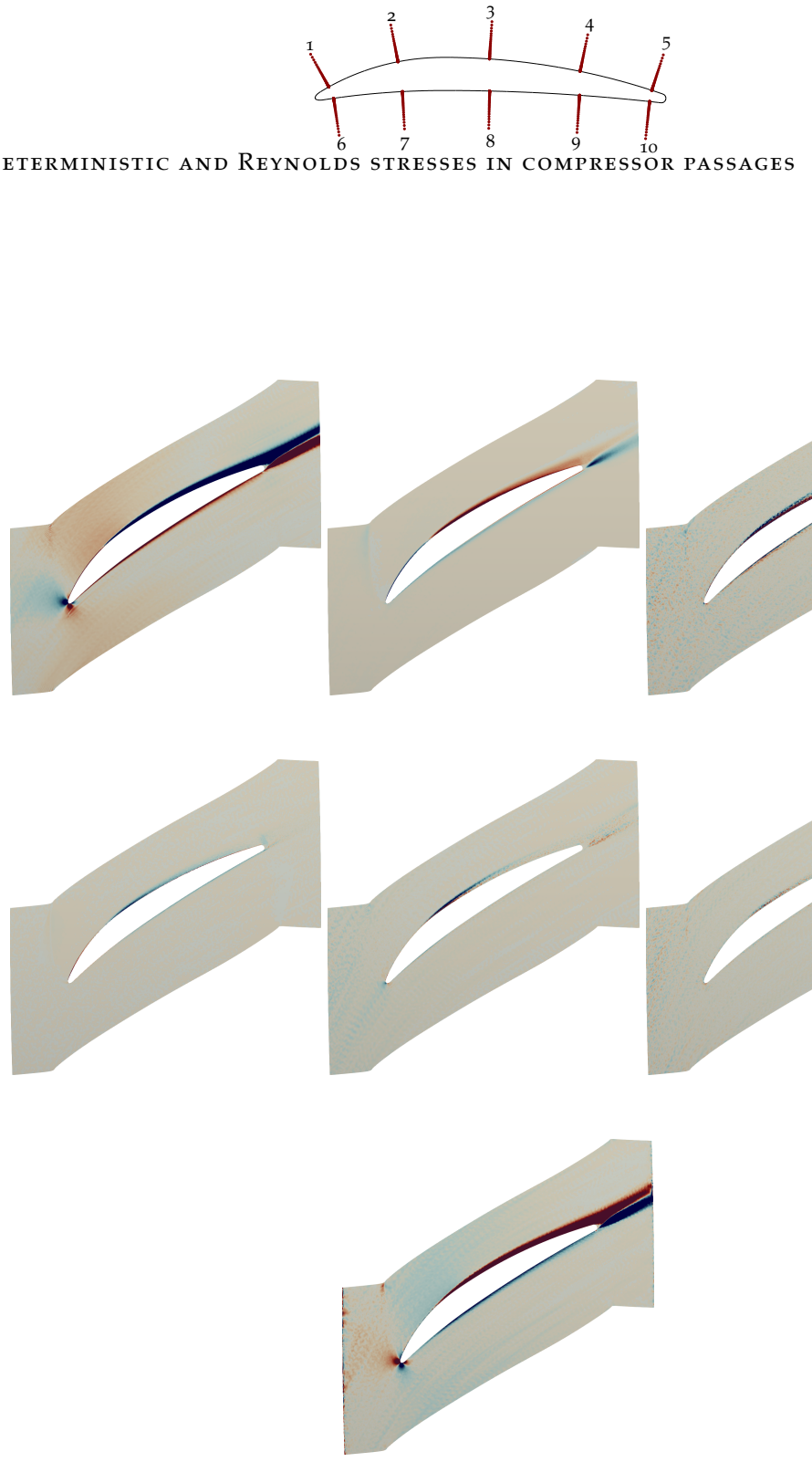
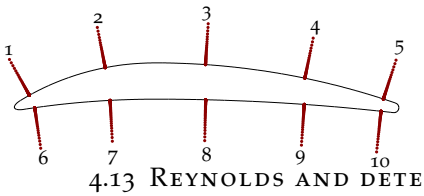


Figure 98: $\overline{u'_s u'_n}$ budget terms for run 1 stator ($\psi = 0.422$). Normalized by u_τ^4/ν, using the global u_τ.



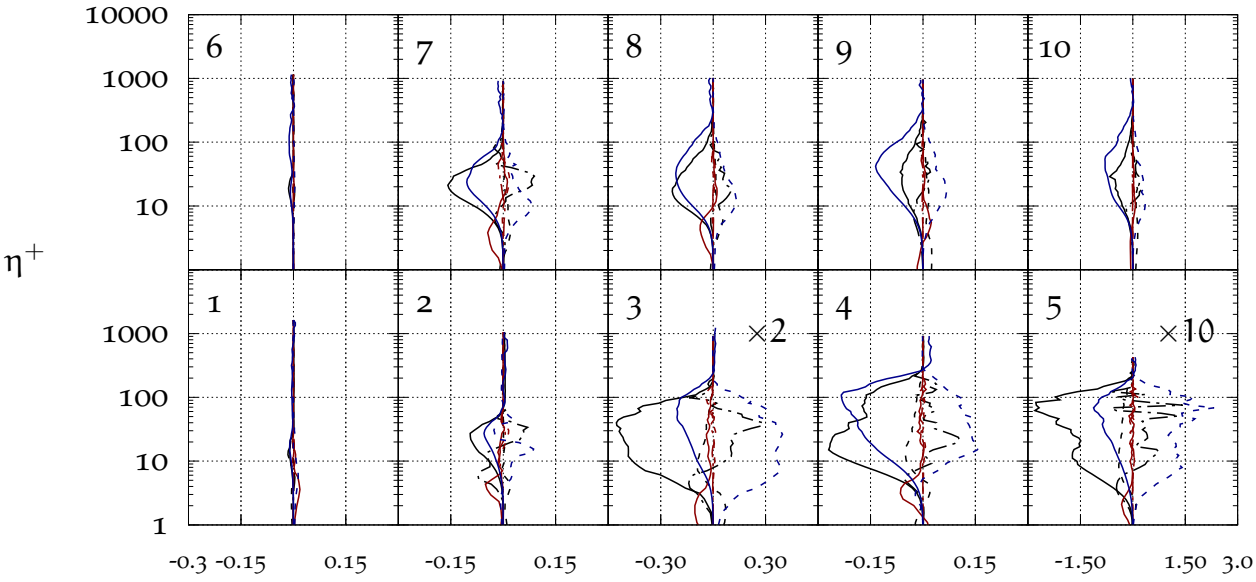
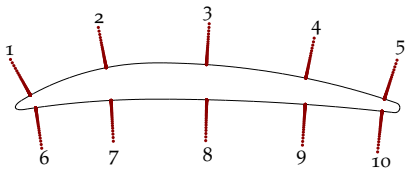


Figure 99: $\overline{u'_s u'_n}$ budget terms in inner coordinates for run 1 ($\psi = 0.422$). Normalized by local u_τ.— $\frac{\nu}{u_\tau^4} P'_{sn}$ - - - $\frac{\nu}{u_\tau^4} \epsilon'_{sn}$ -·- $\frac{\nu}{u_\tau^4} T'_{sn}$ — $\frac{\nu}{u_\tau^4} V'_{sn}$ - - - $\frac{\nu}{u_\tau^4} \widetilde{D}_{sn}$ -·- $\frac{\nu}{u_\tau^4} \Phi'_{sn}$ - - - $\frac{\nu}{u_\tau^4} \Pi'_{sn}$ — $\frac{1}{8u_\tau^2} \overline{u'_s u'_n}$. Probe number in top-left corner.



Similar to the Reynolds shear stress budget for run 1, the most dominant terms in the budget for run 2 are also P'_{sn}, T'_{sn} and Π'_{sn}. On the suction side of the blade, the Reynolds shear stress budget in Figure 101 is very similar to that on the suction side of the blade in run 1: the budget terms are mostly active between $\eta^+ = 10 - 100$, the mean-flow production rate acts as a source term and the turbulent transport rate and pressure-gradient velocity term act as sinks. One notable difference from run 1 however is that probe 2 is operating under a favourable pressure-gradient in run 2, and the budget terms are all essentially zero throughout the boundary layer.

On the pressure side of the blade, although the boundary layer profiles are different to those on the pressure side in run 1, the three largest terms are nevertheless again P'_{sn}, T'_{sn} and Π'_{sn}. The mean-flow production rate is again a source term, and the pressure-gradient velocity correlation a sink term. At probe 6 however, P'_{sn} is no longer active under $\eta^+ = 20$. Instead, T'_{sn} acts as a source term. This continues in probe 7, even though now the mean-flow production rate is also large at $\eta^+ = 20$. $\overline{u'_s u'_n}$ does not however show elevated levels in this region in Figure 76 due to the fact that the dissipative effect of the pressure-gradient velocity correlation is also large in this region. Similar to run 1, the mean-flow convection rate appears not to play much of a role in the boundary layer profiles in Figure 101.

An interesting feature of the Reynolds shear stress budgets of runs 1 and 2 is the high-degree of similarity of the mean-flow production rate and velocity pressure-gradient correlation. In the mid-span contour plots, and almost all boundary layer profiles, P'_{sn} and Π'_{sn} have similar profiles but opposite signs. It is well known that pressure-gradient fluctuations act to redistribute turbulent kinetic energy among the three components, in an effort to make the stress field more isotropic[77]. The behaviour of P'_{sn} and Π'_{sn} in the current section is another manifestation of the pressure acting to make the RS field isotropic. An isotropic tensor can only have non-zero off-diagonal entries. Therefore as the mean-flow strain rate acts to produce $\overline{u'_s u'_n}$, perturbations in the pressure-gradient are induced so as to destroy $\overline{u'_s u'_n}$ and return the Reynolds stress field to isotropy.

Finally, it is worth noting that as Figure 101 shows, the deterministic terms play a much smaller role in the Reynolds shear stress budget than they did in the TKE budget for run 2.

As the contour plot for $\overline{u'_s u'_n}$ in Figure 79 and the TKE budget in Figure 90 suggest, the Reynolds shear stress budget for run 3 is dominated by the activity in the pressure side separation bubble. The results are thus qualitatively very similar to those in the separation bubble in Figure 100 and Figure 101, and have been omitted here for brevity.

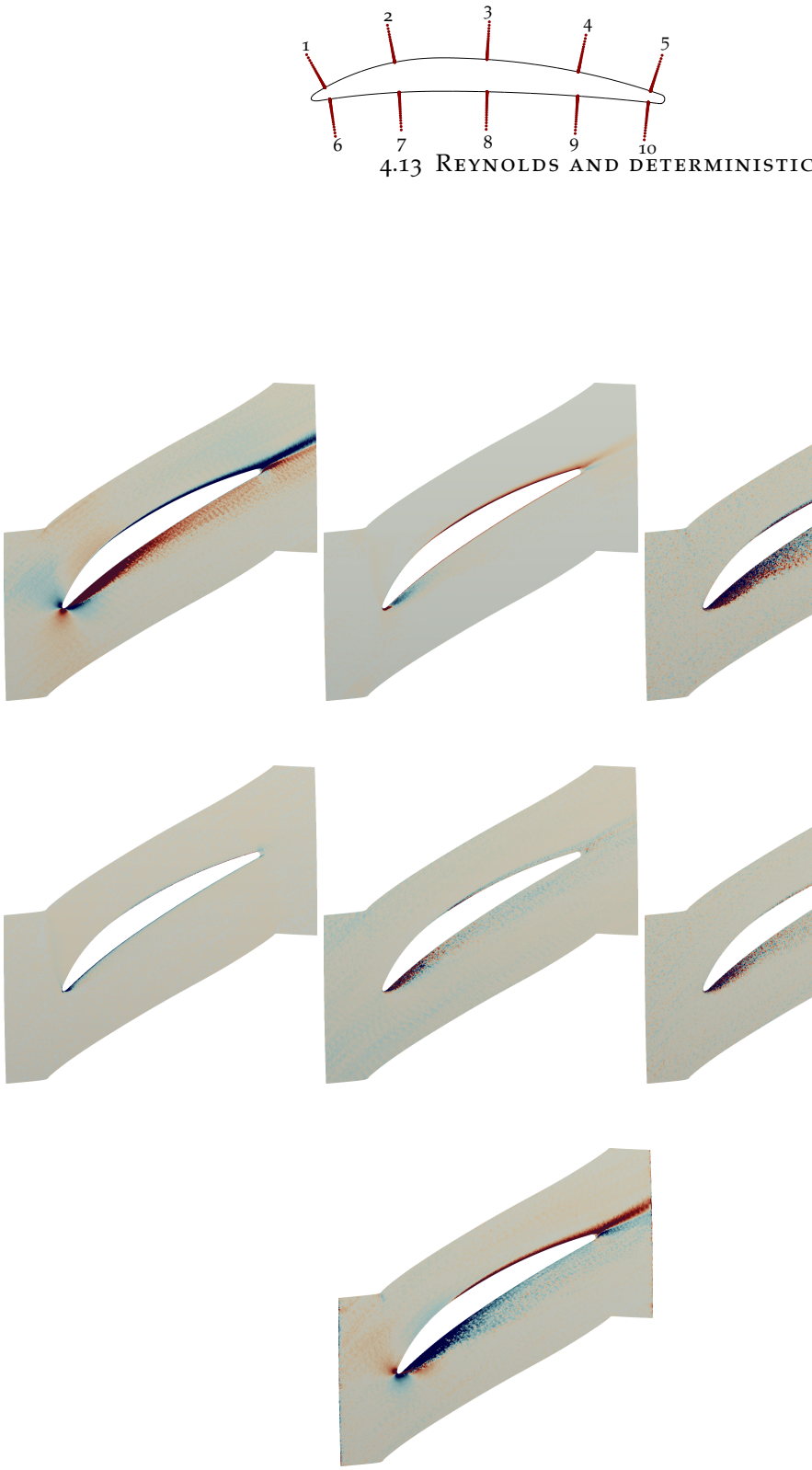
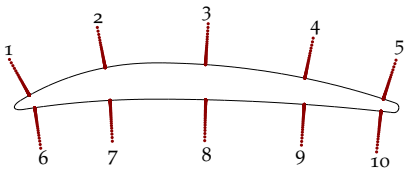


Figure 100: $\overline{u'_s u'_n}$ budget terms for run 2 stator ($\psi = 0.204$). Normalized by u_τ^4/ν, using the global u_τ.



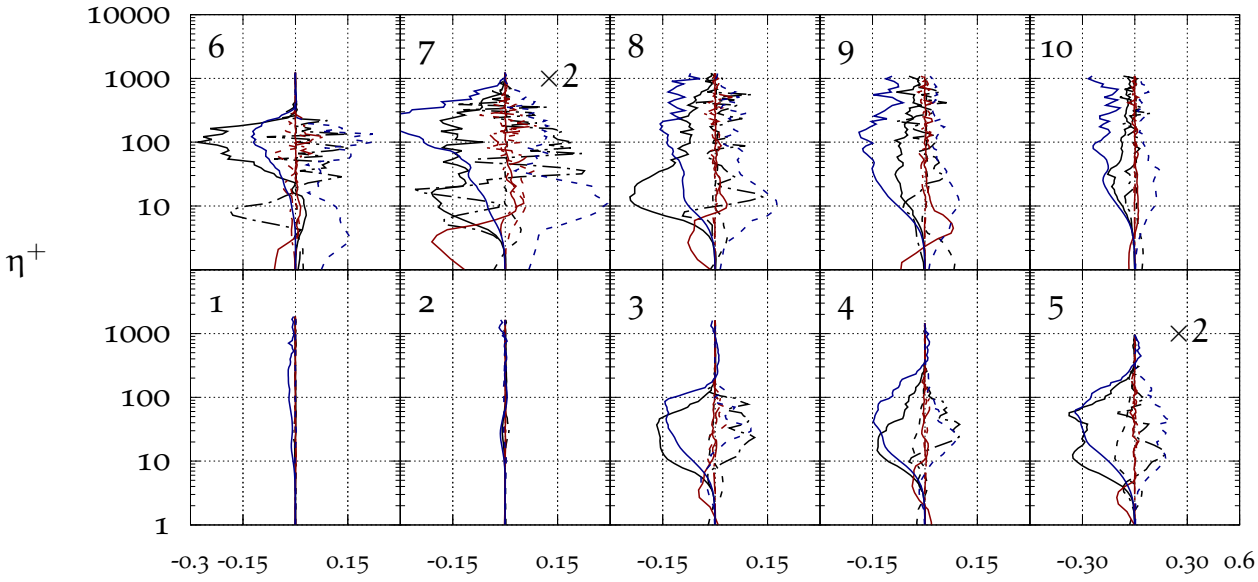
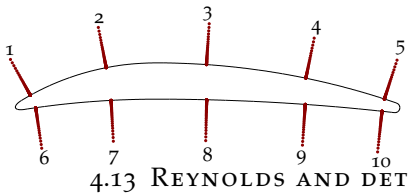


Figure 101: $\overline{u'_s u'_n}$ budget terms in inner coordinates for run 2 ($\psi = 0.204$). Normalized by local u_τ.— $\frac{\nu}{u_\tau^4} P'_{sn}$ - - - $\frac{\nu}{u_\tau^4} \epsilon'_{sn}$ -·- $\frac{\nu}{u_\tau^4} T'_{sn}$ — $\frac{\nu}{u_\tau^4} V'_{sn}$ - - - $\frac{\nu}{u_\tau^4} \widetilde{D}_{sn}$ -·- $\frac{\nu}{u_\tau^4} \Phi'_{sn}$ - - $\frac{\nu}{u_\tau^4} \Pi'_{sn}$ — $\frac{1}{\delta u_\tau^2} \overline{u'_s u'_n}$. Probe number in top-left corner.



4.13.2.2 *Deterministic shear stress*

As Figure 102 shows, the viscous terms are even less significant in the deterministic shear stress budget than they were in the DKE budget in Figure 92. The deterministic transport rate (triple correlation) is again only active at the passage inlet. Similar to the Reynolds shear stress budget, the mean-flow production rate and pressure-gradient velocity correlation show dipole like peaks around the leading edge, but with opposite signs. The link between these two terms is not as strong however as it was in the Reynolds shear stress budget. In Figure 102, this is most clearly seen in the suction side boundary layer, where $\widetilde{P}_{sn}$ and $\widetilde{\Pi}_{sn}$ do not have opposing signs at all locations. The boundary layer profiles in Figure 103 confirm this, as the profiles at none of the probes shown any link between $\widetilde{P}_{sn}$ and $\widetilde{\Pi}_{sn}$. This observation thus suggests that the role of pressure-gradient fluctuations in the DS budget corresponds to more of a true source/sink term, rather than to purely redistribute energy among the components.

The boundary layer profiles also reveal that similar to the DKE budget, the deterministic shear stress budget is dominated by mean-flow convection and the turbulent terms. A clear example of this is visible in probe 3, where the sharp dip in the profile of $\overline{\tilde{u}_s \tilde{u}_n}$ at $\eta^+ = 50$ happens at the exact location of the peak in the turbulent diffusion rate. One notable exception is probe 5, where the profile of $\overline{\tilde{u}_s \tilde{u}_n}$ correlates very well with the mean-flow production rate. At probe 5 therefore, it appears that $\widetilde{P}_{sn}$ is the dominant budget term, as was the case in the DKE budget. This adds further evidence for the hypothesis that regions of high adverse pressure gradient generate deterministic stresses.

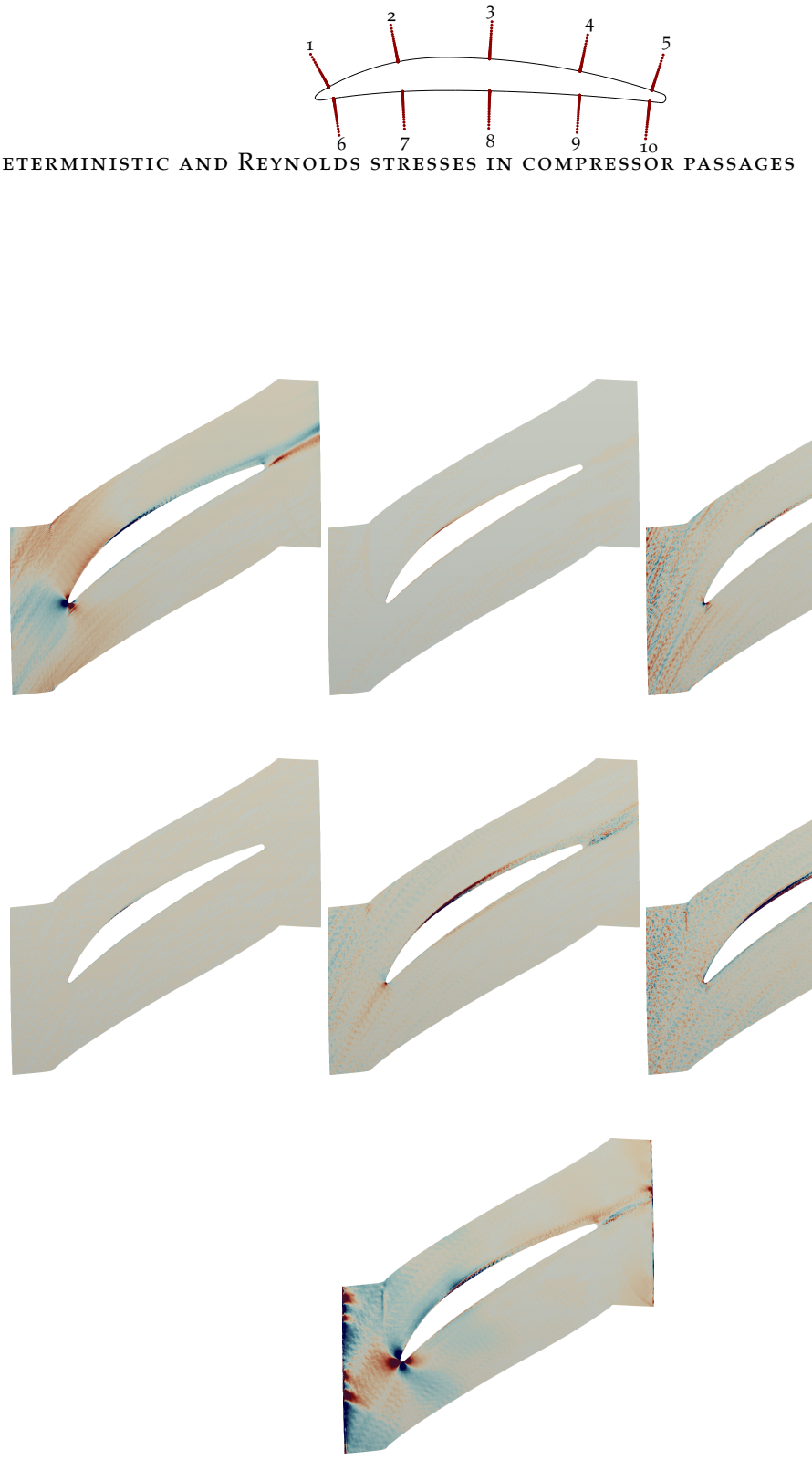
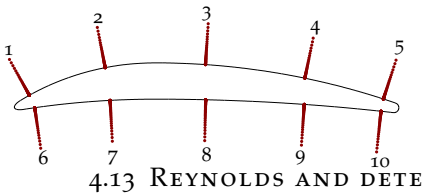


Figure 102: $\widetilde{\widetilde{u}_s\widetilde{u}_n}$ budget terms for run 1 stator ($\psi = 0.422$). Normalized by u_τ^4/ν, using the global u_τ.



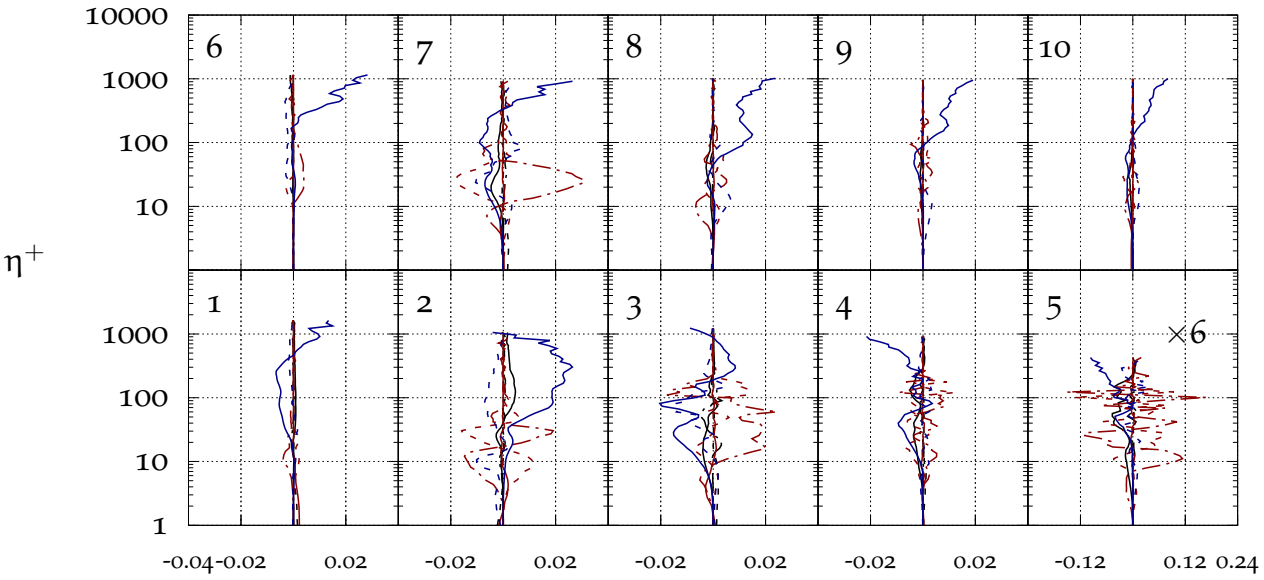
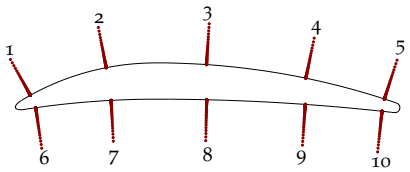


Figure 103: $\overline{\tilde{u}_s\tilde{u}_n}$ budget terms in inner coordinates for run 1 ($\psi = 0.422$). Normalized by local u_τ.— $\frac{\nu}{u_\tau^4}\widetilde{P}_{sn}$ - - - $\frac{\nu}{u_\tau^4}\widetilde{\epsilon}_{sn}$ -·- $\frac{\nu}{u_\tau^4}\widetilde{T}_{sn}$ — $\frac{\nu}{u_\tau^4}\widetilde{V}_{sn}$ - - - $\frac{\nu}{u_\tau^4}\widetilde{D}_{sn}$ -·- $\frac{\nu}{u_\tau^4}\widetilde{\Phi}_{sn}$ - - $\frac{\nu}{u_\tau^4}\widetilde{\Pi}_{sn}$ — $\frac{1}{6u_\tau^2}\overline{\tilde{u}_s\tilde{u}_n}$. Probe number in top-left corner.



The most interesting feature of the Deterministic shear stress budget for run 2 is perhaps the behaviour inside the pressure side separation bubble. In the DKE budget in Figure 95, the mean-flow production rate at probe 6 was positive and was thus contributing to the DKE. In Figure 105 however, the mean-flow production rate at probe 6 is acting in the opposite direction of the deterministic shear stress. The mean-flow is thus acting to remove the deterministic shear stress being convected to probe 6. The effects of this are seen in probe 7, where the profile of $\overline{\tilde{u}_s \tilde{u}_n}$ reverses sign over the entire region where $\widetilde{P}_{sn}$ was active in probe 6. Over the remainder of the probes on the pressure side, the deterministic shear stress budget terms show little activity under $\eta^+ = 100$, above which mean-flow convection dominates.

On the suction side of the blade, both $\overline{\tilde{u}_s \tilde{u}_n}$ and the budget terms show very little activity in probes 1 and 2 in Figure 105. At probe 3, the turbulent terms are very large from the wall up to $\eta^+ = 100$, but all the budget terms appear to cancel each other out. Above $\eta^+ = 100$, $\overline{\tilde{u}_s \tilde{u}_n}$ is large due to convection by the mean-flow. This is also the case at probe 4, although the individual budget terms are much smaller in magnitude under $\eta^+ = 100$. In run 2, the boundary layer at probe 5 is again operating under an adverse pressure gradient, and consequently, $\widetilde{P}_{sn}$ is significant up until $\eta^+ = 200$.

The deterministic shear stress budget terms for run 2 again a show a weaker link between $\widetilde{P}_{sn}$ and $\widetilde{\Pi}_{sn}$ than that between P'_{sn} and Π'_{sn}.

The Reynolds shear stress budget terms showed that the mean-flow production rate and pressure-gradient velocity correlation had very similar profiles throughout the compressor but opposite signs. The pressure-gradient velocity correlation was thus acting to make the Reynolds stress field isotropic. A similar phenomenon was seen in the deterministic shear stress budgets, but the link between the mean-flow production rate and pressure-gradient velocity correlation was a lot weaker.

Section 4.13.3 examines the pressure-gradient velocity correlation in greater detail.

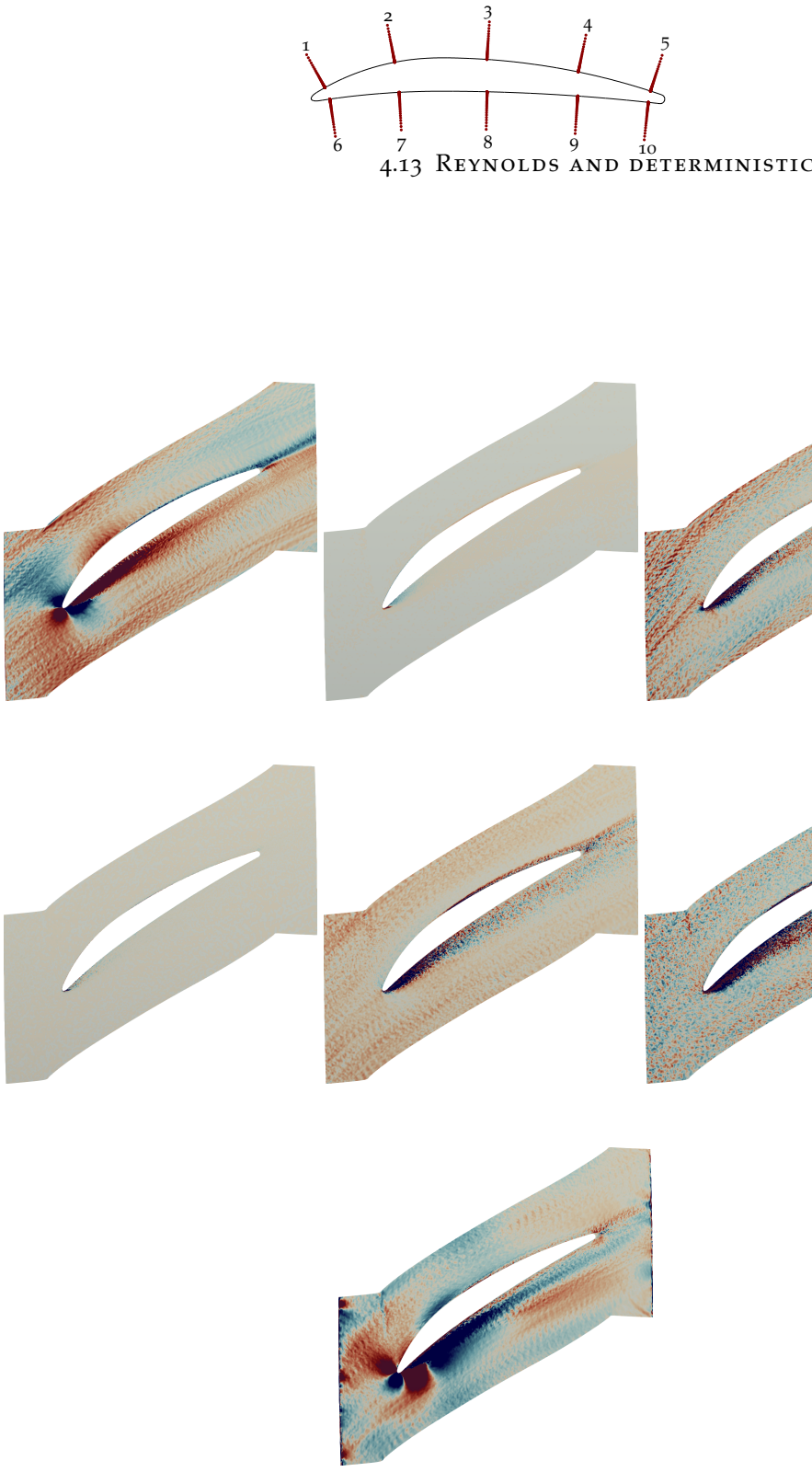
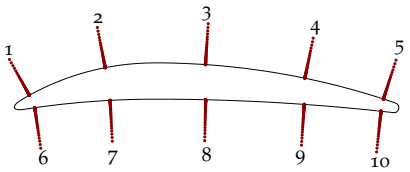


Figure 104: $\widetilde{\overline{u}_s \overline{u}_n}$ budget terms for run 2 stator ($\psi = 0.204$). Normalized by u_τ^4/ν, using the global u_τ.



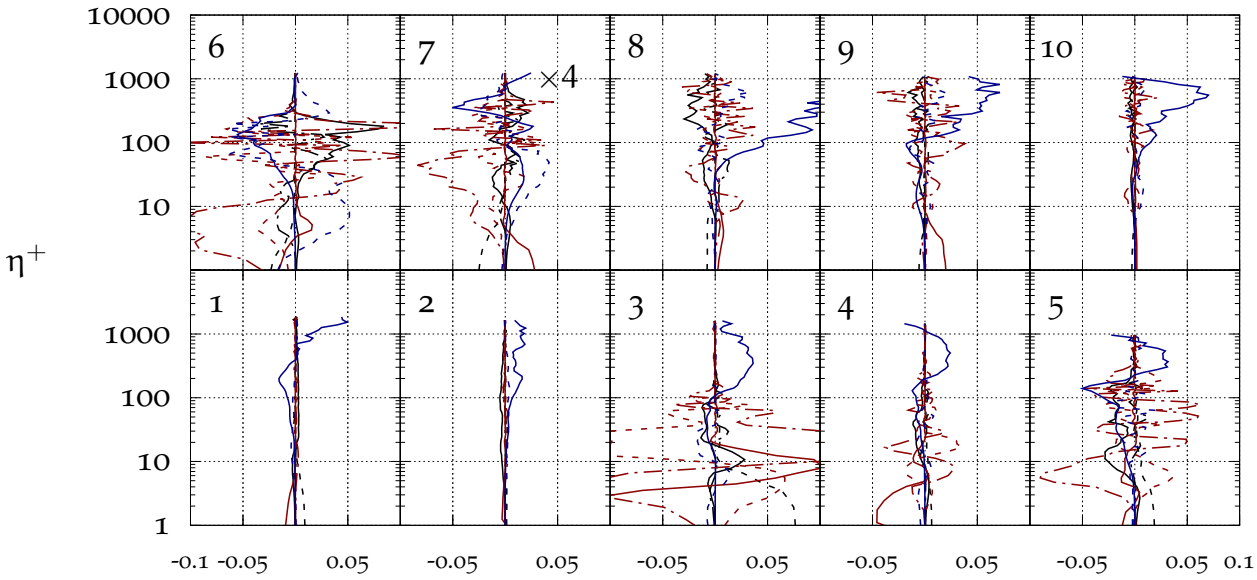
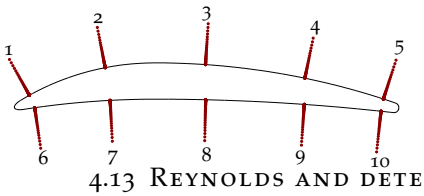


Figure 105: $\overline{\tilde{u}_s \tilde{u}_n}$ budget terms in inner coordinates for run 2 ($\psi = 0.204$). Normalized by local u_τ.— $\frac{\nu}{u_\tau^4}\widetilde{P}_{sn}$ - - - $\frac{\nu}{u_\tau^4}\widetilde{\epsilon}_{sn}$ -·- $\frac{\nu}{u_\tau^4}\widetilde{T}_{sn}$ — $\frac{\nu}{u_\tau^4}\widetilde{V}_{sn}$ - - - $\frac{\nu}{u_\tau^4}\widetilde{D}_{sn}$ -·- $\frac{\nu}{u_\tau^4}\widetilde{\Phi}_{sn}$ - - $\frac{\nu}{u_\tau^4}\widetilde{\Pi}_{sn}$ — $\frac{1}{\delta u_\tau^2}\overline{\tilde{u}_s \tilde{u}_n}$. Probe number in top-left corner.



4.13.3 *Pressure-gradient velocity correlation*

A common way of analysing the pressure-gradient velocity correlation in the Reynolds stress budget is to separate it into a pressure-transport, χ'_{ij}, and redistributive term, ζ'_{ij},[77]:

$$\begin{aligned} \Pi'_{ij} &= -\frac{\partial}{\partial x_k}\left(\overline{p'\left(u'_i\delta_{jk} + u'_j\delta_{ik}\right)}\right) + \overline{p'\left(\frac{\partial u'_j}{\partial x_i} + \frac{\partial u'_i}{\partial x_j}\right)} \\ \Pi'_{ij} &= \chi'_{ij} + \zeta'_{ij} \end{aligned} \tag{63}$$

Figure 106 shows the pressure term split for the Reynolds normal stresses in the blade surface boundary layers for run 1. In their investigations of turbulent channel flow, Moin and Kim[84] discovered that in the near-wall region, the pressure-strain term acts to redistribute turbulent kinetic energy from the wall-normal component to the wall-parallel components. The authors termed this effect as "splatting"[84].

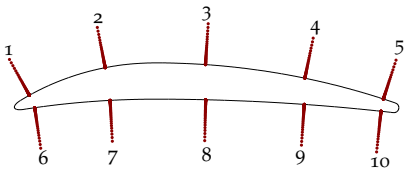
In Figure 106, the "splatting effect" is also visible on the pressure side of the blade from probes 7-9. Under $\eta^+ = 10$, ζ'_{nn} is negative and both ζ'_{ss} and ζ'_{ww} are positive. Splatting is also visible in the viscous sub-layer in probe 5. At all other probes on the suction side however, the opposite effect to splatting can be seen; ζ'_{nn} is positive and ζ'_{ss} and ζ'_{ww} are negative. These locations are also characterized by Π'_{ww} being the largest component of the pressure-gradient velocity correlation, as well as Π'_{nn} being essentially zero in the viscous sub-layer. Nonetheless, even at probes 1-4 on the suction side, there is still a net transfer of TKE between the wall-normal and the wall-parallel components, and the pressure-gradient velocity correlation is thus acting to return the Reynolds stress field to isotropy.

Above $\eta^+ = 10$, there is a transfer of energy from $\overline{u'_s u'_s}$ to the cross-stream components. This is seen most clearly in probes 3-5, where ζ'_{ss} is negative, and ζ'_{nn} and ζ'_{ww} are positive. This effect was also present in the results of Moin and Kim[84].

The pressure-gradient velocity correlation split for the deterministic normal stresses for run 1 is shown in Figure 107. In the viscous sub-layer, the pressure-velocity correlation is again acting to redistribute energy between the wall-normal and wall-parallel components of the DKE. The direction of this energy transfer is not always in the same direction. Moreover, at most probes only one of the wall-parallel components is active in the viscous sub-layer.

Where Figure 107 differs from the pressure-velocity correlation for the TKE budget is the behaviour outside the viscous sub-layer. Above $\eta^+ = 10$, the profiles do not consistently show a transfer of energy between the streamwise and cross-stream components.

Figure 107 thus shows that the pressure-strain term in the deterministic stress budget also plays the role of redistributing energy between the wall-normal and wall-parallel directions in the viscous sub-layer. Above $\eta^+ = 10$, the pressure-strain term has less of a tendency to return the deterministic stress field to isotropy. This is consistent with the contour plots in Figure 102 and Figure 104 which also showed a weaker link between $\widetilde{\Pi}_{sn}$ and $\widetilde{P}_{sn}$ than in the Reynolds shear stress budget.



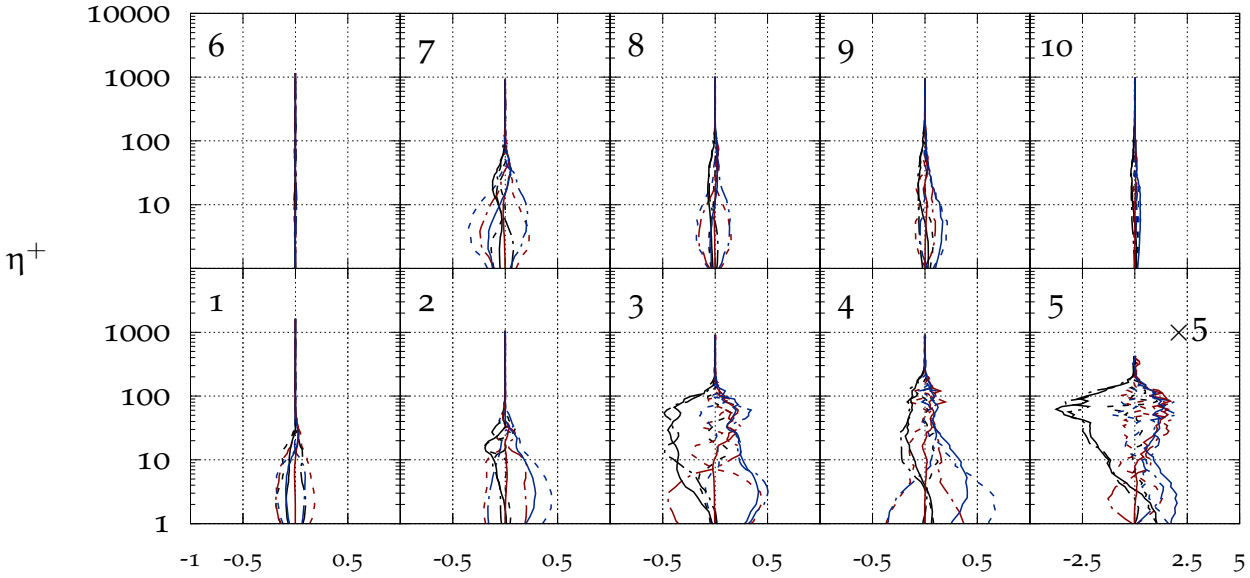


Figure 106: Pressure-gradient velocity correlation split for Reynolds normal stresses in inner coordinates for run 1 ($\psi = 0.422$). Normalized by local u_τ. — $\frac{\nu}{u_\tau^4}\Pi'_{ss}$ — $\frac{\nu}{u_\tau^4}\Pi'_{nn}$ — $\frac{\nu}{u_\tau^4}\Pi'_{ww}$ - - - $\frac{\nu}{u_\tau^4}\chi'_{ss}$ - - - $\frac{\nu}{u_\tau^4}\chi'_{nn}$ - - - $\frac{\nu}{u_\tau^4}\chi'_{ww}$ -·- $\frac{\nu}{u_\tau^4}\zeta'_{ss}$ -·- $\frac{\nu}{u_\tau^4}\zeta'_{nn}$ -·- $\frac{\nu}{u_\tau^4}\zeta'_{ww}$. Probe number in top-left corner.

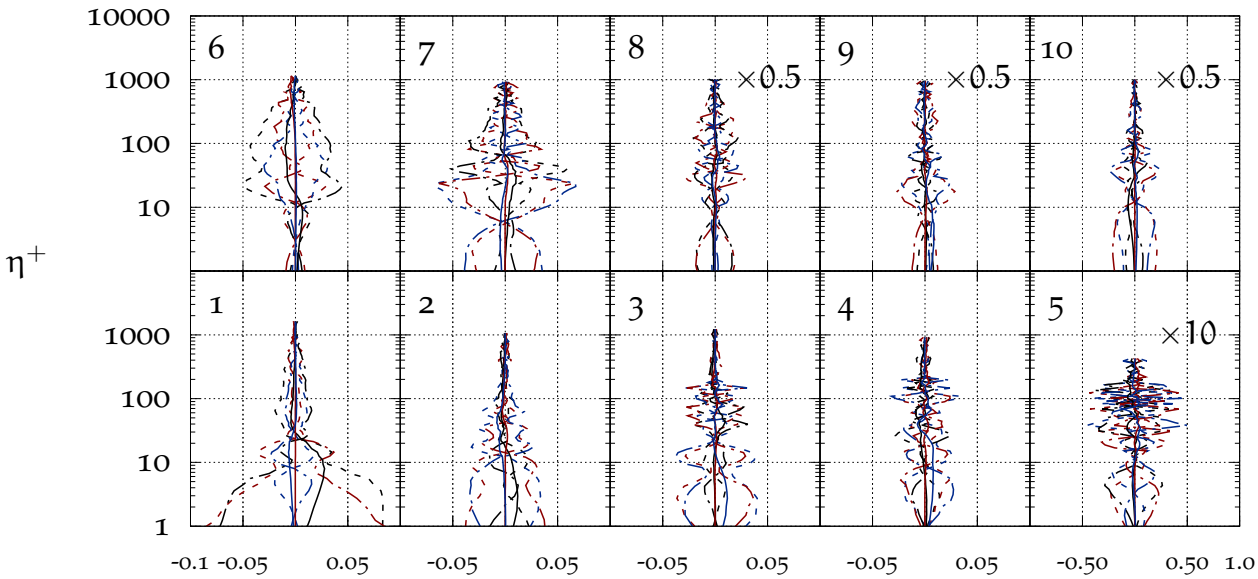


Figure 107: Pressure-gradient velocity correlation split for deterministic normal stresses in inner coordinates for run 1 ($\psi = 0.422$). Normalized by local u_τ. — $\frac{\nu}{u_\tau^4}\widetilde{\Pi}_{ss}$ — $\frac{\nu}{u_\tau^4}\widetilde{\Pi}_{nn}$ — $\frac{\nu}{u_\tau^4}\widetilde{\Pi}_{ww}$ - - - $\frac{\nu}{u_\tau^4}\widetilde{\chi}_{ss}$ - - - $\frac{\nu}{u_\tau^4}\widetilde{\chi}_{nn}$ - - - $\frac{\nu}{u_\tau^4}\widetilde{\chi}_{ww}$ -·- $\frac{\nu}{u_\tau^4}\widetilde{\zeta}_{ss}$ -·- $\frac{\nu}{u_\tau^4}\widetilde{\zeta}_{nn}$ -·- $\frac{\nu}{u_\tau^4}\widetilde{\zeta}_{ww}$. Probe number in top-left corner.

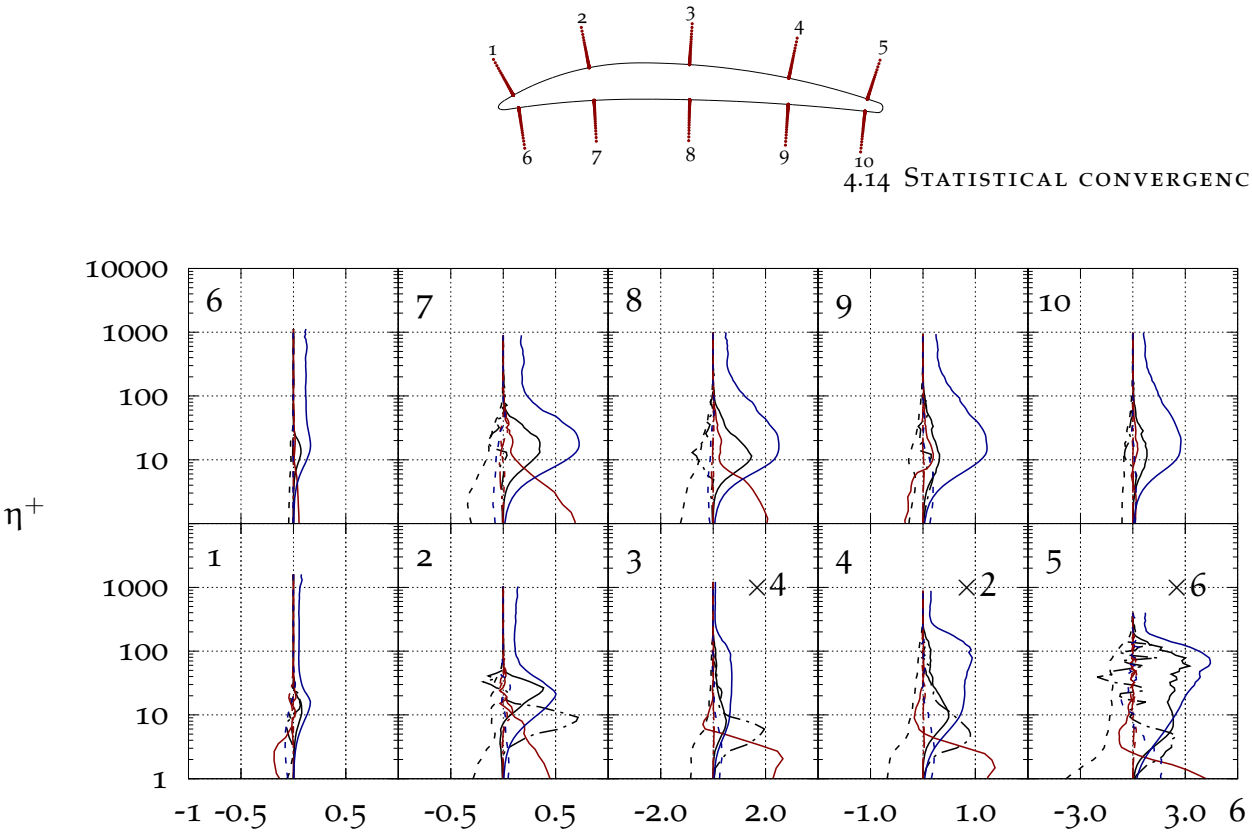


Figure 108: TKE budget terms in inner coordinates for run 1 ($\psi = 0.422$). Statistical sample size corresponds to 43 blade pass periods. Normalized by local u_τ.— $\frac{\nu}{u_\tau^4}P'_{ii}$ - - - $\frac{\nu}{u_\tau^4}\epsilon'_{ii}$ -·- $\frac{\nu}{u_\tau^4}T'_{ii}$ — $\frac{\nu}{u_\tau^4}V'_{ii}$ - - - $\frac{\nu}{u_\tau^4}\widetilde{D}_{ii}$ -·- $\frac{\nu}{u_\tau^4}\Phi'_{ii}$ - - - $\frac{\nu}{u_\tau^4}\Pi'_{ii}$ — $\frac{1}{16u_\tau^2}\overline{u'_i u'_i}$. Probe number in top-left corner.

4.14 Statistical convergence

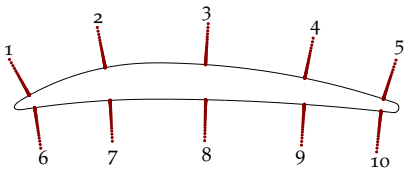
Some of the quantities reported herein suffer from a significant degree of statistical noise, most notably the TKE and DKE budget terms for runs 2 and 3, as well as the deterministic pressure-gradient velocity correlation split for run 1. A mechanism is thus needed for separating the statistically significant results from the noise.

In order to define a statistical convergence metric, it is necessary to first examine the convergence history of the various turbulent statistics. Figure 108 shows the TKE budget terms for run 1 ($\psi = 0.422$) computed over a sample size corresponding to 43 budget terms, and Figure 109 replots the TKE budget terms corresponding to the full time-history.

A comparison of Figure 108 and Figure 109 reveals surprisingly few differences. There is virtually no difference in the pressure side probes. On the suction side, only the turbulent transport rates has noticeably different profiles at probes 2, 3 and 5.

Figure 110 and Figure 111 repeat the same analysis for the DKE budget terms. In this case, the differences between the two sample sets are much more pronounced. The most notable examples are the mean-flow production rates at probes 1 and 2, and the turbulent dissipation and diffusion rates at probes 2-5.

In the case of the pressure-gradient velocity correlation split for $\widetilde{\Pi}_{ii}$, the comparison between the two statistical sample sets is even more pronounced, as Figure 112 and Figure 113 show. All ten probes show significant variation between the reduced and full sample set. Moreover, whereas it is impossible to discern any meaningful trends at probes 1 and 2 in Figure 112, the results from the full sample set show a much clearer picture.



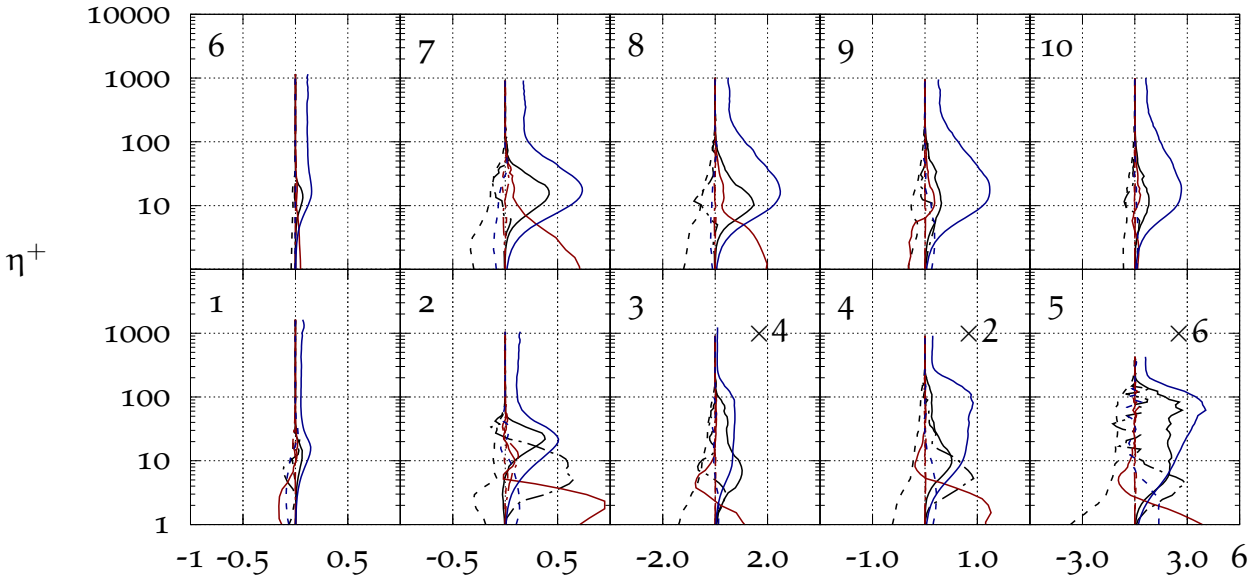


Figure 109: TKE budget terms in inner coordinates for run 1 ($\psi = 0.422$). Statistical sample size corresponds to 70 blade pass periods. Normalized by local u_τ.— $\frac{\nu}{u_\tau^4}P'_{ii}$ - - - $\frac{\nu}{u_\tau^4}\epsilon'_{ii}$ -·- $\frac{\nu}{u_\tau^4}T'_{ii}$ — $\frac{\nu}{u_\tau^4}V'_{ii}$ - - - $\frac{\nu}{u_\tau^4}\widetilde{D}_{ii}$ -·- $\frac{\nu}{u_\tau^4}\Phi'_{ii}$ - - - $\frac{\nu}{u_\tau^4}\Pi'_{ii}$ — $\frac{1}{16u_\tau^2}\overline{u'_i u'_i}$. Probe number in top-left corner.

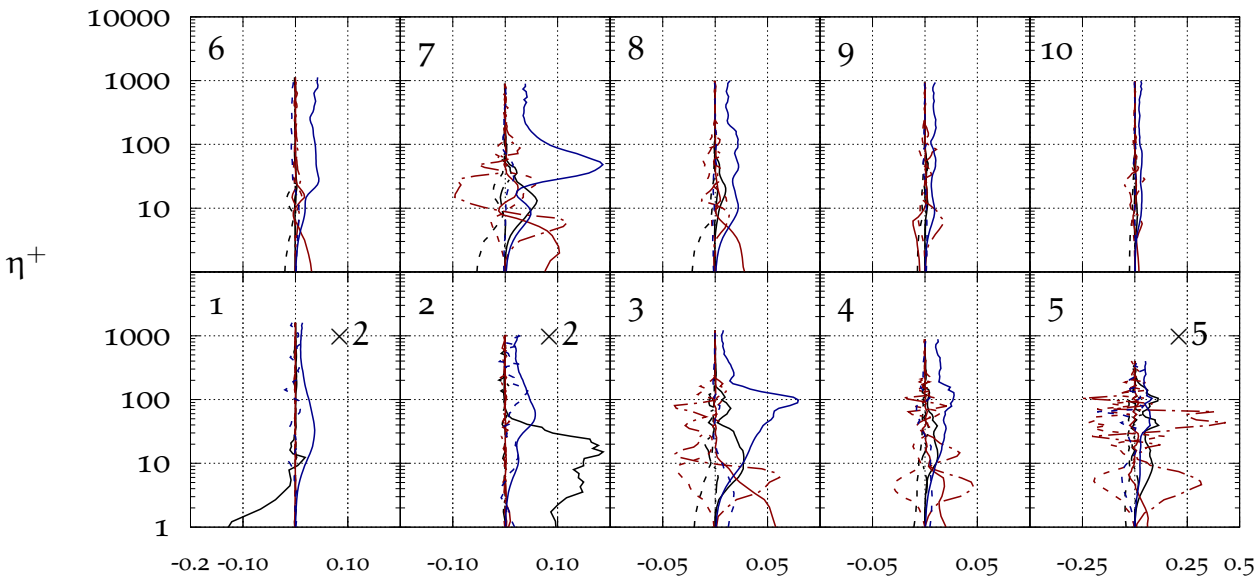


Figure 110: DKE budget terms in inner coordinates for run 1 ($\psi = 0.422$). Statistical sample size corresponds to 43 blade pass periods. Normalized by local u_τ.— $\frac{\nu}{u_\tau^4}\widetilde{P}_{ii}$ - - - $\frac{\nu}{u_\tau^4}\widetilde{\epsilon}_{ii}$ -·- $\frac{\nu}{u_\tau^4}\widetilde{T}_{ii}$ — $\frac{\nu}{u_\tau^4}\widetilde{V}_{ii}$ - - - $\frac{\nu}{u_\tau^4}\widetilde{D}_{ii}$ -·- $\frac{\nu}{u_\tau^4}\widetilde{\Phi}_{ii}$ - - - $\frac{\nu}{u_\tau^4}\widetilde{\Pi}_{ii}$ — $\frac{1}{30u_\tau^2}\overline{\widetilde{u}_i\widetilde{u}_i}$. Probe number in top-left corner.

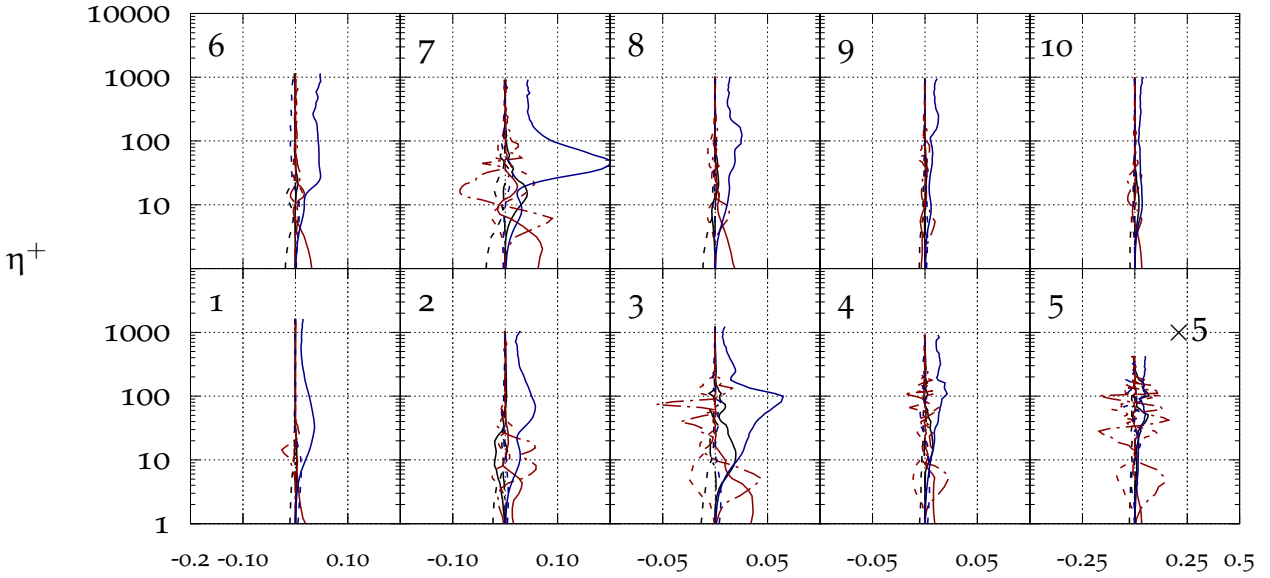


Figure 111: DKE budget terms in inner coordinates for run 1 ($\psi = 0.422$). Statistical sample size corresponds to 70 blade pass periods. Normalized by local u_τ.— $\frac{\nu}{u_\tau^4}\widetilde{P}_{ii}$ - - - $\frac{\nu}{u_\tau^4}\widetilde{\epsilon}_{ii}$ -·- $\frac{\nu}{u_\tau^4}\widetilde{T}_{ii}$ — $\frac{\nu}{u_\tau^4}\widetilde{V}_{ii}$ - - - $\frac{\nu}{u_\tau^4}\widetilde{D}_{ii}$ -·- $\frac{\nu}{u_\tau^4}\widetilde{\Phi}_{ii}$ - - - $\frac{\nu}{u_\tau^4}\widetilde{\Pi}_{ii}$ — $\frac{1}{30u_\tau^2}\overline{\tilde{u}_i\tilde{u}_i}$. Probe number in top-left corner.

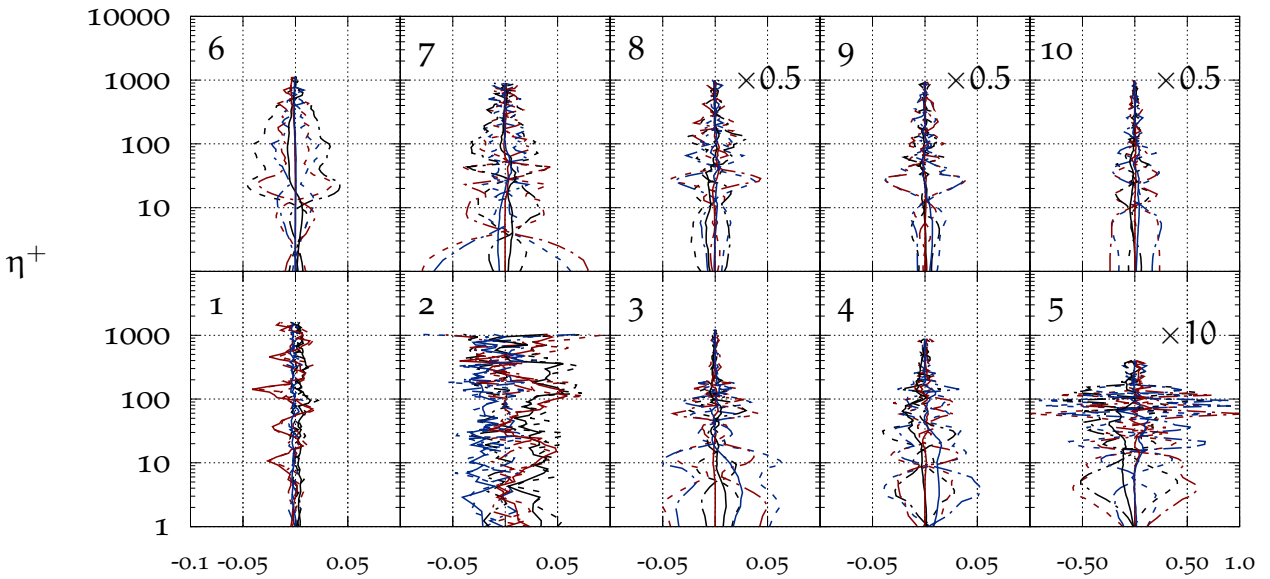
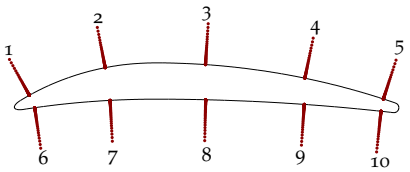


Figure 112: Pressure-gradient velocity correlation split for deterministic normal stresses in inner coordinates for run 1 ($\psi = 0.422$). Statistical sample size corresponds to 43 blade pass periods. Normalized by local u_τ. — $\frac{\nu}{u_\tau^4}\widetilde{\Pi}_{ss}$ — $\frac{\nu}{u_\tau^4}\widetilde{\Pi}_{nn}$ — $\frac{\nu}{u_\tau^4}\widetilde{\Pi}_{ww}$ - - - $\frac{\nu}{u_\tau^4}\widetilde{\chi}_{ss}$ - - - $\frac{\nu}{u_\tau^4}\widetilde{\chi}_{nn}$ - - - $\frac{\nu}{u_\tau^4}\widetilde{\chi}_{ww}$ -·- $\frac{\nu}{u_\tau^4}\widetilde{\zeta}_{ss}$ -·- $\frac{\nu}{u_\tau^4}\widetilde{\zeta}_{nn}$ -·- $\frac{\nu}{u_\tau^4}\widetilde{\zeta}_{ww}$.



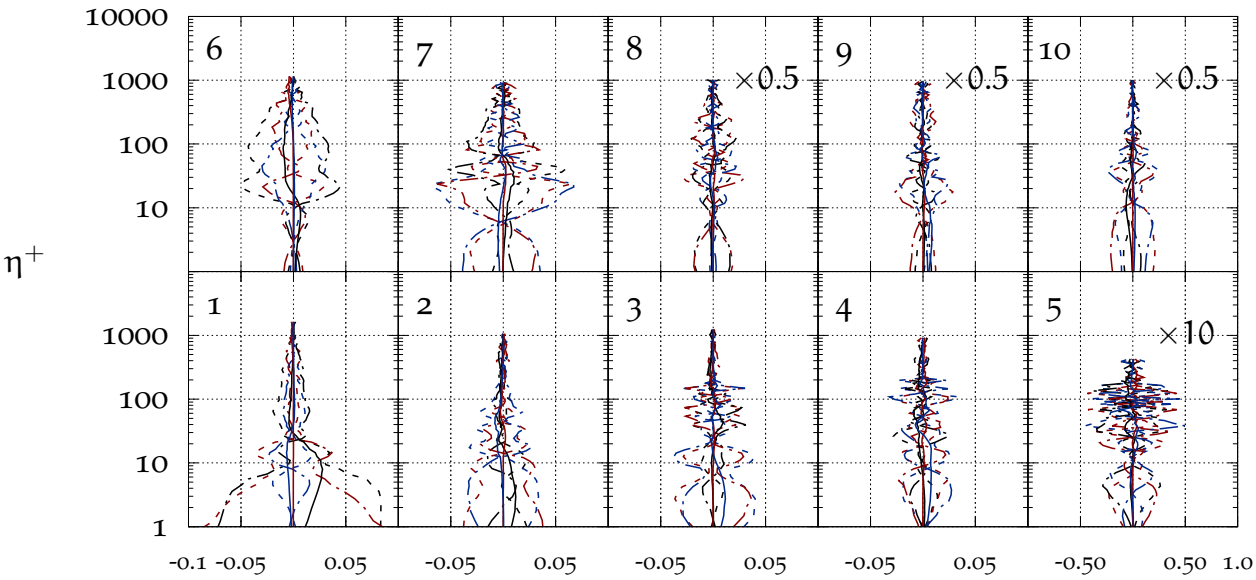


Figure 113: Pressure-gradient velocity correlation split for deterministic normal stresses in inner coordinates for run 1 ($\psi = 0.422$). Statistical sample size corresponds to 70 blade pass periods. Normalized by local u_τ. — $\frac{\nu}{u_\tau^4}\widetilde{\Pi}_{ss}$ — $\frac{\nu}{u_\tau^4}\widetilde{\Pi}_{nn}$ — $\frac{\nu}{u_\tau^4}\widetilde{\Pi}_{ww}$ - - - $\frac{\nu}{u_\tau^4}\widetilde{\chi}_{ss}$ - - - $\frac{\nu}{u_\tau^4}\widetilde{\chi}_{nn}$ - - - $\frac{\nu}{u_\tau^4}\widetilde{\chi}_{ww}$ -·- $\frac{\nu}{u_\tau^4}\widetilde{\zeta}_{ss}$ -·- $\frac{\nu}{u_\tau^4}\widetilde{\zeta}_{nn}$ -·- $\frac{\nu}{u_\tau^4}\widetilde{\zeta}_{ww}$.

The above analysis shows that the convergence rate varies significantly between the various budget terms. A global convergence test would thus be unsuitable, and the convergence status of each of the budget terms should be tested individually.

A statistical convergence residual can be defined based on the Euclidean norm of a boundary layer profile:

$$\|f\|^2 = \int f(\eta)^2 d\eta \tag{64}$$

In Equation 64, f denotes any boundary layer profile, and $\|f\|^2$ its corresponding Euclidean norm. If adding samples of the flowfield yield only a small change in the Euclidean norm of a budget term, it can be deemed to have converged. Based on the experience of the current research, the time period of the additional samples must be at least as large as five blade passes. A change smaller than 5% can be deemed to be sufficiently small.

A meaningful addition to the current work would thus be to collect samples for five more blade passes for all three runs, and check which of the TKE and DKE budget terms reported herein have converged at each of the ten boundary layer probes. Other avenues for extending the work, as well as a summary of all the key findings, are discussed in the next section.

4.15 Summary and conclusions

The current chapter presented the results from LES computations of a compressor repeating stage at three operating points at the same rotational speed. Run 1 represented the design point of the compressor at $\psi = 0.422$, and runs 2 and 3 represented increasingly smaller work coefficients at $\psi = 0.204$ and $\psi = 0.036$. For all three runs, the Reynolds and deterministic stress fields were examined in detail.

In run 1, the Reynolds stresses were most active in the blade boundary layers and wake. Run 2 was operating at negative incidence, and the Reynolds stresses were also active in the pressure side separation bubble. Run 3 was operating at an even larger negative incidence angle, and thus the pressure side separation bubble dominated the Reynolds stress field. Due to the large region of separated flow, the Reynolds stresses were highest in run 3.

The deterministic stresses were generally much smaller than the Reynolds stresses. In run 1, the activity was mostly confined to the front part of the blade surface, the region before the momentum boundary layers begin to grow, including pronounced peaks of all six deterministic stresses at the leading edge. The deterministic kinetic energy was also large at the passage inlet. In runs 2 and 3, the deterministic stresses were greatest in the pressure side separation bubble.

At most locations in the blade passages, the Reynolds stress divergence was much larger than the deterministic stress divergence; the Reynolds stresses thus play a larger role in the time-mean momentum balance. There are however a few regions of the flow where the deterministic stress divergence is significant. In both runs 1 and 2, all three components of the deterministic stress divergence are large at the blade leading edge, and the normal component is also significant at the passage inlet. In run 2, the deterministic stress divergence is also large in the pressure side separation bubble. Although run 3 featured an even larger separation bubble than run 2, the Reynolds stress divergence was nevertheless much larger than the deterministic stress divergence, throughout the blade passage.

The turbulent kinetic energy budget terms were most active in the boundary layers on the blade surface, the wake and in the pressure side separation bubble in runs 2 and 3. In the boundary layers in run 1, viscous dissipation and diffusion are dominant under $\eta^+ = 10$. Above it, the mean-flow production and turbulent transport rate are the largest budget terms. On the latter half of the suction side surface, the mean-flow convection rate is also significant above the viscous sub-layer. As for the deterministic production and diffusion rates, whilst they are not significant in the blade boundary layers, they do show elevated levels at the passage inlet. In run 2, the turbulent kinetic energy budget terms on the suction side of the blade are very similar to those of run 1. On the pressure side of the blade, large amounts of turbulent kinetic energy is generated in the pressure side separation bubble. The deterministic transport rate is also significant in the separation bubble, from the wall up to $\eta^+ \approx 20$. At subsequent probes on the pressure side, the turbulent kinetic energy budget is largely dominated by the mean-flow convection rate. The turbulent kinetic energy budget terms for run 3 are very similar to run 2, and the deterministic transport rate is again significant in the pressure side separation bubble; it is as large as the pressure-gradient velocity correlation at $\eta^+ \approx 100$.

The terms comprising the deterministic kinetic energy budget are mostly smaller than those of the turbulent kinetic energy budget in the boundary layers and wake. Generally, the most active terms in the blade boundary layers are the mean-flow convection rate, mean-flow production rate and the two turbulent terms. The turbulent terms are not only significant in the boundary layers, but also at the passage inlet and the freestream in runs 1 and 2. Another significant feature of the deterministic kinetic energy budget is the dipole-like peaks of the pressure-gradient velocity correlation around the blade leading edge in runs 1 and 2.

The Reynolds shear stress budget showed reduced viscous effects as compared to the turbulent kinetic energy budget. Mean-flow convection, and the deterministic diffusion rate at probe 6 in run 2, were also a lot smaller. Arguably the most interesting term of the Reynolds shear stress budget was the pressure-gradient velocity correlation. Not only did it show the same dipole-like peaks around the leading edge as Π'_{ii}, but throughout the domain it has the same profile as the mean-flow production rate but the opposite sign. Π'_{sn} is thus acting to counter the mean-flow production rate, and make the Reynolds stress field more isotropic.

The pressure-gradient velocity correlation in the deterministic shear stress budget also counteracts the mean-flow production rate, but to a lesser extent than in the Reynolds shear stress budget. Splitting the pressure-gradient velocity correlation into a pressure-transport term and a pressure-strain term reveals that in the Reynolds stress field, the pressure-strain term acts to redistribute turbulent kinetic energy among its three components. In the viscous sub-layer, this is achieved through the well catalogued "splatting" effect[84]. Above $\eta^+ = 10$, there is a transfer of energy from the streamwise to the cross-stream components. The pressure-strain term in the deterministic stress field also exhibits the "splatting" effect. It does not however show the energy transfer between the streamwise and cross-stream components above $\eta^+ = 10$.

The current results show that $\widetilde{D}_{ij}$ and Φ'_{ij} play a significant role in the Reynolds stress budget, and $\widetilde{D}_{ij}$ and $\widetilde{\Phi}_{ij}$ are even more important in the deterministic stress budget. In both cases, the effect is much greater in the presence of large phase-dependent unsteady flow features. A natural way of extending the current results would thus be to run another case at a higher load coefficient, where there would be significant separation on the suction side of the blade. An investigation into the Reynolds and deterministic stress fields in the region influenced by the tip-leakage flow would perhaps be even more interesting. Previous researchers have found very hight levels of deterministic stress in the trajectory of the tip-leakage vortex[124].

Another avenue for future work would be to devise models, to be used in time-averaged computations, for $\widetilde{D}_{ij}$, $\widetilde{\Phi}_{ij}$ and Φ'_{ij}. LES computations on a simplified geometry are best suited to this task, for example, a diverging channel in the presence of synthetic incoming wakes. The data reported herein could then be used to conduct *a priori* tests on the models.

5

CONCLUSION

The current DPhil project investigated turbulence in compressor passages using LES computations of a repeating compressor stage. Several numerical simulations tools were developed in order to conduct this research. This included a new multi-block structured grid generator, capable of generating very high quality numerical grids that are also perfectly partitioned from a load-balancing perspective. A novel sliding plane algorithm was also implemented, which aims to minimize the communication cost and thus allows a sliding plane to be used in massively-parallel computations.

The focus of the research were the Reynolds and deterministic stress fields, their budget terms and the interaction of the two stress fields. Three operating points on a compressor speed line were simulated, one representing the design condition and two representing higher flow coefficients than the design. In most of the domain, the Reynolds stresses were found to be generally larger than the deterministic stresses, and thus also played a larger role in the time-mean momentum balance. Notable exceptions were the blade leading edge and passage inlet, two regions where the deterministic stresses were comparable to the Reynolds stresses, and the deterministic stress divergence was comparable to the Reynolds stress divergence. The deterministic stresses were also significant in large phase-dependent unsteady flow features; pressure side separation bubbles were present in both higher flow coefficient runs.

In the Reynolds stress budget, the deterministic stresses manifest themselves as an additional production term, the deterministic production rate, and a transport term, the deterministic diffusion rate. When examining the turbulent kinetic energy budget terms, the deterministic production and diffusion rates were found to be significant at the passage inlet and in the pressure side separation bubble. The deterministic production rate also appears in the deterministic stress budget, but with an opposite sign than in the Reynolds stress budget. In the deterministic kinetic energy budget, the deterministic production rate and turbulent diffusion rate were found to be dominant budget terms.

Two avenues for extending the research were recommended. The first was to repeat the computations at operating conditions corresponding to more phase-dependent unsteadiness. Two examples are an operating point representing greater loading, and thus separation on the suction side of the blade, and the upper ends of the blade span, where the flowfield is influenced by tip-leakage. Secondly, models for time-averaged computations should be devised for the budget terms encapsulating the interaction of the Reynolds and deterministic stress fields. The data reported herein can be used to conduct *a priori* testing of such models.

In the early stages of the DPhil, an investigation was also carried out into the Re_τ scaling of the Proper Orthogonal Decomposition (POD) modes of the two-point correlation tensor in turbulent channel flow. The two-point correlation tensor quantifies the time-averaged effects of turbulent structures, and the POD modes represent an optimal basis for it. At all the spanwise and streamwise lengthscales examined, the POD modes exhibited good Re_τ scaling once the Chebychev polynomials corresponding to large

wall-normal lengthscales were removed. Even though POD modes at some wavenumbers also scaled well even with the inclusion of the large wall-normal modes, a pattern could not be discerned. Suggestions were made to extend the work by testing the scaling behaviour at even higher values of Re_τ, and by searching for alternative scaling laws for modes corresponding to large wall-normal lengthscales.

BIBLIOGRAPHY

[1] J J Adamczyk. Model Equation for Simulating Flows in Multistage Turbomachinery. *ASME Paper No. 85-GT-226*, 1985.

[2] John J. Adamczyk. Wake Mixing in Axial Flow Compressors. *International Gas Turbine and Aeroengine Congress and Exhibition*, 1996. doi: 10.1115/96-gt-029.

[3] John J. Adamczyk, Richard A. Mulac, and Mark L. Celestina. A Model for Closing the Inviscid Form of the Average-Passage Equation System. *Volume 1: Turbomachinery*, page V001T01A097, 1986. doi: 10.1115/86-GT-227. URL http://proceedings.asmedigitalcollection.asme.org/proceeding.aspx?doi=10.1115/86-GT-227.

[4] a.J. Favre, J J Gaviglio, and R Dumas. Space-time double correlations and spectra in a turbulent boundary layer. *Journal of Fluid Mechanics*, 2(4):313–342, 1957. ISSN 0022-1120. doi: 10.1017/S0022112057000166.

[5] Alvaro A. Aldama. *Filtering Techniques for Turbulent Flow Simulation*, volume 56 of *Lecture Notes in Engineering*. Springer Berlin Heidelberg, Berlin, Heidelberg, 1990. ISBN 978-3-540-52137-2. doi: 10.1007/978-3-642-84091-3. URL http://link.springer.com/10.1007/978-3-642-84091-3.

[6] E Anderson, Z Bai, C Bischof, S Blackford, J Demmel, J Dongarra, J Du Croz, A Greenbaum, S Hammarling, A McKenney, and D Sorensen. *{LAPACK} Users' Guide*. Society for Industrial and Applied Mathematics, Philadelphia, PA, third edition, 1999. ISBN 0-89871-447-8 (paperback).

[7] R F Blackwelder and R E Kaplan. On the wall structure of the turbulent boundary layer. *Journal of Fluid Mechanics*, 76(01):89, 1976. ISSN 0022-1120. doi: 10.1017/S0022112076003145.

[8] W Briggs and V Henson. *The DFT: An Owner's Manual for the Discrete Fourier Transform*. Society for Industrial and Applied Mathematics, 1995. doi: 10.1137/1.9781611971514. URL http://epubs.siam.org/doi/abs/10.1137/1.9781611971514.

[9] Russell A. Brown. Building a Balanced k-d Tree in O(kn log n) Time. 4(1):50–68, 2014. ISSN 2331-7418. URL http://arxiv.org/abs/1410.5420.

[10] K A Browning and C D Watkins. Observations of Clear Air Turbulence by High Power Radar. *Nature*, 227:260–263, 1970. ISSN 00280836. doi: 10.1038/228549a0.

[11] Tuncer Cebeci. Chapter 4 - general behavior of turbulent boundary layers. In Tuncer Cebeci, editor, *Analysis of Turbulent Flows with Computer Programs (Third Edition)*, pages 89 – 153. Butterworth-Heinemann, Oxford, third edition edition, 2013. ISBN 978-0-08-098335-6. doi: https://doi.

org/10.1016/B978-0-08-098335-6.00004-5. URL http://www.sciencedirect.com/science/article/pii/B9780080983356000045.

[12] D H Chambers, R J Adrian, P Moin, D S Stewart, and H J Sung. Karhunen–Loéve expansion of Burgers' model of turbulence. *Physics of Fluids*, 31(9):2573–2582, 1988. ISSN 0031-9171. doi: 10.1063/1.866535. URL http://scitation.aip.org/content/aip/journal/pof1/31/9/10.1063/1.866535.

[13] Dominique Charbonnier and Francis Leboeuf. Steady Flow Simulation of Rotor-Stator Interactions with a New Unsteady Flow Model. *AIAA Joint Propulsion Conference and Exhibit*, pages 1–11, 2004. doi: 10.2514/6.2004-3754.

[14] Haecheon Choi, Parviz Moin, and John Kim. Direct numerical simulation of turbulent flow over a rough bed. *Journal of Fluid Mechanics*, 225:503–539, 1993.

[15] European Commission. *Flightpath 2050: Europe's Vision for Aviation*. Publications Office of the European Union, 2011. URL https://ec.europa.eu/transport/sites/transport/files/modes/air/doc/flightpath2050.pdf.

[16] David B De Graaff and John K Eaton. Reynolds-number scaling of the flat-plate turbulent boundary layer. *Journal of Fluid Mechanics*, 422(May 2009):319–346, 2000. ISSN 00221120. doi: 10.1017/S0022112000001713.

[17] James W Deardorff. A numerical study of three-dimensional turbulent channel flow at large Reynolds numbers. *Journal of Fluid Mechanics*, 41(02):453, 1970. ISSN 0022-1120. doi: 10.1017/S0022112070000691.

[18] Juan C del Alamo and Javier Jimenez. Direct numerical simulation of the very large anisotropic scales in a turbulent channel. *Center for Turbulence Research, Annual Research Briefs 2001*, pages 329–341, 2001.

[19] Juan C del Alamo and Javier Jimenez. Spectra of the very large anisotropic scales in turbulent channels. *Physics of Fluids*, 15(6), 2003. ISSN 10706631. doi: 10.1063/1.1570830.

[20] Juan C Del Alamo, Javier Jimenez, Paulo Zandonade, and Robert D Moser. Scaling of the energy spectra of turbulent channels. *Journal of Fluid Mechanics*, 500:135–144, 2004. ISSN 0022-1120. doi: 10.1017/S002211200300733X. URL http://www.journals.cambridge.org/abstract{_}S002211200300733X.

[21] S. Deutsch and W. C. Zierke. The measurement of boundary layers on a compressor blade in cascade: Part 2—suction surface boundary layers. *Journal of Turbomachinery*, 110(1):138–145, January 1988. doi: 10.1115/1.3262159. URL https://doi.org/10.1115/1.3262159.

[22] S. Deutsch and W. C. Zierke. The measurement of boundary layers on a compressor blade in cascade: Part 3—pressure surface boundary layers and the near wake. *Journal of Turbomachinery*, 110(1):146–152, January 1988. doi: 10.1115/1.3262160. URL https://doi.org/10.1115/1.3262160.

[23] L di Mare, M Klein, W P Jones, and J Janicka. Synthetic turbulence inflow conditions for large-eddy simulation. *Physics of Fluids*, 18(2), 2006. ISSN 10706631. doi: 10.1063/1.2130744.

[24] Luca di Mare. *Large-Eddy Simulation of Wall-Bounded Turbulent Flows*. PhD thesis, Imperial College of Science, Technology and Medicine, 2003.

[25] Douglas Doerfler and Ron Brightwell. Measuring MPI Send and Receive Overhead and Application Availability in High Performance Network Interfaces. pages 331–338, 2006. doi: 10.1007/11846802_46.

[26] Y. Dong and N. A. Cumpsty. Compressor blade boundary layers: Part 2—measurements with incident wakes. *Journal of Turbomachinery*, 112(2):231–240, April 1990. doi: 10.1115/1.2927637. URL https://doi.org/10.1115/1.2927637.

[27] Lars-Erik Eriksson. Practical Three-Dimensional Mesh Generation Using Transfinite Interpolation. *SIAM Journal on Scientific and Statistical Computing*, 6(3):712–741, 2005. ISSN 0196-5204. doi: 10.1137/0906049.

[28] R. L. Evans. Turbulence and Unsteadiness Measurements Downstream of a Moving Blade Row. *Journal of Engineering for Power*, pages 131–137, 1975. ISSN 00220825. doi: 10.1115/1.3445892.

[29] A J Favre, J J Gaviglio, and R J Dumas. Further space-time correlations of velocity in a turbulent boundary layer. *Journal of Fluid Mechanics*, 3(Part 4):344–356, 1958. ISSN 0022-1120. doi: 10.1017/S0022112058000021. URL http://journals.cambridge.org/production/action/cjoGetFulltext?fulltextid=367355{%}5Cnpapers2://publication/uuid/98DA3C5B-74EA-4FDB-B11B-5A52C0A58B22.

[30] J. H. Ferziger and M Peric. Methods for Unsteady Problems. In *Computational Methods for Fluid Dynamics*, chapter 6, pages 135–156. Springer, 3rd edition, 2002.

[31] J. H. Ferziger and M Peric. Solution of the Navier-Stokes Equations. In *Computational Methods for Fluid Dynamics*, chapter 7, pages 157–216. Springer, 3rd edition, 2002.

[32] Joel H Ferziger and Milovan Perić. *Computational Methods for Fluid Dynamics*. Springer Berlin Heidelberg, Berlin, Heidelberg, 2002. ISBN 978-3-540-42074-3. doi: 10.1007/978-3-642-56026-2. URL http://link.springer.com/10.1007/978-3-642-56026-2.

[33] G Berkooz, P Holmes, and J L Lumley. The Proper Orthogonal Decomposition in the Analysis of Turbulent Flows. *Annual Review of Fluid Mechanics*, 25 (1):539–575, 1993. ISSN 0066-4189. doi: 10.1146/annurev.fl.25.010193.002543. URL http://dx.doi.org/10.1146/annurev.fl.25.010193.002543{%}5Cnhttp://www.annualreviews.org/doi/pdf/10.1146/annurev.fl.25.010193.002543.

[34] Massimo Germano, Ugo Piomelli, Parviz Moin, and William H. Cabot. A dynamic subgrid-scale eddy viscosity model. *Physics of Fluids A*, 3(7):1760–1765, 1991. ISSN 08998213. doi: 10.1063/1.857955.

[35] Sandip Ghosal. An Analysis of Numerical Errors in Large-Eddy Simulations of Turbulence. *J. Comput. Phys.*, 125(1):187–206, apr 1996. ISSN 0021-9991. doi: 10.1006/jcph.1996.0088. URL http://dx.doi.org/10.1006/jcph.1996.0088.

[36] Gene H Golub and Charles F Van Loan. *Matrix Computations*. Johns Hopkins University Press, third edition, 1996.

[37] A. Goto. Three-Dimensional Flow and Mixing in an Axial Flow Compressor With Different Rotor Tip Clearances. *Journal of Turbomachinery*, 114:675–685, 1992. ISSN 0889504X. doi: 10.1115/1.2929192.

[38] N. Gourdain, F. Sicot, F. Duchaine, and L. Gicquel. Large eddy simulation of flows in industrial compressors: a path from 2015 to 2035. *Philosophical Transactions of the Royal Society A: Mathematical, Physical and Engineering Sciences*, 372(2022):20130323, August 2014. doi: 10.1098/rsta.2013.0323. URL https://doi.org/10.1098/rsta.2013.0323.

[39] H L Grant. The large eddies of turbulent motion. *Journal of Fluid Mechanics*, 4(02):149–190, 1958. ISSN 0022-1120. doi: doi:10.1017/S0022112058000379. URL http://dx.doi.org/10.1017/S0022112058000379{%}5Cnhttp://journals.cambridge.org/download.php?file=/FLM/FLM4{_}02/S0022112058000379a.pdf{&}code=0bce8509a14cb628d69390f92ddf4fcd.

[40] William D Gropp and David E Keyes. *Domain decomposition methods in computational fluid dynamics*. NASA Langley Research Center, 1991.

[41] C. Hah and B. Lakshminarayana. Measurement and prediction of mean velocity and turbulence structure in the near wake of an airfoil. *Journal of Fluid Mechanics*, 115(-1):251, February 1982. doi: 10.1017/s0022112082000743. URL https://doi.org/10.1017/s0022112082000743.

[42] E J Hall. Aerodynamic modelling of multistage compressor flow fields Part 2: modelling deterministic stresses. *Proceedings of the Institution of Mechanical Engineers, Part G: Journal of Aerospace Engineering*, 212(2):91–107, 1998. ISSN 0954-4100. doi: 10.1243/0954410981532162. URL http://pig.sagepub.com/lookup/doi/10.1243/0954410981532162.

[43] Edward J Hall. Aerodynamic modeling of multistage compressor flowfields - part 1: analysis of rotor/stator/rotor aerodynamic interaction. *International Gas Turbine and Aeroengine Congress and Exhibition*, 1997.

[44] Charles Hirsch. Chapter 3 - The Mathematical Nature of the Flow Equations and Their Boundary Conditions. In Charles Hirsch, editor, *Numerical Computation of Internal and External Flows (Second Edition)*, pages 105–140. Butterworth-Heinemann, Oxford, second edi edition, 2007. ISBN 978-0-7506-6594-0. doi: https://doi.org/10.1016/B978-075066594-0/50043-6. URL http://www.sciencedirect.com/science/article/pii/B9780750665940500436.

[45] Charles Hirsch. Chapter 6 - Structured and Unstructured Grid Properties. In Charles Hirsch, editor, *Numerical Computation of Internal and External Flows (Second Edition)*, pages 249–277. Butterworth-Heinemann, Oxford,

second edi edition, 2007. ISBN 978-0-7506-6594-0. doi: https://doi.org/10.1016/B978-075066594-0/50047-3. URL http://www.sciencedirect.com/science/article/pii/B9780750665940500473.

[46] Charles Hirsch. Chapter 8 - General Properties and High-Resolution Numerical Schemes. In Charles Hirsch, editor, *Numerical Computation of Internal and External Flows (Second Edition)*, pages 337–409. Butterworth-Heinemann, Oxford, second edi edition, 2007. ISBN 978-0-7506-6594-0. doi: https://doi.org/10.1016/B978-075066594-0/50050-3. URL http://www.sciencedirect.com/science/article/pii/B9780750665940500503.

[47] Charles Hirsch. Chapter 10 - iterative methods for the resolution of algebraic systems. In Charles Hirsch, editor, *Numerical Computation of Internal and External Flows (Second Edition)*, pages 491 – 539. Butterworth-Heinemann, Oxford, second edition edition, 2007. ISBN 978-0-7506-6594-0. doi: https://doi.org/10.1016/B978-075066594-0/50053-9. URL http://www.sciencedirect.com/science/article/pii/B9780750665940500539.

[48] J. H. Horlock. Flow Through a Repeating Stage in an Axial Compressor: A Reconsideration. *Journal of Turbomachinery*, 126(4):677, 2005. ISSN 0889504X. doi: 10.1115/1.1791282.

[49] J. H. Horlock and J. D. Denton. A review of some early design practice using CFD and a current perspective. In *Volume 6: Turbo Expo 2003, Parts A and B*. ASMEDC, January 2003. doi: 10.1115/gt2003-38973. URL https://doi.org/10.1115/gt2003-38973.

[50] A.K.M.F. Hussain and W C Reynolds. The mechanics of an organized wave in turbulent shear flow. *Journal of Fluid Mechanics*, 41, 1970. ISSN 0022-1120. doi: 10.1017/S0022112072000667.

[51] Smagorinsky J. General circulation experiments with the primitive equations. *Monthly Weather Review*, 91(3):99–164, 1963. ISSN 0027-0644. doi: 10.1175/1520-0493(1963)091<0099:GCEWTP>2.3.CO;2. URL http://journals.ametsoc.org/doi/abs/10.1175/1520-0493(1963)091{%}3C0099:GCEWTP{%}3E2.3.CO;2.

[52] T O Jelly, I J Day, and L di Mare. Phase-averaged flow statistics in compressors using a rotated hot-wire technique. *Experiments in Fluids*, 58(5):1–17, 2017. ISSN 07234864. doi: 10.1007/s00348-017-2326-x.

[53] Javier Jiménez. The largest scales of turbulent wall flows. *Center for Turbulence Research Annual Research Briefs*, pages 137–154, 1998.

[54] Javier Jiménez, Sergio Hoyas, Mark P Simens, and Yoshinori Mizuno. Turbulent boundary layers and channels at moderate Reynolds numbers. *Journal of Fluid Mechanics*, 657:335–360, 2010. ISSN 0022-1120. doi: 10.1017/S0022112010001370.

[55] L. E. JONES, R. D. SANDBERG, and N. D. SANDHAM. Direct numerical simulations of forced and unforced separation bubbles on an airfoil at incidence. *Journal of Fluid Mechanics*, 602:175–207, April 2008. doi: 10.1017/s0022112008000864. URL https://doi.org/10.1017/s0022112008000864.

[56] W. P. Jones and M. Wille. Large-eddy simulation of a plane jet in a cross-flow. *International Journal of Heat and Fluid Flow*, 17(3):296–306, 1996. ISSN 0142727X. doi: 10.1016/0142-727X(96)00045-8.

[57] Ahmed Khamayseh, Andrew Kuprat, and C. Wayne Mastin. Boundary Orthogonality in Elliptic Grid Generation. In Nigel Weatherill, Bharat Soni, and Joe Thompson, editors, *Handbook of Grid Generation*, chapter 6. CRC Press, dec 1998. ISBN 978-0-8493-2687-5. doi: 10.1201/9781420050349. URL https://www.taylorfrancis.com/books/9781420050349.

[58] H T Kim, S J Kline, and D W C Reynolds. The production of turbulence near a smooth wall in a turbulent boundary layer. *Journal of Fluid Mechanics*, 50(1): 133–160, 1971. ISSN 0022-1120. doi: 10.1017/S0022112071002490.

[59] J Kim, P Moin, and R Moser. Turbulence statistics in fully developed channel flow at low Reynolds number. *Journal of Fluid Mechanics*, 177(-1):133–166, 1987. ISSN 0022-1120. doi: 10.1017/S0022112087000892. URL http://www.scopus.com/inward/record.url?eid=2-s2.0-0023155294{&}partnerID=40{&}md5=e684cff8667802c299fca71d2bafef8f.

[60] S J Kline, W C Reynolds, F A Schraubt, and P W Runstadlers. The structure of turbulent boundary layers. *J . Fluid Meeh*, 30(4):741–773, 1967. ISSN 0022-1120. doi: 10.1017/S0022112067001740.

[61] Toshio Kobayashi, Youhei Morinishi, and Keon-Je Oh. Large eddy simulation of backward-facing step flow. *Communications in Applied Numerical Methods*, 8(7):431–441, 1992. doi: 10.1002/cnm.1630080703. URL https://onlinelibrary.wiley.com/doi/abs/10.1002/cnm.1630080703.

[62] Robert H. Kraichnan. Eddy Viscosity in Two and Three Dimensions. *Journal of the Atmospheric Sciences*, 33:1521–1536, 1976.

[63] A. G. Kravchenko and P. Moin. On the effect of numerical errors in large Eddy simulations of turbulent flows. *Journal of Computational Physics*, 131(2):310–322, 1997. ISSN 00219991. doi: 10.1006/jcph.1996.5597.

[64] Culbert B Laney. *Nonlinear Stability*, pages 272–306. Cambridge University Press, 1998. doi: 10.1017/CBO9780511605604.020.

[65] John Leggett, Stephan Priebe, Aamir Shabbir, Richard Sandberg, Edward Richardson, and Vittorio Michelassi. LES loss prediction in an axial compressor cascade at off-design incidences with free stream disturbances. In *Volume 2A: Turbomachinery*. American Society of Mechanical Engineers, June 2017. doi: 10.1115/gt2017-64292. URL https://doi.org/10.1115/gt2017-64292.

[66] D. K. Lilly. A proposed modification of the Germano subgrid-scale closure method. *Physics of Fluids A*, 4(3):633–635, 1992. ISSN 08998213. doi: 10.1063/1.858280.

[67] D.K. Lilly. On the application of the Eddy Viscosity Concept in the Interital Subrange of Turbulence. *NCAR Manuscript*, 1966. ISSN 09592989. doi: 10.3233/BME-130937.

[68] C. C. Lin. On Taylor's Hypothesis and the Acceleration Terms in the Navier-Stokes Equations. *Quarterly of Applied Mathematics*, X(4):295–306, 1953. doi: 10.1142/9789814415651_0011.

[69] J T C Liu. Contributions to the understanding of large-scale coherent structures in developing free turbulent shear flows. *Advances in Applied Mechanics*, 26:183–309, 1986.

[70] J T C Liu and L Merkine. Energy integral description of the development of Kelvin-Helmholtz billows. *Tellus*, 28(3):197–214, 1976.

[71] Z Liu, R J Adrian, and T J Hanratty. Large-scale modes of turbulent channel flow: transport and structure. *Journal of Fluid Mechanics*, 448:53–80, 2001. ISSN 0022-1120. doi: 10.1017/S0022112001005808.

[72] Z C Liu, R J Adrian, and T J Hanratty. Reynolds number similarity of orthogonal decomposition of the outer layer of turbulent wall flow. *Physics of Fluids*, 6(8): 2815–2819, 1994. ISSN 10706631. doi: 10.1063/1.868169.

[73] J L Lumley. The Structure of Inhomogeneous Turbulent Flows. In A M Yaglom and V I Tatarski, editors, *Atmospheric turbulence and radio propagation*, pages 166–178. Nauka, Moscow, 1967.

[74] John L Lumley. Coherent structures in turbulence. In *Transition and turbulence*, volume 1, pages 215–242, 1981.

[75] T.S. Lund and H.-J. Kaltenbach. Experiments with explicit filtering for LES using a finite-difference method. *Center for Turbulence Research Annual Research Briefs*, pages 91–105, 1995.

[76] R Mankbadi and J T C Liu. A study of the interactions between large-scale coherent structures and fine-grained turbulence in a round jet. *Proceesdings and Philosophical Transactions of the Royal Society*, 298(1443), 1981.

[77] N N Mansour, J Kim, and P Moin. Reynolds-stress and dissipation-rate budgets in a turbulent channel flow. *Journal of Fluid Mechanics*, 194: 15–44, 1988. ISSN 1469-7645. doi: 10.1017/S0022112088002885. URL http://journals.cambridge.org/article{_}S0022112088002885{%}5Cnhttp://journals.cambridge.org/action/displayAbstract?fromPage=online{&}aid=394546{&}fileId=S0022112088002885{%}5Cnhttp://journals.cambridge.org/action/displayFulltext?type=1{&}fid=394547{&}jid=FLM{&}volumeId=.

[78] W.A. McMullan and G.J. Page. Towards large eddy simulation of gas turbine compressors. *Progress in Aerospace Sciences*, 52:30–47, July 2012. doi: 10.1016/j.paerosci.2011.12.002. URL https://doi.org/10.1016/j.paerosci.2011.12.002.

[79] Charles Meneveau. Statistics of turbulence subgrid-scale stresses: Necessary conditions and experimental tests. *Physics of Fluids*, 6(2):815–833, 1994. ISSN 10706631. doi: 10.1063/1.868320.

[80] G.-J. Michon, H. Miton, and N. Ouayhaya. Unsteady off-design velocity and reynolds stresses in an axial compressor. *Journal of Propulsion and Power*, 21(6):961–972, November 2005. doi: 10.2514/1.10326. URL https://doi.org/10.2514/1.10326.

[81] P Moin. Probing turbulence via large eddy simulation. *Aerospace Sciences Meetings*, 1984. ISSN 01463705. doi: 10.2514/6.1984-174. URL http://dx.doi.org/10.2514/6.1984-174.

[82] P. Moin, W. C. Reynolds, and J. H. Ferziger. Large eddy simulation of incompressible turbulent channel flow. (May 1978):21360081, 1978. URL http://hdl.handle.net/2060/19780023440.

[83] P. Moin, K. Squires, W. Cabot, and S. Lee. A dynamic subgrid-scale model for compressible turbulence and scalar transport. *Physics of Fluids A: Fluid Dynamics*, 3(11):2746–2757, November 1991. doi: 10.1063/1.858164. URL https://doi.org/10.1063/1.858164.

[84] Parviz Moin and John Kim. Numerical investigation of turbulent channel flow. *Journal of Fluid Mechanics*, 118(-1):341, May 1982. doi: 10.1017/s0022112082001116. URL https://doi.org/10.1017/s0022112082001116.

[85] Parviz Moin and Robert D Moser. Characteristic-eddy decomposition of turbulence in a channel. *Journal of Fluid Mechanics*, 200: 471, 1989. ISSN 0022-1120. doi: 10.1017/S0022112089000741. URL http://journals.cambridge.org/abstract{_}S0022112089000741{%}5Cnhttp://www.journals.cambridge.org/abstract{_}S0022112089000741.

[86] J F Morrison, W Jiang, B J McKeon, and A J Smits. Reynolds Number Dependence of Streamwise Velocity Spectra in Turbulent Pipe Flow. *Physical Review Letters*, 88(21):214501, 2002. ISSN 0031-9007. doi: 10.1103/PhysRevLett.88.214501. URL https://link.aps.org/doi/10.1103/PhysRevLett.88.214501.

[87] Y. Nagano, M. Tagawa, and T. Tsuji. Effects of adverse pressure gradients on mean flows and turbulence statistics in a boundary layer. In *Turbulent Shear Flows 8*, pages 7–21. Springer Berlin Heidelberg, 1993. doi: 10.1007/978-3-642-77674-8_2. URL https://doi.org/10.1007/978-3-642-77674-8_2.

[88] A. Nawab and L. Di Mare. Re_τ scaling of POD modes in plane channel flow. *Physics of Fluids*, 30(5), 2018. ISSN 10897666. doi: 10.1063/1.5024603.

[89] A. Nawab, L. Di Mare, F. Wang, and Adamczyk J. J. Reynolds stress field and turbulent kinetic energy budget in a repeating compressor stage. *ASME Turbo Expo 2020*, Under review.

[90] Moin P. and Kim J. Numerical investigation of turbulent channel flow. *Journal of Fluid Mechanics*, 118:341–377, 1982.

[91] Ugo Piomelli and Elias Balaras. Wall-Layer Models for Large Eddy Simulations. *Annual Review of Fluid Mechanics*, 34:349–374, 2002. ISSN 0066-4189. doi: 10.1146/annurev.fluid.34.082901.144919. URL http://www.annualreviews.org/doi/abs/10.1146/annurev.fluid.34.082901.144919?journalCode=fluid.

[92] Ugo Piomelli and Junhui Liu. Large-eddy simulation of rotating channel flows using a localized dynamic model. *Physics of Fluids*, 7(4):839–848, 1995. ISSN 10706631. doi: 10.1063/1.868607.

[93] Ugo Piomelli and Thomas A. Zang. Large-eddy simulation of transitional channel flow. *Computer Physics Communications*, 65(1-3):224–230, 1991. ISSN 00104655. doi: 10.1016/0010-4655(91)90175-K.

[94] Ugo Piomelli, Parviz Moin, and Joel H. Ferziger. Model consistency in large eddy simulation of turbulent channel flows. *Physics of Fluids*, 31(7):1884–1891, 1988.

[95] Pawel J. Przytarski and Andrew P. S. Wheeler. The effect of rotor-stator gap on repeating-stage compressor loss. In *Volume 2A: Turbomachinery*. American Society of Mechanical Engineers, June 2019. doi: 10.1115/gt2019-91007. URL https://doi.org/10.1115/gt2019-91007.

[96] Jeffrey Rambo and Yogendra Joshi. Reduced Order Modeling of Steady Turbulent Flows using the POD. *2005 ASME Summer Heat TRansfer Conference*, (July), 2005. doi: 10.2514/6.2016-0462.

[97] W C Reynolds and A.K.M.F. Hussain. The mechanics of an organized wave in turbulent shear flow. Part 3. Theoretical models and comparisons with experiments. *Journal of Fluid Mechanics*, 54:263–288, 1972.

[98] C. M. Rhie and W. L. Chow. Numerical Study of the Turbulent Flow Past an Airfoil with Trailing Edge Separation. *AIAA Journal*, 21(11):1525 – 1532, 1983.

[99] Chae M. Rhie, Aaron J. Gleixner, David A. Spear, Craig J. Fischberg, and Robert M. Zacharias. Development and Application of a Multistage Navier-Stokes Solver: Part I — Multistage Modeling Using Bodyforces and Deterministic Stresses. *International Gas Turbine and Aeroengine Congress and Exhibition*, 1995. doi: 10.1115/95-gt-342.

[100] P Sagaut. *Large Eddy Simulation for Incompressible Flows*. Scientific Computation. Springer-Verlag, Berlin/Heidelberg, 2006. ISBN 3-540-26344-6. doi: 10.1007/b137536. URL http://link.springer.com/10.1007/b137536.

[101] Pierre Sagaut. Functional Modeling (Isotropic Case). In *Large Eddy Simulation for Incompressible Flows*, pages 91–186. Springer-Verlag, Berlin/Heidelberg, 2006. doi: 10.1007/3-540-26403-5_5. URL http://link.springer.com/10.1007/3-540-26403-5{_}5.

[102] Pierre Sagaut. Formal Introduction to Scale Separation: Band-Pass Filtering. In *Large Eddy Simulation for Incompressible Flows*, pages 15–44. Springer-Verlag, Berlin/Heidelberg, 2006. doi: 10.1007/3-540-26403-5_2. URL http://link.springer.com/10.1007/3-540-26403-5{_}2.

[103] Richard D. Sandberg and Vittorio Michelassi. The current state of high-fidelity simulations for main gas path turbomachinery components and their industrial impact. *Flow, Turbulence and Combustion*, 102(4):797–848, February 2019. doi: 10.1007/s10494-019-00013-3. URL https://doi.org/10.1007/s10494-019-00013-3.

[104] M. T. Schobeiri and S. Abdelfattah. On the reliability of RANS and URANS numerical results for high-pressure turbine simulations: A benchmark experimental and numerical study on performance and interstage flow behavior of high-pressure turbines at design and off-design conditions using two different turbine designs. *Journal of Turbomachinery*, 135(6), September 2013. doi: 10.1115/1.4024787. URL https://doi.org/10.1115/1.4024787.

[105] Ulrich Schumann and Brian Edward Launder. Stochastic backscatter of turbulence energy and scalar variance by random subgrid-scale fluxes. *Proceedings of the Royal Society of London. Series A: Mathematical and Physical Sciences*, 451(1941):293–318, 1995. doi: 10.1098/rspa.1995.0126.

[106] Wei Shyy. A study of finite difference approximations to steady-state, convection-dominated flow problems. *Journal of Computational Physics*, 57(3):415–438, 1985. ISSN 10902716. doi: 10.1016/0021-9991(85)90188-3.

[107] Wei Shyy. *Computational Modeling for Fluid Flow and Interfacial Transport (Dover Books on Engineering)*. Dover Publications, Inc., New York, NY, USA, 2006. ISBN 0486453030.

[108] Juan A Sillero, Javier Jimenez, and Robert D Moser. Two-point statistics for turbulent boundary layers and channels at Reynolds numbers up to $\delta^+ \approx 2000$. *Physics of Fluids*, 26(10), 2014. ISSN 10897666. doi: 10.1063/1.4899259.

[109] L H Jr. Smith. Casing Boundary Layers in Multistage Axial-Flow Compressors. *Flow Research in Blading*, 1970.

[110] Lloyd Holly Smith. Wake dispersion in turbomachines. 1966.

[111] Francesco Soranna, Yi-Chih Chow, Oguz Uzol, and Joseph Katz. The effect of inlet guide vanes wake impingement on the flow structure and turbulence around a rotor blade. *Journal of Turbomachinery*, 128(1):82–95, February 2005. doi: 10.1115/1.2098755. URL https://doi.org/10.1115/1.2098755.

[112] Francesco Soranna, Yi-Chih Chow, Oguz Uzol, and Joseph Katz. The effects of inlet guide vane-wake impingement on the boundary layer and the near-wake of a rotor blade. *Journal of Turbomachinery*, 132(4), May 2010. doi: 10.1115/1.3149282. URL https://doi.org/10.1115/1.3149282.

[113] Philippe R. Spalart and Jonathan H. Watmuff. Experimental and numerical study of a turbulent boundary layer with pressure gradients. *Journal of Fluid Mechanics*, 249(-1):337, April 1993. doi: 10.1017/s002211209300120x. URL https://doi.org/10.1017/s002211209300120x.

[114] Stefan P. Spekreisje. Elliptic Generation Systems. In *Handbook of Grid Generation*, chapter 4. 1998.

[115] Stefan Stollenwerk and Edmund Kügeler. Deterministic stress modeling for multistage compressor flowfields. In *Volume 6B: Turbomachinery*. American Society of Mechanical Engineers, June 2013. doi: 10.1115/gt2013-94860. URL https://doi.org/10.1115/gt2013-94860.

[116] G I Taylor. The Spectrum of Turbulence. *Proceedings of the Royal Society of London. Series A - Mathematical and Physical Sciences*, 164(919):476–490, 1938. doi: 10.1098/rspa.1938.0032.

[117] H. Tennekes and J.L. Lumley. *A First Course in Turbulence*. The MIT Press, 1972.

[118] Joe F Thompson, Z U A Warsi, and C Wayne Mastin. *Numerical Grid Generation: Foundations and Applications*. Elsevier North-Holland, Inc., New York, NY, USA, 1985. ISBN 0-444-00985-X.

[119] A A Townsend. Grenzschichtforschung / Boundary Layer Research: Symposium Freiburg/Br. 26.Bis 29. August 1957 / Symposium Freiburg/Br. August 26–29, 1957. chapter The turbul, pages 1–15. Springer Berlin Heidelberg, Berlin, Heidelberg, 1958. ISBN 978-3-642-45885-9. doi: 10.1007/978-3-642-45885-9_1. URL http://dx.doi.org/10.1007/978-3-642-45885-9{_}1.

[120] A A Townsend. *The Structure of Turbulent Shear Flow*. Cambridge University Press, second edition, 1976.

[121] Elie Track, Nancy Forbes, and George Strawn. The end of moore's law. *Computing in Science & Engineering*, 19(2):4–6, March 2017. doi: 10.1109/mcse.2017.25. URL https://doi.org/10.1109/mcse.2017.25.

[122] Eli Turkel. Accuracy of schemes with nonuniform meshes for compressible fluid flows. *Applied Numerical Mathematics*, 2(6):529–550, 1986. ISSN 01689274. doi: 10.1016/0168-9274(86)90006-1.

[123] James Tyacke, Paul Tucker, Richard Jefferson-Loveday, Nagabushana Rao Vadlamani, Robert Watson, Iftekhar Naqavi, and Xiaoyu Yang. Large eddy simulation for turbines: Methodologies, cost and future outlooks. *Journal of Turbomachinery*, 136(6), November 2013. doi: 10.1115/1.4025589. URL https://doi.org/10.1115/1.4025589.

[124] Oguz Uzol, Yi-Chih Chow, Joseph Katz, and Charles Meneveau. Average Passage Flow Field and Deterministic Stresses in the Tip and Hub Regions of a Multistage Turbomachine. *Journal of Turbomachinery*, 125(4):714, 2003. ISSN 0889504X. doi: 10.1115/1.1625692.

[125] Allan G van de Wall. *A transport todel for the Deterministic stresses associated with turbomachinery blade row interactions*. PhD thesis, Case Western Reserve University, 1999.

[126] Allan G van de Wall, Jaikrishnan R Kadambi, and John J Adamczyk. A Transport Model for the Deterministic Stresses Associated With Turbomachinery Blade Row Interactions. *ASME J. Turbomach.*, 122(4):593, 2000. ISSN 0889504X. doi: 10.1115/1.1312802.

[127] Dominic Alexander Von Terzi. Numerical investigation of transitional and turbulent backward-facing step flows, 2004. URL http://hdl.handle.net/10150/280538.

[128] Feng Wang. *Whole Aero-Engine Meshing and CFD Simulation*. PhD thesis, Imperial College London, 2013.

[129] Feng Wang and Luca di Mare. Mesh Generation for Turbomachinery Blade Passages with Three-Dimensional Endwall Features. *Journal of Propulsion and Power*, 33(6):1459–1472, 2017. ISSN 0748-4658. doi: 10.2514/1.b36356.

[130] Feng Wang, Mauro Carnevale, Luca di Mare, and Simon Gallimore. Simulation of multistage compressor at off-design conditions. *Journal of Turbomachinery*, 140 (2), December 2017. doi: 10.1115/1.4038317. URL https://doi.org/10.1115/1.4038317.

[131] Feng Wang, Mauro Carnevale, and Luca di Mare. Numerical Study of Deterministic Fluxes in Compressor Passages. *Journal of Turbomachinery*, 140(10):101005, 2018. ISSN 0889-504X. doi: 10.1115/1.4041450.

[132] R. F. Warming and B. J. Hyett. The modified equation approach to the stability and accuracy analysis of finite-difference methods. *Journal of Computational Physics*, 14(2):159–179, feb 1974. ISSN 10902716. doi: 10.1016/0021-9991(74)90011-4. URL https://linkinghub.elsevier.com/retrieve/pii/0021999174900114.

[133] S. A Weichert. Tip clearance flows in axial compressors: stall inception and stability enhancement. (September), 2011. URL http://ethos.bl.uk/OrderDetails.do?uin=uk.bl.ethos.552849.

[134] Stephanie Weichert and Ivor Day. Detailed Measurements of Spike Formation in an Axial Compressor. *Journal of Turbomachinery*, 136(5):051006, 2013. ISSN 0889-504X. doi: 10.1115/1.4025166.

[135] M. Wille. *Large Eddy Simulation of jets in cross flows*. PhD thesis, Imperial College of Science, Technology and Medicine, 1997.

[136] TAMER A. ZAKI, JAN G. WISSINK, WOLFGANG RODI, and PAUL A. DURBIN. Direct numerical simulations of transition in a compressor cascade: the influence of free-stream turbulence. *Journal of Fluid Mechanics*, 665:57–98, October 2010. doi: 10.1017/s0022112010003873. URL https://doi.org/10.1017/s0022112010003873.